Ultrafast coherent XUV diffractive imaging at nanometer scale

Xunyou Ge

UNIVERSITE PARIS-SUD 11

École Doctorale Ondes et Matière

THÈSE DE DOCTORAT

Effectuée au Service des Photons, Atomes et Molécules (SPAM), IRAMIS, DSM, Commissariat à l'Energie Atomique, Saclay, France

Spécialité : Lasers et Matière

Présentée pour obtenir le grade de DOCTEUR EN SCIENCES DE L'UNIVERSITE PARIS-SUD XI

Xunyou GE

Imagerie ultrarapide à l'échelle nanométrique par diffraction XUV cohérente

Soutenue le 11 décembre 2012 devant le jury composé de :

M. Eric CONSTANT	Rapporteur
M. Vincent FAVRE-NICOLIN	Rapporteur
M. Jan LUNING	
M. David ROS	
M. Hamed MERDJI	Directeur de thèse

Acknowledgements

I owe my gratitude to many people for this achievement. To those who have directly involved in my work, to those who have given me advice and ideas, and to those who have supported me morally and always stood by my side, I would like to say: *Merci beaucoup !!!!*

Great thanks to Hamed Merdji, who has proposed this thesis subject to me and provided academic and research guidance during these three years. He can always lighten up the direction when I got lost in the great amount of confusing experimental data. I very much appreciate his patience for listening to my questions and ideas (even stupid ones). He always cheered me on and gave me a big smile every time I got a little progress. His help is not only in scientific area but also in language, both in English and French. Great thanks to him reviewing this document with countless corrections and suggestions. Thanks also to his generous, inviting the whole imaging group to delicious lunches and dinners.

Many thanks to David Gauthier, Mathieu Ducousso and Willem Boutu, who have deeply involved in different stages of my work. David has taught me step by step how to manipulate the entire beamline and I have learned lots of practical skills from him during the imaging experiments. Along with Mathieu and Willem, we have passed many nights on magnetic experiences. Thanks to Willem who drove me home after exhausting experiment.

Thanks to all the members of our imaging group, Fan Wang, Aura Ines Gonzalès-Angarita, Xiaochi Liu, Ana Borta, Benjamin Barbrel, Thai-Hoa Chung and Mathieu Durero, who have given me many help, advices and discussions for my work and lab life.

Thanks to all the members of Attophysique group, Antoine Camper, Nan Lin, Zolt Diveki, Stephan Haessler, Elizabeth English, Bastian. Manschwetus, Pierre Breger, Marie Géléoc, Thierry Auguste, Thierry Ruchon, Pascal Salière, Christian Cornaggia and Bertrand Carré, with whom I have passed these threes years with great happiness.

Special thanks to Marc Billon, Gilles Le Cheavllier and all the members of mechanical and electronic team for their very important and always promptly support for our experiments.

Many thanks to Benoit Mahieu, Olivier Gobert, Michel Perdrix and all the members of laser group. I very much appreciate Olivier that he stayed very late to maintain the laser for us during countless nights.

Thanks to all the collaborators with whom I have worked together: Pierre Thibault, Manuel Guizar-Sicairos, Filip Maia, Franck Fortuna, Julien Gautier, Guillaume Lambert, Boris Vodungbo, Philippe Zeitoun, Jonathan Potier, Jan Luning ….

Thanks to the administrative staff and the chef of SPAM and EDOM: Jacqueline Bandura, Véronique Gereczy, Martine Basset, Christophe Blondel, Bertrand Bourguignon and Cécile Reynaud.

Great thanks to my thesis committee: Eric Constant, Vincent Favre-Nicolin, Jan Luning, Antoine Rousse and David Ros for taking the time to read this document, for the comments, discussions and feedback that they provided.

Greatest thanks to my girlfriend, Jun Wang, and my parents for their most important support that I have ever got to encourage me going ahead. ***I love you !!!!***

Abstract

Ultrafast coherent XUV diffractive imaging at nanometer scale

Ultrafast imaging of isolated objects with nanometric spatial resolution is a great challenge in our time. The lensless imaging techniques have shown great potential to answer this challenge. In lensless imaging, one can reconstruct sample images from their diffraction patterns with computational algorithms, which replace the conventional lens systems. Using ultrafast and coherent light sources, such as free electron laser and high order harmonics, one can investigate dynamic phenomena at the femtosecond time scale.

In this thesis work, I present the lenless imaging experiments using XUV radiation provided by a laser driven high order harmonic beamline. The manuscript is composed of an introduction, a chapter of theoretical background, three chapters of main research work and a general conclusion with perspectives. The first part of this work concerns the development of the harmonic beamline to optimize the illumination condition for lensless imaging. The second part concentrates on the imaging techniques: the Coherent Diffraction Imaging (CDI), the Fourier Transform Holography (FTH) and the Holography using extended references (HERALDO). The reconstructions have achieved 78 nm spatial resolution in case of CDI and 112 nm resolution in case of HERALDO, both in single-shot regime corresponding to a temporal resolution of 20 fs. The third part presents the first physical application on the harmonic beamline using the lensless imaging. Samples with magnetic nano-domains have been studied with sub-100 nm spatial resolution, which paves the way for ultrafast magnetic dynamic studies. At the end, single-shot 3D imaging and further beamline development have been discussed.

Key-words: Coherent diffraction, Lensless imaging, High order harmonics generation, XUV source, Modal filtering, Fourier transform holography, Extended references, Signal to noise ratio, Resonant elastic scattering, Single shot probing, Ultrafast spectroscopy, Nanomagnetism.

Résumé

Imagerie ultrarapide à l'échelle nanométrique par diffraction XUV cohérente

Imager des objets apériodiques à une échelle nanométrique et à une échelle femtoseconde est un vrai challenge. Les techniques d'imagerie « sans lentille » sont des moyens puissants pour répondre à ce besoin. En utilisant des sources ultrarapides (~fs) et cohérentes (*e.g.* les lasers à électron libre ou les harmoniques d'ordres élevés), ces techniques permettent d'imager des objets à partir de leurs figures de diffraction, remplaçant les optiques conventionnelles du système d'imagerie par un algorithme numérique.

Dans ce travail de thèse, je présente des expériences d'imagerie en utilisant un rayonnement extrême-UV (15~40 nm) produit par la génération d'harmoniques d'ordre élevé d'un laser infrarouge puissant. Ce manuscrit est constitué d'une introduction, un chapitre de bases théoriques, de trois chapitres expérimentaux et d'une conclusion générale dotée de perspectives. La première partie expérimentale de ce travail de thèse porte sur les développements et caractérisations de la ligne de lumière avec l'objectif de générer un maximum de photons harmoniques cohérents avec un front d'onde plat. La seconde est consacrée aux expériences et à l'analyse de trois techniques d'imagerie « sans lentille » : imagerie par diffraction cohérente (CDI), holographie par transformée de Fourier (FTH) et holographie avec références étendues (HERALDO). Nous avons pu imager des objets avec une résolution spatiale de 78 nm en CDI et de 112 nm en HERALDO. Les deux techniques permettent toutes deux une résolution temporelle de 20 fs. La troisième partie expérimentale est une première application en physique du solide des mesures de diffraction cohérente sur la ligne d'harmoniques. Il s'agit d'études statiques et dynamiques de nano-domaines magnétiques avec une résolution spatiale sub-100 nm à l'échelle femtoseconde. Des perspectives des techniques d'imagerie 3D et des développements potentiels de la ligne d'harmoniques sont présentés à la fin.

Mots-clefs : Diffraction cohérente, Imagerie sans lentille, Génération d'harmoniques d'ordre élevé, Source UV-X, Filtrage modal, Holographie par transformée de Fourier, Références holographiques étendues, Rapport signal sur bruit, Diffusion résonante élastique, Mesures simples tirs, Spectroscopie ultrarapide, Nano-magétisme.

Contents

Introduction

Seeing is believing.

1639 J. Clarke Paræmiologia Anglo-Latina 90

Water and oxygen gave us life, and fire lightened the whole world. Since the born of a baby, he has eyes to see, ears to hear, a tongue to taste, a nose to smell, hands to touch and a brain to think. Among all of the sense organs of a human being, eyes are the most important ones for us to perceive the world.

Since the very beginning of human history, people have seen thousands of natural phenomena. Some of them seem "natural" to us, while the others do not. The wise start to think about the logic behind those "natural" ones and try to interpret the "unbelievable" ones. Here comes the **Physics**, which means "*nature*" in ancient Greek. During the development of physics, "*seeing something new*" always leads to big scientific debates and fundamental advances in theory and experimental results, which opens gates of many new scientific areas. For a long time in old ages, eyes were the only tools to explore our world. The ability of an eye to distinguish fine details is often measured in cycles per degree (CPD), called visual acuity [1]. 50 CPD is the maximum theoretical resolution for an eye with excellent vision acuity, which equals to an angular resolution of about 1 minute of arc. The spatial resolution of human eye (about 100 μm at a reading distance of 350 mm) is precise enough in daily life, but far away from satisfying in scientific research.

The invention of optical microscope at the end of sixteenth century enables the visualization of objects or structures that are usually invisible to the naked eye. Standard microscopes combine convex and concave lenses equipped with a light source. As one of its founders, Robert Hooke, said, "…by the help of Microscopes, there is nothing so small as to escape our inquiry…" [2].

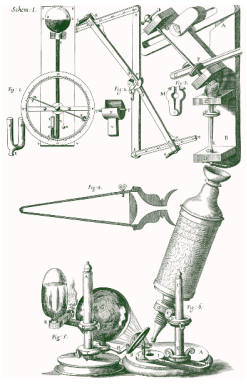

Drawings of instruments used by Robert Hooke.

Many scientific theories have been put forward to push the observation of small specimens down to micrometer scale. In the following decades, various microscope techniques have been developed, such as fluorescence microscope, phase contrast techniques, differential-interference contrast systems, etc. All of these advancements are improving the resolving power of microscopes to their theoretical boarders: the diffraction limit. Ernst Abbe has demonstrated mathematically that the spatial resolution of any conventional microscope is limited to half of the wavelength of the imaging light source [3]. His landmark article set a new spatial resolution barrier of 150-200 nm for human eyes equipped with a microscope, as human vision is usually in the 390-750 nm spectral range. This diffraction barrier has been impossible to break during most of the twentieth century. Only in recent researches, imaging techniques have been proposed to go beyond the diffraction barrier such as stimulated-emission-depletion microscopy, photo-activated localization microscopy, stochastic optical reconstruction microscopy, etc. [2]. However, the "easier" way to get better spatial resolution is to use shorter illuminating wavelength, such as X-ray radiation or electron beam.

The electron microscope is invented in 1930s. Thanks to the short wavelength of electron beam (100 000 times shorter than visible light), electron microscopes have a greater resolving power than optical microscope. Different types of electron microscope are developed to answer to different observation conditions: transmission electron microscope, scanning electron microscope, reflection electron microscope and etc. The spatial resolution achieved was better than 50 pm (1 pm = 10^{-12} m) [4]. The development of electron microscope has led to various applications in many scientific research areas, such as semiconductor, biology, nanotechnology, chemistry, life science and also industry production.

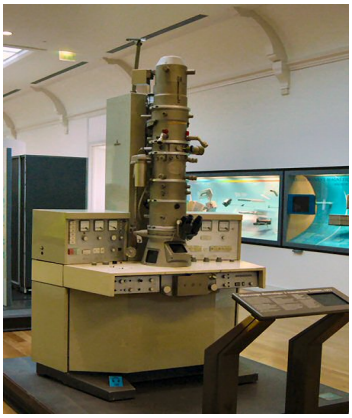

(1973) Siemens electron microscope

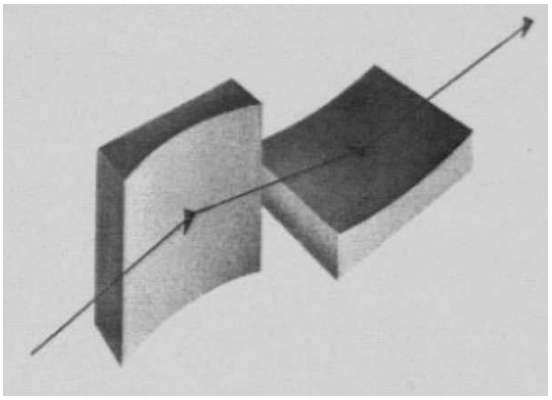

(1948) Kirkpatrick and Baez focusing system

Almost at the same time as the invention of the electron microscope, Paul Kirkpatrick and other pioneers brought first X-ray microscopes to the world in the 40s [5]. Crossed-1D-lenses focusing system using elliptical profile mirrors was first used to focus the X-ray beam, and then zone plates were suggested by Albert Baez to be used as X-ray lenses. With the arrival of synchrotron light sources, the first zone plate transmission X-ray microscopes were developed at DESY (Deutsches Elektronen-Synchrotron) in Hamburg and at ACO (Anneau de Collisions d'Orsay) in Orsay. And a major expansion of X-ray microscope was carried out with new light sources, such as ALS (Advanced Light Source) in Berkeley, ESRF (European Synchrotron Radiation Facility) in Grenoble, Spring-8 in Japan, Elettra in Trieste, etc. The applications of X-ray microscope grew up rapidly to magnetism, polymer science, geochemistry, etc. The spatial resolution of X-ray microscope lies between that of the electron microscope and the optical microscope.

Combining all the microscopy techniques, we have a wide range of spatial resolution to investigate and image different distance scale complex systems. Here comes the questions: can we see the dynamic of what we are looking at? Can we correctly capture the motion of the object that we are studying and understand the causes of its motion? To answer these questions, a time-resolved imaging equipment is required. In 1878, Eadweard Muybridge was successful to capture the first motion pictures of a galloping horse [6]. His pictures did not only answer the famous question: "whether all four feet of a horse were off the ground at the same time while trotting", but also first went beyond the limitation of human eye in time scale. Human eye is not able to identify motions that are more fleeting than an eye blink (~0.1 second). And the galloping horse is moving on a millisecond time scale.

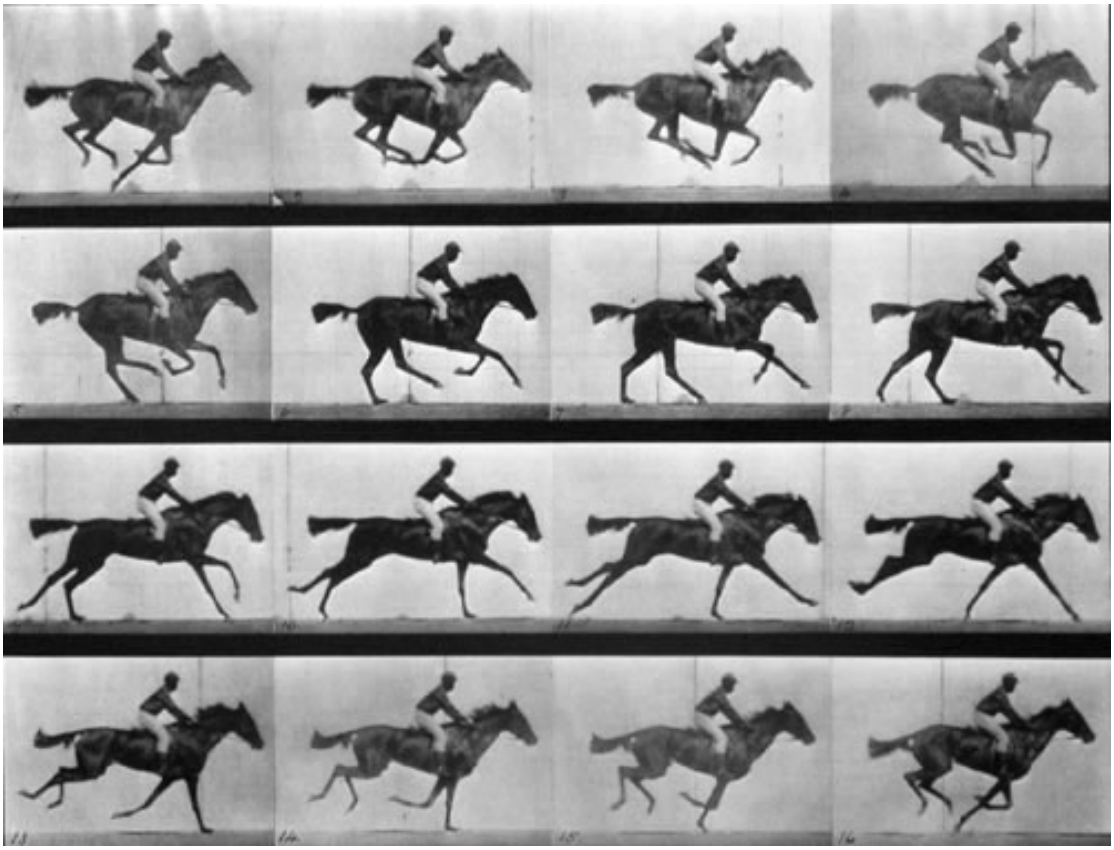

The horse in motion by Eadweard Muybridge in 1878

Science didn't stop here. In 1950, Ronald Norrish and George Porter (chemistry Nobel prize winners in 1967) have investigated the photochemical reactions using flash lamps with varying delays in the millisecond to microsecond range [7].

The invention of lasers the 60s has revolutionized Science: faster time scales have been accessible and new scientific subfields have exploded, such as femto-chemistry and femto-biology (1 femtosecond = 10^{-15} second). In the beginning of 21st century, the first experimental measurement of a train of 250 attosecond (10^{-18} second) pulses was demonstrated [8,9]. This train of attosecond pulses was a superposition of five consecutive harmonics generated by high order harmonic generation (HHG) in an atomic gas jet with an infrared pump laser. HHG source appeared to be a promising tool for ultrafast time-resolved measurements, down to attosecond time scales which are mostly related to electron motion.

Pioneering experiments demonstrated the measurements of electron dynamics with attosecond resolution, such as the measurement of the lifetime of M-shell vacancies of krypton [10], the intra-atomic transient electron dynamics [11] and the observation of the motion of a D_2^+ vibrational wave packet with a precision of about 200 attoseconds [12]. In May 2010, a German group has demonstrated the new world record for the shortest controllable time of light pulse – 12 attoseconds [13], which is half of the atomic unit of time – 24 attoseconds. Now people are talking about zeptosecond (10^{-21} second). However, experimental measurement combining atomic distance scale (sub-nanometer resolution) and attosecond time resolution is not yet demonstrated. This big challenge will require the invention of new imaging techniques with sub-atomic unit resolution simultaneously in space and time. 3D motion of electrons would then be accessible. This foreseen revolution will open a new era of physics and ultimately influence chemistry, biology and future technologies.

Free electron laser (FEL) [14] is a candidate with high potential for achieving this big challenge. It generates tunable, coherent and high power radiation within a large range of wavelengths from millimeter to ultraviolet or even X-ray (XFEL). Recent researches using intense FELs have demonstrated the capability of imaging nano-scale objects with a high spatial resolution on a femtosecond time scale, using the Coherent Diffractive Imaging (CDI) technique. CDI is a new technique that can image non-periodic object with spatial resolution down to the diffraction limit. Using ultrafast sources it has great potential to capture transient processes down to atomic scales. It can be applied using a wide range of radiation wavelength from infrared to X-rays.

The idea of CDI came from the successful crystallography diffraction methods. David Sayre first raised this question that whether a similar diffraction method could be applied to non-periodic objects in 1952 [15]. J.R. Fienup proposed a phase-retrieval algorithm to solve the phase problem in 1978 [16]. His algorithm is a modified version of Gerchberg-Saxton algorithm that is originally inspired from ideas used in electron microscopy [17]. For more details of the historical development of the phase-retrieval algorithm, please refer to the review of Henry Chapman and Keith Nugent [18].

CDI is a “lens-less”, aberration-free technique, so that the theoretical spatial resolution is only limited by the radiation wavelength. In the case of a coherent plane wave illumination, this resolution is determined by the maximum scattering angle of the diffraction pattern recorded by detector. Since the first demonstration of Miao and colleagues [19], many advances have been made using soft or hard X-ray synchrotron radiation or femtosecond soft X-ray free electron laser [20-24]. CDI becomes a powerful tool in many scientific areas ranging from biology to solid-state physics. The key words for CDI are *coherence* and *diffraction*. Indeed, the technique uses the measurement of a far field *diffraction* pattern to retrieve the spatial *amplitude* and *phase* of a real space object. The large-scale facilities – synchrotron light sources and FELs provide a large amount of photons promising a good signal-to-noise ratio in CDI. The high coherence of FELs and synchrotrons (using a pinhole in this case) ensures that the important phase information can be well “written” in the detected diffraction pattern. Moreover, the femtosecond pulse duration of FEL sources promises a bright future for ultrafast dynamic imaging at a nanometer or sub-nanometer scale.

FLASH in Hamburg (VUV FEL)

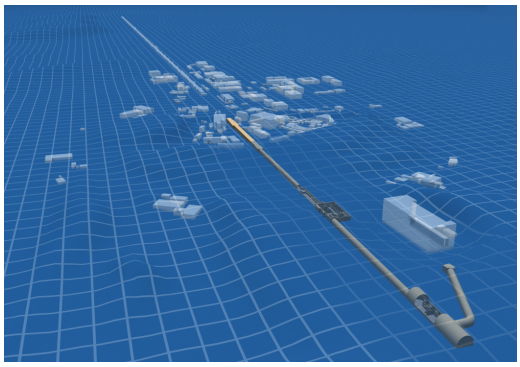

LCLS in Stanford (X-ray FEL)

However, these large-scale facilities cost expensive resources and have limited access beam time. These constraints limit the wide spread of ultrafast coherent diffractive imaging. The applications are then restricted. This limits the impact of this research, for example in the optimization of ultrafast nanoscale devices in communication, medicine or even in more industrial environments. Therefore, an inexpensive source would provide a very interesting alternative: high-order harmonic generation (HHG) sources can provide intense highly coherent soft X-ray photons with ultrafast pulse duration. The relatively small size and low cost of such light source makes the HHG source an ideal alternative to synchrotrons and FELs. Up to recently, the limited brightness of HHG source was a key limitation for a table-top application of CDI. However in 2007, Richard Sandberg and colleagues have succeeded in demonstrating CDI using a kHz table-top laser driven HHG source with a spatial resolution of 214nm [25]. The brightness of the harmonic beam was still limited, and the exposure time of this experiment was on the scale of an hour (up to 10^6 laser shots!) that is far from reaching single-shot ultrafast nanoscale imaging, required in many dynamical studies. In 2009, our research group at CEA (Commissariat à l'Energie Atomique et aux l'Energies alternatives) has demonstrated the first single-shot CDI using a table-top femtosecond soft X-ray laser harmonic source [26]. An isolated test nano-object was reconstructed with 119 nm spatial resolution in a single 20 fs-long shot. A spatial resolution of 62 nm was obtained from multiple laser shots (40 shots). In this context, I have joined the AttoPhysique group of CEA as a PhD student of Dr. Hamed Merdji in 2009.

Motivation and outline of thesis

The principle objective of this work is to perform extended developments and applications of ultrafast coherent imaging techniques using table-top harmonic source. I present all the efforts, either on the source or on the imaging techniques to build a reliable and powerful ultrafast microscope with nanometer spatial resolution and femtosecond temporal resolution. I then present a characterization of magnetic nano-domains at a sub-100 nm scale in a single femtosecond shot. This illustrates the potential of our table-top harmonic beamline for various scientific research areas such as material science, biology and chemistry.

This work is presented in five chapters.

Chapter 1 is dedicated to the description of the theoretical background of the lens-less imaging (also called coherent imaging). It starts with a presentation of the principle of the lens-less imaging. The first part is the mathematical description of diffraction and Fourier Transform that are the basics of diffraction pattern formation of the coherent imaging. The second part is the description of basic phase-retrieval algorithms and holographic techniques that are used in this work. The third part is a discussion of the beam requirements for lens-less imaging, followed by a brief description of the HHG process used as light source in this thesis work. This chapter should give a clear description of CDI and help to understand the ideas and methods used in the following chapters.

The main work and experimental results are presented respectively in Chapter 2, 3 and 4. They are presented around the 6 main publications published during my thesis work.

Chapter 2 starts with the description of the experimental setup – the table-top high flux harmonic beamline at CEA Saclay. The first step of this thesis work has been a complete optimization of the harmonic beamline from the very beginning of the infrared pump laser to the focusing optics at the end of the imaging setup. The optimization processes and results are presented in ***Paper I*** and ***Paper II*** attached to this chapter. The first one shows the optimization of the HHG and the diffraction stages. The objective has been to increase the photon flux, the coherence and the wave front quality of the harmonic beam. Statistic studies using a Hartmann wave front sensor and Young double slits to characterize the wave front and the coherence show the improvement of the harmonic beam and the influence of these beam properties on the image reconstruction quality. The second one discusses the optimization of the infrared pump laser using a modal filtering hollow core fiber, which leads to improvement of the HHG efficiency and stability. After the beamline optimization, spectrum and far field studies of HHG in two different gas mediums (argon and neon) are presented. The experimental studies of a two-color HHG configuration are also shown here. This chapter concludes with the summary of the optimized high flux harmonic beamline and a short discussion of a comparison between large-scale facilities sources (synchrotron and FELs) and table-top harmonic sources for coherent imaging.

Chapter 3 presents the second step of the thesis work: the validation of different coherent imaging techniques at the table-top harmonic beamline. It starts with experimental results of classic CDI and discussion of the spatial coherence implementation in the reconstructions. The second part is the experimental results of Fourier Transform Holography (FTH), which is a complementary imaging technique to CDI. The limitation in spatial resolution in FTH inspired several new imaging techniques such as Holography with Extended Reference by Autocorrelation Linear Differential Operation (HERALDO). This non-iterative image reconstruction method has been investigated and the experimental results are published in ***Paper III***. HERALDO offers an alternative way for ultrafast nanometric imaging, which is easy to implement on all kinds of beamline performing coherent imaging. The step-by-step analysis of the HERALDO reconstruction process leads to a discussion of the influence of reference design and the signal-to-noise ratio issue, which is reported in ***Paper IV***. Indeed, the signal-to-noise ratio gives restrictions in both CDI and holographic techniques for our experiments. A comparison between CDI, FTH and HERALDO techniques concludes this chapter.

Chapter 4 is the last achievement of this thesis work: the first application of coherent imaging techniques in material science using our harmonic beamline. The objective has been to

investigate the ultrafast dynamic phenomena of magnetic nano-domains using our table-top harmonic beamline. The magnetization dynamic study is of high scientific interest for the scientific community. An introduction to magnetism at the beginning of the chapter gives some basic knowledge and helps to understand the ideas and methods used in the experiments. Different experimental setups have been used here: a pair of toroidal mirror coupled to a blazed grating in 4f configuration and the off-axis parabola diffraction stage presented in chapter II. ***Paper V*** presents the first experimental results of single-shot detection of magnetic scattering around resonant edge energy of Cobalt (60eV) using our harmonic beam. This experiment shows the potential of studying ultrafast dynamics of irreversible phenomena using table-top harmonic sources, which was thought to be only possible on FELs. An extensive spectral study of magnetic scattering of different sample series has been conducted to identify the best candidate for single-shot imaging. ***Paper VI*** presents a part of these results. The spectral study provides a scattering efficiency measurement over a 20 eV bandwidth with a sampling of 1.5 eV. The single-shot detection shows that imaging of magnetic nanodomains with nanometric resolution on femtosecond time scale is possible using the CDI setup. At the end, the pump-probe experiment feasibility on our harmonic beamline is discussed for the magnetic study.

Chapter 5 draws the perspectives and gives the general conclusion of this thesis. Some undergoing studies are summarized in the first part, such as stereo imaging, 3D ankylography imaging and future development of the high energy harmonic beamline, followed by conclusions of the harmonic beamline, the investigated imaging techniques (CDI, FTH, HERALDO) and the magnetic nano-domains study.

Chapter I
Principle of lens-less imaging

I.1 Principle of lens-less imaging techniques

In conventional imaging systems, such as optical microscope and photo camera, a simple lens or a group of convex and/or concave lenses are used to form the image of the target object that is illuminated by a proper light source (Fig. 1.1). In complicated imaging systems, the lens system can also contain other optical elements, such as mirrors, windows, etc. The image quality is generally limited by the lens system: the ensemble of each optic's aberration determines the possible alterations of the object image. This imposes strong constraints on manufacturing of optical elements and design of lens system. In X-ray microscopy, the highest spatial resolution to date has been obtained using zone plate Fresnel optics. The constraints on optical elements become more critical. First, the resolution of such image-forming optics is limited by the smallest outer feature of the zone plate, which raises a real challenge on the optics manufacturing if one would like to reach nanometric resolution. Secondly and more fundamentally, the material of such optics has strong photon absorption, which limits its efficiency to typically less than 10% and often as low as few percent [1]. The latter one is critical for high resolution imaging of certain specimens that are sensitive to radiation damage [2,3]. In this context, the lens-less imaging provides an alternative solution for high resolution imaging for various applications from biology to solid-state physics.

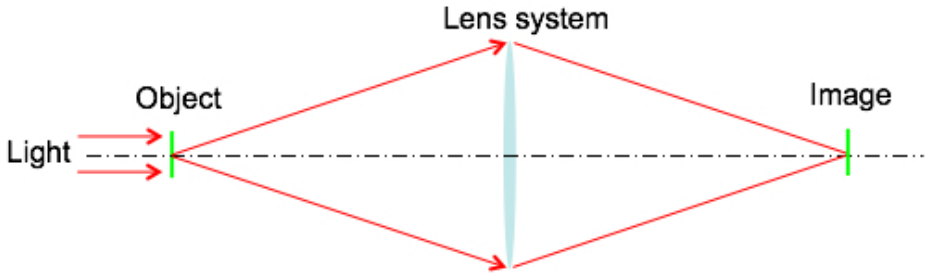

Fig. 1.1. Scheme of conventional imaging systems. Object image is formed by a lens system.

In lens-less imaging, no optics is required after the illumination of the object. Computation algorithms are used to retrieve the object's image instead of a lens imaging system. The isolated object is illuminated by a coherent wave, which ideally has to be monochromatic. The object diffracts and induces modifications in magnitude and/or in phase of the incident wave. The diffraction pattern is then measured in the far field by a pixel-array detector, which is usually a Charge-Coupled Device (CCD) camera (Fig. 1.2).

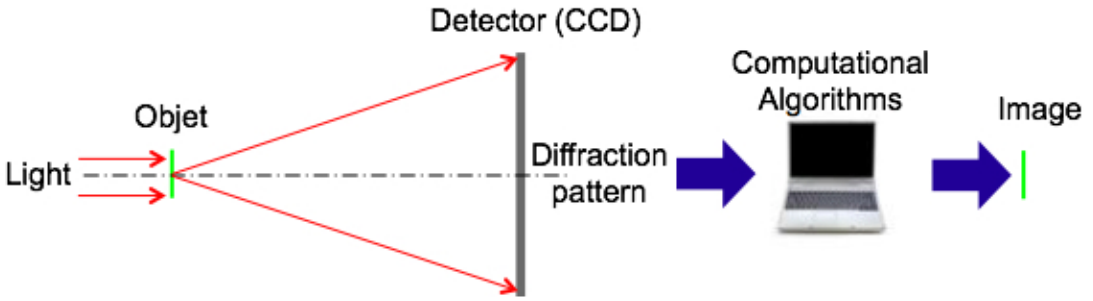

Fig 1.2. Scheme of a lens-less coherent imaging set-up. The computation algorithms replace the lens system conventionally used to image the object.

In the Fraunhofer diffraction regime, the diffraction pattern is proportional to the Fourier transform of the exit wave in the image plane. Theoretically, a simple inversion of the diffraction pattern should give the image of the object. But the pixel-array detector is only sensitive to the intensities of the electromagnetic wave field. Therefore, the phase information of the wave field is not directly measured by the detector. Infinity of possible solutions of the simple inversion can be obtained by applying possible phases to the measured diffraction pattern [4]. Here comes the famous "*phase problem*", which is the main obstacle to extract object information from the measured diffraction pattern. Two main techniques have been proposed to overcome the "*phase problem*": one uses Phase Retrieval Algorithms [6,7,8] and is called Coherent Diffractive Imaging (CDI); the other is Fourier Transform Holography (FTH) [5].

In CDI, iterative algorithms converge to the spatial phase in the diffraction plane using constraints both in real and reciprocal space (the diffraction plane). A scheme of the CDI technique is shown in Fig. 1.3. In the reciprocal space, the diffraction pattern recorded by the detector is equal to the absolute squared value of the Fourier transform of the exit wave. In the real space, the object is contained in a finite dimension (called "*support*"). The autocorrelation defined as the Fourier transform of the measured diffraction pattern will give a first constraint to the support (other constraint can be found). The relation of Fourier transform links these two constraints between real and reciprocal spaces. In general, most phase retrieval algorithms use these two kinds of constraints to reconstruct the "*lost phase*" in the reciprocal space and the object image in the real space. During the detection of the diffraction patterns, the coherence of the incident wave plays an important role. It creates a characteristic "*speckle pattern*" in the diffraction plane. The "*speckle*" is the "*phase signature*" of the diffraction pattern that ensures the convergence of iterative algorithms. The phase retrieval algorithms reconstruct simultaneously the phase in reciprocal space and the object image in real space. The solution is nearly unique for problems that have more than one dimension [9,10].

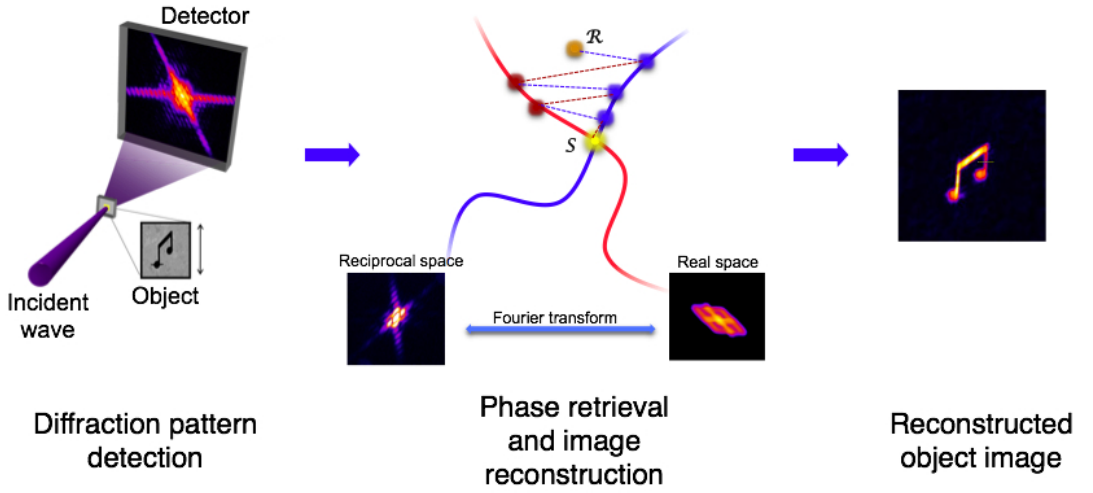

Fig. 1.3. The scheme of CDI can be separated into two steps: the first one is the detection of the object's diffraction pattern. The second step is to use phase retrieval algorithms to reconstruct the "lost phase" of the diffraction pattern and the object image.

Fourier Transform Holography (FTH) is another lens-less imaging technique, which has almost the same experiment setup as the CDI except that the sample geometry holds a holographic reference. The principle of FTH is similar to holography proposed by Dennis Gabor in 1948 [11]. The FTH is inspired by this idea of "full recording": the incident wave is simultaneously diffracted by the object and the reference. The detector located in the far field records the interference between these two diffracted waves, which is called "hologram". The spatial amplitude and phase of the object are encoded in this hologram and a simple Fourier transform is required to reconstruct the object image [12] (Fig. 1.4). The Fourier transform of the hologram is the autocorrelation of the sample (object + pinhole). The reconstructed object image is the correlation between the object and the pinhole.

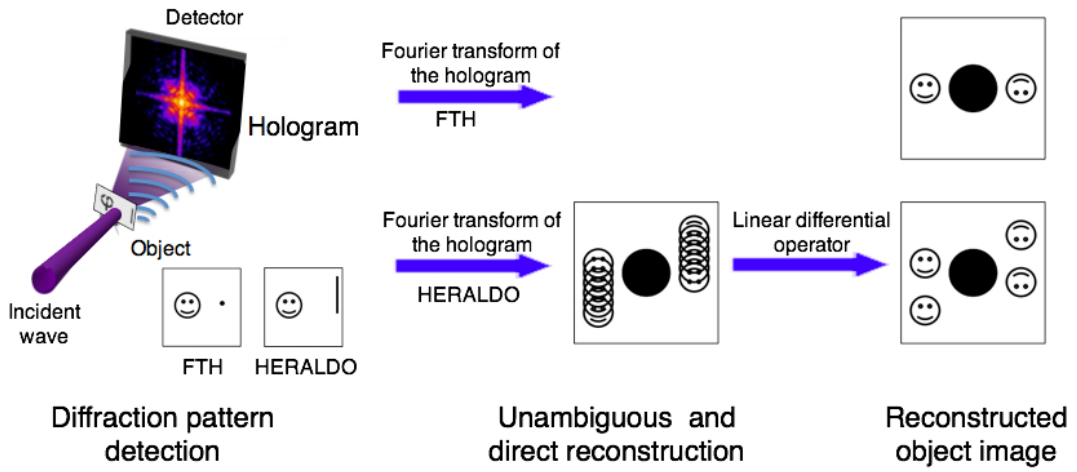

Fig. 1.4. Scheme of FTH and HERALDO: We have used the same experimental setup as in CDI except the sample geometry. In FTH, the sample consists in the object and a pinhole reference in the nearby at a distance that respects the holographic separation given by the size of the object. In HERALDO, the arrangement is similar but the reference is large while

keeping the holographic separation. The reconstruction step is simple and direct: in FTH, the Fourier transform of the hologram gives the object image; in HERALDO, a linear differential operation is applied as a post process of the Fourier transform to finally get the object image reconstruction.

In my thesis work, I have been focused on an extended reference holographic technique initially proposed by S.G. Podorov in 2007 [14], generalized by M. Guizar-Sicairos [13] and entitled "Holography with Extended Reference by Autocorrelation Linear Differential Operator (HERALDO)". In HERALDO, the pinhole reference is replaced by extended references, such as a slit (1 dimension), a square or a rectangle (2 dimensions), a triangle (2D), etc. (Fig. 1.4). The extended references should contain sharp features, such as the two extremities of a slit, the corners of a square, a rectangle or a triangle. When applying a differential operator to the registered hologram (the autocorrelation of the sample), the extended references turn into Dirac delta functions (which correspond to the sharp features at the edges of the extended references). Note that the Fourier transform properties of delta function ensure a high-resolution reconstruction (Fig. 1.4). By this way, the resolution is no longer limited by the reference size, so one can increase the diffraction signal without affecting the resolution. Theoretically, the reconstruction resolution is limited by the quality of the manufactured references. In particular the sharpness of the edges is crucial.

I.2 Image formation in lens-less imaging

The image formation is the fundamental of lens-less imaging and all ideas of reconstruction techniques are based on it and inspired by its properties. As mentioned before, CDI, FTH and HERALDO have the same experimental setup. The image formation is thus the same for these techniques from the incident wave propagation to the Fraunhofer diffraction process, except that different sample preparation for CDI and FTH/HERALDO leads to different diffraction patterns. Since the wave propagation and Fraunhofer diffraction are well known, I present here the relevant equations, formulas and properties in the case of the lens-less imaging to give a clear description of theoretical background with non-exhaustive mathematics. One can refer to the books of J.W. Goodman [12,30] for detailed mathematical and physical deduction of wave propagation and Fraunhofer diffraction in general case. More practically, one can also look at some excellent thesis work such as P. Thibault [31], M. Guizar-Sicairos [32] or D. Gauthier at Saclay [33] that have well-detailed mathematical presentations of the image formation in the case of lens-less imaging.

I.2a Image formation in lens-less imaging: Diffraction

We usually consider in lens-less imaging an isolated object illuminated by a plane wave (Fig. 1.5). The exit wave is the wave field transmitted by the object and detected in the far field (by

a CCD camera in our case). The propagation of the exit wave behaves according to the Helmholtz wave equation:

$$\nabla^2\psi + k^2n^2\psi = 0 \qquad \text{(Eq. 1-1)}$$

where $k = \omega/c$ and $n^2 = c^2\varepsilon\mu$. ω is the frequency of the wave ψ; ε and μ are respectively the electric permittivity and the magnetic permeability of the medium.

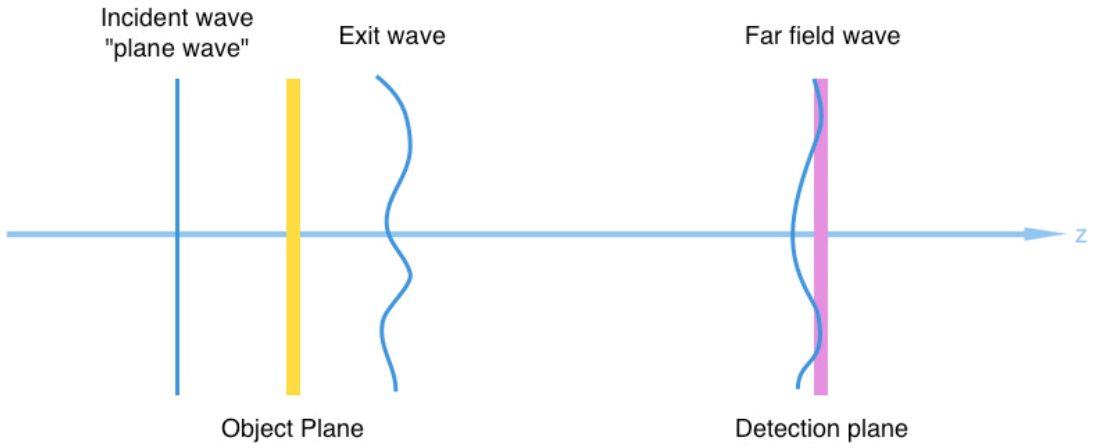

Fig. 1.5. The wave propagation in lens-less imaging.

Commonly in the X-ray community [35], the refractive index n is expressed by its purely refractive (real) and absorptive (imaginary) components, δ and β:

$$n = 1 + \Delta n = 1 - \delta - i\beta \qquad \text{(Eq. 1-2)}$$

Δn is non-zero only in a finite region of the space occupied by the object, and when Δn=0, the wave ψ is the solution of the Eq. 1-1 in free-space propagation condition. The Eq. 1-1 has a simple form in the Fourier space:

$$(k^2 - q^2)\tilde{\psi}(q) = 0 \qquad \text{(Eq. 1-3)}$$

Obviously, $\tilde{\psi}(q) = 0$ unless $|q| = k$, which is called the "Ewald sphere" [36]. In our lens-less imaging experiments, the detection plane is a plane transverse to the wave propagation direction. Thus we can separate the free-space propagating wave field into transverse and parallel components, respectively $r_\perp = (x, y)$ and z. The general solution of Eq. 1-1 is then obtained in Fourier space as follow:

$$\tilde{\psi}(q_\perp, z) = \tilde{\psi}^-(q_\perp)e^{-i\kappa z} + \tilde{\psi}^+(q_\perp)e^{i\kappa z} \qquad \text{(Eq. 1-4)}$$

where $\kappa = \sqrt{k^2 - q_\perp^2}$ (Fig. 1.9) and $\tilde{\psi}^\pm(q_\perp)$ are two independent functions representing forward (+) and backward (-) scattering. In our experiments, back-propagating terms can be neglected, therefore the solution is:

$$\psi(r_\perp, z) = \mathcal{F}^{-1}\left[\tilde{\psi}\,(q_\perp)e^{i\kappa z}\right] \qquad \text{(Eq. 1-5)}$$

From Eq. 1-5, we can deduce the wave function in far field diffraction (Fraunhofer diffraction) [30]:

$$\psi_{\text{far field}}(r_\perp, z) \propto \int d^2q\tilde{\psi}(q)e^{ikz(\sqrt{1-\left(\frac{q}{k}\right)^2}+\frac{q}{k}\frac{r}{z})} \quad \text{(Eq. 1-6)}$$

Since $z \to \infty$ (far field), the integrand will disappear unless the phase term is stationary, which means:

$$\frac{r_\perp}{z} = \frac{q_\perp}{\sqrt{k^2 - q_\perp^2}} = \frac{q_\perp}{\kappa} \quad \text{(Eq. 1-7)}$$

Therefore, we can get the measured intensity by the detector in the far field:

$$I = |\psi_{\text{far field}}(r_\perp)|^2 \propto \frac{1}{1+(\frac{r_\perp}{z})^2}\left|\tilde{\psi}(q_\perp = \kappa\frac{r_\perp}{z})\right|^2 \quad \text{(Eq. 1-8)}$$

In our experiments, Eq. 1-6 can be simplified in the case of small-angle scattering (Fig. 1.6), which is valid when:

$$\frac{q_\perp}{k} < 1 \Rightarrow \frac{r_\perp}{z} = \tan\theta < 1 \quad \text{(Eq. 1-9)}$$

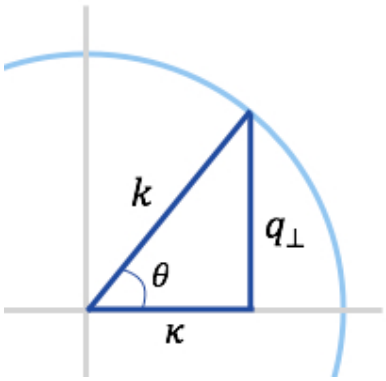

Fig. 1.6. Representation of the wave vector and the diffraction angle relationship in the Ewald sphere.

Applying the paraxial approximation, one can expand κ to the first non-zero order in $q_\perp$, and Eq. 1-5 becomes

$$\psi(r_\perp, z) = \mathcal{F}^{-1}\left[\tilde{\psi}(q_\perp)e^{ikz(1-\frac{q_\perp^2}{2k^2})}\right] \quad \text{(Eq. 1-10)}$$

One gets the small angler scattering version of Eq. 1-8:

$$I \propto \left|\tilde{\psi}(q_\perp = k\frac{r_\perp}{z})\right|^2 \quad \text{(Eq. 1-11)}$$

Note here that the Fraunhofer diffraction approximation is valid when the Fresnel number $FN \ll 1$, which is defined as

$$FN = \frac{a^2}{\lambda z} \quad \text{(Eq. 1-12)}$$

where a is the characteristic dimension of the object. Small and large Fresnel number correspond to respectively the far field regime and the near field regime. In the Fraunhofer diffraction regime (far field), one should have

$$\frac{a^2}{\lambda} \ll z \quad \text{(Eq. 1-13)}$$

I.2b Image formation in lens-less imaging: Object transmittance

As shown in Eq. 1-11, the measured diffraction pattern is proportional to the absolute value of the Fourier transform of the exit wave in the transverse plane. The question now is what is the relation between the object image and the exit wave that we can reconstruct by computational algorithms. For our experiments, we use the projection approximation: the exit wave is the product of the incident wave and the object transmittance:

$$\psi_{\text{exit}} = \psi_{\text{incident}} t_{\text{object}} \quad \text{(Eq. 1-14)}$$

In this approximation, the object can be treated as a two dimensional plane whose thickness is negligible, thus there is no diffraction inside the object. The object transmittance (in two dimensions with complex values) represents the projection of the object on a transverse plane (object plane in Fig. 1.5), which shows how the object modifies the incident wave both in amplitude and in phase. Since we assume that the incident wave is a plane wave, the detected wave (diffraction wave) in the far field is then equal to the Fourier transform of the object transmittance. The reconstruction image that we get by computational algorithms should then reflect the object transmittance. To validate the projection approximation, the object should be "*optically thin*". If e is the object thickness and d is the reconstruction resolution that we want to attend, then the "*optically thin*" condition can be described as [37]

$$e < \frac{2d^2}{\lambda} \quad \text{(Eq. 1-15)}$$

The term $\frac{2d^2}{\lambda}$ describes the "*depth of focus*" (DOF), which is also a function of diffraction angle $\theta_{\max}$:

$$DOF = \frac{2\lambda}{\theta_{\max}^2} \quad \text{(Eq. 1-16)}$$

When the object thickness is smaller than the DOF, the exit wave is associated to a single object plane, which corresponds to the reconstruction plane visualized with computational algorithms. Otherwise, there will be more than one object plane, thus more than one possible phase associated to the measured diffraction pattern. This can prevent convergence of

iterative algorithms. One may need additional constraints on the object support to associate one and only one object plane for the reconstruction. In holographic experiments (FTH, HERALDO), the phase information is encoded in the hologram. Thus, there is one unique solution obtained in the plane of the object and the reference.

To conclude, in our lens-less imaging experiments, objects are "optically thin" and the diffraction wave is detected in the far field regime (Fraunhofer diffraction) in the small angle scattering regime.

I.2c Image formation in lens-less imaging: Detection

The detection of the diffraction pattern is realized by a CCD camera, which accumulates incoming photons (diffraction and noise) during the exposure time. Thus temporal information such as the phase of the wave function is lost during the detection. This is the *phase problem* well known in lens-less imaging. The measured term is the photon flux, whose unit is J/m^2 or $photons/m^2$. Eq. 1-11 becomes (if we omit the constant factors)

$$F = I = \left|\tilde{\psi}(q_\perp = k\frac{r_\perp}{z})\right|^2 \qquad \text{(Eq. 1-17)}$$

The measured diffraction signal (F) is then digitalized with a certain sampling ratio. We can use a discrete Fourier transform function to present the numerical data. The one-dimensional discrete Fourier transform of a N long vector f_m is

$$\widetilde{f_n} = \frac{1}{\sqrt{N}}\sum_{m=0}^{N-1} f_m e^{2\pi inm/N} \qquad \text{(Eq. 1-18)}$$

If a continuous function f(x) is sampled by a sampling interval Δx, and its discrete Fourier transform is also sampled by a sampling interval Δq, then we have the following relation:

$$\Delta x \Delta q = \frac{2\pi}{N} \qquad \text{(Eq. 1-19)}$$

With a given sampling interval Δx, the highest frequency present in a discrete Fourier transform is the Nyquist frequency:

$$q_{\text{Nyquist}} = \frac{N\Delta q}{2} = \frac{\pi}{\Delta x} \qquad \text{(Eq. 1-20)}$$

In our diffraction experiments, when applying the Fourier transform on the detected diffraction signal, we get the autocorrelation of the object (or the object transmittance). The Eq. 1-19 becomes

$$\Delta k = \frac{2\pi}{N\Delta r} \qquad \text{(Eq. 1-21)}$$

where Δk is the pixel size of the CCD camera which contains N X N pixels, and Δr is the pixel size of the autocorrelation of the object transmittance. If the object transmittance

occupies a region of n X n pixels in the matrix of N X N pixels and the object size is a X a, we can deduce the relation between real physical terms and the discrete functions:

$$a\frac{k}{z} = n\Delta r \qquad \text{(Eq. 1-22)}$$

During the phase retrieval reconstruction process, the sampling ratio is a key factor. When the sampling interval is too large, frequencies higher than the Nyquist frequency will be wrapped and will appear as lower frequencies [31]. This is called "*aliasing*". A suitable diffraction pattern for the reconstruction should be "*oversampled*". The notion of "*oversampling*" is first proposed by D. Sayre in 1952 [38] using the Shannon sampling theorem for the phase problem in crystallography. The oversampling is possible only if the object transmittance is contained in a "*support*" (non-zero inside the support and null outside). We can define the oversampling ratio [39] as:

$$O = \frac{A_{\mathrm{FOV}}}{A_{\mathrm{object}}} = \frac{N_{\mathrm{measured}}}{N_{\mathrm{object}}} \qquad \text{(Eq. 1-23)}$$

where A_{FOV} is the "field of view" corresponding to the image containing N_{measured} pixels of measured amplitudes, in which the object occupies an area A_{object} of N_{object} pixels. Since the object transmittance is a complex-valued, there are $2N_{\mathrm{object}}$ real variables to be recovered. The whole image provides N_{measured} equations. By considering the degrees of freedom of such a set of equations, one cannot get a unique solution unless: $2N_{\mathrm{object}} \leq N_{\mathrm{measured}}$. Therefore,

$$O \geq 2 \qquad \text{(Eq. 1-24)}$$

Another approach to the oversampling ratio is based on Nyquist–Shannon sampling theorem [40,41]. According the theorem, the sampling interval Δk (the pixel size of the CCD camera) of the diffraction pattern should obey

$$\Delta k \leq \frac{2\pi}{2q_{\mathrm{Nyquist}}} \qquad \text{(Eq. 1-25)}$$

where q_{Nyquist} is the maximum frequency detected in the diffraction pattern. Since in the reciprocal space of the diffraction pattern, the maximum frequency is given by the size of the autocorrelation of the object that is the double of the object size, we deduce from Eq. 1-20:

$$q_{\mathrm{Nyquist}} = \frac{2n\Delta r}{2} = n\Delta r \qquad \text{(Eq. 1-26)}$$

Applying Eq. 1-26 to Eq. 1-25, we get

$$\Delta k \leq \frac{2\pi}{2n\Delta r} = \frac{\lambda z}{2a} \qquad \text{(Eq. 1-27)}$$

From Eq. 1-21, Eq. 1-22 and Eq. 1-23, one can get the relation between Δk and the oversampling ratio:

$$O = \frac{\lambda z}{a\Delta k} \quad \text{(Eq. 1-28)}$$

Therefore, we recover the oversampling condition as Eq. 1-24.

Note that Eq. 1-24 is a necessary condition for solving a unique reconstruction, but in general not sufficient. In one dimension case, the uniqueness is never guaranteed [42,43]. Fortunately, in case of more than one dimension, the uniqueness is almost guaranteed with an oversampled diffraction pattern [9,10].

When a diffraction pattern is taken, the theoretical resolution (which is diffraction limited) can be calculated as:

$$r = \frac{1}{2\sigma_{max}} = \frac{\lambda z}{N_{pixel} P_{pixel}} \quad \text{(Eq. 1-29)}$$

where σ_{max} is the largest spatial frequency of the diffraction signal recorded by the CCD camera, N_{pixel} and P_{pixel} are respectively the corresponded pixel number and pixel size. This equation gives the first insight of the diffraction pattern quality.

I.3 Reconstruction: Phase retrieval algorithms

The phase retrieval algorithms for lens-less imaging are inspired by those used in crystallography. The first phase retrieval algorithm is proposed by Gerchberg and Saxton in 1972 [44]. The Gerchberg-Saxton algorithm can reconstruct an object using two intensity measurements (one in Fourier space and one in direct space), which introduced the "modulus constraint" notion in the iterative process. In late 70's, Fienup has improved this algorithm by using only one intensity measurement in the Fourier space (the diffraction pattern) to reconstruct the object [7,8]. Fienup's hybrid input-output algorithm (HIO) has a significant contribution to the imaging community and is probably the most popular phase retrieval algorithm nowadays. In general, there are four steps in the iterative process (Fig. 1.7)

1) Apply the Fourier transform to the object (g): $G = |G|e^{i\emptyset}$ to get the phase term ϕ.
2) Apply the constraint in Fourier space (replace the amplitude by the measured diffraction intensity ($|F|$): $G' = |F|e^{i\emptyset}$.
3) Apply inverse Fourier transform on the G' to get g'.
4) Apply the constraint in direct space (such as the object support) to get object (g).

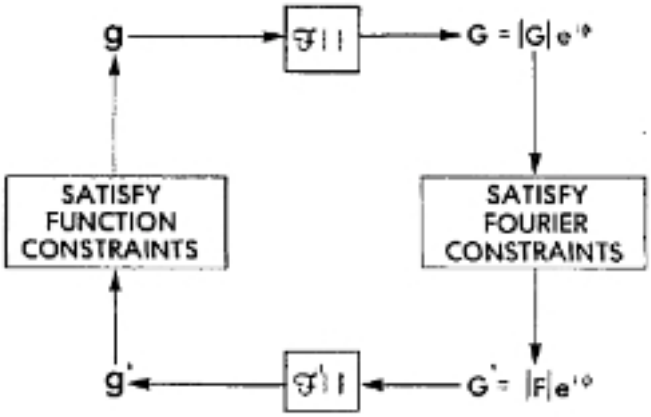

Fig. 1.7. Scheme of the phase retrieval algorithm. Picture extracted from Ref 6.

To start the iteration, one uses a random phase ϕ_r in step one. During the iterative process, an error factor based on the satisfaction of the constraints is calculated. A reconstruction solution can be achieved when the error factor is minimized (or under a fixed threshold).

In 2003, V. Elser has proposed a more general phase retrieval algorithm, the "difference map" [45], which is based on the "*projections*" of solutions on "*constraints sets spaces*". The notion "*constraints sets*" (presented by $C_1, C_2, C_3,\ldots$) are defined as subsets of a finite-dimensional Hilbert space ($\mathcal{E}$). The "*constraints sets*" can have two or more constraints corresponding to real physical meanings, such as the measured diffraction pattern intensity, the object support in direct space, etc. The goal of the reconstruction algorithm is to find the solution $x \in \mathcal{E}$, which satisfies:

$$x \in C_1 \cap C_2 \cap C_3 \cap \ldots \quad \text{(Eq. 1-30)}$$

The notion "*projection*" (P_C corresponding to a constraint C) is then defined as: for every $x \in \mathcal{E}$ returns a point $P_C(x) = y \in C$ and such that $\|x - y\|$ is minimized [31]. The condition (1-30) then becomes

$$x_{\text{sol}} = P_{C_1}(x_{\text{sol}}) = P_{C_2}(x_{\text{sol}}) = P_{C_3}(x_{\text{sol}}) = \cdots \quad \text{(Eq. 1-31)}$$

For a two-constraint problem, the difference map iteration can be defined as:

$$x_{n+1} = x_n + \beta D(x_n) \quad \text{(Eq. 1-32)}$$

where

$$D(x) = y_2 - y_1 \quad \text{(Eq. 1-33)}$$

$$y_2 = P_1[(1+\gamma_2)P_2(x) - \gamma_2 x]$$

$$y_1 = P_2[(1+\gamma_1)P_1(x) - \gamma_1 x]$$

where β, γ_1 and γ_2 are complex parameters.

Note that the HIO is a special case of the difference map when $\gamma_1 = -1$ and $\gamma_2 = \beta^{-1}$, which can be presented as

$$x_{n+1} = x_n + \beta[P_S\big((1+\beta^{-1})P_M(x_n) - \beta^{-1}x_n\big) - P_M(x_n)] \quad \text{(Eq. 1-34)}$$

where P_S and P_M are respectively the constraints on the object support and the measured diffraction signal.

The Relaxed Averaged Alternating Reflections (RAAR) algorithm is another popular algorithm proposed by Russel Luke in 2005 [46]. This algorithm can be defined as

$$x_{n+1} = x_n + \beta[P_S(2P_M(x_n) - x_n) - P_M(x_n)] + (1-\beta)(P_M(x_n) - x_n) \quad \text{(Eq. 1-35)}$$

Note that when $\beta = 1$, it is equivalent to the HIO.

During the last decade, many algorithms have been developed (not presented here) and it is hard to say which algorithm is the best. Each algorithm is proposed for specific problems and applications. The experiments conditions and criterion of constraints for each algorithm is hardly the same. Some works [47, 48] comparing different phase retrieval algorithms suggest that the HIO is the most efficient algorithm for well-controlled scattering experiments.

In this thesis work, phase retrieval reconstructions are realized using two computational codes:

1) The "Hawk" code [34] developed by our collaborator Filipe Maia in the research group of Professor Janos Hajdu in Uppsala University, Sweden. The code "Hawk" contains a set of phase retrieval algorithms, for example HIO and RAAR. I usually use the HIO algorithm for preliminary reconstruction of experiment data, and a combination of algorithms to get better reconstruction results.
2) The code "difference map" code developed by Pierre Thibault in the research group of Professor Veit Elser in Cornel University, USA.

Practically, the solution (reconstructed image) is not exactly the same from one iteration to the other one. After sufficient iterations (typically several hundreds of iterations), each iteration gives a very similar reconstruction solution with a corresponding error factor value. The error factor value is calculated based on the measured diffraction pattern and shows how "close" the reconstruction is compared to the measured data. One usually averages all reconstruction solutions whose error factor values are lower than a defined threshold to get the final image of the object. The resolution of reconstructed image is then estimated by the Phase Retrieval Transfer Function (PRTF) (Chapter III, section III.4).

I.4 Reconstruction: FTH and HERALDO

The phase problem is easily solved in FTH, which is a great advantage compared to the phase retrieval algorithms. But FTH involves more strict constraints on the sample preparation, which is not obvious in certain applications. In FTH, a pinhole (reference) is placed in the vicinity of the object at a certain distance (holographic separation) in the same transverse

plane (object plane in Fig. 1.5). The entire sample (object + reference) transmittance can be defined as

$$t = o + r \quad \text{(Eq. 1-36)}$$

where o and r are respectively the transmittance of the object and the reference. As mentioned in the previous section, in Fraunhofer diffraction regime and projection approximation, the measured hologram (the diffraction pattern) by CCD camera is the module square of the Fourier transform of the sample transmittance:

$$H = |\mathcal{F}\{t\}|^2 \quad \text{(Eq. 1-37)}$$

The holographic lens-less technique offers a direct and non-ambiguous reconstruction. When applying the inverse Fourier transform to the measured hologram, according to the property of the autocorrelation (presented at the beginning of the chapter), we get

$$\mathcal{F}^{-1}\{H\} = \mathcal{F}^{-1}\{|\mathcal{F}\{t\}|^2\} = t \otimes t \quad \text{(Eq. 1-38)}$$

Developing this equation, we have

$$\mathcal{F}^{-1}\{H\} = t \otimes t = o \otimes o + r \otimes r + r \otimes o + o \otimes r \quad \text{(Eq. 1-39)}$$

The first two terms $o \otimes o + r \otimes r$ are the "central" terms, which correspond to the autocorrelations of the object transmittance and the reference transmittance. These two terms are centered and overlap at the origin. The last two terms, i.e. the complex conjugates $r \otimes o + o \otimes r$, are the holographic reconstructions located at the opposite sides of the "central" terms. Note that they are not two independent reconstructions, since they are complex conjugate "mirror" of each other. The FTH reconstruction is not the object transmittance itself but the cross-correlation between the object transmittance and the pinhole reference. In addition, one should respect the "holographic spatial separation" between the object and the reference to avoid the spatial overlap between the reconstruction terms and the "central" terms. If a is the size of object, then the distance between the object and the pinhole reference should be larger than $1.5a$.

The spatial resolution of the object image is limited by the size of the pinhole reference. A large reference will lower the resolution whereas a small one will increase it. Since the signal quality of the hologram depends also on the reference signal strength, there is a contradictory for the choice of the pinhole size [16,17,20]. To optimize the reconstruction quality, the basic idea is to find strategies to increase the reference signal while keeping the reference size small. Various techniques have been proposed such as multiple references FTH [18], FTH with a well-prepared extended reference and deconvolution operator for reconstruction [17], massively parallel X-ray holography [19], holography with a well-prepared mask reference [16], etc. In addition, running CDI reconstruction algorithms on FTH experiment data can also lead to a better performance [15].

HERALDO has been proposed to overcome the "paradox" in FTH. The pinhole reference in FTH configuration is replaced by an extended reference, such as a slit (1 Dimension), a rectangular (2 Dimensions), a triangle (2D), and etc. The extended reference $r(x, y)$ is placed close to the object $o(x, y)$ in the same transverse plane with a given holographic spatial separation. The measured hologram H has the same equation as Eq. 1-37. A linear differential

operator $L^{(n)}\{\cdot\}$ is applied to the Fourier transform of the hologram. We then get the sum of a point Dirac delta function at (x_0, y_0) and some other function $g(x, y)$:

$$L^{(n)}\{r(x,y)\} = A\delta(x - x_0)\delta(y - y_0) + g(x,y) \quad \text{(Eq. 1-40)}$$

where A is an arbitrary complex-valued constant, and $L^{(n)}\{\cdot\} = \sum_{k=0}^{n} a_k \frac{\partial^n}{\partial x^{n-k}\partial y^k}$ is an n-th order linear differential operator and a_k are constant coefficients. Note that the function $g(x, y)$ can be another Dirac delta function or any extended function.

Applying such linear differential operator on the autocorrelation (the inverse Fourier transform of the measured hologram), we have

$$\begin{aligned} L^{(n)}\{\mathcal{F}^{-1}\{H\}\} &= L^{(n)}\{t \otimes t\} \\ = L^{(n)}\{o \otimes o\} + L^{(n)}\{r \otimes r\} &+ \left[L^{(n)}\{r\} \otimes o\right] + (-1)^n [o \otimes L^{(n)}\{r\}] \end{aligned} \quad \text{(Eq. 1-41)}$$

According to the relation between cross-correlation and convolution when applying the differential operator, one get

$$L^{(n)}\{f \otimes g\} = (-1)^n [f \otimes L^{(n)}\{g\}] = [L^{(n)}\{f\} \otimes g] \quad \text{(Eq. 1-42)}$$

Applying this property on Eq. 1-41, we get

$$\begin{aligned} L^{(n)}\{\mathcal{F}^{-1}\{H\}\} &= L^{(n)}\{t \otimes t\} \\ &= L^{(n)}\{o \otimes o\} + L^{(n)}\{r \otimes r\} + (-1)^n o \otimes g + g \otimes o \\ &\quad + (-1)^n A^* o(x + x_0, y + y_0) + A o^*(x_0 - x, y_0 - y) \end{aligned} \quad \text{(Eq. 1-43)}$$

As similar to FTH, the last two complex conjugate terms are the reconstructions located at opposite sides of the central autocorrelation terms. Unlike FTH, the reconstruction resolution is not limited by the reference size. Practically, the resolution is closely dependent on the "sharpness" of the reference edge that determines the Dirac delta function. For example, the two extremes of slit and the corners of rectangular and triangle, which define respectively 2, 4 or 3 references.

The "HERALDO separation conditions" have a similar constraint like the FTH one: the features of the extended reference that will "produce" the Dirac delta function should have a minimum distance of $2a$ to the object, where a is the object size. An additional constraint should be respected to avoid the overlap between different reconstructions associated to different Dirac delta functions when there is more than one Dirac delta function: the distance between any pair of two features that "produce" Dirac delta functions should be larger than the object size a.

I.5 Beam requirements for lens-less imaging

CDI and HERALDO are both lens-less imaging techniques. As mentioned before, these two techniques can be realized using the same experimental setup, only the sample arrangement differs. The image reconstructions are performed separately using either a phase retrieval algorithm in CDI or direct mathematical operations in HERALDO. Obviously, high quality diffraction pattern is the key factor for both CDI and HERALDO (also for FTH). For a high-resolution reconstruction, we need a beam with the following requirements:

- Short wavelength
- High coherence
- High beam flux
- Ultrashort pulse duration

Short wavelength and ultrashort pulse duration are required to get high spatial resolution (nanometric scale or even atomic scale) and to perform dynamic studies on a femtosecond scale (or even attosecond scale in a near future). High coherence and beam flux ensure a high quality diffraction pattern with a good signal to noise ratio. Free Electron Laser facilities (FEL), Synchrotron facilities and High order harmonics beamlines are all qualified sources. In this thesis work, I have been interested in lens-less imaging techniques (CDI and HERALDO) using bright high order harmonics (HH) beam source. The High flux harmonic beamline developed at Saclay can provide intense coherent photons in the soft X-ray region (from several nanometers to several tens of nanometers) with brief pulse duration (typically in the femtosecond scale or even down to the attosecond scale). Compared to large-scale laser facilities, the inexpensive cost and relatively easy construction of harmonic beamline are of great advantage. The full control of beam properties makes it accessible to numerous applications from physics to biology. It is becoming a powerful imaging tool for users in various scientific domains.

I.6 High order harmonics generation

This section is a brief introduction to the High order Harmonics Generation (HHG) process. The purpose is to give few basics to understand the optimization of the source discussed in Chapter II. The more fundamental aspects of HHG are not presented here.

Thanks to the invention and the fast development of the laser, the research of light-matter interaction entered into a new era. At the end of the 20^{th} century, powerful lasers can deliver peak intensities up to 10^{18} W/cm^2, which makes it possible to realize the frequency up-conversion from visible to the extreme ultra violet (XUV) domain [23]. The HHG phenomenon is first discovered by research groups in Chicago [21] and in Saclay [22] at almost the same time (in 1987). They have observed intense harmonic emission by the atoms of a rare gas jet of a focused ultra-short infrared laser (Fig. 1.8a). In the studies conducted here, Argon (Ar), Krypton (Kr) and Xenon (Xe) gases have been mostly used. A typical spectrum is shown in Fig. 1.8b.

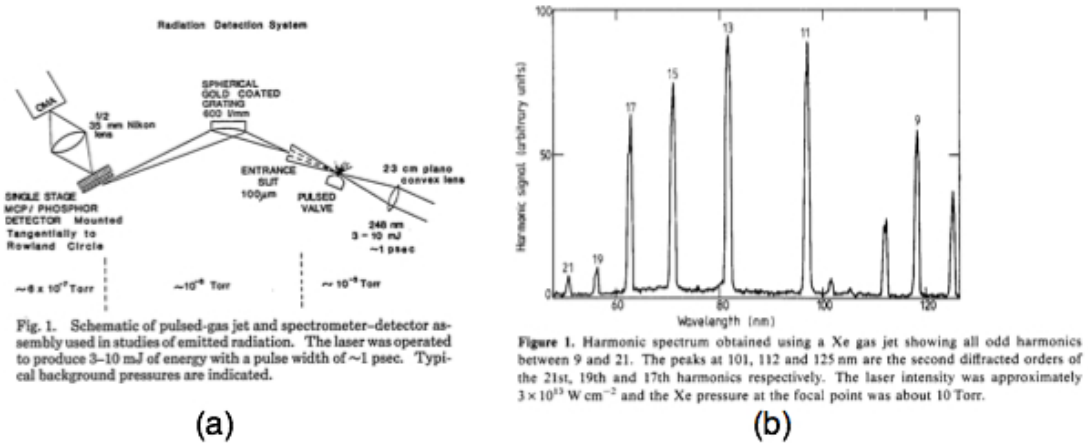

Fig. 1. Schematic of pulsed-gas jet and spectrometer–detector assembly used in studies of emitted radiation. The laser was operated to produce 3–10 mJ of energy with a pulse width of ~1 psec. Typical background pressures are indicated.

Figure 1. Harmonic spectrum obtained using a Xe gas jet showing all odd harmonics between 9 and 21. The peaks at 101, 112 and 125 nm are the second diffracted orders of the 21st, 19th and 17th harmonics respectively. The laser intensity was approximately 3×10^{13} W cm^{-2} and the Xe pressure at the focal point was about 10 Torr.

Fig. 1.8. (a) Scheme of HHG observation, picture extracted from Ref 21. (b) HHG spectrum obtained using Xe gas jet, extracted from Ref 22.

The HHG phenomenon can be described in a semi-classic three-step model: tunnel ionization, classical acceleration and recombination (Fig. 1.9) [25,26].

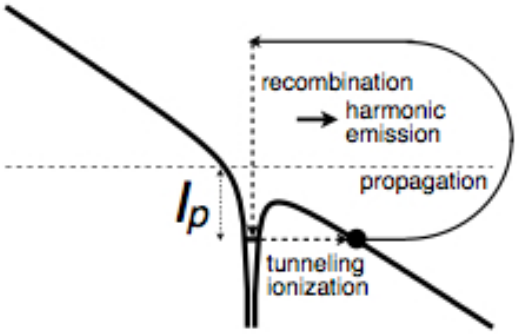

Fig. 1.9. Three-step model of high order harmonic generation.

In the first step, when close to the maximum of laser electric field that lowers the potential barrier, an electron can go through by tunnel effect. In the second step, the influence of atomic Coulomb potential is neglected. The electron is accelerated in the electric field. When the sign of the electric field changes, the electron might be driven back towards the ionic core, with whom it can recombine in the third step.

The recombination gives rise to the emission of a burst of soft X-ray light. The photon energy is equal to the sum of the electron kinetic energy acquired during its oscillation in the electric field and the ionization potential (I_p) of the atom/molecule. The maximum photon energy is governed by Eq. 1-44, which is called "*cut-off*" [24]. U_p is the ponderomotive energy -- the cycle averaged quiver energy of a free electron in an electric field.

$$h\upsilon_{max} = I_p + 3.17U_p \qquad \text{(Eq. 1-44)}$$

Depending on the different behavior of electrons, there are two trajectories of recombination in the *plateau*: long and short, which contributes differently to HHG. The spatial and spectral properties of the harmonic emission differ for each trajectory.

The spectrum of high order harmonics has a characteristic form, which contains three parts: the perturbative region, the *plateau* and the *cut-off* (Fig 1.10). It can be well calculated using a semi-classical model except the behavior of the *cut-off* region. Accurate HHG calculations are now obtained using a quantum model based on the strong field approximation (Lewenstein model) [27].

Since the HHG process is trigged by the laser's electric field, the emitted photons are coherent, which is the basic for lens-less imaging. HHG has other advantages, such as the attosecond pulse structure, which is demonstrated in form of attosecond pulse train in 2001 [28]. We can also cite its natural synchronization with the driving infrared laser, which makes it suitable for ultrafast dynamics studies in a pump-probe geometry. I also would like to point out that the HHG source has been used to seed a soft X-ray FEL resulting in pulse with improved temporal coherence [29].

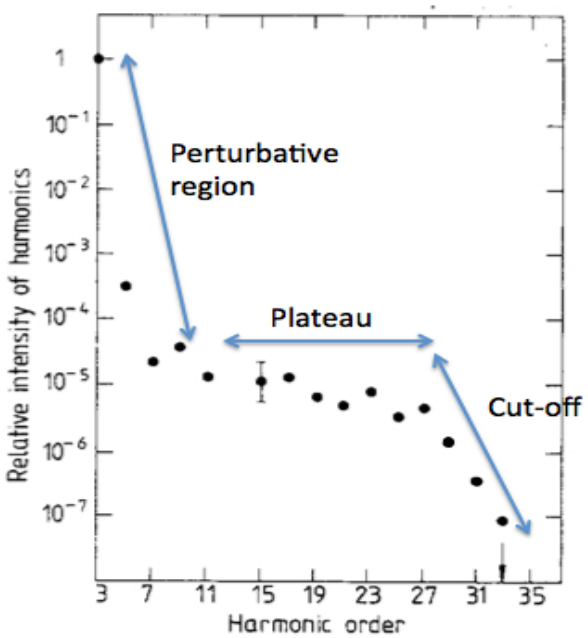

Fig. 1.10. A typical spectrum of HHG with three parts: perturbative region, *plateau* and *cut-off*. The original spectrum is extracted from Ref 22.

Practically, in the context of the application of HHG in lens-less imaging, we usually choose the harmonics in the *plateau*. They are usually more intense and stable than the *cut-off* harmonics. We also select through phase matching the short trajectory that exhibits better spatial and spectral coherence properties than the long trajectory.

I.7 Conclusion

This chapter has presented first the principle of lens-less imaging, in which the main obstacle for image reconstruction is the phase problem caused by the detection mechanism of the CCD camera. The phase retrieval algorithms and the Fourier transform holography are two main approaches to solve the phase problem. The former is an iterative process based on oversampling and constraints in both Fourier and direct space, while the latter encodes phase information into hologram by interference between object and reference. A discussion of the requirements of the suitable source for such imaging techniques has shown the potential of the high-order harmonic beam source, which provides high coherent and ultrafast (femtosecond scale) beam of short wavelength with a sufficient photon flux. A brief introduction of HHG is then presented, following by an introduction of the imaging formation process that occurs in lens-less imaging experiments. I present then several phase retrieval algorithms and the principle of holography style techniques (FTH, HERALDO) that are used for the scattering experiments realized during my PhD studies. A suitable source to perform ultrafast coherent imaging in the soft X-ray is the high harmonic generation. I briefly recall the principle of the source and more details are given about the practical aspects of source in the following chapter.

Chapter II
High flux harmonic beamline

II.1 Introduction

All the imaging experiments in this thesis work have been accomplished using the High flux harmonic beamline at the CEA Saclay research center, France. The harmonic beamline is a table-top femtosecond soft X-ray harmonic source driven by the table-top infrared femtosecond laser LUCA (Laser Ultra Court Accordable). LUCA is a Ti:sapphire laser system, which delivers up to 50 mJ energy pulses at 800 nm with a pulse duration of 50 fs and a repetition rate of 20 Hz. The experiment is composed of a lens stage (in air) and three experimental chambers (in vacuum). At the lens stage, a long focal length lens (f = 5.56 m) focuses the infrared beam into the gas cell located in the first experimental chamber. We can adjust the IR beam aperture by a diaphragm located in front of the lens. The lens is motorized by a translation stage in the beam propagation direction with a movement range of 15 cm, which offers an easy control of the relative position of the beam focus and the gas cell.

The three experimental chambers of the High flux harmonic beamline are (Fig. 2.1):

1) HHG chamber: Up to 50 mJ laser energy can be focused into a gas cell to generate harmonics beam. The gas cell is a metal tube with two pinholes at its extremes filled with rare gas. We have easy and full motorized control of the gas cell in vacuum: the cell length is variable from 0 to 15 cm and its lateral position (y direction) to the beam propagation direction (z) is motorized by a translation stage; we can also adjust the orientation of the cell in z direction by tilting it in x and y directions (perpendicular to z) with precision.
2) Optics chamber with "imaging configuration": The harmonics and IR beams propagate together into the optics chamber. An IR antireflective mirror separates them and sends the harmonics beam to the diffraction chamber. The residual IR is then filtered by aluminum filters located between the optics chamber and the diffraction chamber.
3) Optics chamber with "spectrum configuration": We can also replace the IR antireflective mirror by a set of toroidal mirror and plane grating for spectrum studies. The thin slit and the photomultiplier tube (PMT) are located at the end of the setup. We can also replace the PMT by an XUV camera to measure the harmonic beam profile in the far field or even an XUV wave front sensor.
4) Diffraction chamber (Fig. 2.2): The multilayer parabolic mirror (coated by Institut d'Optique) selects one harmonic order (25^{th} harmonic in our experiments) and focuses the beam onto the sample located at its focus. The CCD camera behind the sample holder detects the diffraction pattern in the far field regime.

This harmonic beamline has delivered its first photons in 2007. First demonstration of CDI reconstructions of a test object has been published in 2009. This has encouraged further

studies in lens-less imaging and beamline optimization. This chapter will follow the time line to present the High flux harmonic beamline developments.

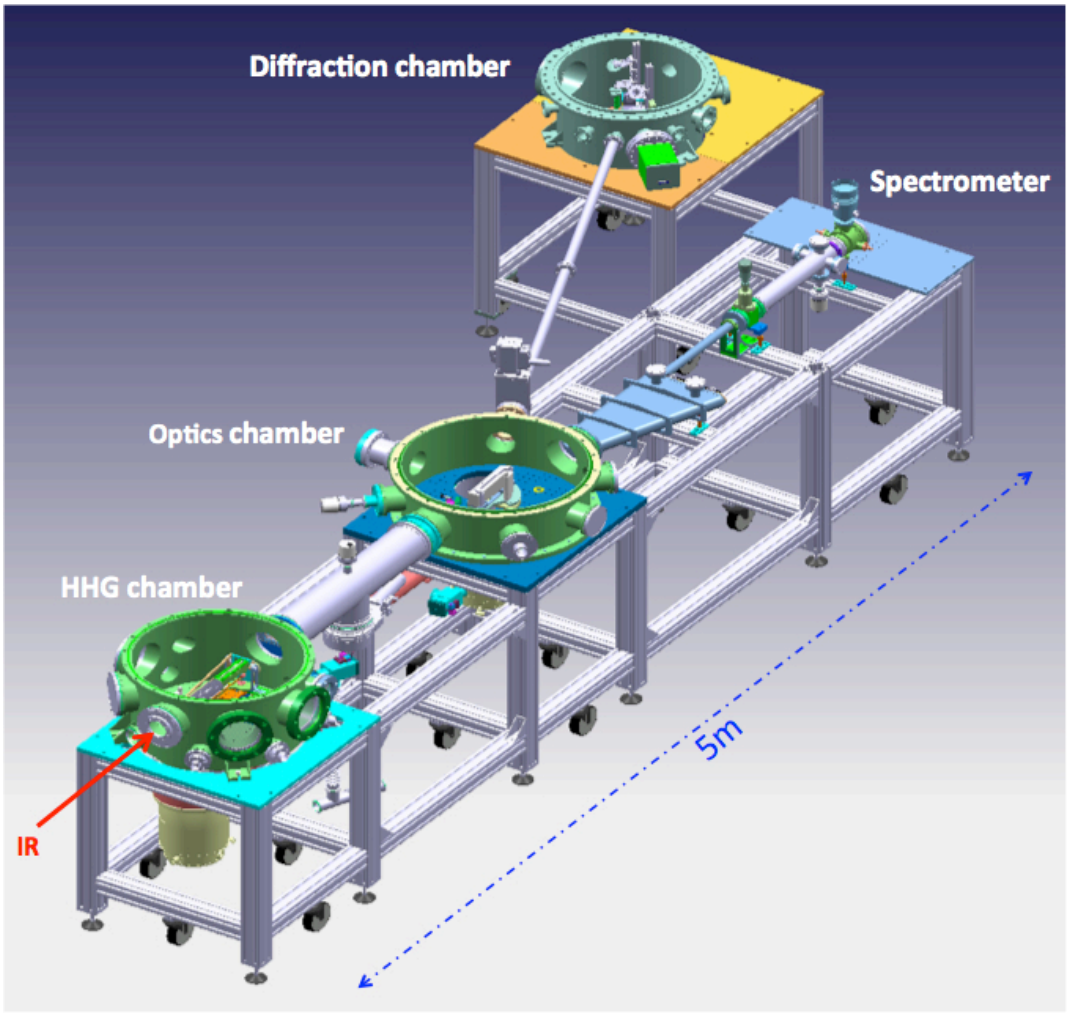

Fig. 2.1. Scheme of the High flux harmonic beamline. The red arrow at left bottom indicates the beam propagation direction. The infrared beam is first focused into a gas cell in the harmonic generation chamber. The optics chamber separates the harmonics beam from the IR beam and sends it into the diffraction chamber where the lens-less imaging experiments will take place. The optics chamber can also switch to a TM-PGM (Toroidal Mirror-Plane Grating Monochromator) type spectrometer for HHG studies. The entire setup is about 5 meters long.

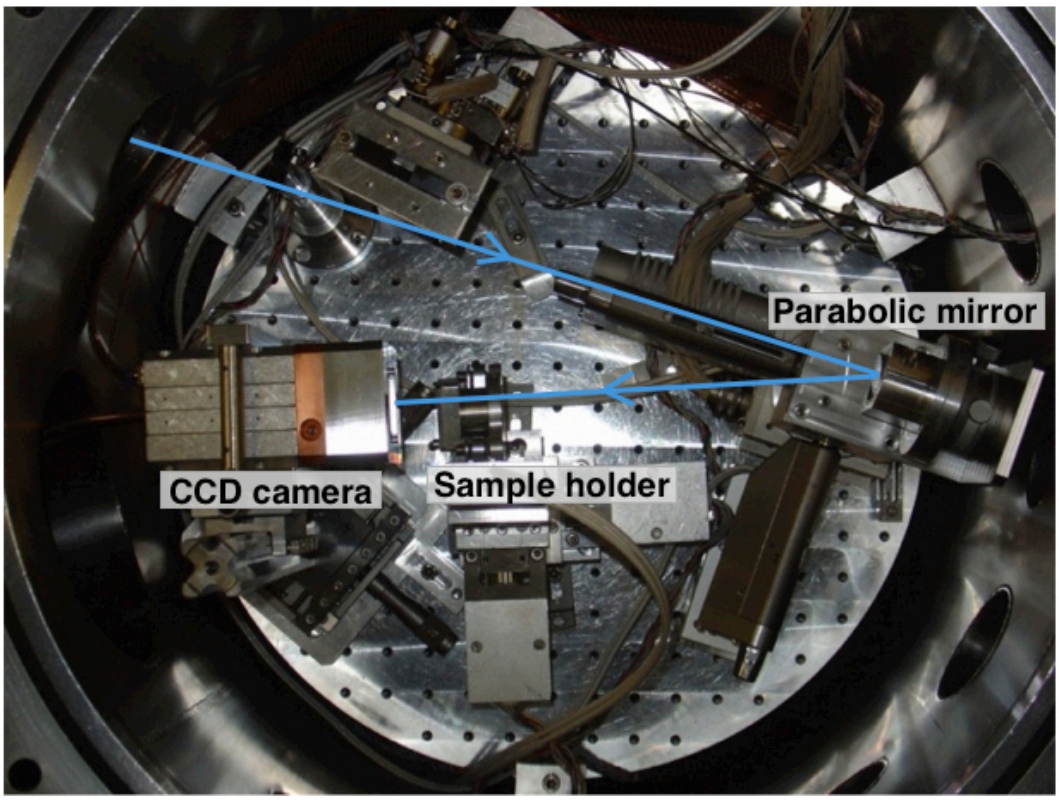

Fig. 2.2. Picture of the diffraction chamber. The parabolic mirror focuses the harmonics beam onto the sample, and the CCD camera located behind the sample holder detects the diffraction pattern.

II.2 Historical development of the High flux harmonic beamline

At the end of last century, encouraged by the great potential of high-order harmonics (HH) source for probing matter with XUV pulses on ultrafast time scales, numerous studies have demonstrated significant HHG conversion efficiencies, using ultrashort laser pulses focused in gases, in hollow core fibers [1,2,3] and cells [4,5] in a tight focusing geometry. However, even they reached the saturation intensities of the generating rare gases, the harmonic energies was still low (in the nanojoule range) because of the very low pump laser energies (less than 1 mJ). In 2002, the CEA research group has demonstrated higher harmonic energies (more than 1 μJ) with a pumping energy of 27 mJ focused into a gas jet by long focal length lenses (f = 2 m or 5 m) [6]. The HHG conversion efficiencies in loose focusing geometry have been shown to be higher than in the tight focusing geometry by a factor 6. The thorough study of HHG in different gases resulted in high harmonic yields are at least one order of magnitude higher than previously reported values. A report of HHG optimization in different configurations (hollow core fibers, tight focusing in high pressure medium and loose focusing in gas cell) presented an interesting discussion about the "absorption limit" concept, phase matching, harmonic dipole and conversion efficiency [7]. Conversion efficiencies (at that time) of 1.5×10^{-5} for harmonic 21 and 3×10^{-5} for harmonic 23 have been demonstrated in a long gas cell of Argon (Ar) and loose focusing geometry. These results have stimulated the idea of building a harmonic beamline for single-shot lens-less imaging applications.

From 2005 to 2007, various experiments of HHG optimization and beam characterization have been accomplished on the harmonic beamline at Saclay. The HHG optimization is a complex process with numerous parameters. At the macroscopic level, the interplay between phase matching, medium absorption and focusing geometry has to be balanced in the HHG optimization process. One of the basic ideas developed at Saclay is to couple the maximum energy available at the LUCA laser facility (around 50 mJ/pulse at 800 nm, and up to 100 mJ/pulse in extreme conditions). The total number of generated harmonic photons will increase with the laser intensity until the saturation intensity limit. Note that for 25th harmonic generated in Argon gas (the setup for imaging experiments), the intensity saturation is about 1×10^{14} W/cm^2 [8]. Another basic idea is to use a long cell as generating medium with adjustable length and gas density. Increasing the gas density (by increasing the gas pressure) seems to be a simple way to increase the harmonic photon number. However the phase matching condition and medium reabsorption have to be taken into account. E. Constant *et al.* [2] have established a relationship and criterion between the "coherence length", the "absorption length" and the "useful medium length". The HHG optimization requires optimum values for these three lengths.

Some important experimental results will be shown here briefly. They are extracted from the first part of the thesis of W. Boutu [9]. The experiment setup is a TM-PGM type spectrometer (section II.1). First, the effects of the medium density (changed by gas pressure) on HHG are studied. Fig 2.3(a) shows the harmonics signal (from 11th to 15th harmonics) generated in Xenon with two different cell lengths as a function of the gas pressure. Fig 2.3(b) shows the dependence of the harmonics signal with the gas pressure at two different laser intensities. There is an optimal pressure value for each curve, after which the harmonic signal decreases. In addition, the optimum gas pressure depends on the gas type.

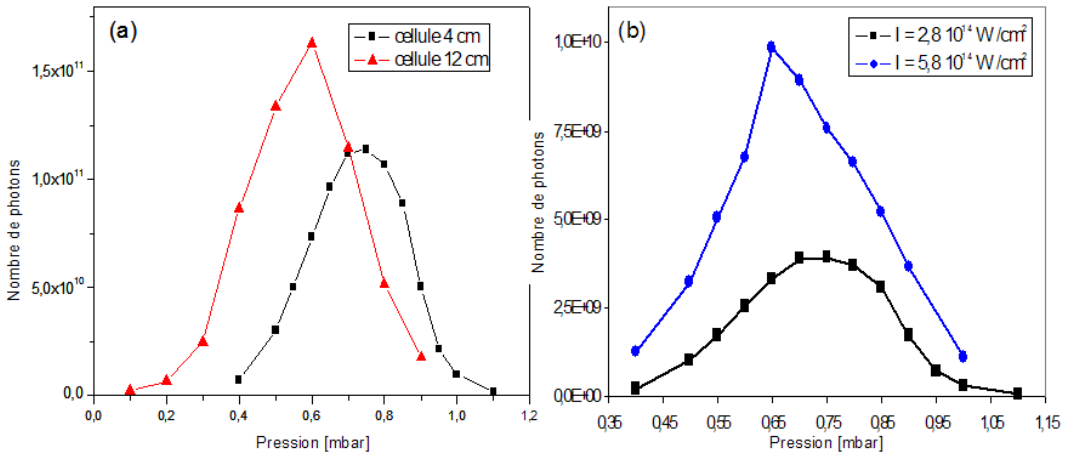

Fig. 2.3. Variations of the harmonics signal (from 11th to 15th) generated in Xenon in function of the gas pressure: (a) with a laser intensity of 2×10^{14} W/cm^2 and two cell lengths (the red line for 12 cm and the black line for 4 cm); (b) with a cell length of 4 cm and two laser intensities (the blue line for 5.8×10^{14} W/cm^2 and the black line for 2.8×10^{14} W/cm^2).

A series of HHG experiments with different focal length have been accomplished with the aim of increasing the useful pumping energy in the generating medium while keeping the laser intensity at the focus close to the saturation limit. The transverse section of the

interaction volume between the pump laser and the generating medium is then increased leading to a higher harmonic yield. A larger focal volume is obtained with a longer focal length. For example, a lens with 2 times longer focal length leads to a 2 times larger beam radius and 4 times larger focusing volume, thus 4 times more harmonic photons can be potentially generated or even more if phase matching is enhanced. Fig. 2.4a presents the variation of the harmonic energy as a function of the focal length generated in different gases. The laser energy is 20 mJ for the focal length of 4 m and 38 mJ for the focal length of 7.5 m. The harmonic energy values are estimated at the position of the cell exit by taking into account of the transmissions of the different optics and filters. Fig. 2.4b presents the increments of the harmonic energy with different focal length compared to focal volume increment. From 4 m to 7.5 m, the focal volume is increased by a factor of 3.5, while the harmonic energy is only increased by a factor of 1.9 for 21th order and 1.5 for 25th order. The effect is lower than expected. This can be related to the refraction of the laser beam caused by the ionization of the gas, which increases with the focal length. W. Boutu *et al.* [10] has discussed it with both numerical simulations and experimental results. The increment is also limited by the laser energy and the spatial mode. Practically, we have to use a diaphragm to control the beam focalization and optimize the phase matching conditions.

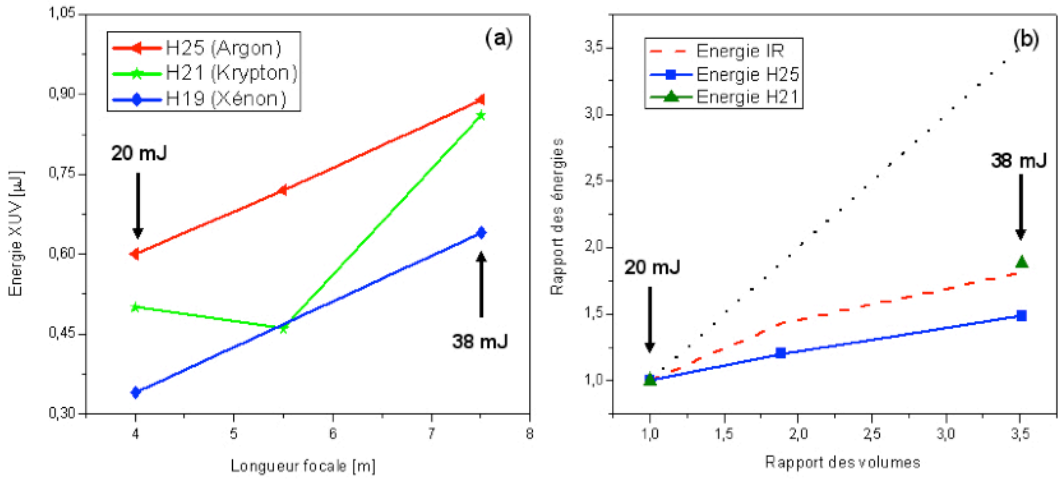

Fig. 2.4. (a) Variations of the harmonic energy as a function of the focal length for different harmonic orders generated in different gases (red line: H25 in Argon, green line: H21 in Krypton, blue line: H19 in Xenon). (b) Normalized harmonic energies as a function of the increment ratio of the interaction volume (green points: H21 in Krypton, blue line: H25 in Argon). The red dot line is the normalized increment ratio of IR beam. The black dot line is the ideal increment ratio of harmonic energy with the focal volume.

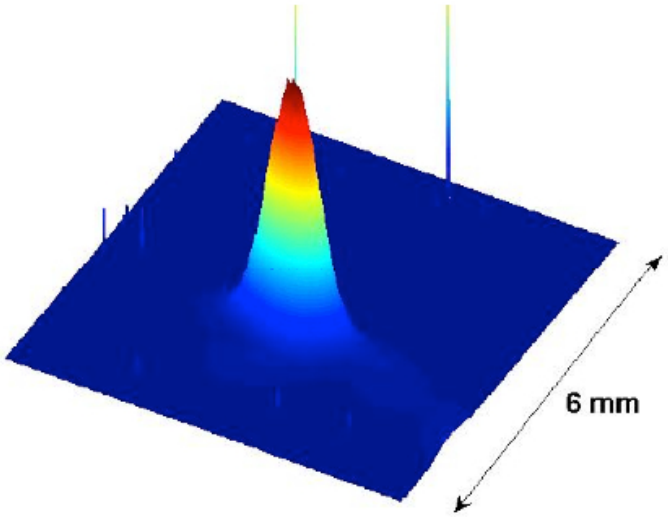

Fig. 2.5. Spatial profile of the 25th harmonic generated in Argon with a focal length of 7.5 m and a laser energy of 38 mJ detected by a XUV camera in far field. The measured harmonic beam has a very low divergence of about 0.4 mrad.

The beam coherence is another important factor, particularly in lens-less imaging. A characterization has been realized using a set of Young's double slits located at 1 m from the focus of the toroidal mirror. A CCD camera located at 1.6 m from the slits records the interference patterns. Measurements have been performed for the 25th harmonic generated in Argon with two different focal lengths (5.5 m and 7.5 m). The spatial coherence is estimated from the fringe visibility in the center part of the interference figures. Fig 2.6 shows that the coherence degree is at least higher than 0.4 and is relatively independent with respect to the focal length.

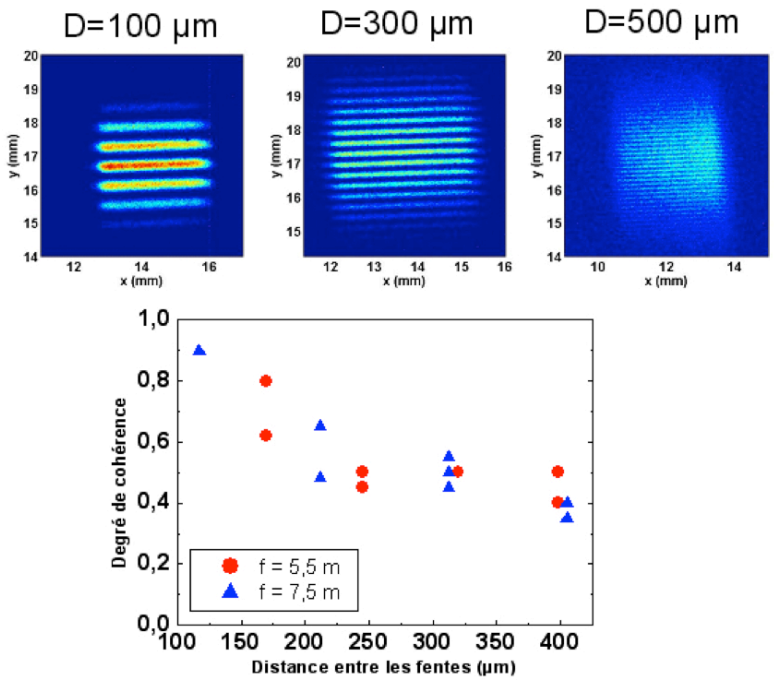

Fig. 2.6. Measured interference figures of the 25th harmonic (generated in Argon) with a set of Young's double slits separated 100 µm, 300 µm and 500 µm. The Young's double slits are located at 1 m from the focus of the toroidal mirror and the XUV camera is placed at 0.6 m from the slits.

Thanks to all these optimization and characterization work, a harmonic beamline was finally built up to perform single-shot coherent diffractive imaging applications. In 2009, A. Ravasio *et al.* reported the first demonstration of CDI on a test object [11] using a single harmonic pulse (20 fs) from a femtosecond table-top HHG source. The images of the test object "music note" were reconstructed with a resolution of 119 nm in single-shot regime and 62 nm in multiple shots regime (Fig. 2.7).

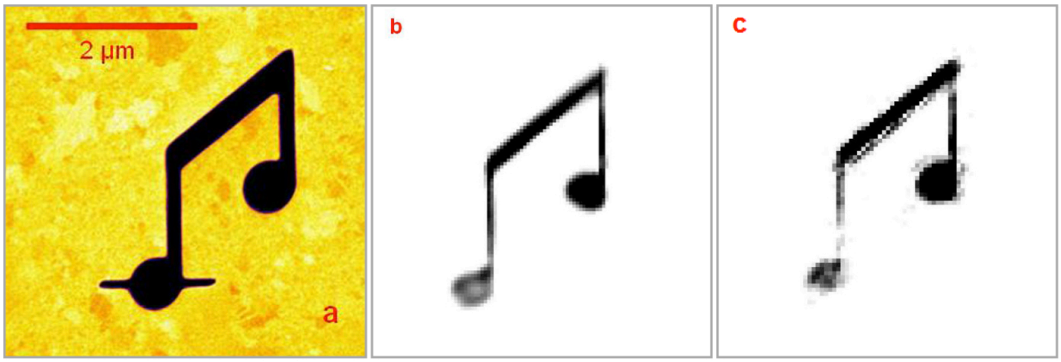

Fig. 2.7. (a) Scanning microscopy image (SEM) of the test object "music note"; (b) Reconstructed image from a diffraction pattern accumulated over 40 shots (2s exposure time) with 62 nm resolution; (c) Reconstructed image from a single-shot diffraction pattern (20 fs exposure time) with 119 nm resolution.

This promising image reconstruction of an isolated nanometric object with a single femtosecond harmonic pulse opens fascinating perspectives in dynamic studies in many scientific areas, such as ultrafast spin reversals of magnetic nanodomains (Chapter IV). The HHG pulses are naturally synchronized with the pump laser with sub-femtosecond time jitter. This significantly facilitates time resolved studies. Moreover, HHG sources offer an inexpensive and compact alternative to FEL facilities.

II.3 HHG optimization and beamline standardization

I present in this section the effort to build *a powerful, stable and reproducible harmonic beamline for imaging applications*. The main goal is to realize dynamical visualization (2D or 3D) of ultrafast physical phenomena on a femtosecond scale with nanometric spatial resolution. In coherent imaging, the X-ray photon flux on sample (single-shot or multiple shots) determines the signal extension on the diffraction pattern (the maximum spatial frequency of the diffracted signal). A high signal extension corresponds to a high theoretical spatial resolution (Eq. 1-29, Chapter I). Moreover, the radiation damage of samples (especially biological ones) limits the maximum pulse energy for each shot, which is an real limitation for light sources that provide high average but low peak flux beam, such as synchrotrons. However, one can achieve high-resolution imaging with another strategy. The idea is to irradiate the sample with a single pulse short enough to capture the image before the onset of the radiation damage [12, 13]. The FEL or XFEL facilities can provide such X-ray pulses. HHG source has demonstrated such potential however further work was necessary to improve the quality of the CDI diffraction patterns. In this thesis work I present the optimization of the entire beamline (HHG process and all the optics) to finally get the maximum pulse energy available on sample for high-resolution single-shot imaging. It has been also important to standardize the beamline to have stable beam performance, which was at the very beginning of my work unstable from day to day.

The harmonic beamline optimization has been realized in two steps:

1) HHG optimization: As mentioned before, we would like to maximize the harmonic pulse energy to get higher reconstruction resolution. However, it is not the only factor that influences the reconstruction quality. The wave front, the coherence and the spatial distribution of the intensity of the harmonic beam are also critical factors. The HHG optimization process conducted here has been to find an optimum compromise between all these factors to enhance the quality of diffraction patterns or holograms.
2) Focusing optimization: The sample is located at the focus of the parabolic mirror. The phase retrieval algorithms reconstruct the exit wave at the object plane (Chapter I, section I.2) that is equal to the sample transmittance in case of a plane wave illumination. Thus the harmonic beam focusing quality has a large influence on the reconstruction result. We need a homogenous focal spot and a proper spot size compared to samples.

We have used a Hartmann type wave front sensor to characterize and evaluate the quality of the generated harmonics beam before and after focusing optics (the parabolic mirror). The wave front sensor measures the wave front and the intensity of the harmonic beam, and

reconstructs the beam profile using back-propagation functions. First we place the wave front sensor at a distance of 5 m from the gas cell without any focusing optics (Fig. 2.8). We measure the direct harmonics beam in far field and optimize the wave front as a function the HHG parameters, such as IR laser energy, IR beam aperture, gas cell length, gas pressure and etc. Then, we align the wave front sensor after the focus of the parabolic mirror to characterize and optimize the focal spot.

After the optimization process with the wave front sensor, we use a Young's double slits to characterize the harmonic beam coherence, and study the influence of the coherence on phase retrieval reconstructions. We measure the variations of the beam coherence using a similar process as the HHG optimization with the wave front sensor. The results show that it could be an alternative way to optimize the beamline, but less efficient and less accurate than the wave front sensor, because one has to check manually the fringe visibility of each interference pattern and only a small part of the beam is characterized in each measurement.

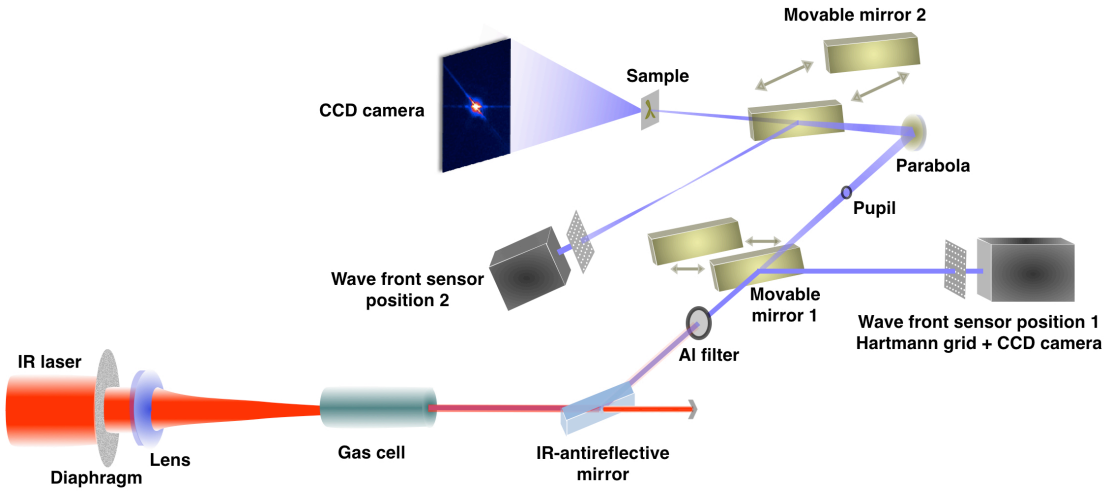

Fig. 2.8. Scheme of the optimization experiment setup. 1) HHG optimization configuration: Movable mirror 1 (multilayer plane mirror) is in and the wave front sensor is located at position 1 to measure the direct harmonics beam. 2) Focusing optimization configuration: Movable mirror 1 is out and mirror 2 is in; the wave front sensor is located at position 2 to measure the focused harmonic beam by the parabola. 3) Diffraction configuration: Two movable mirrors are out and no wave front sensor. The sample (Young's double slits) is located at the focus of the parabola and the XUV camera detects the diffraction pattern (far field interference of the slits exit waves).

II.3a HHG optimization and beamline standardization: wave front sensor

The Hartmann type wave front sensor "HASO" (produced by Imagine Optics Corp.) is composed of a Hartmann pattern grid and a XUV camera located 20 cm behind the grid (Fig. 2.9a). The harmonic beam goes through the Hartmann grid, which is an array of holes, and projects the "beamlets" sampled by each hole onto the XUV camera. The positions of the individual spot centroids are measured (Fig. 2.9c) and compared with reference positions (calibrated with perfect wave front, Fig. 2.9b). The measured local shifts of each beamlet can

reconstruct the wave front of the harmonic beam. The measured beamlets present also the harmonic beam's intensity profile at a sampling rate of the grid. One can then deduce the aberrations of the beam. Using back-propagation functions, the harmonic beam profile at the point source can be reconstructed. These numerical calculations are realized within the paraxial approximation.

The wave front sensor is calibrated and provided by the research group of P. Zeitoun at Laboratoire d'Optique Appliquée (LOA), France. The Hartmann grid is 19 x 19 mm^2 large and contains 51 x 51 square holes that each is 80 x 80 μm^2 large and separated by 380 µm. The back-illuminated CCD camera has 2048 x 2048 pixels of 13.5 x 13.5 μm^2 each, operating at -40 °C. The typical calibration method is presented in Ref 14. In our case, a 10 µm pinhole positioned in the beam propagation path at 1 m from the gas cell output diffracts the beam and generates a perfect wave front. The sensor accuracy is then experimentally measured to be λ/50 RMS (root mean square) at a wavelength λ = 32 nm, i.e. an accuracy of 0.64 nm RMS [15]. Note that an aberration of λ in amplitude corresponds to local phase aberration of 2π. One should be careful when using such a sensor to measure a wave front with very strong aberrations. The mismatch of beamlets and the reference positions could lead to wrong reconstruction of wave front if the aberration exceeds 2π. In our case, the harmonic beam has relatively week aberrations so that the sensor is well adapted.

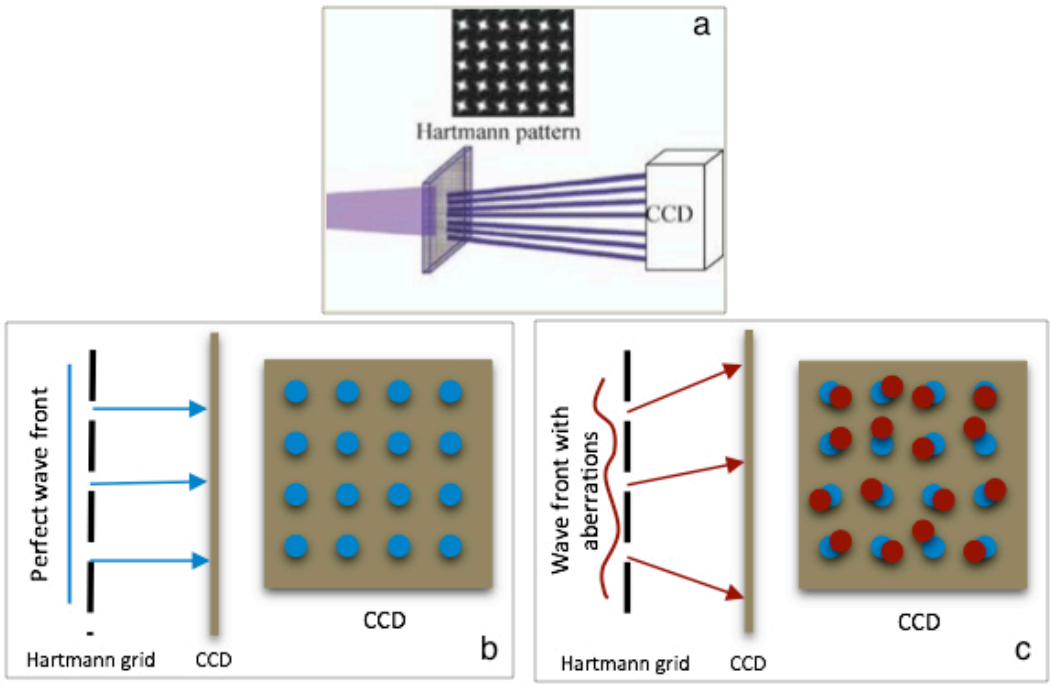

Fig. 2.9. Scheme of the Hartmann type wave front sensor. (a) The target beam goes through the Hartmann pattern grid, which is an array of holes, and projects onto the XUV camera behind. The XUV camera detects the sampled intensity of the beam. (b) The wave front sensor should be calibrated with a perfect beam before first use. The positions of the beamlets on the camera will be registered as reference positions (blue points). (c) The wave front is reconstructed from the measured local shift (red points) of each beamlet compared to the reference positions.

II.3b HHG optimization and beamline standardization: HHG optimization

In the first step, we have explored systematically several HHG parameters to optimize the harmonic flux and the beam wave front RMS value. The wave front RMS value describes how the measured wave front is distorted compared to a plane wave. According to the Maréchal's criterion [16], a beam is diffraction-limited at a given wavelength λ when the aberrant wave front amplitude is lower than λ/14 rms. As we assume a plane wave illumination in CDI, if the beam is far away from a plane wave, then the reconstruction will not correctly represent the sample transmittance but the ensemble exit wave (sample transmittance + incident wave). However, we can still extract the sample transmittance if we know the incident wave in priori, which requires a measurement of the incident wave front.

Practically, if the beam is not stable (aberrations change from shot to shot), simultaneous measurements of the incident wave and the sample diffraction pattern will be required. If the beam is stable that measurements can be achieved in different shots, the relative position of the beam when hitting onto the sample should be known for extracting correctly the sample transmittance information.

In our experiment, we have optimized the wave front RMS value to the diffraction-limited (λ/14) and maximized the harmonic flux. Some of the experimental results are presented in the following figures. Fig. 2.10 to Fig. 2.12 show the variations of harmonic pulses intensities (blue curves) and wave front RMS values (red curves) in function of one HHG parameter, while others are fixed. The variant parameter and fixed parameters' values for each figure are listed below.

Curves in	Beam aperture	Gas pressure	Gas cell length	Laser energy
Fig. 2.10	21 mm	8 mbar	Variant	~ 15 mJ
Fig. 2.11	20 mm	Variant	8 cm	~ 15 mJ
Fig. 2.12	Variant	8 mbar	8 cm	Variant

Table 2.1. Generating parameters' value range for HHG optimization studies

The initial IR beam has a diameter of about 40 mm and is then limited in aperture by a diaphragm located in front of the focusing lens. The gas pressure is measured at the upper stream of the gas cell, which is proportional to the one inside the cell. The laser energy is measured behind the diaphragm, which is the effective pulse energy focused into the generating medium. For all the measurements presented in these three figures, the beam is focused at 2 cm behind the gas cell output by the lens of 5.65 m focal length. All the intensity measurements curves are normalized to the maximum value and then rescaled to fit the display of the wave front RMS curves.

During the studies of gas cell length (from 3 to 12 cm, Fig. 2.10) and gas pressure (from 6 to 10 mbar, Fig. 2.11), the variations of the wave front RMS values are moderate and slow. The maximum variations of the two curves are ~ 0.06λ (λ/17) for the gas cell length and ~ 0.05λ (λ/20) for the gas pressure. They both have a region of minimum RMS values around 0.1λ

(λ/10) for gas cell length from 5 to 8 cm and for gas pressure from 8 to 9 mbar. The two intensity curves have similar behavior with relatively fast growths and decays, before and after the maxima. The maximum intensities are achieved at gas cell length = 8 cm (Fig. 2.10) and at gas pressure = 8 mbar (Fig. 2.11) that are both located in the optimum range of the wave front RMS. The variations between maxima and minima of measured intensities in both cases are more than 50% ($\frac{max-min}{max}$). These intensity curves are similar to the results of previous work (Fig. 2.3) of HHG studies.

The study of beam aperture (from 18 to 26 mm, Fig. 2.12) presents interesting results of wave front RMS values, which keep stable around minimum value 0.1λ (λ/10) until beam aperture equal to 21 mm and increase rapidly from 22 mm. This dramatic variation can be explained by the effects of HHG phase matching. During the study, the laser energy before the diaphragm is fixed at 42 mJ, thus the effective laser energy increases with the beam aperture. As the size of the laser beam focal spot decreases when we open the diaphragm, the laser intensity at the focus increases at the fourth power of the diaphragm radius. When the intensity saturation of the generating medium is reached, the ionization occurs and leads to destructive effects in phase matching. This affects the harmonic beam quality. The ionization also influences the IR laser beam propagation and will significantly degrade the spatial profile of the laser beam when the beam aperture is larger than 22 mm (section II.4c). The intensity curve has a usual behavior that increases with higher laser energy (larger beam aperture) until a maximum at a beam aperture of 21 mm. It then decreases when the ionization occurs.

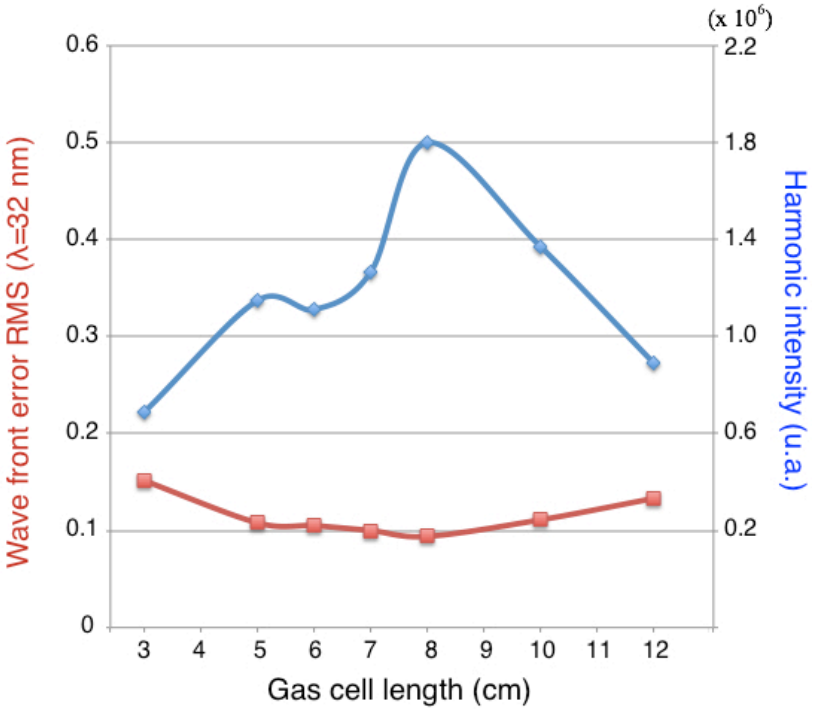

Fig. 2.10. Generating condition: beam aperture = 21 mm, gas pressure = 8 mbar, laser energy = ~15 mJ. The blue and red curves present respectively the variations of harmonic intensity and harmonic wave front RMS in function of gas cell length.

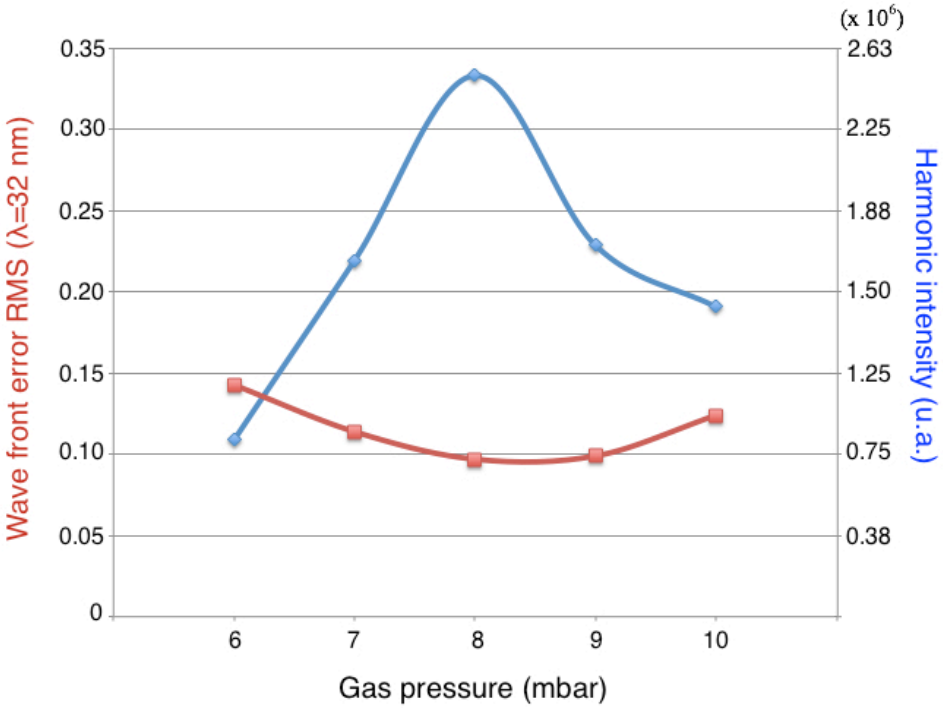

Fig. 2.11. Generating condition: beam aperture = 20 mm, gas cell length = 8 cm, laser energy = ~15 mJ. The blue and red curves present respectively the variations of harmonic intensity and harmonic wave front RMS in function of gas pressure.

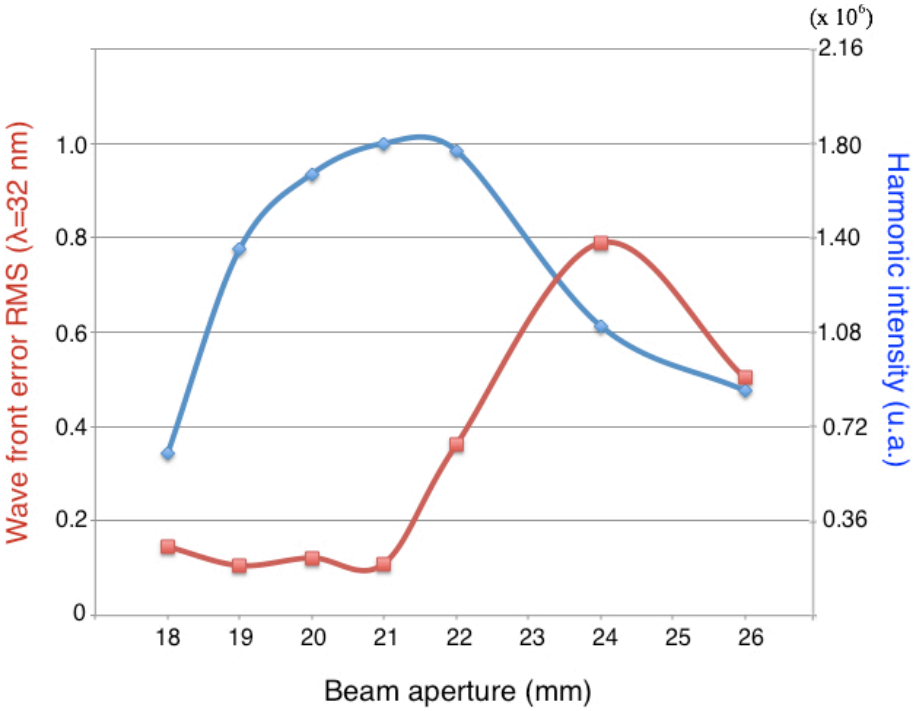

Fig. 2.12. Generating condition: gas pressure = 8 mbar, gas cell length = 8 cm, laser energy before diaphragm = 42 mJ. The blue and red curves present respectively the variations of harmonic intensity and harmonic wave front RMS in function of beam aperture.

We conclude the optimum parameters' value range: beam aperture = 20~21 mm, gas pressure = 8~9 mbar, gas cell length = 5~8 cm, effective laser energy = 15 mJ and the focus position is 2 cm behind the gas cell output. The beam aperture of 20~21 mm corresponds to a laser focal radius of 137~143 μm and the confocal parameter = 14,7~16 cm. The harmonic flux and the wave front RMS share the same optimum value range and are maximized with the same parameter values, which agrees with previous work [15,19].

The optimum gas pressure values can change slowly after some experimental time, since the IR laser ablates the input and output pinholes of the gas cell during the harmonic generation. An optimization of the gas pressure by analyzing the far field harmonic beam profile and intensity is necessary when installing new pinholes of the gas cell.

Note that during these studies, we didn't change the laser focus position because of some practical limitations. After setting up the laser modal filtering (section II.4c), we have studied the optimization of the laser focus position by analyzing the far field spatial profile of the harmonic beam (detected by CCD camera). There is an optimum range of the laser focus position from 0 to 5cm behind the gas cell output. If the laser is focused before the gas cell output, the intensity and the spatial profile of the harmonic beam become worse while approaching the laser focus towards the gas cell input. When the laser focus goes further behind the gas cell output (maximum 8 cm behind, limited by the translation stage of the lens), the harmonic beam intensity decreases slowly and its spatial profile remains relatively good. This phenomena is related to the self-guiding of the laser pulse during the propagation in the generating medium. The self-guiding effect can enhance the laser properties (such as the laser intensity distribution) and the phase-matching condition. In a previous work [17], it has indeed been shown that the laser self-guiding condition strongly depends on the gas cell position. When the gas jet (9 mm long) is located before the laser focus, they observed that the harmonic beam intensity increases dramatically (two orders of magnitude higher). Our experimental results show similar effect on the generated harmonic beam with about three times higher intensity. More important, the spatial profile of harmonic beam is more homogeneous in the optimum range.

For each wave front measurement, aberration contributions are calculated with Zernike polynomials, which is unstable from shot to shot. There is no obvious relation between aberration contributions and the harmonic generating conditions. Previously, two groups working on HHG optimization with wave front sensor reports contradictory conclusions of harmonic aberrations dependence on pump laser aberrations [15,19]. A further study on the aberration dependence of the High flux harmonic beamline is planned and it may lead to new HHG optimization.

The harmonic beam generated with optimum parameters has a wave front RMS of 0.11λ (λ/9), compared to a non-optimized harmonic beam whose wave front RMS is 0.79λ (Fig 2.13). Meanwhile, the spatial profile of the harmonic beam in far field has also been optimized, which is important for coherent imaging. The reconstructions of the harmonic beams at the source are shown in the Fig. 1 of Paper I.

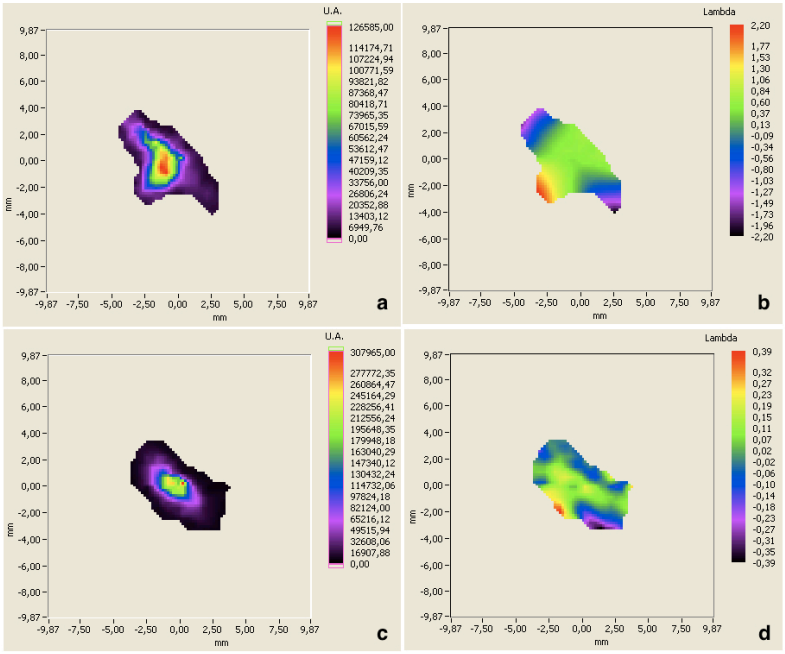

Fig. 2.13. Generating condition: gas pressure = 8 mbar, gas cell length = 8 cm, laser energy = 15 mJ, beam aperture = 24 mm for (a) and (b), and 21 mm for (c) and (d). (a) is the measured intensity and (b) is the measured phase of the non-optimized harmonic beam by the wave front sensor in far field. (c) and (d) are respectively the intensity and the phase of the optimized harmonic beam. Note that the absolute phase scales in (b) and (d) are different.

II.3c HHG optimization and beamline standardization: Focusing optimization

In the second step, the wave front sensor is located behind the focus of the parabolic mirror to characterize the harmonic focal spot, which represents the illumination condition for coherent imaging. In the beam path from the harmonic source (output of the gas cell) to the sample (focus of the parabolic mirror), there are only two optics (IR-antireflective mirror and parabola) and one aluminum filter. The focusing quality, thus the illumination quality is strongly related to the alignment of the parabola. The parabola is motorized by translation stages and goniometers. It is initially aligned with residual IR beam as reference. The study with a wave front sensor allows direct measurements of the focusing quality with the harmonic beam (25^{th} order) in the same condition as the coherent imaging. A fine adjustment is then possible for the parabola motorized in all translation and tilt directions to optimize the focal spot. Finally, the wave front sensor measurements in this configuration characterize the whole harmonic beamline until the diffraction stage by taking account of all elements in the beamline except the detection part. The optimization of the detection stage is associated to each particular imaging configuration, including sample conditions, imaging technique, final resolution, illumination quality, etc. It will be discussed in the following chapter.

Experimental results show that a fine adjustment of the parabola with the harmonic beam can optimize the focal spot's spatial profile and aberrations. Fig 2.14 shows the enhancement of the harmonic beam before and after the fine adjustment of the parabola. We get a harmonic beam of 0.154λ (~λ/6) RMS (Fig. 2.14d) instead of 0.326λ (~λ/3) RMS (Fig. 2.14b) measured

at the Hartmann grid. Usually, the dominant aberration of the harmonic beam is the coma, which should be associated to the miss-alignment of the parabola. It is clearly observed in the reconstruction of the focal spot (Fig. 2 in Paper I) before fine adjustment. The focal spot after fine adjustment presents a homogenous and quasi-circular beam profile, with reduced coma aberration. The beam size (at $1/e^2$) is optimized from 7.8 μm to 5 μm, which matches better our samples (usually within a window of 5 x 5 μm). Compared to the 20 μm focal spot used in the previous work of "music note" (also within a window of 5 x 5 μm), the effective harmonic photons for diffraction are largely increased.

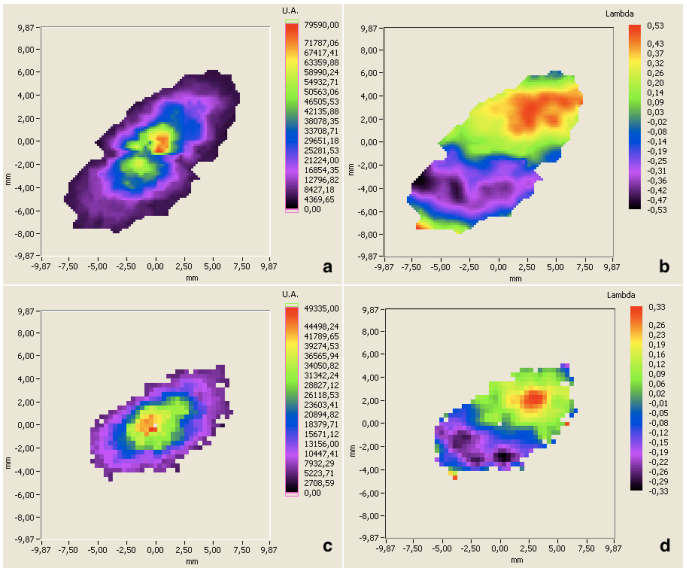

Fig. 2.14. (a) is the intensity and (b) is the phase of the 25th harmonic beam with initially aligned measured by wave front sensor. (c) and (d) are respectively the intensity and the phase of the harmonic beam with finely tuned parabola.

In the beam propagation direction (*z* direction), the focused harmonic spot changes quickly before and after the parabola focus position. The evolutions in both conditions (before and after fine adjustment) are similar, while the optimum adjustment provides quasi-circular focal spot in a range of ±0.5 mm around the focal position, larger than in the other case (Fig. 2.15). This range is important for the coherent imaging as it give flexibility in positioning the sample. Usually, we use a sharp edge (for example, the edge of the sample membrane) to look for the focus position (Fig. 2.16). Typically, we can find the focus position with a precision of ±0.2 mm, which fits the previous range of ±0.5 mm. Note that a daily alignment of the IR laser during the initiating stage of the harmonic beamline is required, which could be critical for the harmonic focusing quality. The IR laser should be aligned as it was for the fine adjustment with wave front sensor to ensure an optimum focal spot. A permanent installation of wave front sensor in focusing optimization configuration could be a precise method for daily alignment, especially for experiment projects spanning over months. According to our experience, careful daily alignment (without wave front sensor) is sufficient for short-term experiments.

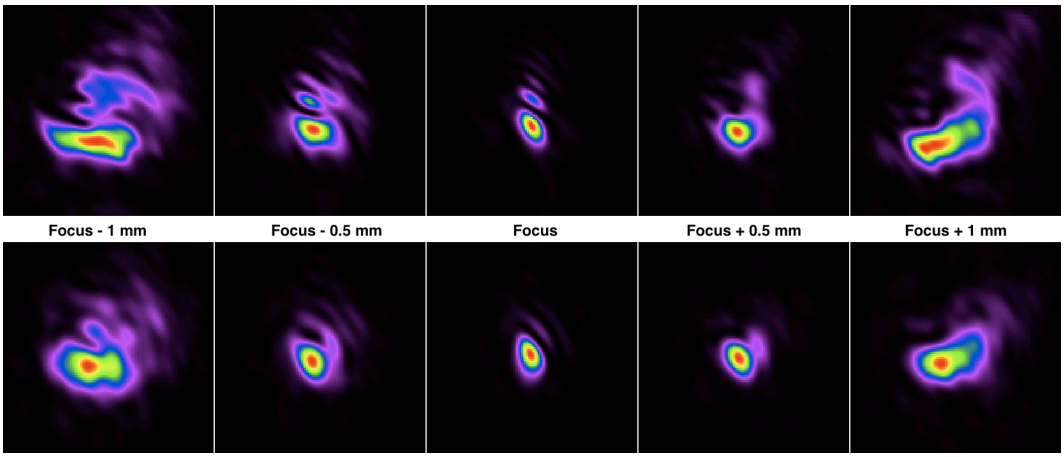

Fig. 2.15. The top line presents the evolution of the reconstructed harmonic beam spatial profile around the focus of the parabola before fine adjustment. The bottom line is for the case after fine adjustment.

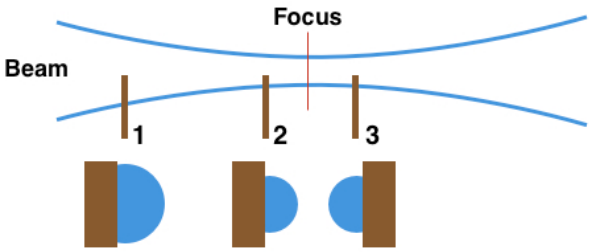

Fig. 2.16. Practically, to find the focus position of the beam, we move a testing edge (the brown squares) from position 1 to position 3 along the beam propagation direction at certain step. In position 1 and 2, the beam (blue circles) is cut from one side (for example, the left side). When we path the focus position, the beam will be cut from the opposite side (the right side in position 3). Then the focus position is fixed in a range and we can get more precise position by repeating the process with smaller step

II.3d HHG characterization: spatial coherence at the focus

We are now interested in the behavior of the spatial coherence of the harmonic beam generated with different HHG conditions. We switch the harmonic beamline to the diffraction configuration (Fig. 2.8), and place a double Young slits at the sample position. The double slits are 1.5 µm long and 300 nm wide, separated by 4 µm, fabricated by a nano-focused ion beam (FIB, CSNSM facility in Orsay University). The CCD camera records the interference pattern in the far field (19 mm behind the double slits). We use the similar exploration process of the HHG parameters as the optimization with wave front sensor. The studied parameters are gas cell length, gas pressure and beam aperture.

The evolutions of the fringe visibility and the diffraction pattern intensity are compared as a function of other generating parameters (Fig. 2.17 to Fig. 2.19). All the measurements are in single-shot regime. The measured fringe visibility is up to 0.8 ~ 0.84 in optimum range of HHG parameters, and lower than 0.5 in certain conditions. The fringe visibility, thus the spatial coherence of the harmonic beam, has the same evolution behavior as the diffraction

intensity (which is proportional to the harmonic beam intensity at focus). We conclude that the harmonic flux, wave front quality and the spatial coherence can be optimized under the same HHG condition. These three factors are essential for coherent imaging. They influence the diffracted signal strength (or signal to noise ratio), the illumination wave front and the accuracy of the phase information encoded in the diffraction pattern.

Compared to the harmonic beam size (5 µm), the Young double slits (separated by 4 µm) measurements characterize the beam of its outer part. One should use a set of Young double slits separated by different distances to have a full characterization of the beam coherence (one measurement for one distance). Otherwise, a coherence-testing pattern can be used to measure the beam coherence of several different distances within one measurement (Chapter 5, section V.1).

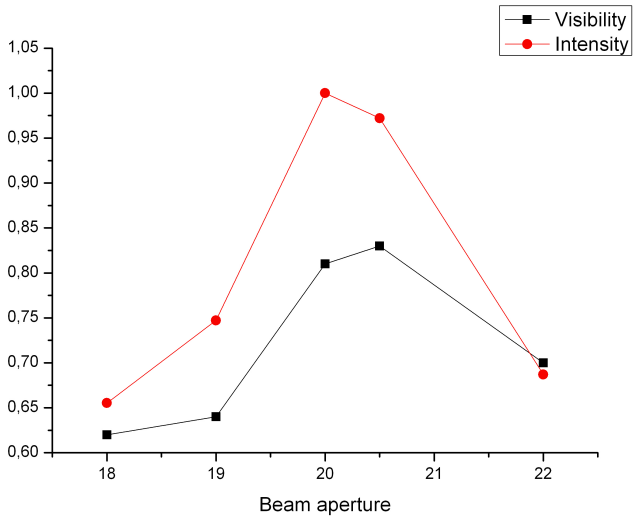

Fig. 2.17. The black and red curves present respectively the variations of fringe visibility and the diffraction pattern intensity as a function of beam aperture. The intensity curve is normalized to the maximum intensity detected.

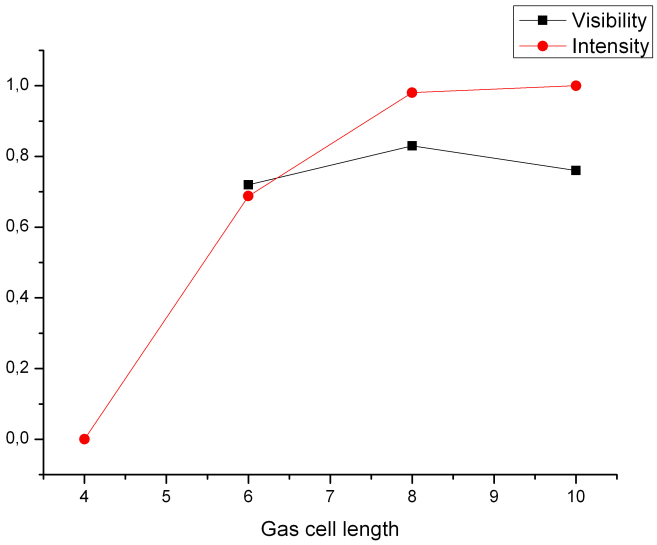

Fig. 2.18. The black and red curves present respectively the variations of fringe visibility and the diffraction pattern intensity as a function of the gas cell length. The intensity curve is normalized to the maximum intensity detected. Note that the diffraction intensity for gas cell length = 4 cm is too weak to be detected; however the direct harmonic beam without the presence of the double slits can be detected by the CCD camera.

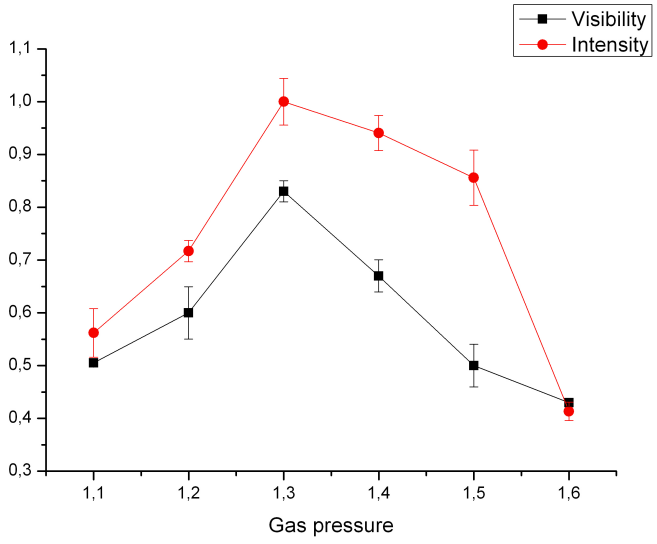

Fig. 2.19. The black and red curves present respectively the variations of fringe visibility and the diffraction pattern intensity in function of gas pressure. The intensity curve is normalized to the maximum intensity detected.

II.4 IR Laser Modal Filtering

We have shown how the harmonic beamline, optics filters and also wave front and coherence can be controlled and improved. Is it possible to accomplish further optimization of the HHG properties by improving the driving laser beam? Since the HHG phase matching depends on the IR laser focusing quality and its propagation in the generating medium, the wave front and the spatial profile of IR laser along with its temporal properties have important roles in the HHG process. Some previous studies showed some correlation between the IR laser and the generated harmonic pulse of their wave fronts [15,19,20]. Further enhancement of the harmonic beam can be expected from spatial and/or temporal improvement of our IR laser beam. In practice, the IR beam (LUCA laser described earlier) before and after the temporal compression stage looks inhomogeneous with a triangle-like shape in the center part of the beam. There is a clear need of improving the spatial profile of the IR beam. The diaphragm that we located before the focusing lens to control the beam aperture is somehow a kind of spatial filter of the IR beam, which optimizes the HHG by adjusting its focal geometry, ionization and harmonic dipole properties [21]. However its application is quite limited. We have shown for example during the wave front studies that the HHG beam is strongly affected when the diaphragm is too widely opened. Phase matching is in particular destroyed when "bad" infrared modes superimposes in the HHG generating media.

In this section, studies of further improvement of the IR beam before injection into the gas cell will be presented, and followed by the results of HHG in condition of these improvements.

II.4a Modal Filtering: setup

There are various approaches to improve the IR beam quality. We can cite the use of a pinhole to filter high spatial frequencies of a focused laser beam [18], or a set of transmission phase plates to create a flat-top laser beam to increase the interaction volume and the HHG efficiency [22], or using a truncated Bessel beam produced by argon-filled hollow fiber for HHG [23], or improving the laser wave front by deformable mirrors and genetic algorithms to optimize HHG efficiency [24], and etc. Our approach is inspired by the hollow fiber compression technique [25], which generates sub-10 fs laser pulses by a capillary filled with gas, called "*post compression*". In our case, the fiber will not be filled with gases. We will mainly use the coupling between the laser modes and the fiber modes to improve the IR beam.

In the femtosecond regime, intense laser beam can easily lead to degradation of optical elements in the beam path, including the compression gratings. Therefore, we decide to place the hollow fiber before the compression stage and after the final amplification stage of LUCA laser. We then operate in picosecond regime, where related problems (mainly thermal problems) are easy to handle experimentally. The setup is shown in Fig. 2.20. A hollow-core fiber in silica of 30cm-long with a core radius a = 125μm is located after the amplification stage of LUCA laser, which delivers a laser beam of up to 180 mJ/pulse centered at 795 nm, at a repetition rate of 20 Hz, with a pulse duration of about 200 ps. The hollow-core fiber is operated in vacuum of about 10^{-3} mbar. The IR beam is first focused into the hollow-core

fiber, then couples with the fiber mode and diverges at the fiber output. A set of lenses located after the fiber collimates the filtered IR beam into the compression stage. Finally, the compressed femtosecond laser beam (up to 50 mJ/pulse) is used for HHG.

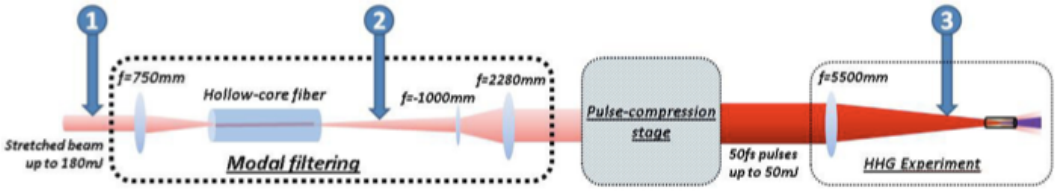

Fig. 2.20. Scheme of the modal filtering. The hollow-core fiber is located between the compression stage and the amplification stage of LUCA laser to filter the IR beam.

This scheme of hollow-core fiber is based on the theory of propagation of an electromagnetic wave in a cylindrical dielectric waveguide. In theory, the laser beam will be coupled with the fundamental mode of the fiber, which is EH_{11} in our case [26,27]. The reason to choose EH_{11} mode is because it has a similar transverse distribution as the Gaussian mode TEM_{00} in both near and far field (Fig. 2 in Paper II). The optimum coupling efficiency of a Gaussian mode is about 98%, corresponding a beam waist $\omega_0 = 0.65a$. It gives a first idea of the beam size at the entrance of the fiber. Moreover, the other guided modes are strongly attenuated during the propagation in the fiber. Thus, a spatial filter by modes selection of the laser beam is established. We call this technique "modal filtering".

II.4b Modal Filtering: experimental results

The modal filtering is tested and quantified by several series of measurements of the laser beam by beam profilers and wave front sensor. We are interested in the laser beam's spatial profile, the wave front quality, the modal composition, the pulse energy (energy transmission of the modal filtering) and its temporal properties after pulse compression stage, which are measured by SPIDER [28]. The wave front sensor used here is a Shack-Hartmann type that the grid is an array of micro-lenses, instead of holes in XUV sensor, and using the same principle of wave front measurement. We quantify the laser beam at different stages with and without the presence of the modal filtering. Fig. 2.21 is an overview of the laser beam quality comparison, measured and simulated by wave front sensor.

1) Before the compression stage: The beam without modal filtering (Fig. 2.21a) has an inhomogeneous spatial profile in a triangle-like shape and the wave front RMS is about λ/12 (λ = 795 nm). The latter has been improved by a factor of 5 with the modal filtering (Fig. 2.21b), which is λ/59, more than 4 times smaller than the Maréchal's criterion for diffraction limited beam, with a central symmetric profile that can be considered as free of aberration. Moreover, the M^2 factor of the beam [29] has been calculated by the ratio of the divergences between the measured laser beam and the Gaussian beam [30]. The diminution of the M^2 factor (from 2.1 to 1.4) confirms the spatial quality improvement of the beam. After the propagation in the hollow-core fiber, the mode EH_{11} presents about 95% in the filtered beam with 3% of EH_{12} and less than 2% of other modes. This high

portion of EH_{11} mode in the output beam is ensured by its coupling efficiency of about 88% with a low attenuation of about 2% (corresponding to the fiber length of 30 cm). The energy transmission of the modal filtering is in general from 60% to 70% depending on the input pulse energy. A maximum transmission of 78% has been observed, compared to the theoretical value (83%). The difference between daily experimental value (~70%) and the theoretical value is mainly due to the injection of the beam. Indeed, the beam size at the entrance of the fiber (radius of ~142 μm estimated from beam profilers measurements) is larger than the core radius of the fiber (125 μm), thus about 11% energy of the beam is outside the fiber core.

2) After compression stage: The wave front measurements (Fig. 2.21c,d) show some degradation of the laser beam after pulse compression. The measurements are realized at 3.85 m from the focusing lens (focal length of 5.65 m) to adapt the beam size to the aperture of the wave front sensor. The non-filtered beam has a wave front RMS of λ/5 while the filtered one is λ/14. We have still an obvious improvement on the beam quality by the modal filtering. The energy transmission of the compression stage is about ~ 40%. The pulse durations of the beam with and without the modal filtering are quantified by the SPIDER method for three different pulse energies after compression (4 mJ, 18 mJ and 42 mJ). Compared to the non-filtered beam (45-50 fs pulse duration), the filtered beam's pulse duration is equivalent at 4 mJ (47 fs) and 18 mJ (43 fs) and degrades at 42 mJ (65 fs). The higher energy density in the central part of the filtered beam could lead to compression defects, such as self-phase modulation.

3) At the focus of the lens for HHG: From the wave front measurements, we simulate the beam at the focus of the lens by propagation functions. Fig. 2.21e,f present the focal spot of the full laser beam without and with modal filtering, and Fig. 2.21g,h for the beam with a diaphragm aperture = 22 mm. The Strehl ratio represents the focusing quality by calculating the ratio between the reconstructed beam focus and a perfect beam [31]. A diffraction-limited beam corresponds to a Strehl ratio of more than 0.8. In our case, the ratio for the full beam is equal to 0.83 (with modal filtering) and 0.33 (without), which is a strong improvement. The laser beam diameter is about 42 mm for non-filtered case and ~ 32 mm for filtered one (measured at $1/e^2$). The diaphragm located before the focusing lens plays an important role for the beam's focal spot. When the diaphragm aperture is equal to 22 mm, the beams with and without modal filtering have similar focal spot (Fig. 2.21g,h), with different energy transmission, ~ 60% for filtered beam and ~ 50% for the non-filtered. However, the non-filtered beam's focal spot degrades quickly when the diaphragm opens larger than 22 mm. Note that the reconstructed focal spots do not represent the real HHG source size. Nevertheless, the reconstructions give us a first insight of the focusing quality for efficient HHG.

The measurements and simulations have demonstrated the high efficiency of the modal filtering on the laser beam quality improvement. The experimental results and theoretical predictions agree with each other. A quasi-mono-mode diffraction-limited beam of up to 50 mJ pulse energy and pulse duration of ~ 50 fs is given after the compression stage. In the point of view of laser systems, the modal filtering is a successful system of beam spatial quality improvement. With respect to our purpose, the modal filtering is made to increase the harmonic phase matching and the harmonic beam quality. Since the filtered beam loses about 30% pulse energy compared to the non-filtered beam and the highly non-linear property of

the HHG process, we are not sure whether this modal filtering can optimize the harmonic beam in our generating conditions. A campaign of HHG experiments has taken place to compare the harmonic flux and the spatial profile of the harmonic beam in far field with and without the modal filtering. Unfortunately, we didn't have the opportunity to do the complete measurements of the harmonic beam with a XUV wave front sensor as presented in the previous section. However the previous conclusion shows that when the harmonic flux and the beam coherence are optimized, the wave front is not far from optimization. A good compromise is then found for coherent imaging.

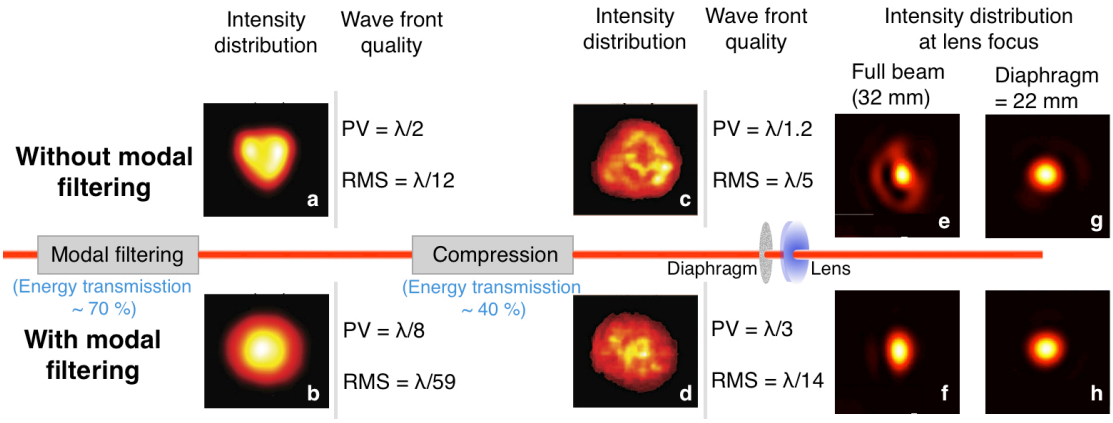

Fig. 2.21. (a-d) Wave front measurements of the beam with and without modal filtering at different places on the beam path. Intensity distributions and wave front variations of the beam are presented for each position. (e-h) At the lens focus, beam profiles are obtained from propagation simulation.

II.4c Modal Filtering: HHG

The HHG measurements with and without the modal filtering are realized in the "spectrum configuration" of the harmonic beamline (section II.1). A Toroidal mirror and a plane grating are located in the optics chamber. We use a thin slit and a photomultiplier tube (PMT) for the spectrum measurements and a CCD camera for the harmonic spatial profile measurements. The HHG optimization with modal filtering is realized using the same process as presented in the section II.3b. We are looking for a good compromise between harmonic flux and the spatial profile of the beam by varying different generating parameters, such as gas pressure, gas cell length, beam aperture, lens's focus position and IR pulse energy. The first campaign of HHG optimization is done with Argon gas and the optimum parameters' value range is similar to the case without modal filtering: beam aperture = 18~20 mm, gas pressure = 12~14 mbar, gas cell length = 6~8 cm, effective laser energy = 8~10 mJ and the focus position is 2 cm behind the gas cell output.

As mentioned previously, in the non-filtered beam case, the optimum diaphragm is around 20~21 mm with maximum laser energy possible. If we want to generate more harmonic photons, we have to open the diaphragm to have more laser energy pumped into the generating medium. However, a larger diaphragm means a tighter or even a worse focusing

quality (see Fig. 2.21e) with more instability. This leads to bad wave front quality of the harmonic beam. Fig. 2.22a-d shows the evolution of the harmonic beam's spatial distribution detected by XUV CCD camera in the far field. The harmonic beam is "stretched" into two spots as the diaphragm opens from 22 mm to 30 mm. Note that, for a beam aperture larger than 23 mm, the stability of the harmonic beam is not ensured.

When using the modal filtering, the laser energy is in general 30% less than the non-filtered one, but with a better spatial profile, especially in the central part of the beam (Fig. 9 in Paper II). The experimental results show that less laser energy is required to generate the same harmonic flux with the same beam aperture (Fig. 2.22a,h). For a beam aperture = 19.5 mm, with a laser energy = 8.5 mJ, we measured 2.4×10^7photons/pulse by the CCD camera with filtered beam. While the non-filtered beam has 2.2×10^7photons/pulse with beam aperture = 20 mm and laser energy = 20.5 mJ. The other generating parameters are the same in both cases. We can conclude that the harmonic conversion efficiency is increased by a factor more than 2. The optimized harmonic beam has 2.7×10^7photons/pulse obtained with a beam aperture = 18.5 mm and a laser energy = 10 mJ (Fig. 2.22g). We can get more photons by increasing the laser energy, for example, 3.3×10^7photons/pulse with laser energy = 13 mJ and beam aperture = 18.5 mm (Fig. 2.22k), but the spatial profile is worse in this case. In the case of modal filtering, to get a good compromise between spatial profile and harmonic photons, we are forced to reduce the laser energy to avoid the laser intensity saturation in the generating medium, which will lead to strong ionization effects and will somehow "distort" the generated harmonic beam (Fig. 2.22k-m). An extreme example is the case of full laser beam with 23.5 mJ/pulse that the harmonic beam is completely distorted. One solution is to close the diaphragm to get a larger focal spot. However experimental results show that simply decreasing the beam aperture by closing the diaphragm cuts too much laser energy for the harmonic generation (Fig. 2.22e,f). The harmonic photons/pulse is not increased by this way, which is limited by the maximum useful laser power. Another solution (not tested here due to limited beam time) is to use longer focal length lens have a larger focal spot, thus the laser intensity in the generating medium could possibly remain at a correct level when we increase the laser energy. Therefore, we can get a bigger interaction volume with sufficient laser intensity to generate as more harmonic photons as possible.

The laser beam filtered by the modal filtering can increase the harmonic conversion efficiency, and also improve the spatial profile of the harmonic beam in far field. Note that the elliptical shape of the harmonic beam presented in Fig. 2.22 is probably due to the aberrations of the toroidal mirror or the grating. Indeed, a circular beam is detected by the CCD camera in the diffractive imaging configuration.

In the second step, spectrum studies and optimization of HHG with Neon are accomplished. The goal was to generate efficient harmonics around 20 nm to be applied for an application in single-shot imaging of cobalt magnetic nanodomains (Chapter IV). The HHG optimization procedure in Neon is similar to that in Argon. As a result, the harmonic photon number generated in neon is increased by a factor ~ 4 when using the modal filtering. Fig. 2.23 presents an example of the 37th harmonic generated in Neon with (a) and without (b) the modal filtering. With a beam aperture = 24 mm and a laser energy = 21.5 mJ, 2.9×10^6photons/pulse are measured by the CCD camera with the modal filtering, instead of 0.8×10^6photons/pulse without modal filtering and with a laser energy of 33.5 mJ. This time, the harmonic flux ($\times4$) and the HHG efficiency ($\times6$) are both increased. This is related to the

fact that the laser intensity saturation in Neon (8.7×10^{14}W/cm^2) is much higher than in Argon. In general, the harmonic photon number generated in Neon is about one magnitude order less than in Argon. However we are interested in very high orders, not reached in argon with our laser, such as the 37th harmonic (57.4 eV) close to the M-edge of Cobalt (60 eV) (Chapter IV, section IV.2). The spectrum studies of the HHG in Neon are related to this application. The results are presented in Chapter IV.

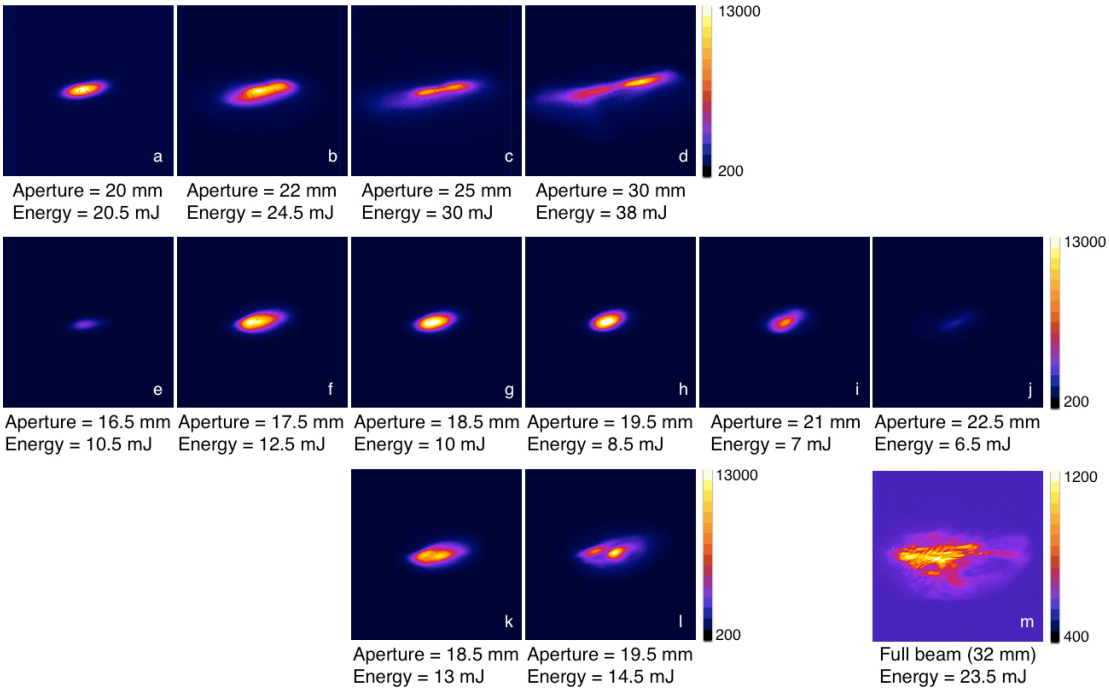

Fig. 2.22. Spatial profiles of the 25th harmonic generated in Argon detected by the CCD camera located in far field, with and without the modal filtering. Generation without (from a to d) and with (from e to m) the modal filtering for following parameters: lens's focus position is at 2 cm behind the gas cell output, gas pressure = 14 mbar and gas cell length = 8 cm. All the measurements are in single-shot regime with a window size of 10.8 x 10.8 mm^2. The increased gas pressure (compared to 8 mbar before) is due to the laser ablation of the cell input hole that gas tends to leak more. However the pressure inside the cell remains constant.

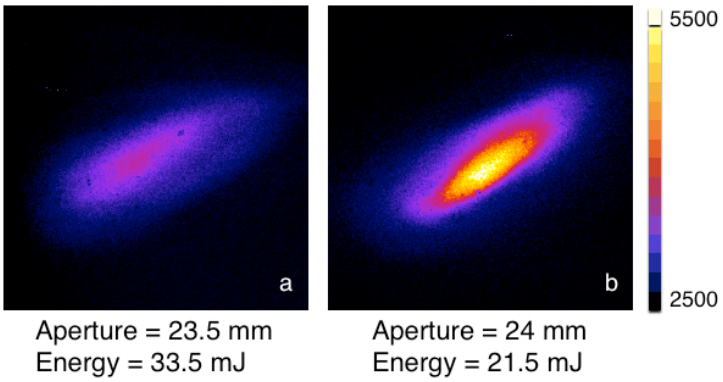

Fig. 2.23. 37th harmonic generated in Neon without (a) and with (b) the modal filtering in such conditions: lens's focus position is at 2 cm behind the gas cell output, gas pressure = 48 mbar and gas cell length = 7 cm. The measurements are in single-shot within a window of 3.37 x 3.37 mm^2 detected by the CCD camera in the far field.

II.4d Modal Filtering: Conclusion

The modal filtering is a successful laser beam optimization system by filtering the laser modes with a high coupling efficiency. The filtered laser beam is quasi-mono-mode of EH_{11}, close to Gaussian beam, and is diffraction-limited before and after the pulse compression stage. Meanwhile, the pulse duration after compression remains comparative with non-filtered case. In the point of view of HHG, the modal filtering increases the harmonic conversion efficiency by a factor of 2.5 in Argon and 6 in Neon. The harmonic flux is increased by a factor of 4 in Neon. However, it can be further improved in Argon but we had to cut off a large amount of laser energy to have a good spatial profile. To increase the harmonic flux in Argon with a proper spatial profile, we should change our experiment setup, for example, using a longer focal length lens (>5.65 m) to avoid too high laser intensity in the generating medium.

Another advantage of such device is the stability of the laser beam position on the focusing lens and inside the generating medium, which is important for a good alignment between the laser beam and the gas cell, and thus a stable HHG during a full day. The harmonic beam detected by the CCD camera is more stable in its spatial profile, intensity and position on the camera from shot to shot, compared to the case without modal filtering. We have observed a slow movement of the beam position in vertical direction after the output of the fiber, which is correlated to the working period of the air conditioner in the laser room. This slow movement is then corrected by a servomotor mounted on one plane mirror in the beam path before injection into the fiber. To have a full vision of the modal filtering system and its influence on the HHG, a campaign of wave front measurements in XUV and in IR will take place in the near future, along with further studies on the temporal properties of the filtered laser beam.

II.5 Conclusion

In this chapter, the High flux harmonic beamline is presented with three main parts, the historical development, the optimization with XUV wave front sensor and the modal filtering device. The actual setup of the harmonic beamline for coherent imaging applications is presented in Fig. 2.24. The hollow-core fiber is installed between the amplification stage and the compression stage. The filtered beam is then focused into the gas cell by a lens of 5.65 m focal length. The harmonic beam is separated from the IR beam by an IR-antireflective mirror and an aluminum filter. A multilayer parabola selects one harmonic order and focuses it onto the sample located at the focus of the parabola. The CCD camera detects the diffraction pattern of the sample in far field. Note that, we have optimized the harmonic transmission of the beamline by using a high-tech aluminum filter (purchased from LUXEL Corp.) of 60% transmission for concerned wavelength in our case, compared to previous Al filter of 10% transmission (used in Ref. 11).

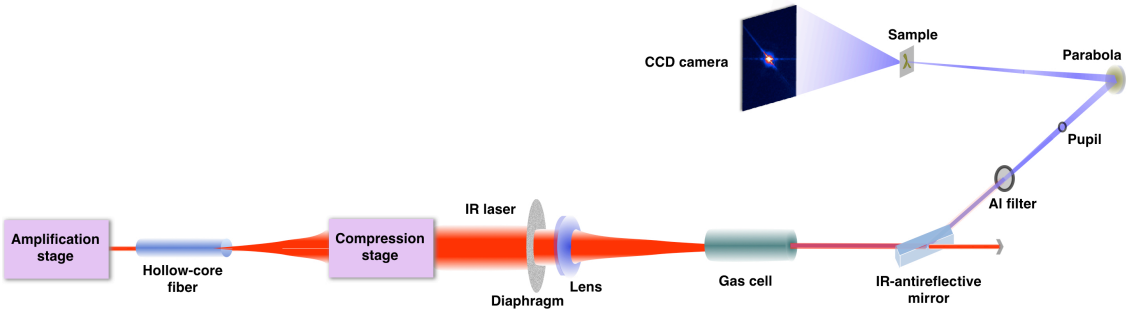

Fig. 2.24. Up-to-date setup of the High flux harmonic beamline for coherent imaging applications.

The High flux harmonic beamline is easy to switch to the spectrum configuration for other studies than coherent imaging. In both case, a μJ harmonic source (about 10^{11} photons per shot for 25th harmonic, $\lambda = 32$ nm) is generated at the output of the gas cell, with a wave front RMS of $\lambda/9$ before parabola and $\lambda/6$ after focusing, which is two times the diffraction-limited ($\lambda/14$). The combination of the intense harmonic flux and the good wave front quality promise high-quality diffraction pattern for coherent imaging. The campaign of harmonic wave front measurements result in an optimized HHG and a standardization of the beamline's daily operation conditions. Different generating parameters have been studied in this campaign. The finely adjusted parabola offers a focal spot size with a better quality and with a size well adapted to our imaging samples. The Young's double slits study has demonstrated a high coherent harmonic beam (fringe visibility more than 0.8 at the focus) and concludes that the harmonic flux, the wave front quality and the beam coherence can be optimized at the same generating condition. The modal filtering device provides a quasi-mono-mode laser beam for HHG and leads to improvement of the harmonic conversion efficiency. Even though we are actually not able to focus all the laser energy into Argon to generate much more harmonic photons than before, some feasible modifications on the beamline (space needed) can potentially resolve the problem. Nevertheless, the harmonic flux in Neon is increased 6 times with the modal filtering. In both gases, the spatial profile of the harmonic beam in far field and the beam stability from shot to shot are better with the modal filtering. Fig. 2.25 is a typical spectrum of the HHG in Argon on the High flux harmonic beamline. The measured spectral width of the 25th harmonic (full width at half maximum) is 0.65 nm that the temporal coherence ($\Delta\lambda/\lambda$) is 0.02.

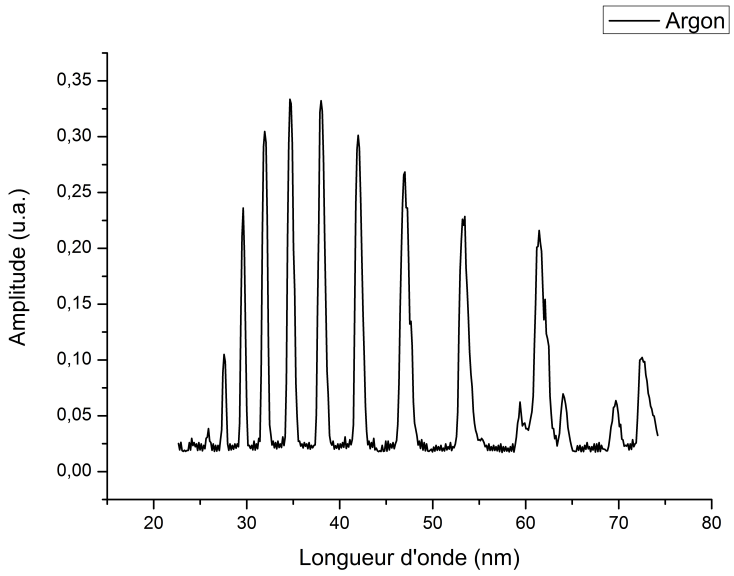

Fig. 2.25. The spectrum of the harmonics generated in Argon.

The harmonic beam used for coherent imaging in the Chapter III is summarized below:

Wavelength	32 nm
Pulse energy at the focus of the parabola	5×10^8 photons/pulse, ~ 3 nJ/pulse
Pulse duration	20 fs
Repetition rate	20 Hz
Intensity of the focal spot (5 μm diameter)	~ 10^{12} W/cm^2
Spatial coherence	> 0.8
Temporal coherence	0.02

Table 2.2. Summery of the harmonic beam's properties

This ultrafast and brilliant harmonic source promises high-resolution reconstructions of coherent imaging with a femtosecond time scale. The imaging experiments will be presented in the following chapter.

Even though our harmonic beam is 3 to 4 magnitude orders less than the beam delivered by the FEL facilities (for example, FLASH at Hamburg and LCLS at Stanford). Our beamline facilitates the experimental working conditions, with a relative easy control of the harmonic beam. The inexpensive cost and compact dimension of such beamline promises wider implementation in the world, thus much more beam time for various applications. Dynamic studies can be realized by a simple installation of a pump-probe setup.

Paper I

This paper consists of three parts: the optimization with the wave front sensor, the coherence influence on CDI reconstructions and the demonstration of 78 nm spatial resolution in single-shot regime (20 fs pulse duration). The optimization and the coherence measurements are developed above. The coherence influence on CDI and the experimental results will be developed in Chapter 3.

Accepted in Optics Express in October 2012.

Impact of wave front and coherence optimization in coherent diffractive imaging

X. Ge[1], W. Boutu[1], D. Gauthier[1], F. Wang[1], A. Borta[1], B. Barbrel[1], M. Ducousso[1], A.I. Gonzalez[1], B. Carré[1], D. Guillaumet[1], M. Predrix[1], O. Gobert[1], J. Gautier[2], G. Lambert[2], F.R.N.C. Maia[3], J. Hajdu[3], P. Zeitoun[2] and H. Merdji[1,*]

[1]*Commissariat à l'Energie Atomique, Service des Photons, Atomes et Molécules, Bâtiment 522, Centre d'Etude de Saclay, 91191 Gif-sur-Yvette, France.*
[2]*Laboratoire d'Optique Appliquée, ENSTA ParisTech – CNRS – Ecole Polytechnique, Chemin de la Hunière, 91761 Palaiseau, France*
[3]*Laboratory of Molecular Biophysics, Department of Cell and Molecular Biology, Uppsala University, Husargatan 3 (Box 596), SE-751 24 Uppsala, Sweden.*

* hamed.merdji@cea.fr

Abstract: We present single shot nanoscale imaging using a table-top femtosecond soft X-ray laser harmonic source at a wavelength of 32 nm. We show that the phase retrieval process in coherent diffractive imaging critically depends on beam quality. Coherence and image fidelity are measured from single-shot coherent diffraction patterns of isolated nano-patterned slits. Impact of flux, wave front and coherence of the soft X-ray beam on the phase retrieval process and the image quality are discussed. After beam improvements, a final image reconstruction is presented with a spatial resolution of 78 nm (half period) in a single 20 fs laser harmonic shot.

OCIS codes: (140.7090) Ultrafast lasers; (140.7240) UV, EUV, and X-ray lasers; (340.7480) X-rays, soft x-rays, extreme ultraviolet (EUV); (030.1640) Coherence; (340.7440) X-ray imaging.

References and links

1. R. Neutze, R. Wouts, D. van der Spoel, E. Weckert, J. Hajdu, "Potential for biomolecular imaging with femtosecond X-ray pulses," Nature 406, 752-757 (2000).
2. K. J. Gaffney, H.N. Chapman, "Imaging Atomic Structure and Dynamics with Ultrafast X-ray Scattering," Science **316**, 1444-1448 (2007).
3. J.R. Fienup, "Phase retrieval algorithms: a comparison," Appl. Opt. **21**, 2758-2769 (1982).
4. J. W. Miao, P. Charalambous, J. Kirz, D. Sayre, "Extending the methodology of X-ray crystallography to allow imaging of micrometre-sized non-crystalline specimens," Nature **400**, 342-344 (1999).
5. H.N. Chapman, A. Barty, M.J. Bogan, S. Boutet, M. Frank, S.P. Hau-Riege, S. Marchesini, B.W. Woods, S. Bajt, W.H. Benner, R.A. London, E. Plonjes, M. Kuhlmann, R. Treusch, S. Dusterer, T. Tschentscher, J.R. Schneider, E. Spiller, T. Moller, C. Bostedt, M. Hoener, D.A. Shapiro, K.O. Hodgson, D. van der Spoel, F. Burmeister, M. Bergh, C. Caleman, G. Huldt, M.M. Seibert, F.R.N.C. Maia, R.W. Lee, A. Szoke, N. Timneanu, J. Hajdu, "Femtosecond diffractive imaging with a soft-X-ray free-electron laser," Nature Physics **2**, 839-843 (2006).
6. H.N. Chapman, A. Barty, S. Marchesini, A. Noy, S.P. Hau-Riege, C. Cui, M.R. Howells, R. Rosen, H. He, J.C.H. Spence, U. Weierstall, T. Beetz, C. Jacobsen, D. Shapiro, "High-resolution ab initio three-dimensional x-ray diffraction microscopy," J. Opt. Soc. Am. A **23**, 1179-1200 (2006).
7. A. Barty, S. Boutet, M.J. Bogan, S. Hau-Riege, S. Marchesini, K. Sokolowski-Tinten, N. Stojanovic, R. Tobey, H. Ehrke, A. Cavalleri, S. Dusterer, M. Frank, S. Bajt, B.W. Woods, M.M. Seibert, J. Hajdu, R. Treusch, H.N. Chapman, "Ultrafast single-shot diffraction imaging of nanoscale dynamics," Nature Photonics **2,** 415-419 (2008).
8. H. Jiang, C. Song, C.-C. Chen, R. Xu, K.S. Raines, B.P. Fahimian, C.-H. Lu, T.-K. Lee, A. Nakashima, J. Urano, T. Ishikawa, F. Tamanoi, J. Miao, "Quantitative 3D imaging of whole, unstained cells by using X-ray diffraction microscopy," Proc. Natl. Acad. Sci. U.S.A. **107**, 11234-11239 (2010).
9. A.P. Mancuso, T. Gorniak, F. Staier, O.M. Yefanov, R. Barth, C. Christophis, B. Reime, J. Gulden, A. Singer, M.E. Pettit, T. Nisius, T. Wilhein, C. Gutt, G. Grübel, N. Guerassimova, R. Treusch, J. Feldhaus, S. Eisebitt, E.

Weckert, M. Grunze, A. Rosenhahn, I.A. Vartanyants, "Coherent imaging of biological samples with femtosecond pulses at the free-electron laser FLASH," New J. Phys. **12,** 035003 (2010).
10. H.N. Chapman, S.P. Hau-Riege, M.J. Bogan, S. Bajt, A. Barty, S. Boutet, S. Marchesini, M. Frank, B.W. Woods, W.H. Benner, R.A. London, U. Rohner, A. Szoke, E. Spiller, T. Moller, C. Bostedt, D.A. Shapiro, M. Kuhlmann, R. Treusch, E. Plonjes, F. Burmeister, M. Bergh, C. Caleman, G. Huldt, M.M. Seibert, J. Hajdu," Femtosecond time-delay X-ray holography" Nature **448,** 676-679 (2007).
11. R.L. Sandberg, A. Paul, D.A. Raymondson, S. Hädrich, D.M. Gaudiosi, J. Holtsnider, R.I. Tobey, O. Cohen, M.M. Murnane, H.C. Kapteyn, C. Song, J. Miao, Y. Liu, F. Salmassi, "Lensless Diffractive Imaging Using Tabletop Coherent High-Harmonic Soft-X-Ray Beams," Phys. Rev. Lett. **99,** 098103 (2007).
12. R.L. Sandberg, C. Song, P.W. Wachulak, D.A. Raymondson, A. Paul, B. Amirbekian, E. Lee, A.E. Sakdinawat, C. La-O-Vorakiat, M.C. Marconi, C.S. Menoni, M.M. Murnane, J.J. Rocca, H.C. Kapteyn, J. Miao, "High numerical aperture tabletop soft x-ray diffraction microscopy with 70-nm resolution," Proc. Natl. Acad. Sci. U.S.A. **105,** 24-27 (2008).
13. A. Ravasio, D. Gauthier, F.R.N.C. Maia, M. Billon, J.-P. Caumes, D. Garzella, M. Géléoc, O. Gobert, J.-F. Hergott, A.-M. Pena, H. Perez, B. Carré, E. Bourhis, J. Gierak, A. Madouri, D. Mailly, B. Schiedt, M. Fajardo, J. Gautier, P. Zeitoun, P.H. Bucksbaum, J. Hajdu, H. Merdji, "Single-Shot Diffractive Imaging with a Table-Top Femtosecond Soft X-Ray Laser-Harmonics Source," Phys. Rev. Lett. **103,** 028104 (2009).
14. D. Gauthier, M. Guizar-Sicairos, X. Ge, W. Boutu, B. Carre, J. R. Fienup, and H. Merdji, "Single-shot Femtosecond X-Ray Holography Using Extended References," Phys. Rev. Lett. **105,** 093901 (2010).
15. X. Huang, H. Miao, J. Steinbrener, J. Nelson, D. Shapiro, A. Stewart, J. Turner, C. Jacobsen, "Signal-to-noise and radiation exposure considerations in conventional and diffraction x-ray microscopy," Opt. Express 17, 13541-13553 (2009).
16. G. Williams, M. Pfeifer, I.A. Vartanyants, I.K. Robinson, "Effectiveness of iterative algorithms in recovering phase in the presence of noise," Acta Crystallographica Section A **63**, 36-42 (2007).
17. J.C.H. Spence, U. Weierstall, M. Howells, "Coherence and sampling requirements for diffractive imaging," Ultramicroscopy **101**, 149-152 (2004).
18. G.J. Williams, H.M. Quiney, A.G. Peele, K.A. Nugent, "Coherent diffractive imaging and partial coherence," Phys. Rev. B. **75,** 104102 (2007).
19. L.W. Whitehead, G.J. Williams, H.M. Quiney, D.J. Vine, R.A. Dilanian, S. Flewett, K.A. Nugent, A.G. Peele, E. Balaur, I. McNulty, "Diffractive Imaging Using Partially Coherent X-Rays," Phys. Rev. Lett. **103,** 243902 (2009).
20. I.A. Vartanyants, I.K. Robinson, "Imaging of quantum array structures with coherent and partially coherent diffraction," Journal of Synchrotron Radiation **10**, 409-415 (2003).
21. P. Mercère; P. Zeitoun; M. Idir; S.L. Pape; D. Douillet; X. Levecq; G. Dovillaire; S. Bucourt; K.A. Goldberg; P.P. Naulleau; S.Rekawa, "Hartmann wave-front measurement at 13.4 nm with λ_{EUV}/120 accuracy," Opt. Lett. **28**, 1534-1536 (2003).
22. J. Gautier, P. Zeitoun, C. Hauri, A.-S. Morlens, G. Rey, C. Valentin, E. Papalarazou, J.-P. Goddet, S. Sebban, F. Burgy, P. Mercère, M. Idir, G. Dovillaire, X. Levecq, S. Bucourt, M. Fajardo, H. Merdji, J.-P. Caumes, "Optimization of the wave front of high order harmonics,"Eur. Phys. J. D **48,** 459-463 (2008).
23. J. Lohbreier, S. Eyring, R. Spitzenpfeil, C. Kern, M. Weger, C. Spielmann, "Maximizing the brilliance of high-order harmonics in a gas jet," New Journal of Physics **11,** 023016 (2009).
24. D. Russell Luke, "Relaxed averaged alternating reflections for diffraction imaging," Inverse problems **21** 37-50 (2005).
25. F.R.N.C. Maia, T. Ekeberg, D. van der Spoel, J. Hajdu, "Hawk: the image reconstruction package for coherent X-ray diffractive imaging," Journal of Applied Crystallography **43**, 1535-1539 (2010).

1. Introduction

In many scientific areas, imaging with a high spatial and temporal resolution provides meaningful ways to study and understand physical, chemical or biological processes. Recent advances have been made in combining nanometric resolution to ultrafast time scales. Among the advanced imaging techniques, Coherent X-ray Diffractive Imaging (CDI) is a powerful tool to investigate single particle with potentially atomic resolution in a femtosecond time scale [1,2].

CDI uses computation algorithms to reconstruct the object image from its far-field diffraction pattern recorded by an X-ray detector. However detectors are only sensitive to field intensities, so CDI uses iterative methods based on oversampling [3]. This "lens-less" technique is aberration-free so that the theoretical spatial resolution is only limited by the radiation wavelength. In the case of a coherent plane wave illumination, the actual resolution is determined by the maximum scattering angle of the diffraction pattern recorded by the

detector. The first demonstration by Miao and coworkers [4] has been followed by many convincing experiments using either X-ray synchrotron radiation or femtosecond free electron laser (FEL) [5-9]. Thanks to an almost full spatial coherence, high photon flux and ultra-short pulse duration, XFELs have been foreseen as of high potential to resolve down to atomic scale processes occurring on femtosecond time scale [5,7,10]. Laboratory-scale laser driven coherent X-ray sources such as high harmonic generation (HHG) provide now another alternative for ultrafast CDI at nanometer resolutions [11-14].

However in CDI the reconstructed image quality and resolution are limited by the signal to noise ratio (SNR) of the diffraction pattern [15,16] and the beam properties (in particular wave front and coherence) [17-20]. The phase retrieval in the CDI algorithm is an iterative process seeded with a random initial phase. In the present work the convergence is driven by standard constraints: the measured diffraction and a real "support", usually built from the Fourier transform of the measurement (i.e. the autocorrelation of the object) [3]. Although those two constraints can be refined, using for instance known properties of the sample, the SNR of the diffraction pattern is always a critical factor for the reconstruction algorithm. However, a high SNR (high flux) cannot always provide high quality diffraction patterns. Since the phase information is encoded in the diffraction pattern by interference from different parts of the object, the beam coherence and the wave front quality are the other key factors to have high quality diffraction patterns. These issues impose constraints on beamline quality, preparation and data collection either on third generation synchrotrons, XFELs or HHG beamlines.

In this letter, we show how the improvement of the beam transport and quality improves the CDI image reconstruction of a nano-scale sample. These studies have been conducted in single shot using an optimized HHG source with a high photon flux and controlling the beam wave front and spatial coherence. In addition, accurate focusing of the soft X-rays onto the sample also impacts on the reconstruction quality.

2. Wave front optimization

The experiments were performed using the table-top infrared femtosecond laser LUCA (Laser Ultra Court Accordable) at the CEA Saclay research center, France. It delivers up to 50 mJ energy pulses at 800 nm with a pulse duration of 50 fs and a repetition rate of 20 Hz. The experimental setup is described elsewhere [13].

The beamline characterization and optimization has been done using a Hartmann type wave front sensor (λEUV HASO, Imagine Optics Corp.) [21]. We used the RMS (root mean square) wave front error inferred from the measurements to characterize the quality of the X-ray beam: a lower RMS value indicates a beam close to the diffraction limit (lambda/14 RMS according to the Marechal criterion). The wave front sensor accuracy is λ/50 RMS. The Hartmann sensor was used in two steps; firstly on the direct beam without any focusing optics (Fig. 1) and then after the focusing optics (Fig. 2). We recorded both intensity and phase of the soft X-ray wave front and reconstructed the harmonics beam profile using back-propagation functions.

In a first step, a systematic exploration of the influence of several parameters (gas pressure, cell length and IR beam aperture) on the beam quality provided a range of generation conditions (beam aperture = 20~21 mm, gas pressure = 8~9 mbar and cell length = 5~8 cm) leading to a minimum value of the measured RMS, corresponding to the best soft X-ray beam profile. A comparison between the optimized and the non-optimized source profiles calculated at the exit of the cell is shown in Figure 1a and b. The latter has a low spatial quality with a RMS value of 0.79 λ (λ=32 nm) calculated with the entire wave front and presents strong astigmatism and coma aberrations. At optimized phase matching conditions, we obtain the best beam profile with a quasi-circular shape, little astigmatism aberration and a RMS of 0.11 λ ~λ/9. Moreover, the central intensity of the optimized beam

profile is twice higher. The diameter of the optimized spot is 0.07 mm (at $1/e^2$) with 90% of the energy in the diffraction-limited (DL) portion. Note that the maximum beam flux is obtained at the best RMS value, in agreements with previous results [22,23].

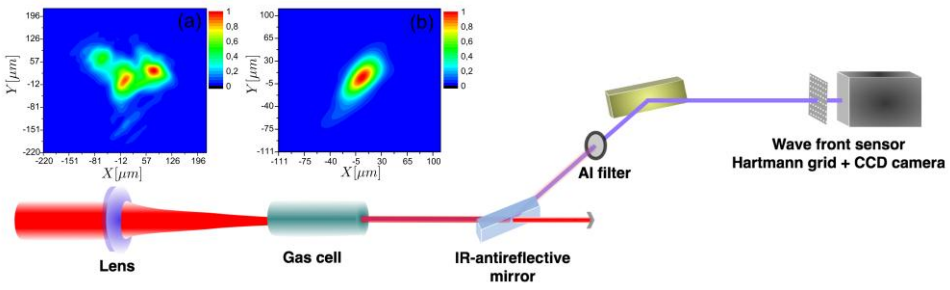

Fig. 1. (Color online) Experimental setup for the harmonic beam wave front measurement and reconstructed intensity profiles of the beam at the source before (a) and after (b) optimization. Generation parameters in (a): cell length = 8 cm, gas pressure = 8 mbar, beam aperture = 24 mm and laser energy = 15 mJ, in (b), cell length = 8 cm, gas pressure = 8 mbar, beam aperture = 21 mm and laser energy = 15 mJ.

In a second step, the wave front sensor was used to align the off axis parabola and to optimize the 25th harmonic (λ=32 nm) focal spot using the optimized harmonic beam (Fig. 2). The sensor is set in the far-field after the parabola. The spatial amplitude and phase at focus were reconstructed from the measurements. The RMS value criterion is again used to accurately align the parabola. The initial focal spot has a size of 7.6 μm (diameter at $1/e^2$) with 50% of the total energy in the DL portion and an RMS value of $\lambda/3$ (Fig. 2a). After optimization the beam has a diameter of 5 μm (at $1/e^2$) with 88% of the energy in the DL portion and RMS ~$\lambda/6$, i.e. twice the diffraction-limit (Fig. 2b). Compared to the 20 μm in diameter focal spot reported by Ravasio and coworkers [13], the optimized focal spot better matches the objects size (3.2 μm x 2 μm). We consequently increased the total "useful" flux interacting with the object by a factor 25. Finally, we placed a diaphragm 10 cm ahead of the parabola. It acts like a spatial filter and removes the boundary wave of the soft X-ray beam. This leads to a more homogeneous wave front (Fig. 2c).

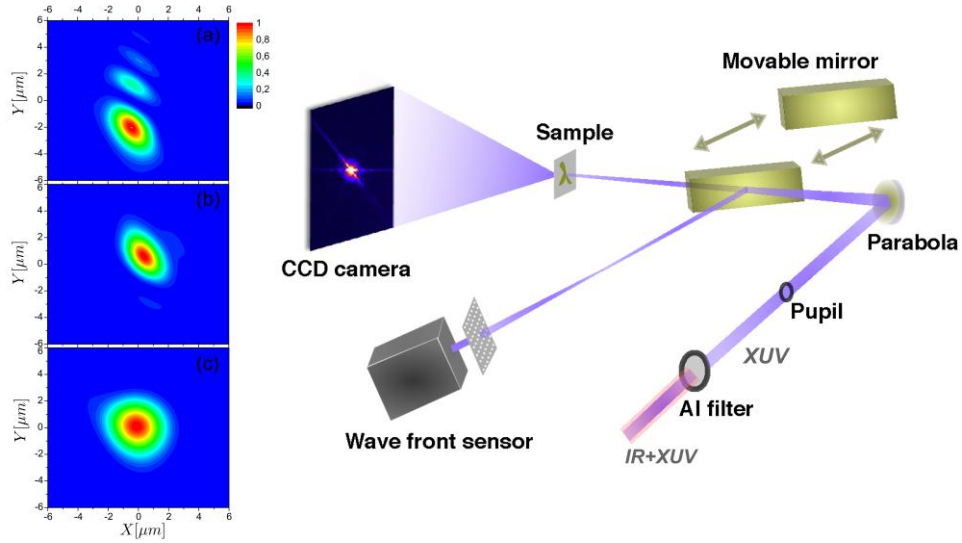

Fig. 2. (Color online) Experimental setup for the off-axis parabola alignment and profiles of the X-ray focal spot at different stages: (a) Non-optimized X-ray focal spot, presenting strong aberrations. (b) Optimized X-ray focal spot without the pupil. (c) X-ray focal spot after a pupil of 3.8 mm in diameter (reconstructed from the measured full beam wave front and a simulated pupil).

3. Impact of coherence on coherent diffractive imaging

We now explore how the spatial coherence of the HHG beam affects image reconstruction. In CDI, the phase information is encoded in the diffraction pattern through the interference modulations between different parts of the object. Therefore, a high coherence is required to ensure the convergence of the phase retrieval algorithm. Here, we use a Young's double slits to quantify the beam coherence necessary for the CDI reconstruction. The slits are produced using a nanoscale ion beam focused on a 150 nm thick gold coated silicon nitride membrane. They are separated by 4 μm and are 1.5 μm long by 300 nm wide. We then measured the evolution of the beam coherence with respect to several HHG parameters (gas pressure, cell length and IR beam aperture). As an illustration, we show in Fig. 3a the beam coherence evolution as a function of the gas pressure. The beam coherence is presented as the fringe visibility (V) of the Young double slits experiment. The total diffracted photon flux is also shown normalized to the maximum measured value for a gas pressure of 13 mbar (backing pressure). The fringe visibility varies from 0.45 (non optimized HHG) to 0.84 (optimized HHG), and evolves together with the number of diffracted photons.

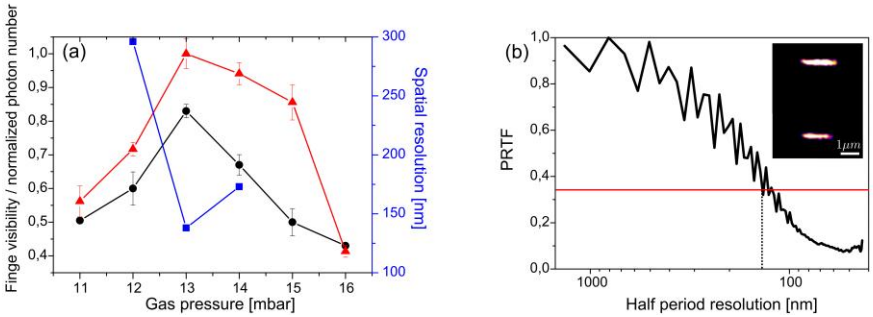

Fig. 3. (Color online) (a): Black circles: Evolution of the fringe visibility of Young's double slits with the generating gas pressure. Red triangles: Total photon number diffracted by the Young's double slit, normalized to the maximum value. Blue squares: Spatial resolution of the reconstruction of the Young's double slit. All the points are from single shot data. (b): Reconstructed image of the Young's double slit for gas pressure = 13 mbar and fringe visibility = 0.85 and the corresponding Phase Retrieval Transfer Function. The estimated half period resolution is equal to 138 nm. The pressure range used here is different from the one in Section 2 due to a change of the cell entrance and exit holes.

A phase retrieval algorithm was then applied to reconstruct the double slits for each fringe visibility case. We evaluated the spatial resolution of the reconstructed image using the Phase Retrieval Transfer Function (PRTF) criterion as shown in Fig 3b (the double slits image reconstruction is also shown). All the results are compiled in Fig. 3a. The best reconstruction resolution (138 nm) is achieved for the best fringe visibility (V=0.85) (see PRTF in Fig. 3b), while lower fringe visibilities (0.67 and 0.6) lead to resolutions of respectively 173 nm and 296 nm. Note that we have not been able to observe convergence for fringe visibilities equal to or below 0.5. If we now compare the reconstruction at fringe visibilities of 0.85 and 0.67, we see that the resolution drops quickly with the coherence even though the photon flux remains comparable. The limiting factors for the reconstruction capacity at a given degree of spatial coherence are the photon flux and the wave front quality: while for a gas pressure

equals to 12 mbar and 14 mbar, the fringe visibilities are very close (0.67 and 0.6 respectively), the obtained spatial resolutions differ by a factor of almost two. We conclude that the three-coupled factors (flux, wave front and spatial coherence) have a strong impact on the phase retrieval image reconstruction process but they can be optimized simultaneously. Note that our experimental observations on the impact of the spatial coherence in CDI confirm a previous work based on simulation with partially coherent beams [18].

Combining all these improvements, we used the soft X-ray harmonic at 32 nm to image a nanometric test sample similar to the one described in ref. [13]. The patterned object "λ" is 3.2 μm high and 2 μm wide with sub-100 nm details (see Fig. 4). The object placed at the focal plan of the parabola diffracts the X-ray light collected by a back-illuminated CCD camera located 19 mm behind the sample. A single-shot diffraction pattern is shown in Fig. 4a. The number of photons diffracted by the sample and detected by the CCD is about ~ $2x10^7$. The high contrast in the diffraction pattern indicates a high coherence length.

By applying an iterative algorithm to the diffraction pattern, we calculated the average from 30 best different reconstructions to get the final reconstruction of the object. Each one was calculated using the relaxed averaged alternating reflectors (RAAR) algorithm [24] with 3000 iterations with a starting beta value of 0.9 reduced to 0.6 after 2000 iterations. The initial support of the object was determined using the SHRINKWRAP algorithm combined with the hybrid input-output (HIO) algorithm. It was updated every 20 iterations using a threshold update corresponding to 10% of the maximum pixel intensity [25]. The reconstructed object is shown in Fig. 4b. The image quality is good with all the edges of the object clearly reconstructed, including small details. We note in the reconstruction image that the upper part of lambda is more intense than the bottom part. This is due to the slight misalignment of the X-ray beam with respect to the object (the X-rays are focused on the upper part of the sample).

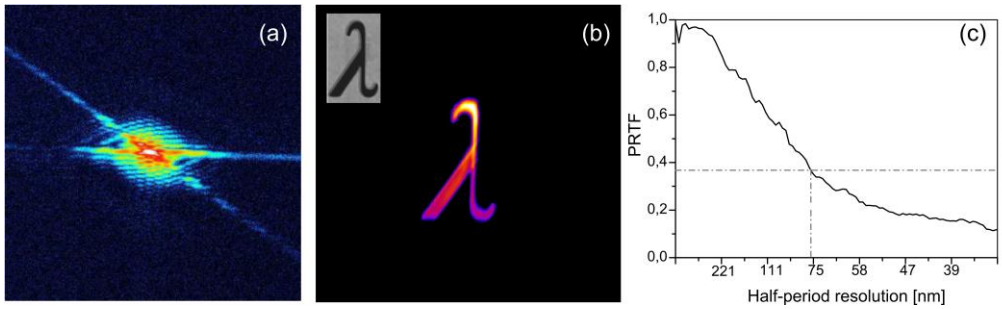

Fig. 4. (Color online) Single-shot coherent soft X-ray diffraction pattern and the reconstructed image. (a) Measured diffracted intensity from the sample (log scale), obtained in single-shot (20 fs exposure time). (b) Reconstructed object amplitude with a 56 nm pixel size. On the upper left corner is the SEM image of the sample. (c) PRTF of the image reconstructed with a half-period resolution of 78 nm, given at 1/e.

The signal far from the center of the pattern corresponds to higher momentum transfer and determines the maximum resolution of the reconstructed image, estimated here to 56 nm (corresponding to a spatial frequency of 8.88 μm^{-1}). The effective image resolution is however lower than this value depending on how the phase retrieval process can be affected (as mentioned in the discussion above). Applying the PRTF criterion leads to a resolution of 78 nm (see Fig. 4c). Compared to the 119 nm resolution reported in [13], we have largely improved the resolution down to 2.5 λ, bringing it closer to the theoretical resolution. The resolution here is still limited by the SNR and the coherence. The blur on the two main diffraction directions of the diffraction pattern indicates that the illumination is not fully coherent. In the high spatial frequency region (far from the pattern center), the signal drops

quickly. As discussed above this limits the final resolution of the reconstructed images. However some methods have been proposed to improve the reconstruction for a partially coherent source, such as using a “Multi-modal propagation” algorithm [19].

4. Conclusion

In summary, we have presented the improvement of a soft X-ray laser harmonic beamline and how the beam properties can affect the image reconstruction process in coherent diffractive imaging. Control over the high harmonic generation source parameters and the focusing of the beam has been achieved. A wave front error of $\lambda/9$ has been obtained corresponding to 1.5 times the diffraction limit according to the Marechal criterion. A regular focal spot of 5 μm is also obtained using control given by a wave front sensor feedback. We have then investigated how CDI phase retrieval convergence depends on the spatial coherence of the HHG source. We demonstrated that a substantial degree of coherence is required to ensure an image reconstruction. No image has been obtained for a fringe visibility equal to or lower than 0.5. Finally, with the highest flux, highest coherence and the best focal spot we have reconstructed a nanoscale object with a spatial resolution of 78 nm in a single 20 fs duration shot. These results confirm the high potential of the table-top soft X-ray laser harmonic source for dynamic studies at a femtosecond temporal scale with a sub-80 nm spatial resolution. Indeed, high control of all HHG parameters and pump-probe operation of our table-top source offer a good alternative to FEL source for ultrafast imaging of nanoscale objects.

Acknowledgments

We acknowledge support from the Saclay SLIC laser team. We acknowledge financial support from the European Union through the EU-LASERLAB and the EU–FP7 X-Motion and ATTOFEL programs, from the French ministry of research through the 2009 ANR grants ”I-NanoX” and ”Femto-X-Mag”, from the ”Triangle de la Physique” through the COX grant and the C’NANO research program through the X-NANO grants. Further support came from the Swedish Research Council, The European Research Council, Knut och Alice Wallenbergs Stiftelse, and the DFG Cluster of Excellence at the Munich Centre for Advanced Photonics.

Paper II

This paper presents the modal filtering device from the conception to the characterization. Theoretical and experimental studies are discussed. Detailed illustrations of the laser beam in different stages of the beamline show the evolution of the filtered beam. Various measurements in spatial and temporal domains give us the characterization of the modal filtering performance. It is concluded by a short example of the HHG improvement using the device.

Submitted.

Spatial quality improvement of Ti:Sa laser beam by Modal Filtering

B. Mahieu[a,b,c], D. Gauthier[a], M. Perdrix[a], X. Ge[a], F. Lepetit[a], F. Wang[a], W. Boutu[a], B. Carré[a], T. Auguste[a], O. Gobert[a], H. Merdji[a,d], D. Garzella[a]

[a] *Service des Photons Atomes et Molécules, Commissariat à l'Energie Atomique, Centre d'Etudes de Saclay, Bâtiment 522, 91191 Gif-sur-Yvette, France*
[b] *Sincrotrone Trieste Elettra, S.S.14 - km 163.5 in AREA Science Park, 34149 Basovizza, Italy*
[c] *University of Nova Gorica, Vipavska 11c, 5270 Ajdovščina, Slovenia*
[d] *Stanford PULSE Center, SLAC, Menlo Park, California 94025, USA*

Abstract

The study and characterizations of a setup aimed at spatial quality improvement of an amplified Ti:Sa laser beam are presented. The technique used, called modal filtering, consists in the selection of the EH_{11} mode, close to the TEM_{00} one, by propagating the beam over a short distance in a hollow-core fiber. The output beam exhibits a stable and nearly gaussian transverse intensity profile and its wavefront is significantly flattened, while the temporal distribution is not affected. High-order Harmonic Generation in gas, a highly nonlinear process, which is phase matching dependent, was used to test the effect of the filter and showed a clear improvement of the generation. Overall, the qualities demonstrated by the beam make the modal filtering technique of prime interest for many other experiments.

Introduction

Laser beams from amplified Ti:Sa chains, commonly used for the production of high peak power femtosecond pulses, often suffer from bad spatial quality. Aberrations resulting from anisotropic thermal dissipation in the amplification media [1], self-phase modulation during propagation of such intense pulses in the air or in materials [2], intracavity beam distortions [3] and imperfections in optical components involve a deterioration of both wavefront and transverse intensity profile. Hence the laser beam cannot be considered as a TEM_{00} mode, the fundamental mode of a laser cavity [4]. A common technique to recover a good spatial quality is to focus the laser through a pinhole. The lens used to focus the beam does a Fourier transform of the field in the plane of the pinhole where there is a one to one mapping between transverse position and spatial frequencies. This allows filtering of high spatial frequencies [5]. However the beam keeps its low spatial frequencies distortions and a significant amount of energy may be lost. Moreover, unless specific conic pinhole is used [6], any misalignment of the laser beam can permanently damage the pinhole. Other or complementary techniques include the use of a saturable absorber [7] or a deformable mirror [8] and diffraction from Bragg gratings [9]. Moreover, active filtering can be achieved through nonlinear processes like second harmonic generation via nonlinear crystal [10] or plasma mirror [11] and cross-polarized wave generation (XPW) [12].

A scheme based on the theory of propagation of an electromagnetic wave in a cylindrical dielectric waveguide is considered here. In the field of ultrafast lasers, it has been initiated by the post compression technique used to generate sub-10fs laser pulses, where a mJ-level femtosecond laser beam propagates over a short distance in a capillary filled with gas [13]. When propagating into the capillary, the electromagnetic field of the laser beam is decomposed on the modes specific to this waveguide. Choosing appropriate parameters, the beam couples preferentially into the EH_{11} mode, very similar to the TEM_{00} one, and other guided modes suffer from higher attenuation. Therefore, if the capillary is sufficiently long, a modal filtering is made on the laser beam. The latter keeps the Gaussian shape of EH_{11} during subsequent free propagation. Thus a setup aimed at spatial quality improvement of a laser beam can

Email address: benoit.mahieu@cea.fr (B. Mahieu)

be conceived by propagation in a carefully chosen waveguide. Modal filtering techniques have already been used in other frames than ultrafast lasers, for instance stellar interferometry [14].

A modal filtering setup has been built on the LUCA facility of CEA Saclay (France), a Ti:Sa chirped pulse amplified [15] laser source. The chosen cylindrical waveguide has been a straight, 30cm-long hollow-core fiber in silica with a core radius $a = 125\mu m$. The purpose of the article is to provide a comprehensive characterization of this modal filtering setup and the demonstration of its practical prominence for numerous applications. The initial motivation of present work was the general optimization of the generation of high-order harmonics (HHG [16]) in loose-focusing geometry [17] on the beamline dedicated to experiments of coherent diffraction imaging [18, 19]. Thereby, after a presentation of the theoretical background, a description of the setup and the analysis of the measurements, first successful results of HHG optimization are also discussed at the end of this article.

1. Propagation and mode-matching in a hollow-core fiber

The equation (in cylindrical coordinates) of propagation of electromagnetic waves in cylindrical structures, such as the used fiber, has been expressed in [20]. The functions (electric and magnetic field components over each coordinate) that are solutions of this equation correspond to the modes of propagation into this waveguide. Doing some approximations, simple analytical solutions are found [21, 22]. These solutions can be divided in three families: transverse electric TE_{0m}, transverse magnetic TM_{0m} and hybrid EH_{nm} modes. Hybrid modes can also be considered as transverse, since the longitudinal component of their electric field is negligible. Thus, in the frame of this study, each mode can be reduced to three main characteristics: a radial and azimuthal equation for the transverse electric field (depending mainly on Bessel functions), an attenuation coefficient α and a phase constant β. The less attenuated mode (lowest α) is called the fundamental one. This mode will be the one "selected" by the modal filtering, due to higher attenuation of other modes. Modes having the same β are degenerate and their linear combinations form other possible modes, called composite modes, such as EH_{2m} + TM_{0m} or EH_{2m} + TE_{0m}.

The vertical polarization of the laser beam matches vertically polarized waveguide modes, which can be denominated as follows:

- for n=1: EH_{1m}
- for n=2: EH_{2m} + TM_{0m} and EH_{2m} - TE_{0m}
- for $n \geq 3$: EH_{nm} + $EH_{(2-n)m}$ and EH_{nm} - $EH_{(2-n)m}$

Every linearly polarized electromagnetic wave inside the fiber propagates as a linear combination of these modes [25]. The symmetry of the electric field of composite modes with respect to the transverse vertical axis arises two families: symmetric (convention of a "+" sign within the composition) and antisymmetric ("-" sign) modes. Intensity patterns of some of these modes are plotted in Fig.1. One has to note that, since degenerate modes EH_{2m}, TM_{0m} and TE_{0m} have different attenuations, the polarization of their composite modes does not remain identical along the waveguide. In our case, this effect can be neglected.

If the refraction index of the cladding is smaller than 2, EH_{11} is the fundamental mode. It is around 1.5 for silica, making EH_{11} the fundamental mode of the used fiber. This choice is not innocent: the shape of EH_{11} is similar to a Gaussian mode both in near and far field (Fig.2). The transverse amplitude of its electric field inside the core of the fiber is given by the radial-dependent function $E(r) = J_0(2.405r/a)$ where J_0 is the Bessel function of zeroth order, a is the radius of the fiber core and r the radial coordinate. For $r > a$, as for other guided modes, the amplitude is assumed to be zero, due to the absorption in the silica. Hence the electric field is truncated in $r = a$, which is also the first zero of J_0. It gives rise, according to the diffraction theory within the paraxial approximation, to a ring in the far field amplitude profile. The central lobe of the far field profile contains 99.2% of the total energy of the beam.

To favor as much as possible EH_{11}, one also have to optimize the coupling conditions. Indeed, when the laser beam is injected into the fiber, its energy is distributed between the different modes. The proportion of energy coupled into a mode depends on the mode-matching at the entrance of the fiber between the injected laser beam and this mode. For every mode, the quality of this mode-matching can be quantified by the following overlap function [23]:

$$\eta = \frac{(\iint E^*_{inj} E_{mode} dS)^2}{\iint |E_{inj}|^2 dS \cdot \iint |E_{mode}|^2 dS} \tag{1}$$

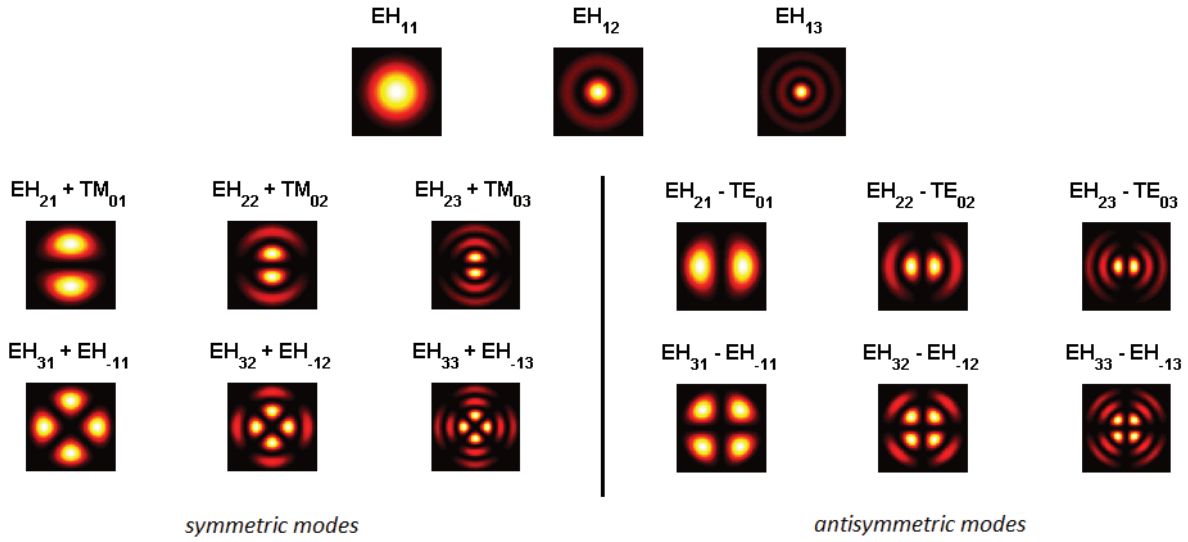

Figure 1: Intensity patterns and denomination of linearly polarized modes for n=1,2,3 (respectively first, second and third line) and m=1,2,3. For n=1, modes are centrosymmetric EH_{1m}. For n>1, two families can be distinguished: modes having their electric field symmetric (left part) or antisymmetric (right part) with respect to the transverse vertical axis.

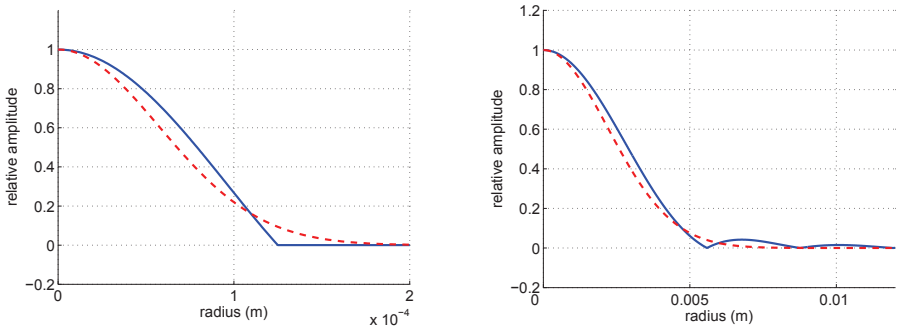

Figure 2: Left side: comparison of radial electric field amplitudes of EH_{11} (full line) and Gaussian (dotted line) modes inside the fiber for $w_0 = 0.65a$. Right side: after one meter of propagation in free space.

η is called the coupling efficiency. The integrals are taken over the whole transverse plane of the fiber entrance, i.e. where the injected laser beam couples into the fiber modes. E_{inj} and E_{mode} are the complex electric fields of respectively the injected laser beam and the considered fiber mode, e.g. EH_{11}. Technically, the shape of the electric field of the injected laser beam will have to match as much as possible the shape of the mode to couple.

For a Gaussian beam, i.e. $E_{inj}(r) = e^{\frac{-r^2}{w_0^2}}$, one can calculate using Eq. 1 the optimal value of the waist size w_0 in order to maximize the coupling efficiency in EH_{11} (Fig.3). The optimal condition appears to be around $w_0 = 0.65a$,

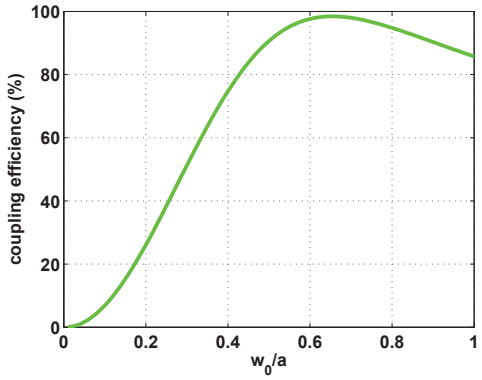

Figure 3: Coupling efficiency of a Gaussian beam of radius w_0 in the EH_{11} mode of a fiber of radius a. The maximum is found for $w_0 = 0.65a$.

where the coupling efficiency is close to 98.5%. Moreover, it remains above 80% for $w_0 > 0.43a$. Of course, this condition is valid only for a perfect Gaussian transverse intensity distribution with a flat phase. Nevertheless it gives a first insight of the optimum beam size at the entrance of the fiber.

2. Layout of the experiment

In order to reduce nonlinear effects due to the propagation of an intense laser beam in the air, the fiber has been put under vacuum ($\sim 10^{-3}$mbar). For the same reason, the whole modal filtering setup has been placed before the pulse compression stage of the chirped-pulse amplified Ti:Sa chain, i.e., where the pulse has been stretched to a duration of about 200 ps. The latter choice is also motivated by the larger incovenience of the femtosecond regime for optical elements, where higher peak power facilitates their degradation. In the picosecond regime, most troubles are linked to thermal effects, which can easily be handle experimentally. The central wavelength of the LUCA source is 795 nm, the repetition rate is 20 Hz and the pulses have a maximum energy of 180 mJ before pulse compression. Such a high energy per pulse justifies the choice of a hollow-core waveguide, allowing to overcome thermal, dispersion and nonlinear effects into the core.

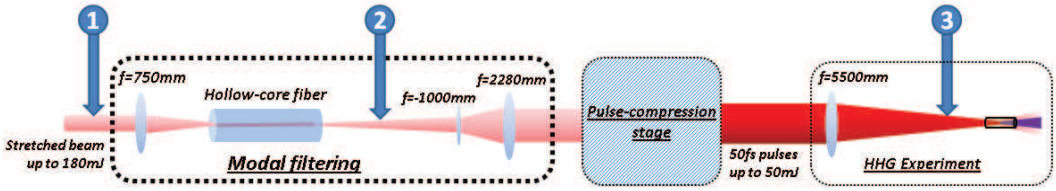

Figure 4: Beamline layout with modal filtering setup and three main positions of measurements. The picosecond laser beam, of radius 3.5 mm, is focused into the fiber with a 750 mm focal-length lens. In order to adjust the coupling conditions, the fiber is mounted on x-y translation stages and the lens on a z translation stage. A control loop has been implemented for correcting the beam pointing at the fiber entrance. By means of a set of two lenses, the output beam is collimated to a radius of 16 mm and sent to the compression stage. It is then used for a HHG experiment, being loosely focused into a gas cell filled with argon.

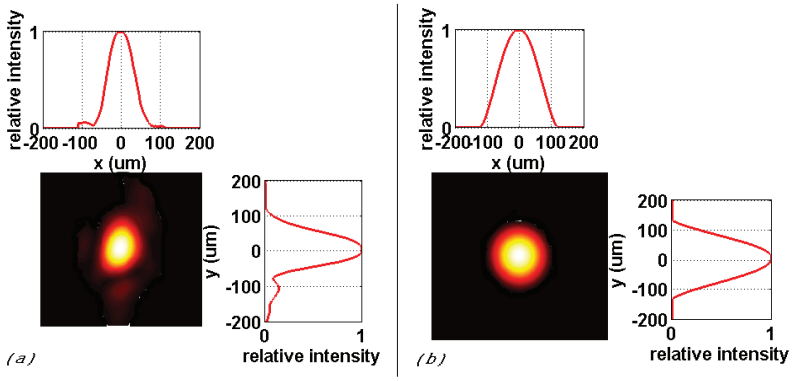

Figure 5: Intensity patterns and profiles before (a) and after (b) modal filtering (r≈100 μm).

A maximum fiber transmission of 78% has been measured. Since the transmission of the compression stage is around 40%, the total energy available for the HHG experiment is of the order of 50mJ, which is enough to generate a μJ extreme-ultraviolet beam [24].

The characterizations have been performed mainly for 3 different positions: before the modal filtering system (position 1 Fig.4), after the fiber (position 2), and on the HHG-path, 4 meters downstream the lens of focal 5500 mm (position 3). Initially, using a beam profiler, intensity patterns have been measured at the focus of a lens of focal 500 mm placed in position 1, and similar measurements have been done after a 4f-system placed in position 2, imaging the output of the fiber. The purpose of this first set of measurements was to characterize the typical transverse intensity pattern of the beam at the focus of a short-focal lens and to compare the divergence of the filtered/unfiltered beam. In a second step, in positions 1, 2 and 3, a Shack-Hartmann sensor has been used to retrieve both the wavefront and the transverse intensity of the beam, leading to the knowledge on the spatial phase and the amplitude of the transverse electric field. In position 2, a lens of focal 1000 mm was placed in order to collimate the beam to a diameter smaller than 1.5cm, which is the size of the entrance pupil of the sensor. The complete information on the transverse electric field provided by the Shack-Hartmann measurements enables to simulate its propagation for retrieving its properties in any position along the propagation axis. Especially, it has been done at the input of the fiber, the output of the fiber and the focal spot in the HHG gas cell.

In addition to these spatial characterizations, SPIDER measurements [26] have also been performed after the stage of pulse compression, providing a comprehensive information on the spectral and temporal characteristics of the femtosecond pulses. All these characterizations are described within the two next sections.

3. Modal filtering characterization

3.1. Beam profiler measurements

Before the fiber (Fig.5a), the beam is elliptic, and moreover "twisted" along the longitudinal axis (general astigmatic beam). After the fiber (Fig.5b), astigmatism and high spatial frequencies are mainly suppressed, so that the transverse beam profile can be assimilated to a Gaussian one. These first characterizations already show an improvement of the spatial quality of the beam in near-field. Since on Fig.5a (i.e. at the focus of a lens of focal 500 mm) the mean radius of the beam is measured to be 95 μm, it is estimated to be 1.5 times larger at the entrance of the fiber (i.e. at the focus of a lens of focal 750 mm), hence 142.5 μm.

Furthermore, such characterizations enable to calculate the M^2 factor of the beam [27]. It has been done with the standard technique which considers the measurements of the second moment widths of the beam [28, 29]. The second moment width corresponds to 4 times the standard deviation σ of the transverse intensity distribution at a given position z along the propagation axis. This is the beam diameter definition used in this paper. For a Gaussian beam, it matches the parameter w ($2w = 4\sigma$, including 95% of the beam energy). Fig.6 shows the evolution of the mean diameter of the beam around the waist and the one of a Gaussian beam with same width at focus. The ratio of their divergences gives the M^2 of the beam: it is equal to 2.1 before the fiber (Fig.6a) and 1.4 after the fiber (Fig.6b).

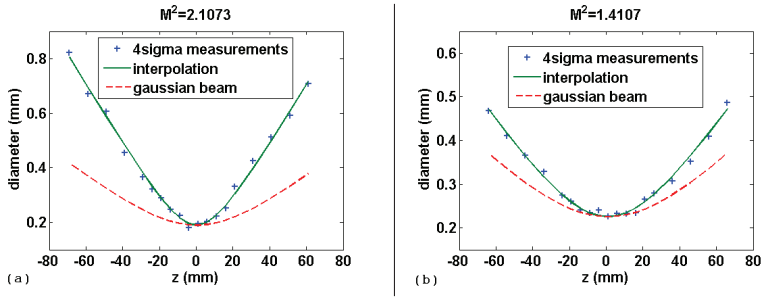

Figure 6: Evolution of the beam mean diameter along the propagation axis before (a) and after (b) the fiber. Crosses are experimental values and full-line curves their interpolations. The dashed curve represents the diameters of a Gaussian beam of same size at focus.

Table 1: Measurements of the wavefront amplitude of the laser beam before and after modal filtering. Peak-to-valley and RMS mean amplitudes of the wavefront are indicated with the standard deviation of the series of measurements. The central wavelength of the laser beam from the LUCA source is 795nm.

Wavefront amplitude	*Before modal filtering*	*After modal filtering*
Peak-to-valley (nm)	414.75 ± 17.94	82.84 ± 13.33
RMS (nm)	66.13 ± 2.30	13.80 ± 1.87

This diminution of M^2 after the propagation in the fiber is a second clear indication of the enhanced spatial quality of the laser beam. Using M^2 as a correction factor of propagation laws for Gaussian beams, the laser beam radius at the output of the fiber is found to be $105\mu m$.

3.2. Shack-Hartmann measurements

The Shack-Hartmann wavefront sensor displays a phase map calculated by integration of the local wavefront tilt. The knowledge of the wavefront gives access to the quantitative phase distortions of the beam in comparison to the ideal plane wave. This section focuses only on the measurements performed on the collimated beam before the injection and after the exit of the fiber. At these positions, and thanks to the wavefront knowledge, the efficiency of the modal filtering setup is clearer. Before the fiber (Fig.7a), the beam is non-circular and the wavefront highly distorted, whereas a non-aberratic beam should have a flat wavefront when collimated. The transverse intensity is roughly top-hat with three hot points forming a triangle, corresponding to peaks in the wavefront profile. After filtering (Fig.7b), the wavefront exhibits no huge aberration any more, and the transverse intensity is closer to that of a Gaussian beam. The beam is rather circular, only a weak ellipticity is observed making the beam longer in the vertical direction. Besides, experimentally one can see a ring surrounding the main lobe of the pattern, which is in agreement with the theory of far-field propagation of EH_{11} evoked in previous section. Only a small part of the energy is included in this ring, too small for the sensitivities of both beam profiler and Shack-Hartmann sensor. During the subsequent propagation, this ring is cut by the mounts of the optics.

The measurements are summarized in Table 1. The amplitude of the wavefront is about 5 times smaller after the propagation in the fiber. Indeed, considering peak-to-valley values, the amplitude is decreased from more than $\lambda/2$ to $\lambda/8$. In addition, the RMS amplitude of the filtered beam is more than 4 times smaller than $\lambda/14$, which according to the Maréchal's criterion is the value qualifying a diffraction limited beam [30]. Thereby, thanks to the benefit of modal filtering, the laser beam can be considered as free of aberration.

3.3. Simulation of beam propagation

The back-propagation of the transverse electric field at the focal plane is performed in the paraxial approximation with diffraction formalism. Data filtering is made to prevent artefact from noise and the $1/e^2$ intensity cut off of the wavefront sensor measurements. The simulated intensity patterns and wavefront are presented in Fig.8, at the entrance of the fiber (a) and at its output (b). The simulated intensity patterns are similar to typical measured ones (Fig.5). Moreover, as in previous measurements on the collimated beam, the peak-to-valley amplitude of the wavefront becomes 5 times smaller after the fiber (from 169 nm$\approx \lambda/5$ to 34 nm$\approx \lambda/25$). It has been measured on the central part

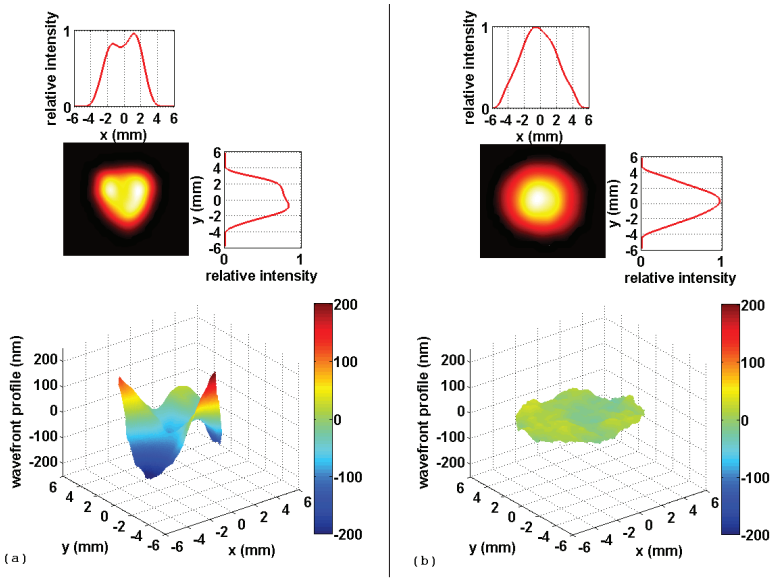

Figure 7: Reconstructions of the transverse intensity and the wavefront from the measurements performed by the Shack-Hartmann sensor before (a) and after (b) the fiber on the collimated beam (r ≈ 5mm).

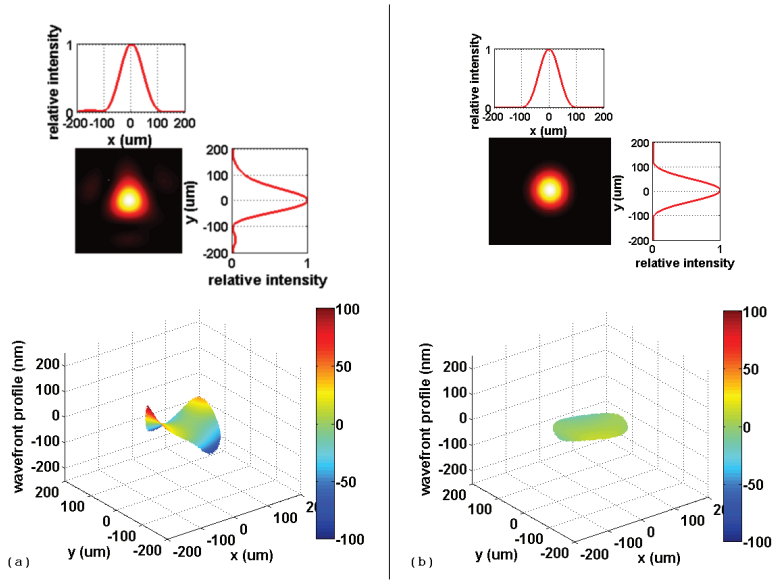

Figure 8: Retrieved transverse intensity and wavefronts at the entrance (a) and at the output (b) of the fiber. The wavefront is displayed only on a diameter of 190μm.

Table 2: Mode matching at the fiber input and fiber output. First column: modes of interest; second column: coupling efficiency calculated from the simulated electric field of the beam at the fiber entrance; third column: output proportion of each mode according to their coupling efficiencies and attenuation in the fiber; fourth column: output proportion of each mode directly calculated with the electric field at the fiber output simulated from the wavefronts measurements.

Mode	Coupling efficiency (%)	Output rate 1 (%)	Output rate 2 (%)
EH_{11}	88.64	91.40	95.01
EH_{12}	3.96	3.72	3.15
$EH_{21} + TM_{01}$	0.97	0.95	0.45
$EH_{31} + EH_{-11}$	1.46	1.39	0.96
$EH_{41} + EH_{-21}$	2.03	1.83	0.03
$EH_{21} - TE_{01}$	0.24	0.24	0.03
$EH_{31} - EH_{-11}$	0.48	0.46	0.01
$EH_{41} - EH_{-21}$	0.03	0.03	0.02

of the beam, where the amount of energy is meaningful. From these simulations, one finds that the mean radius of the beam at the entrance of the fiber is 160 μm. Similarly, at the output of the fiber, the radius is 89 μm. These values are close to previous estimations (142.5 μm at the fiber entrance and 105 μm at its output).

With the overlap integral defined in Section 1, the full knowledge of the transverse electric field brought by these simulations enables the calculation of the mode-matching at the entrance and the output of the fiber. The results are summarized in Table 2. The good coupling proportion into EH_{11} and its low attenuation (~2%) regarding higher-order modes result in an output beam mostly composed of EH_{11} (>90%). From these results, the theoretical transmission through the fiber is ~83%, while a maximum of 78% is found experimentally. The slight difference stems probably from the uncertainty on the transverse beam position, losses during beam propagation and thermal effects at the edges of the core of the fiber. Indeed, as stated before, the injected beam is larger than the core of the fiber: relying on previous simulations, 11.5% of the laser energy is outside the fiber-core radius, which leads to an observable deterioration of the fiber entrance. Increasing the input power emphasizes these thermal effects and the transverse beam instability, resulting in a decrease of the energy transmission in the fiber.

Due to the vertical symmetry of the initial beam in the transverse plane, modes having such symmetry are favoured. Antisymmetric modes could thus be neglected within the decomposition of modes in the fiber. It is worth noting that high-order modes may be under-valuated, since the Shack-Hartmann measurements do a sharp filtering of the beam in $1/e^2$, thus cancelling some high spatial frequencies.

4. Characteristics after pulse compression

4.1. SPIDER characterization

The pulses compressed down to the femtosecond level to reach final beam characteristics have been spectrally characterized by a SPIDER apparatus. The results are summarized in Table 3. Three measurements have been done, with respectively 4, 18 and 42 mJ of IR energy after the pulse compression stage. For the two first measurements, the flatness of the spectral phase leads, in the time domain, to a laser pulse near the Fourier-Transform limit, with a pulse duration smaller than 50 fs i.e., what was usually reached without modal filtering. In terms of the standard deviations of the temporal intensity σ_t and the spectral intensity $\sigma_\omega = 2\pi c\sigma_\lambda/\lambda^2$, this limit is the one of the time-bandwidth product $\sigma_t\sigma_\omega$ which minimizes the pulse duration according to the wideness of the spectrum. This limit cannot be less than 0.5, accessible to Gaussian intensity shapes. For the spectrum of LUCA laser beam, the limit of the time-bandwidth product is around 0.6. Increasing the beam energy up to the maximum accessible value results in a decrease of the spectral beam quality, leading to pulses much farther from the Fourier-transform limit, which is seen in the last measurement reported in Table 3. This deterioration can be due to a too high fluence on the compression gratings, inducing self-phase modulation.

4.2. Shack-Hartmann measurements and beam propagation

The wavefront measurements highlight a deterioration of the beam in the compression stage (Fig. 9). Defects in the gratings induces the presence of a hole in the wavefront of the filtered beam (Fig. 9b). However the non-filtered

Table 3: Summary of SPIDER measurements. First column: beam energy after pulse compression; second column: full width at half maximum of the temporal intensity; third column: ratio of the measured time-bandwidth product and its Fourier-transformed limit, calculated with standard deviations values of the spectral and temporal intensities.

IR energy	Pulse duration (FWHM)	Ratio vs. Fourier limit
4 mJ	47 fs	1.33
18 mJ	43 fs	1.28
42 mJ	65 fs	2.68

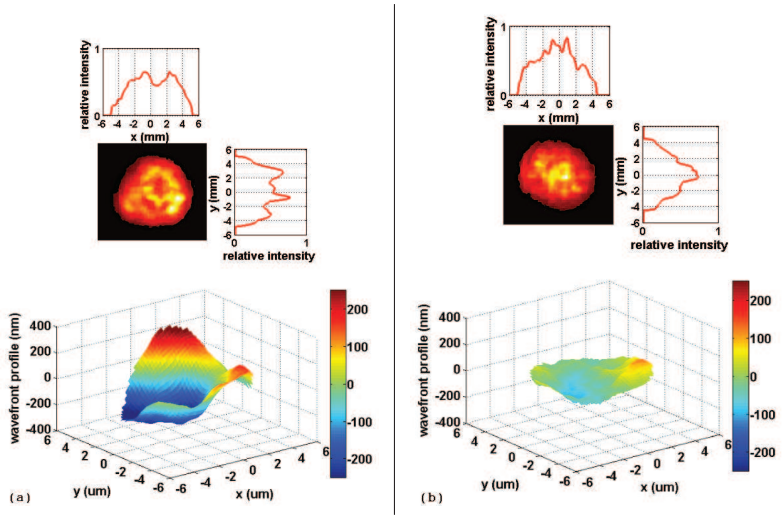

Figure 9: Measured intensity patterns and wavefronts after pulse compression, without (a) and with (b) modal filtering (r≈5 mm). In both cases, the beam mean intensity is similar (~15 TW/cm^2).

beam remains much more aberrated (Fig. 9a). Obviously, the high laser intensities in these measurements (more than 50 mJ at a femtosecond level in a diameter less than 20 mm) likely instigate spatial distortions.

Hence, the results summarized in Table 4 show that the wavefront amplitude is ~2.5 times smaller for the filtered beam after pulse compression, twice less than before pulse compression. Placing an iris on the beam path allows an improvement of the beam quality by filtering its high spatial frequencies.

For the need of its user's application, the beam is then focused by a lens of focal f=5500 mm. Relying on the previous Shack-Hartmann measurements, the beam characteristics have been retrieved at the focal point (Fig. 10). These simulations show that the modal filtering allows to provide a beam where the astigmatism and the amount of high spatial frequencies have been strongly reduced, in comparison with the standard setup. This benefit is well illustrated by the Strehl ratio, which evaluates the beam quality by comparison of the transverse intensity distribution beside the Airy disk [31]: it is ~2.5 times better for the benefit of modal filtering (0.83 vs. 0.33). The importance of this spatial quality improvement for the particular case of our HHG experiment is stressed in the next subsection.

4.3. Application to HHG

On the experimental point of view of HHG, spatial phase is crucial for the macroscopic construction of high-order harmonics. Moreover, in loose-focusing geometry, the interaction with the gas occurs on a long distance (some

Table 4: Measurements of the wavefront amplitude of the laser beam after the compression stage, with and without modal filtering. Peak-to-valley and RMS mean amplitudes of the wavefront are indicated with the standard deviation of the series of measurements.

Wavefront amplitude	*Without filtering*	*With filtering*
Peak-to-valley (nm)	681.00 ± 45.19	288.00 ± 49.68
RMS (nm)	146.75 ± 9.71	54.40 ± 11.08

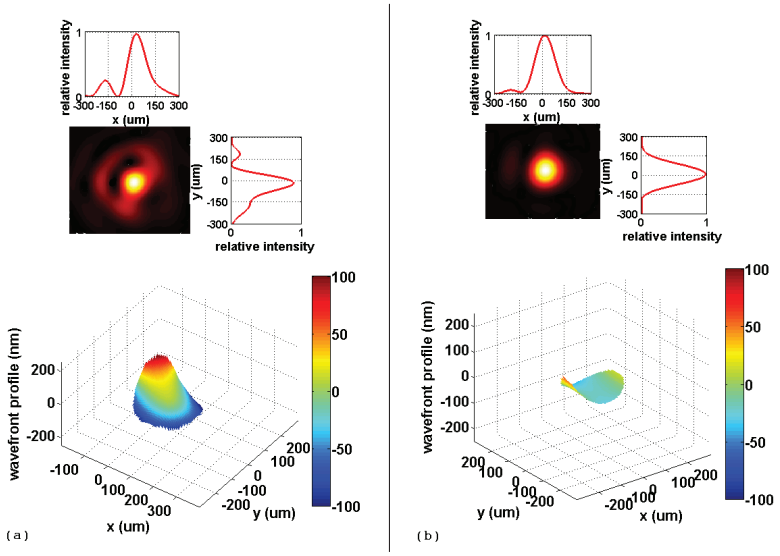

Figure 10: Retrieved intensity patterns and wavefront at the focus spot of the laser beam in the HHG gas cell, without (a) and with (b) modal filtering. The wavefront is displayed only on a diameter of 250 μm, on which the peak-to-valley amplitudes are respectively 245 nm and 104 nm.

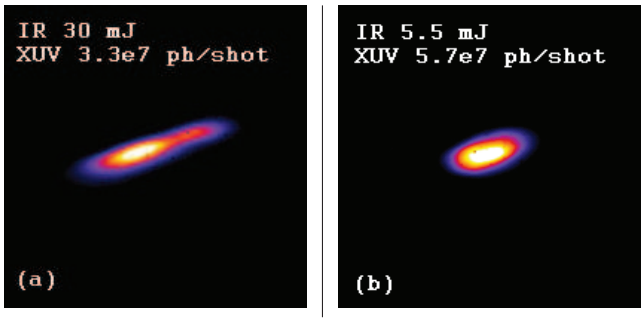

Figure 11: Spatial profiles of the twenty-fifth harmonic (32 nm) without (a) and with modal filtering (b). In both cases, the iris is closed (respectively to a diameter of 25 and 19.5 mm) so as to filter the outer part of the beam. Harmonic were generated in a gas cell filled with argon at a backing pressure of 10 mbars. Patterns are measured on a CCD camera placed at the plane where a 2f-2f system images the XUV beam at the end of the gas cell. The energy of the drive IR beam is the one after the iris; the number of photons per shot is measured on the CCD.

centimeters) compared to the wavelength of the fundamental beam (795 nm), which makes its spatial quality even more important. That is why simulations of the transverse electric field at the focal spot in the gas cell, presented above, are of prime interest. The profile in the case of the unfiltered beam includes a non-negligible amount of high spatial frequencies (Fig. 10a), which are not engaged in the HHG process and thus represent a waste of IR energy. On the other hand, the filtered beam is Gaussian-like at its focus (Fig. 10b).

As a consequence, similarly to what was observed by Bandulet et al. [32], the first HHG results show a significant improvement of the harmonic conversion efficiency (Fig. 11) together with an enhancement of the stability and an improvement of the spatial quality of the harmonic beam. These advantages make insignificant the drawback of the loss of ~30% of IR energy within the modal filtering stage.

Conclusion

We demonstrated, by means of comprehensive characterizations, the significant spatial quality improvement of a Ti:Sa laser beam using the simple technique of modal filtering. A good agreement has been found between direct measurements, simulation and theory. The filtered beam can be assimilated to a Gaussian one which, together with its

stability, makes the setup very attractive for experiments. In particular, using it for driving HHG involves a strong enhancement of the process. Further SPIDER measurements on the infrared beam, spatial and spectral characterizations of high-order harmonics and overall setup improvements will thus be pursued.

Acknowledgements

This work has been sustained by ANR I-NanoX project and femtoXmag. We thank the Triangle de la Physique for its financial support and Romain Bachelard for constructive discussions.

References

[1] V. Ramanathan, J. Lee, S. Xu, X. Wang, and D. H. Reitze, "Analysis of Thermal Aberrations in a High Average Power Single-Stage Ti:Sapphire Regenerative Chirped Pulse Amplifier" in Frontiers in Optics, OSA Technical Digest (CD) (Optical Society of America, 2006), paper FTuS4.

[2] G. P. Agrawal, *Nonlinear Fiber Optics* (Academic Press, New York, 2006).

[3] R. Paschotta, "Beam quality deterioration of lasers caused by intracavity beam distortions," Opt. Express **14**, 6069-6074 (2006).

[4] H. Kogelnik and T. Li, "Laser Beams and Resonators," Appl. Opt. **5**, 1550-1567 (1966).

[5] E. Hecht, *Optics* (Addison Wesley, 2001).

[6] P. M. Celliers, K. G. Estabrook, R. J. Wallace, J. E. Murray, L. B. Da Silva, B. J. MacGowan, B. M. Van Wonterghem, and K. R. Manes, "Spatial Filter Pinhole for High-Energy Pulsed Lasers," Appl. Opt. **37**, 2371-2378 (1998).

[7] S. Sinha, K. Dasgupta, S. Sasikumar, and S. Kundu, "Saturable-absorber-based spatial filtering of high-power laser beams," Appl. Opt. **45**, 4947-4956 (2006).

[8] R. K. Tyson, "Using the deformable mirror as a spatial filter: application to circular beams," Appl. Opt. **21**, 787-793 (1982).

[9] H. Yan-Lan, Z. Hao-Bin, T. Ji-Chun, D. Dao-Yi, Z. Guang-Wei, W. X. Dong, W. Xiao, "Two-dimensional non-spatial filtering based on holographic Bragg gratings," Chinese Phys. B **19** 074215 (2010).

[10] S. Szatmári, Z. Bakonyi and P. Simon, "Active spatial filtering of laser beams," Optics Comm. **134**, 199 (1997).

[11] G. Doumy, F. Quéré, O. Gobert, M. Perdrix, P. Martin, P. Audebert, J.-C. Gauthier, J.-P. Geindre, and T. Wittman, "Complete characterization of a plasma mirror for the production of high-contrast ultraintense laser pulses," Phys. Rev. E **69**, 026402-1 (2004).

[12] A. Jullien, O. Albert, F. Burgy, G. Hamoniaux, J.-P. Rousseau, J.-P. Chambaret, F. Augé-Rochereau, G. Chériaux, J. Etchepare, N. Minkovski, and S. M. Saltiel, "10^{-10} temporal contrast for femtosecond ultraintense lasers by cross-polarized wave generation," Opt. Lett. **30**, 920 (2005).

[13] M. Nisoli, S. De Silvestri, and O. Svelto,"Generation of high energy 10 fs pulses by a new pulse compression technique," Appl. Phys. Lett. **68**, 2793 (1996).

[14] A. Ksendzov, T. Lewi, O. P. Lay, S. R. Martin, R. O. Gappinger, P. R. Lawson, R. D. Peters, S. Shalem, A. Tsun, and A. Katzir, "Modal filtering for midinfrared nulling interferometry using single mode silver halide fibers," Appl. Opt. **47**, 5728-5735 (2008).

[15] D.Strickland and G. Mourou, "Compression of amplified chirped optical pulses", Opt. Comm. **56**, 219 (1985)

[16] P. Salières, A. L'Huillier, P. Antoine, and M. Lewenstein, "Study of the spatial and temporal coherence of high-order harmonics," Adv. At. Mol. Opt. Phys. **41**, 83-142 (1999).

[17] E. Takahashi, Y. Nabekawa, M. Nurhuda, and K. Midorikawa, "Generation of high-energy high-order harmonics by use of a long interaction medium," J. Opt. Soc. Am. B **20**, 158-165 (2003).

[18] A. Ravasio, D. Gauthier, F. R. N. C. Maia, M. Billon, J-P. Caumes, D. Garzella, M. Géléoc, O. Gobert, J-F. Hergott, A-M. Pena, H. Perez, B. Carré, E. Bourhis, J. Gierak, A. Madouri, D. Mailly, B. Schiedt, M. Fajardo, J. Gautier, P. Zeitoun, P. H. Bucksbaum, J. Hajdu and H. Merdji, "Single-Shot Diffractive Imaging with a Table-Top Femtosecond Soft X-Ray Laser-Harmonics," Physical Review Letters **103**, 028104 (2009).

[19] D. Gauthier, M. Guizar-Sicairos, X. Ge, W. Boutu, B. Carré, J. R. Fienup, and H. Merdji, "Single-shot Femtosecond X-Ray Holography Using Extended References," Physical Review Letters **105**, 093901 (2010).

[20] J. A. Stratton, "Electromagnetic theory," McGraw–Hill Book Co., New-York and London (1941).

[21] E. Marcatili and R. Schmeltzer, "Hollow metallic and dielectric waveguides for long distance optical transmission and lasers," Bell Syst. Tech. J. **43**, 1783–1809 (1964).

[22] E. Snitzer, "Cylindrical Dielectric Waveguide Modes," J. Opt. Soc. Am. **51**, 491-498 (1961).

[23] E. G. Neumann, *Single Mode Fibers: Fundamentals* (Springer-Verlag Berlin and Heidelberg GmbH and Co. K, 1988).

[24] J. F. Hergott, M. Kovacev, H. Merdji, C. Hubert, Y. Mairesse, E. Jean, P. Breger, P. Agostini, B. Carré and P. Salières, "Extreme-ultraviolet high-order harmonic pulses in the microjoule range," Phys. Rev. A **66**, 021801 (2002).

[25] H. Norman and W. Horst, "Laser Resonators and Beam Propagation: Fundamentals, Advanced Concepts and Applications," Springer (2005).

[26] C. Iaconis and I. A. Walmsley, "Spectral Phase Interferometry for Direct Electric-Field Reconstruction of Ultrashort Optical Pulses," Opt. Lett. **23**, 792–794 (1998).

[27] M. W. Sasnett, "Propagation of multimode laser beams - the M^2 factor," in Physics and Technology of Laser Resonators, D. R. Hall and P. E. Jackson, Hilger (1989).

[28] ISO 11146-1:2005.

[29] A. E. Siegman, "How to (Maybe) Measure Laser Beam Quality," in DPSS (Diode Pumped Solid State) Lasers: Applications and Issues, M. Dowley, ed., Vol. 17 of OSA Trends in Optics and Photonics (Optical Society of America, 1998), paper MQ1.

[30] A. Maréchal, Revue d'Optique **26**, 257 (1947).

[31] K. Strehl, "Aplanatische und fehlerhafte Abbildung im Fernrohr," Zeitschrift für Instrumentenkunde **15**, 362-370 (1895).

[32] H.-C. Bandulet, D. Comtois, A. D. Shiner, C. Trallero-Herrero, N. Kajumba, T. Ozaki, P. B. Corkum, D. M. Villeneuve, J.-C. Kieffer and F. Légaré, "High harmonic generation with a spatially filtered optical parametric amplifier," J. Phys. B: At. Mol. Opt. Phys. **41**, 245602 (2008).

Chapter III
Coherent Diffractive Imaging and Holographic imaging

III.1 Introduction

In this chapter, I present the demonstration of different coherent imaging techniques (CDI, HERALDO) at our high flux harmonic beamline. The diffraction experiments are accomplished after the wave front sensor HHG optimization (Chapter II, section II.3), and without the laser modal filter (which was added into the beamline later). CDI and HERALDO share the same experimental setup as described in Chapter II (Fig. 2.24 without modal filter). Typical image reconstructions in single-shot regime for CDI and HERALDO are respectively reported in Paper I and Paper III. The important aspects of coherent imaging, such as the beam's coherence, the signal-to-noise ratio of diffraction patterns, the comparison of different extended references in HERALDO, the comparison of CDI and HERALDO are also discussed here.

III.2 Sample preparation

All the test objects presented in this chapter have been fabricated using the focused ion beam (FIB) facility at the Centre de Spectromètre Nucléaire et de Spectrométrie de Masse (CSNSM, Orsay, France). The silicon nitride membranes are supported by silicon substrate on one side (Fig. 3.1), which defines the membranes aperture varying from 150 x 150 μm^2 to 500 x 500 μm^2. On such large window, we can fabricate more than 100 objects in one membrane. The thickness of the membranes varies from 50 nm to 150 nm to ensure that objects are two dimensional for our harmonic beam (Chapter I, section I.2b). Before etching, the membranes are covered by a gold layer (around 50 nm thick) whose transmission efficiency is less than 1.5 x 10^{-3} (CXRO database) for the 25^{th} harmonic (wavelength of 32 nm). This layer removes the direct beam and ensures that we have a pure transmission object for our imaging tests. Test objects are designed on 512 x 512 pixels bitmap files, which guide the focused ion beam [1] during the drilling process. The object definition is achieved with a precision of about 10 nm. The fabrication result can then be observed by scanning electron microscope (SEM) combined with the FIB (Fig. 3.2). The manipulation of FIB is delicate and one should respect strictly the precautions and operation rules. For example, the alignment of the membrane with the focal plane of the ion beam and the choice of the parameters to tune the ion beam directly influence the fabrication quality.

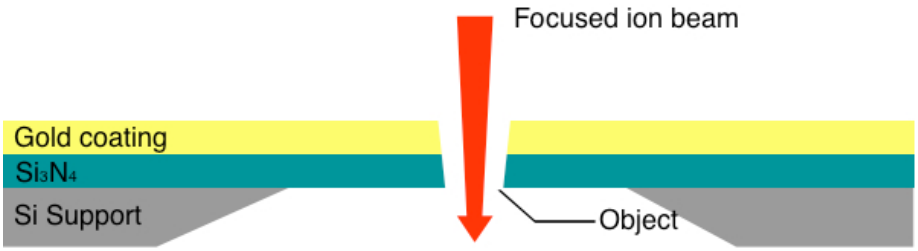

Fig. 3.1. Scheme of test objects fabrication.

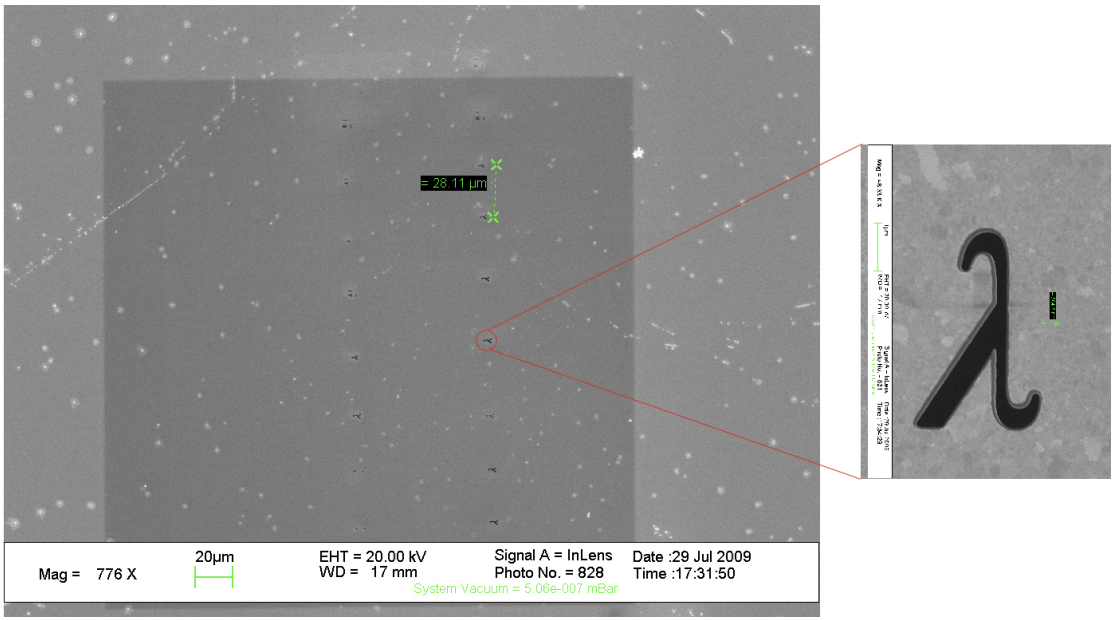

Fig. 3.2. Example of SEM image of a membrane's overview after FIB fabrication, with a zoon-in on one single object.

As mentioned previously, CDI requires an isolated object located in an extended vacuum space to fulfill the oversampling condition. In this case, the measured diffraction pattern is composed of the diffracted photons by the object and the direct beam, which is not blocked by the object. In our case, the test object acts as an opaque mask with a binary transmission. This means that the transmission of etched area is "1" and the membrane is "0". According to the Babinet's principle [2], the diffraction pattern from an opaque body is identical to that from a hole of the same size and shape except for the overall forward beam intensity. Therefore, our test objects can be considered as "conjugate" term of a real object, which would be well isolated. The direct beam for such objects is composed of the transmitted photons of the membrane and the photons going through the object hole without diffraction, which usually presents as an intense spot in the center of the measured diffraction pattern. In FEL facilities, due to the high intensity of the pulse, the direct beam even in single-shot saturates the CCD camera so that one should place a beam stop to block it. However, the beam stop blocks also the low frequencies of the object diffraction. Since our harmonic beamline is less intense than a FEL, the beam stop is not necessary and the measured diffraction pattern contains all information. Note that even if our test objects used here are pure transmission object without

phase modulation, CDI is also suitable for resolving objects presenting phase modulation (Chapter I, section I.2b).

III.3 Detection of the diffraction pattern

During the diffraction experiments, the first difficult task is to find the test objects. The objects (having a size smaller than 5 x 5 μm^2) are located in a membrane window of hundreds µm large, which is held by a sample holder with motorized translation stages. First without pumping, we use a HeNe laser, which is pre-aligned with the IR pump laser at a distance of ~ 8 m, to find the membrane window position by checking the different transmission of the silicone nitride membrane and the silicone substrate. Then in vacuum, we use the harmonic beam to find the position of the membrane window's edges. Note that the translation stages of the sample holder used in this chapter provide a precision of 1 µm, which has been upgraded to 1 nm during my thesis work (new sample holder used in Chapter IV). With the help of the SEM image (such as presented in Fig. 3.2), we scan over the possible regions containing objects with harmonic beam (size of ~ 5 x 5 μm^2) to find one first object. Since the objects have been etched in a strict line frame, it is then easy to find other ones with a pre-calculation of the objects separation shown in SEM image. At last, we align the object with the harmonic focal spot in the beam propagation direction (Chapter II, section II.3c).

Considering the spectral range (10 – 100 nm) explored during our experiments, we use a UV-X PI-MTE CCD camera fabricated by Princeton Instruments. It has a chip size of 2048 x 2048 pixels with a pixel size of 13.5 x 13.5 μm^2. The compact CCD camera (about 10 cm in the longest direction) can be located inside the experiment chamber and operates with a vacuum down to 10^{-7} mbar. It is then easy to motorize the CCD camera with translation stages. The camera can be cooled down to -40°C by water-cooling system to reduce the readout noise. The detection efficiency can be presented as:

$$I_{ADU} = \frac{\gamma_e Q}{G} N_{photon} \qquad \text{(Eq. 3-1)}$$

The intensity I_{ADU} of the diffraction pattern on each pixel corresponds to the analog-to-digital unit (ADU), which is the CCD's output count. The ADU (or the *count*) is linearly proportional to the incident photon number on each pixel (N_{photon}), and has a dynamic range from 0 to 65535 encoded on 16 bits. G is the system gain defines the relationship between the number of electrons acquired on a CCD and the ADU generated. Q is the quantum efficiency of the CCD camera presenting its probability to produce electrons from incident photons, N_{photon}. γ_e is the number of electrons generated by one incident photon, described as:

$$\gamma_e = \frac{Photon\ Energy\ (eV)}{3.65} \qquad \text{(Eq. 3-2)}$$

For the 25th harmonic beam (38.74 eV), 10 electrons are generated for one incident photon. For the 39th harmonic beam (60.45 eV) used in Chapter IV, 16 electrons are generated. The quantum efficiency is ~ 40% for the spectral range from 30 eV to 100 eV. The system gain is 1.3 electrons/ADU as designed and measured by the manufacturer. The relation can then be simplified to $I_{ADU} = 3N_{photon}$ for H25.

III.4 Implication of the spatial coherence in the CDI reconstructions

As presented in Chapter II, we have estimated the spatial coherence of our harmonic beam using Young's double slits (fabricated by FIB, Fig. 3.3a). The idea is to optimize the HHG for CDI with a good compensation between photon flux, wave front quality and beam coherence. Since the Young's double slits can also be considered as a CDI object, I have tried to reconstruct them using diffraction patterns (interferogram) taken under different HHG conditions (Fig. 3.3). This procedure will evaluate the sensibility of the CDI reconstruction process to the beam coherence. The double slits are 1.5 µm long and 300 nm wide, separated by 4 µm which is close to the size of the beam (about 5µm). The measured diffraction photons in these single-shot detections range from 10^5 (Fig. 3.3b,c,g) to 10^6 (Fig. 3.3d-f). The spot in the center is the direct beam transmitted by the membrane, which does not influence significantly the CDI reconstruction process.

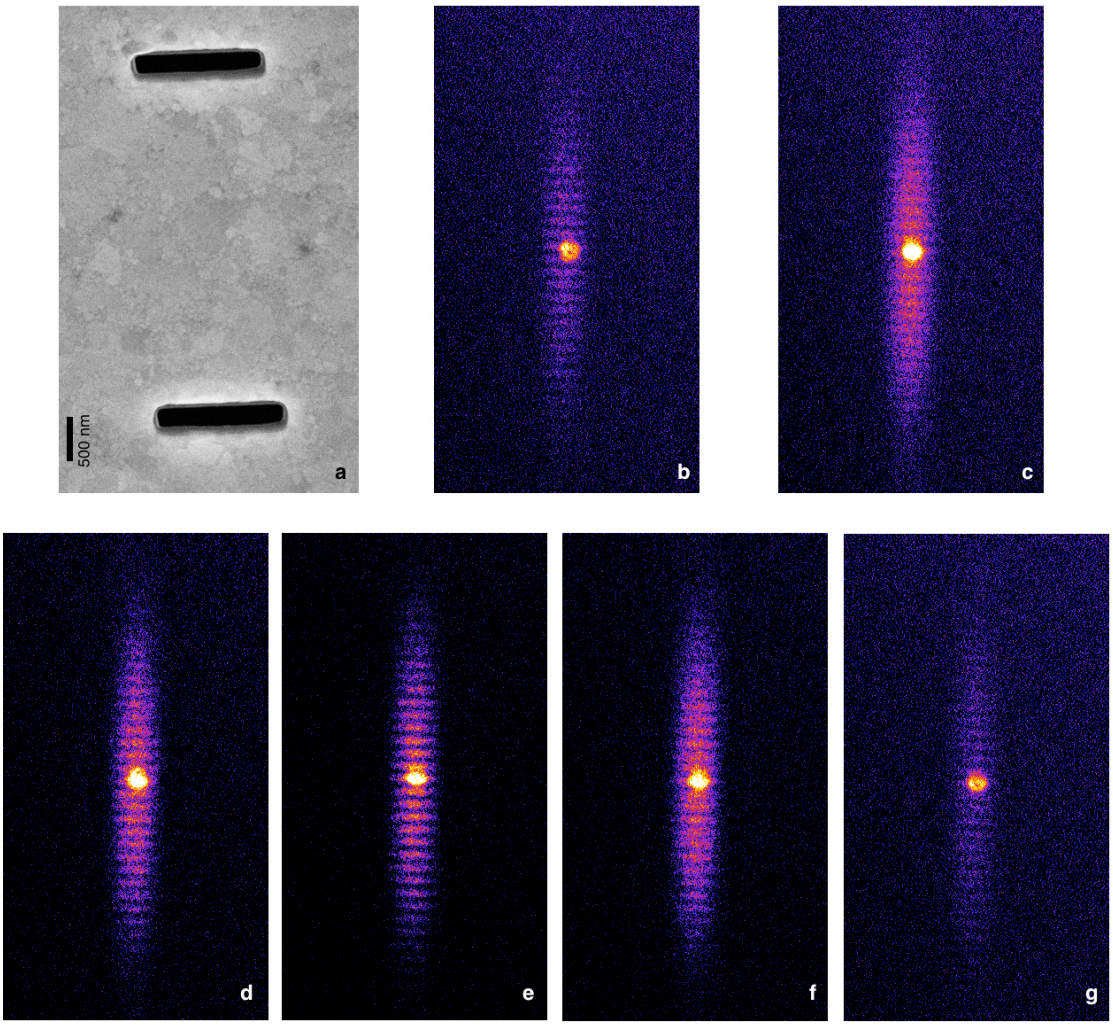

Fig. 3.3. (a) SEM image of the Young's double slits. (b) to (g) typical fringes measurements corresponding to different HHG conditions presented in Fig. 2.19. The gas pressure varies from 11 mbar (b) to 16 mbar (g). All fringes are measured with a window size of 800 x 800 pixels. Here they are cropped for a better presentation.

A reconstruction of the double slits has been possible only in certain cases. In the case of poor visibility combined with poor intensity (such as Fig. 3.3g), the iterative process cannot converge. Good reconstructions are achieved for HHG conditions combining both intensity and visibility optimization (such as Fig. 3.3c-e). Reconstructions are less good for fringes with a visibility around 0.5 (such as Fig. 3.3b and f), even for fringes with maximized diffraction photons (such as Fig. 3.3f). The reconstruction with best resolution (138 nm) is presented in Fig. 3 of Paper I. Here, Fig. 3.4 presents the two reconstructions for Fig. 3.3c and d, corresponding to a fringe visibility respectively 0.6 and 0.67, and the measured diffraction intensity of Fig. 3.3d is about 1.3 times higher than the other. Note that Fig. 3.3f has similar diffraction intensity as Fig. 3.3d, but a poor fringe visibility of ~ 0.5 makes the iterative algorithm not able to identify the two slits. For all slits reconstructions, the initial support is calculated by the Fourier transform of the measured diffraction pattern, which correspond to the autocorrelation of the double slits (Fig. 3.5). If the beam is totally coherent, based on the definition of the autocorrelation, the ratio between the maximums of the center part (green circle) and the side part (red circle) should be equal to 2. This ratio is directly related to the beam coherence, which becomes smaller when the coherence is limited. During the iterative process, the support is refined (reduced in space) for each iteration with a threshold, usually defined by its intensity distribution. Thus, for fringes with limited coherence, the side parts will have a weak intensity. In such case, the information will be eliminated by the threshold, which is set to avoid any unreliable reconstruction. In such case we usually obtain only one slit reconstruction, the second slit being missed by the artificially truncated support used in the algorithm. This is a standard problem in CDI when using a symmetric object. CDI applies better for non-symmetric objects as the support ambiguity is removed.

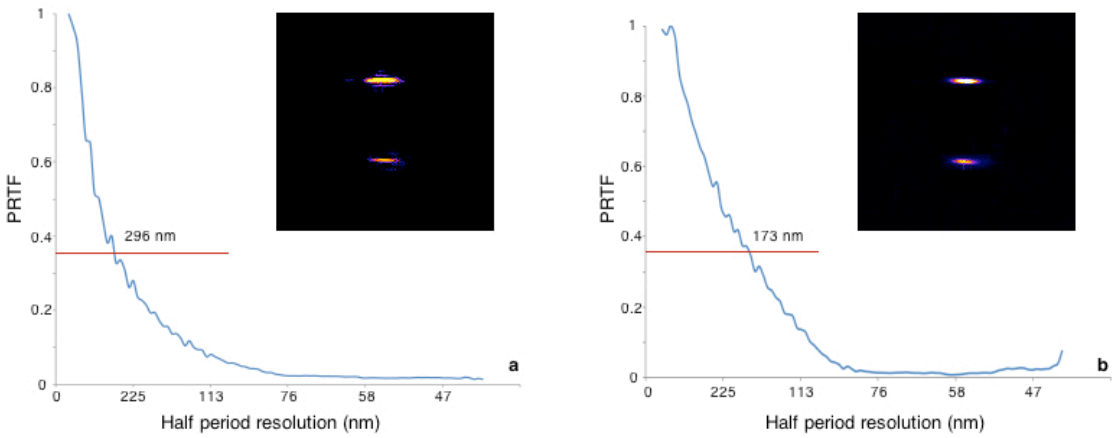

Fig. 3.4. (a) and (b) are respectively the reconstructions of Fig. 3.3c,e. The resolution estimated is 296 nm and 173 nm.

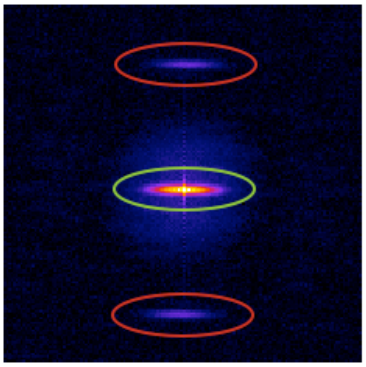

Fig. 3.5. Autocorrelation of the Young's double slits, calculated from a measured diffraction pattern.

We estimate the reconstruction resolution in CDI using the phase retrieval transfer function (PRTF), which is the ratio between the absolute value of the Fourier transform of the reconstruction and the square root the measured diffraction intensity:

$$PRTF(\nu) = \frac{|\mathcal{F}\{Reconstruction\}|}{\sqrt{I_{Diffraction\ pattern}}} \quad \text{(Eq. 3-3)}$$

The resolution is given at the ratio of 1/e, according to the PRTF criterion [3]. ν is the spatial frequency of the diffraction pattern, equal to D/λz, where D is the distance of the concerned pixel to the center of the diffraction pattern, and z is the distance between the detection plane and the object plane.

III.5 Experimental results of CDI

After the beamline optimization, we have performed CDI experiments using texts objects, such as the "lambda" presented in Paper I. We have been able to reconstruct the "lambda" (3.2 µm x 2 µm) from a single-shot acquisition (20 fs pulse duration) with a spatial resolution of 78 nm (equal to 2.5λ), which is largely improved compared to the 119 nm reported in A. Ravasio *et al.* [4], which was realized with a non-optimized beam and focus. The object "note" (3 µm x 2.8 µm) in the latter has been retested and we got a single-shot reconstruction with 75 nm spatial resolution, which is close to the 40-shot reconstruction reported in previous work. The final reconstruction presented in Fig 3.6 is an average of 14 best different reconstructions output after 1000 iterations of the RAAR algorithm. The original diffraction pattern is recorded in a window size of 2048 x 2048 pixels. It is cut into a size of 848 x 848 pixels and then binning 4 x 4 (16 pixels integrated into one large pixel) for the reconstruction to accelerate the algorithm calculation. Thus, each pixel of the reconstruction has a size of 53 nm (p_{object}), calculated by following equation:

$$p_{object} = \frac{\lambda z}{N_{pixel} p_{camera}} \quad \text{(Eq. 3-4)}$$

where N_{pixel} is the number of pixels of the window size and p_{camera} is the pixel size of the camera. Note that, the oversampling ratio for these CDI objects is about 10, thus the 4 x 4 binning still qualifies for the oversampling condition. The improvement of the reconstruction quality is mainly due to the increased photon flux. Indeed, we have detected a few 10^7 diffracted photons in the single-shot measurements of "lambda" and "note", compared to 5 x 10^5 photons in the previous work. Since there is no measurement of the beam's wave front and coherence in the former experiment, the comparison on these aspects is not possible. Note that the relative poor reconstruction quality of Young's double slits (with good coherence) is due to the lack of diffracted photons (~ 10^6 photons are detected in the best case). The low diffraction efficiency is caused by the geometry of the double slits, which are situated at the edges of the beam when well aligned. On the contrary, our test objects are perfectly aligned with the more intense part of the soft X-ray focused beam.

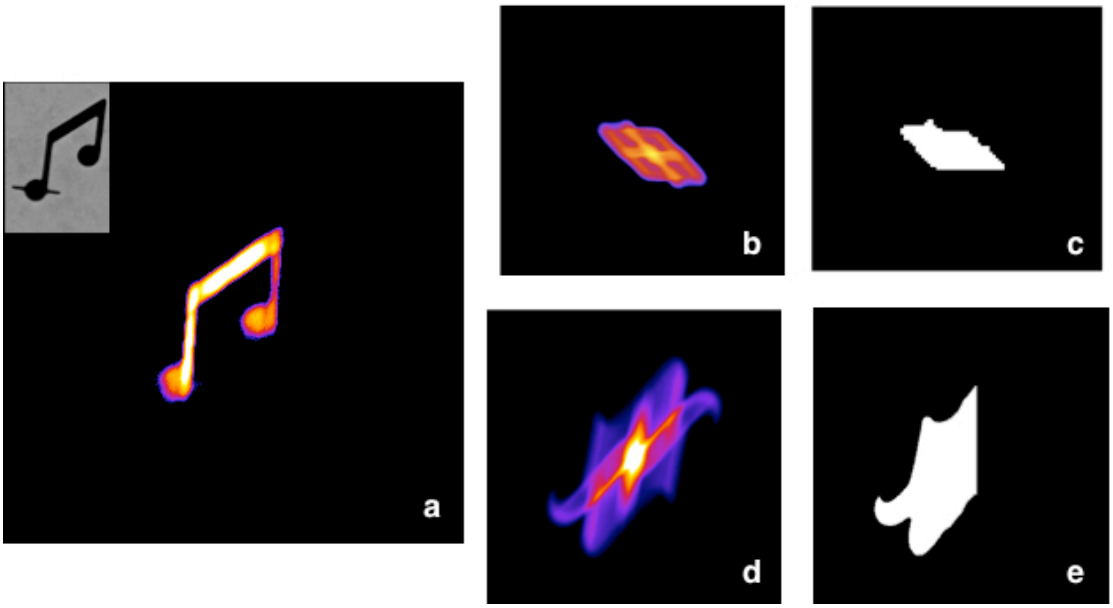

Fig. 3.6. (a) The "note" reconstruction in single-shot detection with a presentation of its SEM image. The missing slit is due to the radiation damage after long time exposure. The radiation damage is an important constraint on FEL facilities, especially for biological samples. Discussions have arisen on this subject [5,6]. (b) and (d) are respectively the autocorrelation for "note" and "lambda". During the iterations, the reconstruction of the object can flip horizontally or vertically due to the symmetry of the autocorrelation. Thus non-symmetry masks (c and e) are applied to the autocorrelation when calculating the support to avoid the flip.

In fact, the object geometry is another important factor for the CDI reconstruction, beside the three-coupled factors of the harmonic beam (wave front, coherence and photon flux). For example, "note" and "lambda" are simple objects that present in general two main directions of diffraction. Compared to objects that have diffraction signals extended in all directions (such as the Airy disk of a circle), the diffraction pattern of objects like "note" and "lambda" will have higher photons/pixel values, as the photons are mainly located in the main diffraction axes. Thus better signal-to-noise ratio and higher spatial frequencies are obtained for the reconstruction under the same illumination condition. Fig. 3.7 illustrates the importance of the object geometry for CDI with comparison between objects "note" and

"phos". The latter is composed of 3 Greek letters with a total size of 3.2 µm x 2.5 µm. The red rectangles in the diffraction patterns show the spatial extension of the diffracted signal: 1100 x 850 pixels for "note" and 460 x 460 pixels for "phos". The maximum spatial frequencies of the diffracted photons are ± 12.2 μm^{-1} and ± 9.4 μm^{-1} for "note", and ± 5.1 μm^{-1} for "phos". The theoretical resolution is then limited to 53 nm for "note" and 98 nm for "phos". However, the measured diffracted photons are the same: 2.8 x 10^7 for "note" and 2.7 x 10^7 for "phos". The reconstruction of "phos" is not satisfying: only the "ω" is resolved while the other two letters are partially or non-resolved at all. Since the objects have similar size, the poor reconstruction should not be related to illumination problem or coherence problem. The object geometry could be therefore a constraint for single-shot CDI experiments at our harmonic beamline. In multiple-shot regime, we are able to accumulate enough signals to have sufficient spatial extension of the diffraction pattern for high-resolution reconstructions, as demonstrated in previous work of A. Ravasio *et al*.. The other method to amplify the diffraction signal is to use extended reference, which still keeps the possibility of high-resolution reconstruction (section III.10).

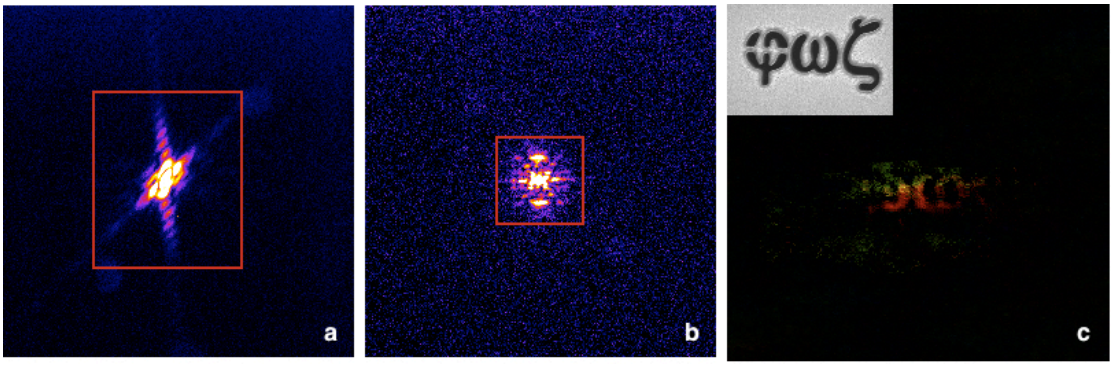

Fig. 3.7. (a) and (b) Diffraction patterns of "note" and "phos", displayed with the same color scale. The red rectangles present the extension of the diffracted signals. Images are taken with a window size of 2048 x 2048 pixels. The two half-circle at the edge of the red rectangle in (a) are parasite signals. (c) is a typical reconstruction after 2000 iterations of object "phos". The SEM image of "phos" is on the top corner.

We have tested another object "Eiffel tower" (Fig. 3.8a), which has a size of 5 µm x 4 µm and is more complex than "note" and "lambda". The single-shot diffraction pattern presented here has three main diffraction directions and is more "homogeneous" than "note" and "lambda" with signal extension size of 800 x 800 pixels. The maximum spatial frequency is ± 8.88 μm^{-1}, corresponding to a theoretical resolution (Chapter I, section I.2c) of 56 nm. The calculated autocorrelation (Fig. 3.8b) shows a high agreement with the simulation (Fig. 3.8c). Thanks to the presence of the star beside the tower, which acts like a holographic reference in the autocorrelation calculation, we can clearly identify the Eiffel tower in the autocorrelation. However no FTH or HERLADO reconstructions can be processed, except that applying a particular de-convolution operator well adapted to the star shape on the autocorrelation may probably lead to reliable reconstruction. Fig. 3.8d is the CDI reconstruction of the single-shot diffraction pattern after 3000 iterations, compared to the reconstructions of 400-shots (Fig. 3.8e) accumulation taken before the harmonic beamline optimization. The single-shot reconstruction presents a lack of illumination on the top and the bottom part of the tower, which can also be observed in the autocorrelation. The star is blurred which could be related to the radiation damage suffered by the object during long time exposure. Due to the

instability of the beam before optimization, the reconstruction of the multi-shot detection does not show significant improvement, but is in fact more blurred. However, the accumulated illumination provides more photons and thus a "clearer" vision over the entire object.

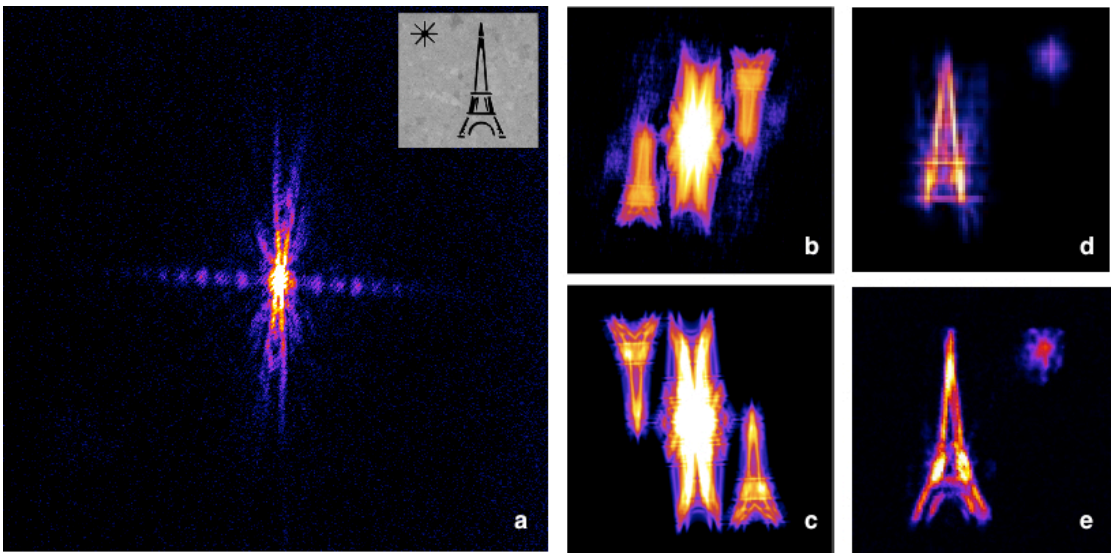

Fig. 3.8. (a) Single-shot detection of the "Eiffel tower" object with its SEM image on the top. (b) Autocorrelation calculated from (a), compared to the numerical simulation of the SEM image (c). (d) Reconstruction of single-shot detection with a spatial resolution of about 110 nm. (e) Reconstruction of 400-shots detection obtained before the harmonic beamline optimization. The reconstruction has been realized by Pierre Thibault (Cornell Univ. and now TU Munchen).

III.6 Experimental results of Fourier Transform Holography

We have prepared two test objects to perform Fourier Transform Holography (FTH) experiments. Object "h" has a size of ~ 1.6 µm x 2.4 µm and the other is a "geometric grid" object with a size of 1 µm x 1 µm (Fig. 3.9). For each test object, we have etched two identical reference pinholes in vertical and horizontal directions. Different pinhole sizes have been combined to the objects: 300 nm or 240 nm (diameter) for "h"; 110 nm or 145 nm for "geometric grid". The FTH experiment will be then confronted to the HERALDO technique using different extended references. The comparison of these two techniques is discussed in Paper IV. Here, I would like to show some complementary experimental results that are not presented in the manuscript.

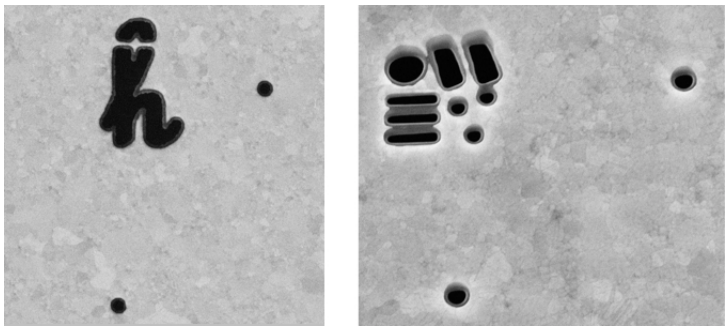

Fig. 3.9. SEM images of holographic objects “h” and “geometric grid”.

The “h” object can be constructed from single-shot detection as shown in Fig. 3.10. The diffraction pattern is recorded in a window size of 2048 x 2048 pixels with a signal extension of ~ 350 x 350 pixels, corresponding to a maximum spatial frequency of 3.89 μm^{-1}. The hologram contains ~ 7 x 10^6 photons and presents no privilege diffraction directions and contains the full speckles that encodes the phase information. Applying a Fourier transform on the hologram, we get the two pairs of reconstructions associated to the two pinholes references. Note that there are only two independent reconstructions in this case, since the reconstructions in opposite positions are the complex conjugates. In the case of Fig. 3.10, the images obtained with the vertical pinhole are much intense than the ones by the horizontal pinhole. This is due to a misalignment between the object (including the references) and the harmonic beam. To estimate the spatial resolution, I plot the profile of the reconstruction along the white line (Fig. 3.10). This allows us to visualize the noise and the sharpness of the object edges. According to the 10%-90% Rayleigh criterion, the resolution is estimated to be around 220 nm, which is close to the resolution limitation defined by the pinhole size of 300 nm. A low-pass filter (Gaussian filter) has then been applied on the hologram to knock out the noise in high frequencies where no diffractive signals are recorded. The width of the Gaussian filter is chosen to adapt the maximum diffraction extension and the filtered hologram is presented in Fig. 3.10b. The reconstruction of the filtered hologram highly agrees with the non-filtered one. The profile plotted at the same position is the smooth “version” of the previous one, which is the convolution between the noised profile and the Gaussian filter. The two profiles have same contrast of ~ 0.64. In the case of FTH, the low-pass filter only leads to a more comfortable vision of the reconstruction, the spatial resolution being the same. But in the case of HERALDO of two-dimensional references, the low-pass filter is essential for the reconstruction (section III.9). However, in all cases, it imposes a resolution limit related to the filter width.

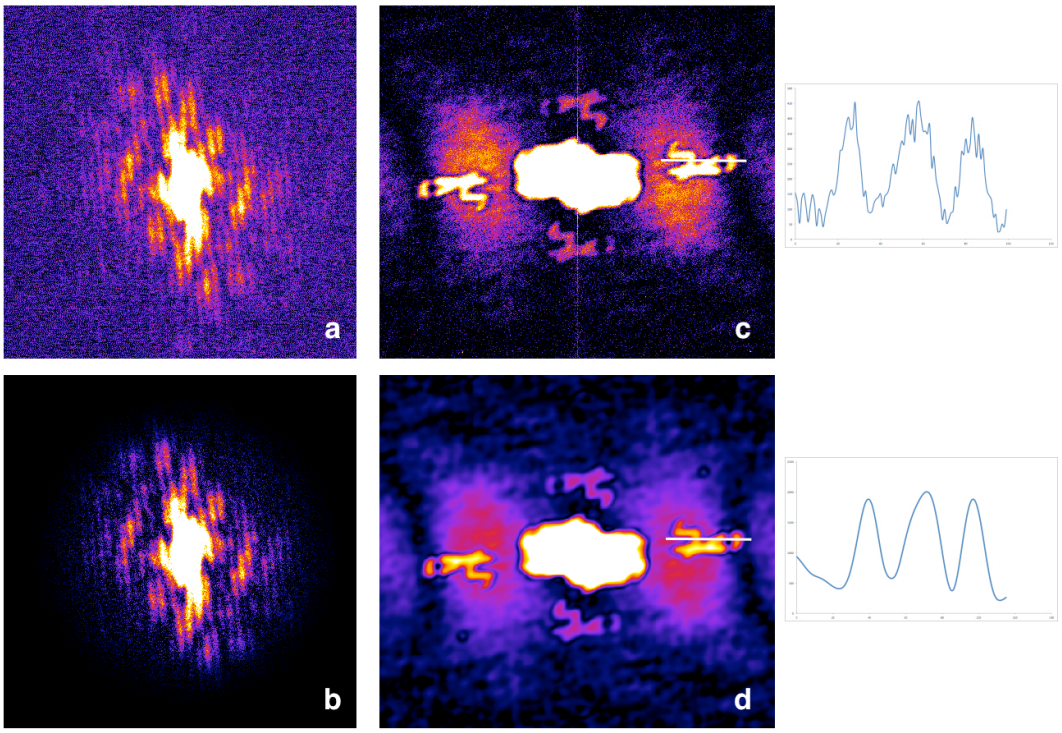

Fig. 3.10. (a) A zoom-in (400 x 400 pixels) of the original single-shot detection (2048 x 2048 pixels) of "h" object with pinholes of 300 nm. (c) Reconstructions from the original data, with the profile plotted at the white line position. (b) Hologram filtered by a low-pass filter with respect to the diffraction signal extension. (d) Reconstructions of the filtered data, which presents the same profile as the previous one.

The "geometry gird" is also reconstructed from single-shot measurement (Fig. 3.11b). The measured diffraction photons is ~ 2 x 10^6 that is less than the "h" diffraction due to the smaller object size and smaller pinholes. The diffraction pattern (Fig. 3.11a) is recorded with a binning ratio of 2 (4 pixels integrated into a large one). The signal extension of 320 x 200 "large" pixels (thus, 640 x 400 normal pixels) corresponds to maximum spatial frequencies of 7.1 μm^{-1} and 4.4 μm^{-1} respectively. A low-pass filter has been applied onto the hologram to have a better vision of the reconstruction. All the components of the grid are well reconstructed (Fig. 3.11c). The profiles in vertical and horizontal directions show a contrast of ~ 0.6. Note that the tree horizontal slits have a width of 95 nm and are separated at a center-to-center distance of 95 nm. Fig. 3.11d is another single-shot diffraction pattern obtained for the same object which contains ~ 3.2 x 10^6 diffracted photons, higher than Fig. 3.11a. However, we cannot observe fringes in the speckles in Fig. 3.11d, compared to the clear interference signature in Fig. 3.11a. The lack of interference fringes leads to worse reconstruction quality so that the components of the gird are "missed" in the reconstructions (Fig. 3.11e). The zoom-in of the two independent reconstructions shows that the big circle and the three small holes are not resolved in different reconstructions. Moreover, the other components are also less resolved, compared to Fig. 3.11c. We can obtain the "missed" components by averaging coherently (complex value calculation) the two independent reconstructions, as shown in Fig. 3.11f. However, the final reconstruction present a contrast of ~ 0.4 in vertical and horizontal profiles, which demonstrates a worse resolution compared to that in Fig. 3.11c. The lack of interference fringes should be related to a coherence problem of the harmonic beam for this acquisition. Note that these two diffraction patterns were taken

before the modal spatial filter upgrade of the harmonic beam (Chapter II, section II.4). Indeed, the statistics over ten single-shot acquisitions recorded consecutively for the same object show a total of three holograms lacking of interferences. Still, the stability was enough for the data recorded during this campaign. The comparison here demonstrates the importance of the balance between the photon flux and the beam coherence in coherent imaging. A relatively less intense beam but with a higher coherence can lead to a better reconstruction quality than a more intense beam with less coherence.

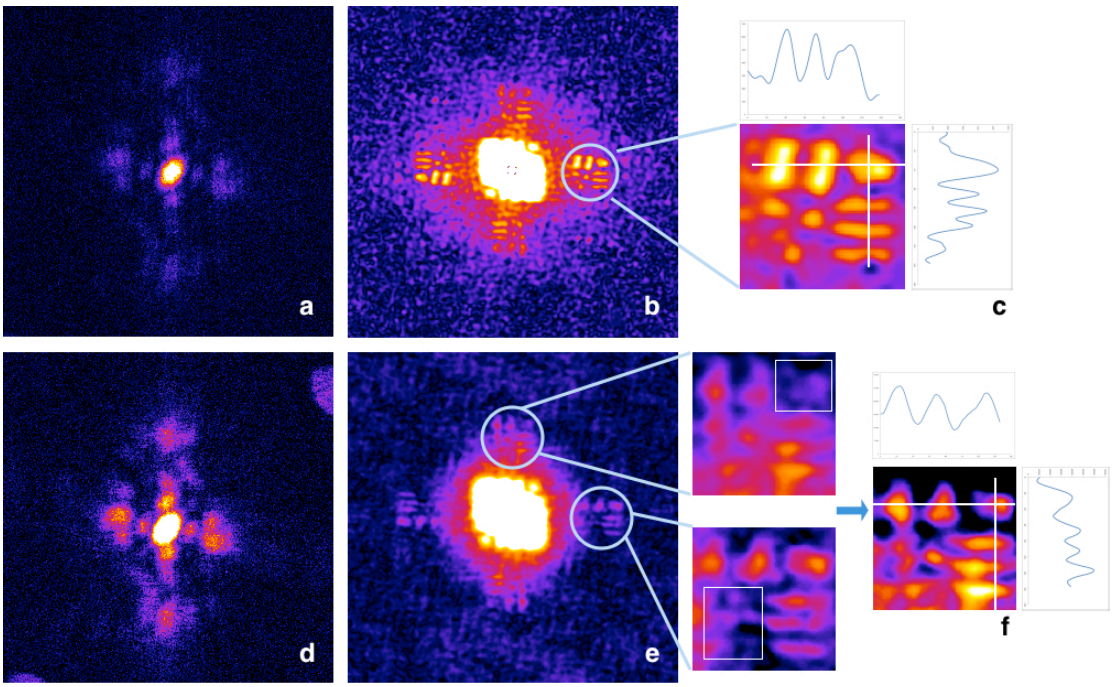

Fig. 3.11. (a) A zoom-in (400 x 400 pixels) of the single-shot acquisition (600 x 600 pixels) with clear interference fringes of test object "geometric grid". (b) Reconstructions of (a) and its zoom-in (c). (d) A zoom-in (300 x 300 pixels) of the single-shot acquisition (682 x 682 pixels) of the same object, with a higher diffraction signal and a lack of interference fringes. The signals at the top and bottom corners are parasite light. (e) Reconstructions of (d) with non-resolved components of the object. (f) The final reconstruction by coherent averaging of the two independent reconstructions in (e).

III.7 Experimental results of holography with extended reference

Holography with extended references (HERALDO) has been tested with a linear slit reference. In this configuration, the reconstruction resolution is limited by the slit width in the direction perpendicular to the slit orientation. By applying a linear differential operator along the slit reference shown in Fig. 3.12, we get two Dirac functions that are similar to the pinhole reference in FTH at its extremities (Fig. 3.12b). The holographic separation condition requires that our test object (letter "φ") should be separated from the reference slits at a distance at least equal to two times the object size (Fig. 3.12d). The object "φ" covers an area of 2 µm x 1.7 µm and the slit width is 130 nm and 145 nm respectively for horizontal and vertical one

with a length slightly longer than the object. The total object and references are within a window size of 4.5 μm x 4.5 μm.

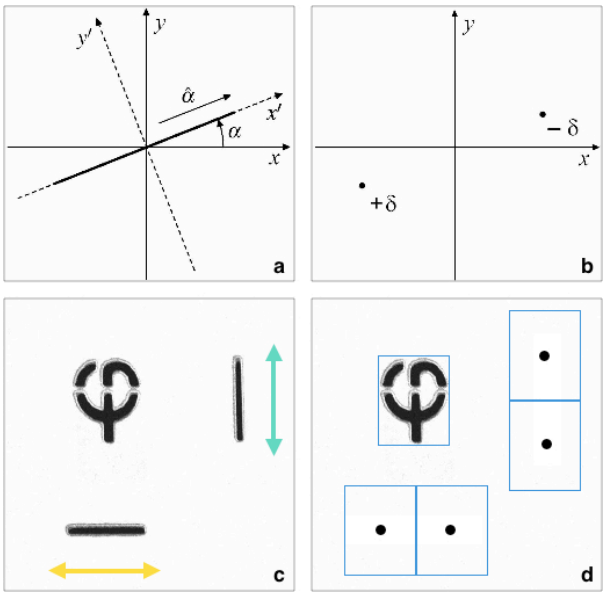

Fig. 3.12. (a) Applying linear differential operator ($\hat{\alpha}$) on slit reference (at angle α) leads to two Dirac functions (b) at the extremities of the slit. (c) The test object "φ" with two slit references. (d) The slits' length and the distance to the object are chosen to satisfy the holographic separation condition. There should be no recovery between the blue rectangles, which is the object size.

Fig. 3.13 show both single-shot and multiple-shot acquisitions of the HERALDO holograms. In Fig.3.14, we see that by applying a linear differential in each direction given by the slits to the autocorrelation of the hologram (a) we get four independent reconstructions (b,c). They can be averaged to enhance the reconstruction quality. The single-shot reconstructions are shown in Fig. 2 and 3 in Paper III. The estimated resolution is 110 nm, corresponding to a spatial frequency of 4.55 μm^{-1}, while the multiple-shot (10 shots) reconstructions have a resolution of 80 nm (corresponding to 6.25 μm^{-1} spatial frequency, red circle in Fig. 3.13b), which is limited by the width of the slit reference. However, the signal extension in multiple-shot (yellow circle in Fig. 3.13b) is much larger than the limit given by the spatial resolution of the recovered image. Indeed, in the reconstruction process, the spatial resolution is limited by the manufactured size and quality of the references. It is possible to estimate this limit by applying a linear differential operator to the slits presented in the high resolution SEM image (Fig. 3.15). The particular shape of the calculation result is our reference. The deviation from a perfect pinhole (or a Dirac function) will affect the final reconstruction resolution. In the case of a slit reference, the resolution limit is not uniform for all orientations. The longest side of the "point source" imposes a resolution limitation of ~ 85 nm, which agrees with the estimated reconstruction resolution.

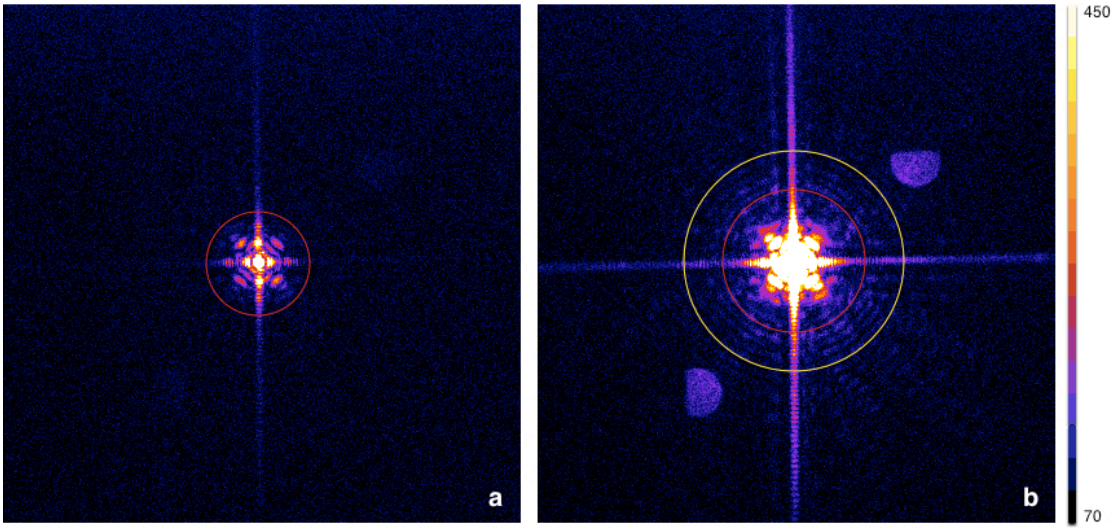

Fig. 3.13. (a) Single-shot diffraction pattern of the HERALDO object "φ". (b) 10-shot diffraction pattern of the same object presented in the same color scale. The signals of two half-circle outside the yellow circle are parasite light. Red circles shows the spatial frequencies corresponding to the estimated reconstruction resolutions. The yellow circle shows the signal extension given by the resolution limit.

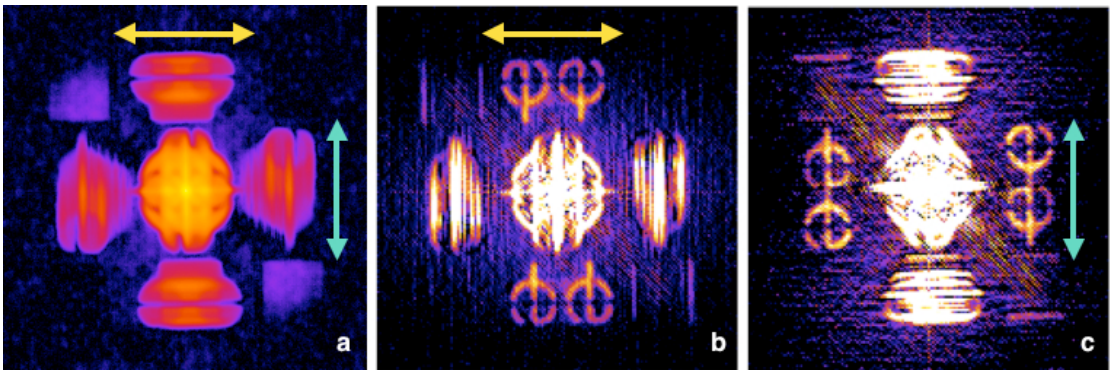

Fig. 3.14. (a) Autocorrelation for the 10-shot acquisition hologram. (b) is the derivation along the horizontal slit (yellow arrow) of the autocorrelation (a). (b) is the derivation along the vertical slit (green arrow) of the autocorrelation (a). Each reconstruction (b) and (c) shows two independent reconstructions. The crossed terms between the object and the reference show already the shape of "φ". The crossed term between the two references (the square at left top and right bottom) shows that the illumination is not uniform for the entire sample. This can also be observed in the reconstructions (b, c) where the object "φ" is more intense in the inner part.

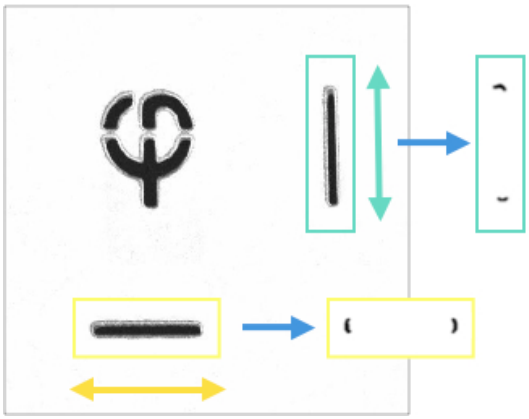

Fig. 3.15. SEM image of the sample. The derivations of the slits are shown in the rectangles at the right of the blue arrow. They exhibit four moon shape patterns, which are the deviation from an equivalent "point source" of the slit references simulated from the SEM image by applying linear differential operator. The green square is the result of vertical linear differential operator, and the yellow square is the horizontal one.

III.8 Signal-to-noise ratio (SNR) analysis

For all the three imaging configurations (CDI, FTH, HERALDO), the signal-to-noise ratio is a key factor for the reconstruction quality. In our experimental conditions, the noise can be separated into four independent components according to their nature:

1) The parasite light noise: as shown in the measured diffraction patterns, we have sometimes detected parasite light signals, usually at the outer part of the diffraction pattern (Fig. 3.13b). It is due to the IR and/or harmonic reflections inside the experimental chamber, and/or the transmission of the parasite light through the sample holder.
2) The photon noise: it is directly related to the diffraction signal and obeys to the Poisson distribution. The signal-to-noise ratio can be described as $SNR = \frac{N}{\sqrt{N}} = \sqrt{N}$, where N is the photon flux (or photon numbers).
3) The readout noise: it is related to the CCD camera readout quality, which is the uncertainty introduced during the process of quantifying the electronic signal. The readout noise mainly arises from the on-chip preamplifier [7]. It is characterized by its standard deviation $\sigma_{readout}$ (or its variance $\sigma^2_{readout}$).
4) The dark noise (dark current): it is introduced by the thermally generated electrons within the silicon layers of the CCD. The dark current describes the statistical variation of the thermal electrons at a given CCD temperature and a given exposure duration, obeying also to the Poisson law. It is characterized by electrons/pixel/sec.

Practically, the noise reduction has been realized at the detection stage through several steps. The parasite light noise can be easily removed after detection, since it is usually located in the region without diffraction signal in our experiment. We have also added light shields and filters (as what we did for magnetism experiments in Chapter IV) to stop the parasite light before detection. We cannot reduce the photon noise due to its nature, but we can increase the

associated SNR by increasing the total photon number (beamline output, light transport and focus optimization) because of the square root relation of the photon noise SNR. One can also bring the CCD camera closer to the object plane to have a higher photons/pixel ratio to enhance the SNR associated to the photon noise. Note that, the CCD-object distance should always fulfill the sampling ratio for FTH/HERALDO or the oversampling condition for CDI. Moreover, multiple-shot accumulation can also enhance the SNR. The dark noise can be reduced by cooling down the CCD camera, which is 0.05 electrons/pixel during 100 seconds exposure at -40°C, according to the CCD camera fabricant. The readout noise depends on the readout frequency of the camera. Our CCD camera has two available readout frequencies: 1 MHz and 100 kHz. The reference value (standard deviation) given by the CCD camera fabricant is 8.8 electrons for 1 MHz and 4 electrons for 100 kHz, corresponding respectively to 6.8 ADU and 3.1 ADU. The disadvantage of using 100 kHz is the long CCD readout time, which is up to 30 seconds, compared to the 4.5 seconds for 1 MHz. Note that the readout time depends on the CCD chip size (or total pixel numbers).The CCD camera offers an option to read only a part of the CCD chip defined by users (called region of interest) to reduce the readout time. In practice, according to the measurement in dark condition (Fig. 3.16), the measured readout noise for 1 MHz and 100 kHz is respectively 9.2 ADU and 3.2 ADU, thus ~ 12 electrons and ~ 4 electrons. The other option provided by the CCD camera to enhance the readout SNR is the hardware binning, which combines charge from adjacent pixels into a single large pixel during the readout process. In the ideal case, the enhancement is equal to the binning ratio. For example, if each normal (non-binning) pixel has signal of 20 electrons and a readout noise of 10 electrons, then a single large pixel of 3 x 3 binning ratio will have a signal of 180 electrons and a readout noise of 10 electrons (it is introduced only once during the readout process). The SNR of a large pixel is then 9 times larger than that of a basic pixel unit. Note that the *hardware* binning is different to the *software* (or *numerical*) binning, which combines adjacent pixels after the readout process, thus the software binning does not change the SNR associated to the readout noise, but still increases the SNR of photon noise for each large pixel. One should again be careful of the sampling ratio when binning the pixels. The measured diffraction pattern is the superposition of the diffracted signal and the different noises, among which the dark noise and the parasite light noise are easy to handle. Usually, with a low diffraction signal, the noise is dominated by the readout noise, which is called readout-noise limited; with a high diffraction signal, the photon noise is dominant, which is called photon-limited. For the wavelength used in our imaging experiment (H25, 32 nm), one detected photon generates 10 electrons (Eq. 3-2), which is comparable to the readout noise at 1MHz. In our experiment, the measured diffraction patterns are mainly influenced by the readout noise and the photon noise. The SNR of the diffraction pattern is then

$$SNR_{diffraction\ pattern} = \frac{N_{detected\ signal}}{\sqrt{N_{detected\ signal} + \sigma^2_{readout}}} \qquad \text{(Eq. 3-5)}$$

Overall, we distinguish in our diffraction patterns two regions: the region of low spatial frequencies is photon limited and the region of high spatial frequencies is readout-noise limited.

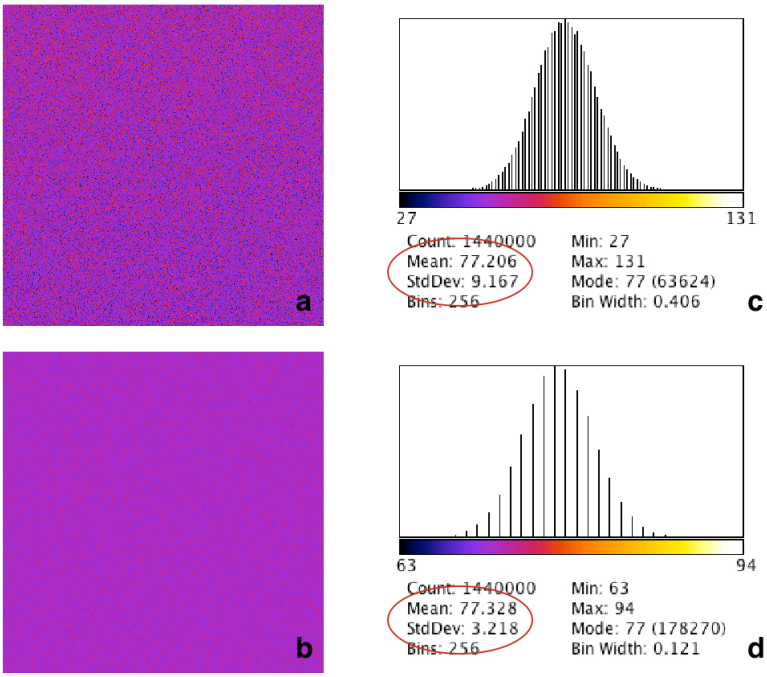

Fig. 3.16. Measurements in dark condition at 1 MHz (a) and 100 kHz (b) and the respective histogram (c) and (d).

III.9 HERALDO reconstruction and noise

An analysis of the photon noise influence in the HERALDO technique can be found in the thesis of M. Guizar-Sicairos ([8], Chapter 5, section 5.6). The SNR is analyzed in photon-limited statistics with theoretical discussions and numerical simulations. The findings are that the HERALDO technique is robust to the photon noise, and the bulk of noise contribution by the extended reference is effectively filtered during the reconstruction procedure. However, in our experiment, the diffraction patterns are far from photon-limited, due to the harmonic flux and its relatively low photon energy. An important step in the HERALDO reconstruction process is to apply the linear differential operator associated to the reference shape in the object space (the autocorrelation). This step, in practice, is realized by applying a point-by-point multiplicative filter, $W_{p,q}$, in the Fourier domain (the diffraction pattern or the hologram), where p and q is the index of the diffraction pattern pixel. Then, the object image is reconstructed by applying an inverse Fourier transform on the "filtered" diffraction pattern. In fact, $W_{p,q}$ is a high-pass filter, as presented in Fig. 3.17. This kind of high-pass filter will amplify the high spatial frequency region that is dominated by the readout noise. As a consequence this will degrade the HERALDO reconstructions of our recorded holograms. To eliminate the amplified readout noise, one can apply a low-pass filter, such as a Gaussian filter. In Fig. 3.17, the high-spatial-frequency region of the multiplicative filters is eliminated by a super Gaussian filter (third order) with a diameter of 2000 pixels (full width at half maximum). The multiplicative filters are calculated in a window size of 2200 x 2200 pixels. In the following example of experimental data, I will show that the low-pass filter is essential to the HERALDO reconstruction process, especially with diffraction patterns significantly influenced by readout noise.

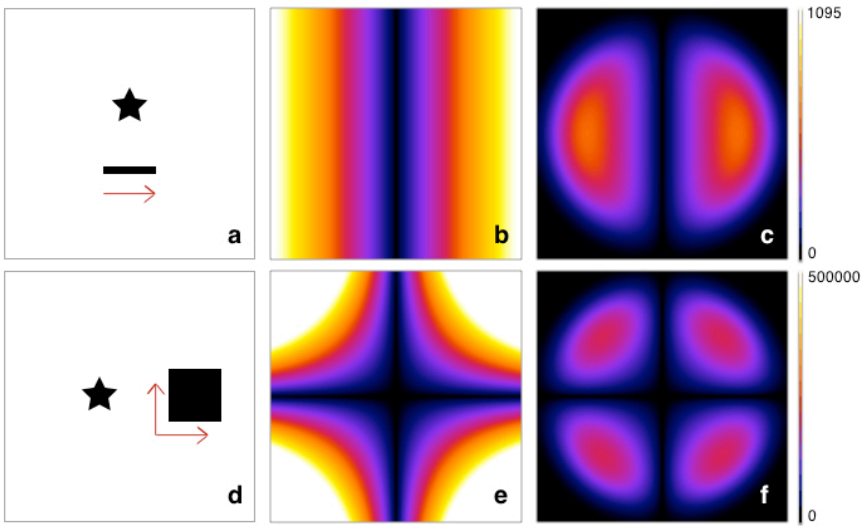

Fig. 3.17. Numerical simulation of the multiplicative filters (b and e) associated to one-dimensional slit reference (a) and two-dimensional square reference (d). The "star" is the object. (c) and (f) are the results of applying a super Gaussian filter (third order) on the multiplicative filters.

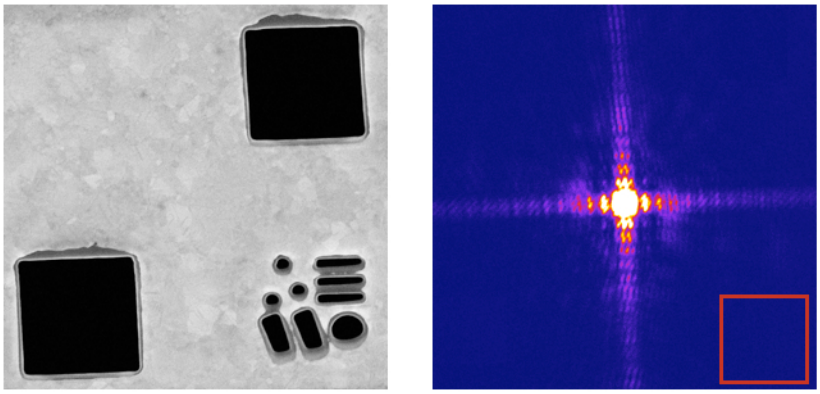

Fig. 3.18. (left) Test object A: SEM image of the geometric grid object with two square references. (right) Measured single-shot diffraction pattern of test object A.

The test object A (Fig. 3.18 left) is a geometric grid object (1µm x 1µm) with two square references (slightly larger than 1 µm x 1µm). The object-reference distances are slightly larger than the object size (holographic separation). The two squares can provide eight independent reconstructions (associated to the eight corners of the two squares) in one acquisition. We obtained a single-shot diffraction pattern with a readout frequency of 100kHz and within a window size of 600 x 600 pixels of 2 x 2 binning ratio (corresponding to 1200 x 1200 non-binned pixels). The measured diffraction signal is ~ 6 x 10^7 photons. The readout noise has a standard deviation of 4 ADU and an average of 14 ADU, measured in the red square (Fig. 3.18 right) where there is no diffraction signal.

Fig. 3.19 presents the effect of the low-pass filter during the reconstruction process. When no low-pass filter is used (left column), the high spatial frequencies of the hologram are significantly amplified after applying the multiplicative filter. The reconstructions are

completely covered by the noise. When applying a low-pass filter, whose diameter is too large (800 pixels) to eliminate all the amplified readout noise (middle column), the object is reconstructed but with a low quality. Applying a suitable low-pass filter (right column), whose diameter (400 pixels) is small enough to eliminate most readout noise at high spatial frequencies, the object is then clearly reconstructed. To quantify the noise contribution, we can use the power SNR of the reconstructed image [8]:

$$SNR_r = \frac{\sum_{p,q}^{N_o} \left| o_{p,q} \right|^2}{N_o \left\langle \left| \sigma_{p,q} \right|^2 \right\rangle} \qquad \text{(Eq. 3-6)}$$

SNR_r is the ratio between the signal energy and the noise energy presented in the reconstruction image. The signal energy $\sum_{p,q}^{N_o} \left| o_{p,q} \right|^2$ is calculated by integrating the signals inside the object region N_o (bleu square in Fig. 3.19), and the noise energy is the multiplication of N_o and its variance calculated in the region without signals (white square). Here, the noise energy is the total contribution of photon noise and readout noise. Note that SNR_r only accounts for the statistical noise and does not include the effects of resolution loss.

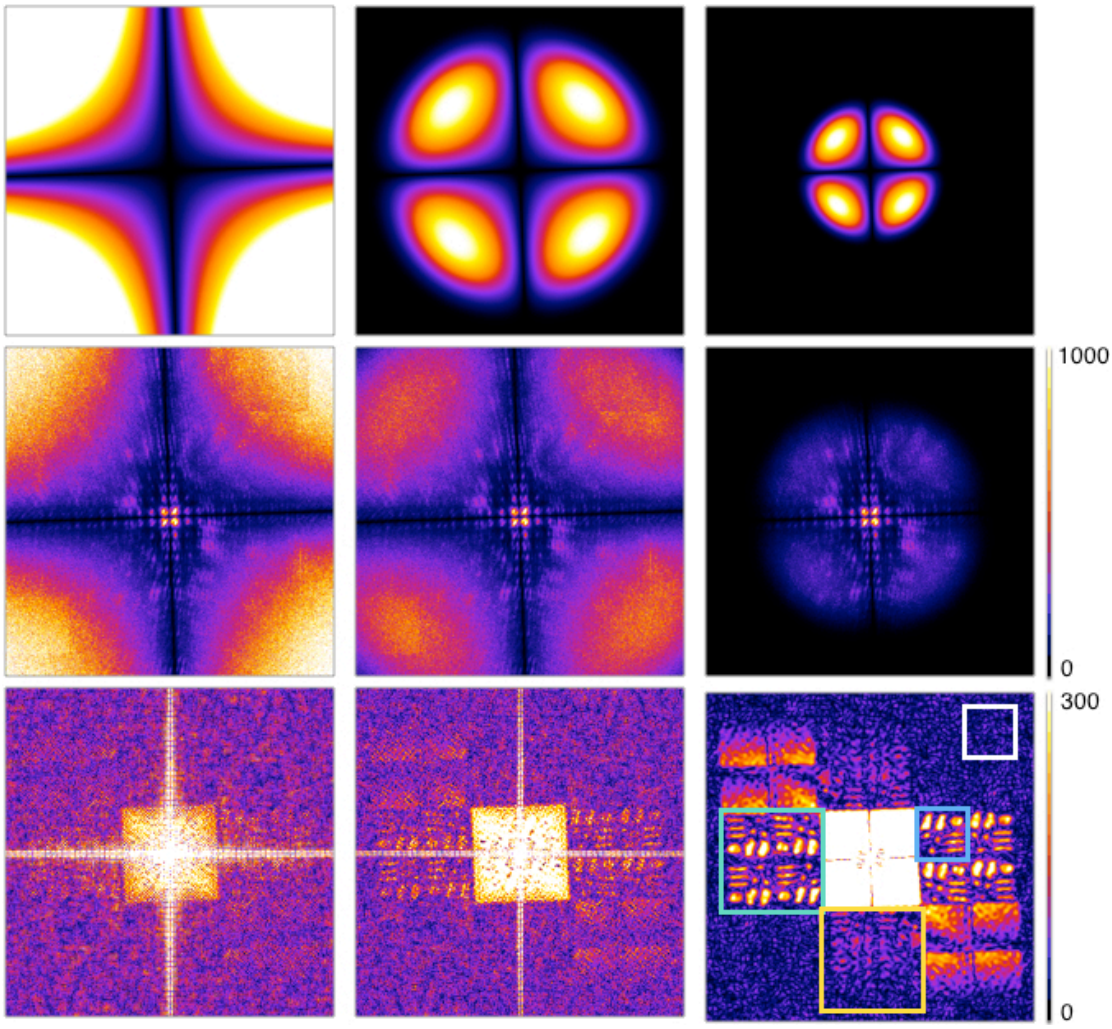

Fig. 3.19. Influence of the low-pass filter during the reconstruction process. (first row) Multiplicative filter with and without Gaussian filter. (second row) Results of the multiplication (in Fourier space) of the measured diffraction pattern by the HERALDO multiplicative filter with and without Gaussian filter. (third row) Inverse Fourier transform of

the second row, giving the reconstructions. The eight independent reconstructions are within the green and the yellow square (each associated to a square reference). The bad reconstructions in the yellow square should be due to a miss-alignment that one reference has not been sufficiently illuminated. Note that the multiplicative filter is slightly tilted to agree with the diffraction axis.

I have then reconstructed the object A with different diameter of the low-pass filter (from 200 to 1000 pixels, every 100 pixels). The reconstructions are shown in Fig. 3.20. When the filter diameter increased, it is more difficult to reconstruct the object and more noise appears. We also note that the reconstruction is more blurred with smaller filter diameter. To estimate the resolution, I have plotted the profile of the reconstruction at the white line position in Fig. 3.21, and compared it to the calculated SNR_r. The SNR_r increases with smaller filter diameter that high spatial frequencies (dominated by the readout noise) are eliminated. But the measured contrast (reflecting the resolution) does not always increase. It is maximized (0.76) at a filter diameter = 400 pixels, then decreases quickly at smaller diameters. The corresponding theoretical resolution for different filter diameter is presented in Table 3.1. Note that the measured contrast for diameter = 300 pixels (2 x 2 binning) is 0.65 and the period of the three horizontal slits of the object is ~ 190 nm. It means that the reconstruction resolution is worse than 95 nm, which is not limited by the filter diameter (75 nm). Therefore, the contrast decrease should be related to other factor like a loss of constructive diffraction signal.

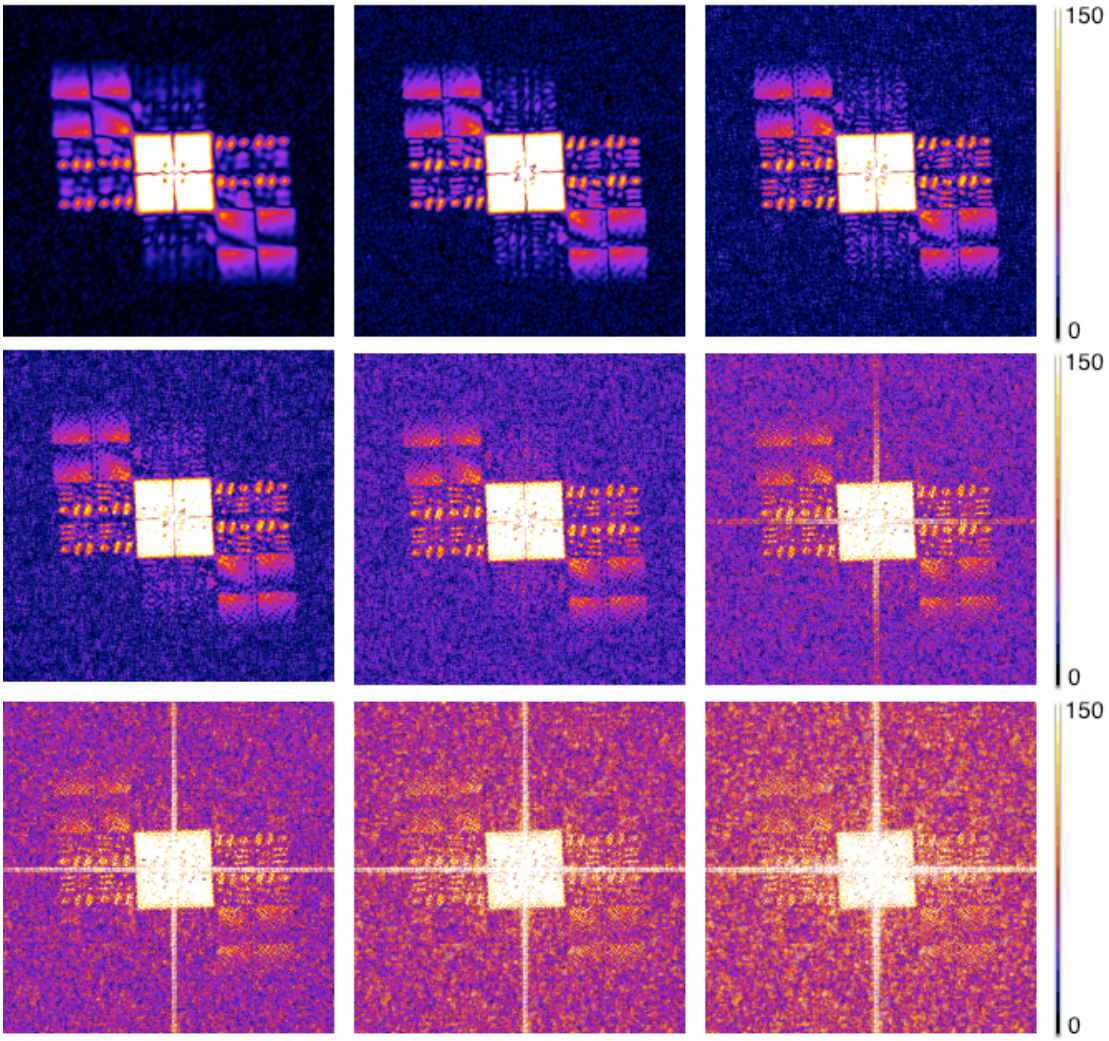

Fig. 3.20. Reconstructions with different low-pass filter diameter. (first row from left) Diameter = 200, 300 and 400 pixels. (second row from left) Diameter = 500, 600 and 700 pixels. (third row from left) Diameter = 800, 900 and 1000 pixels. All images are presented with the same color scale.

Filter diameter / Non-binning	400	600	800	1000	1200	1400	1600	1800	2000
2 x 2 binning	200	300	400	500	600	700	800	900	1000
3 x 3 binning	130	200	260	330	400	470	530	600	670
Theoretical resolution (nm)	113	75	56	45	38	32	28	25	23

Table 3.1. Theoretical resolution for different low-pass filter diameter with different binning ratio.

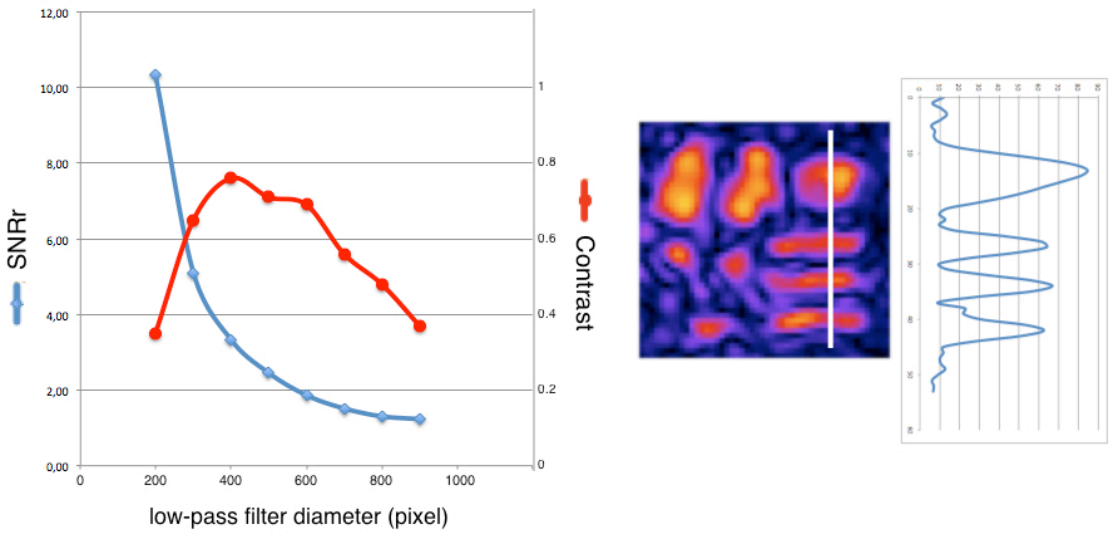

Fig. 3.21. (right) For each reconstruction, the measured contrast corresponds to the white line position. (left) Evolution of the SNR_r and the contrast with different low-pass filter diameter.

Since the readout noise is not correlated from one pixel to another, we can classify the pixels of the diffraction pattern by choosing two reasonable thresholds. To simplify the calculation, I use the ADU as the signal and noise unit in this section. I assume that for one pixel, it is *readout-limited* when there is no diffraction signal, which means that the ADU count of this pixel is within the readout noise distribution. The latter can be measured in a region far away from the diffraction signals, such as the red square in Fig. 3.18. A pixel is *photon-limited* when the ADU count of the pixel gives a photon noise 10 times higher than the readout noise. For example, with 1MHz readout frequency, the readout noise is equivalent to one photon signal (see section…). Moreover, a pixel whose ADU count is between these two thresholds is said to be *mixed-noise*. And a pixel is *non-ADU* if its ADU count is zero after applying the low-pass filter. Therefore, all pixels are classified into four types, among which *photon-limited* and *mixed-noise* pixels provide useful signals for the reconstructions, and *non-ADU* pixels have no contribution to noise or useful signal. Fig. 3.22 presents the evolution of these four kinds of pixels when different filter diameters are used. Clearly, tighter low-pass filter turns more *readout-limited* pixels to *non-ADU* pixels, and that's the reason why the contrast of the reconstruction increases. However, for filter diameter smaller than 600 pixels, the *photon-limited* and *mixed-noise* pixels begin to decrease (eliminated by the tight filter, turned to *non-ADU* pixels). This can explain why the contrast decreases after the maximum. Therefore, one should find a good compromise between eliminating more *readout-limited* pixels and keeping more *photon-limited* and *mixed-noise* pixels. Fig. 3.23 shows the three kinds of pixels' distribution for a filter diameter of 400 pixels, where *mixed-noise* pixels are as important as *photon-limited* pixels for reconstruction. The sum of these two kinds of pixels presents almost the entire diffraction signals. The *mixed-noise* pixels are more influenced by the low-pass filter, as we can see in Fig. 3.22 where it decreases two times quicker than the *photon-limited* pixels.

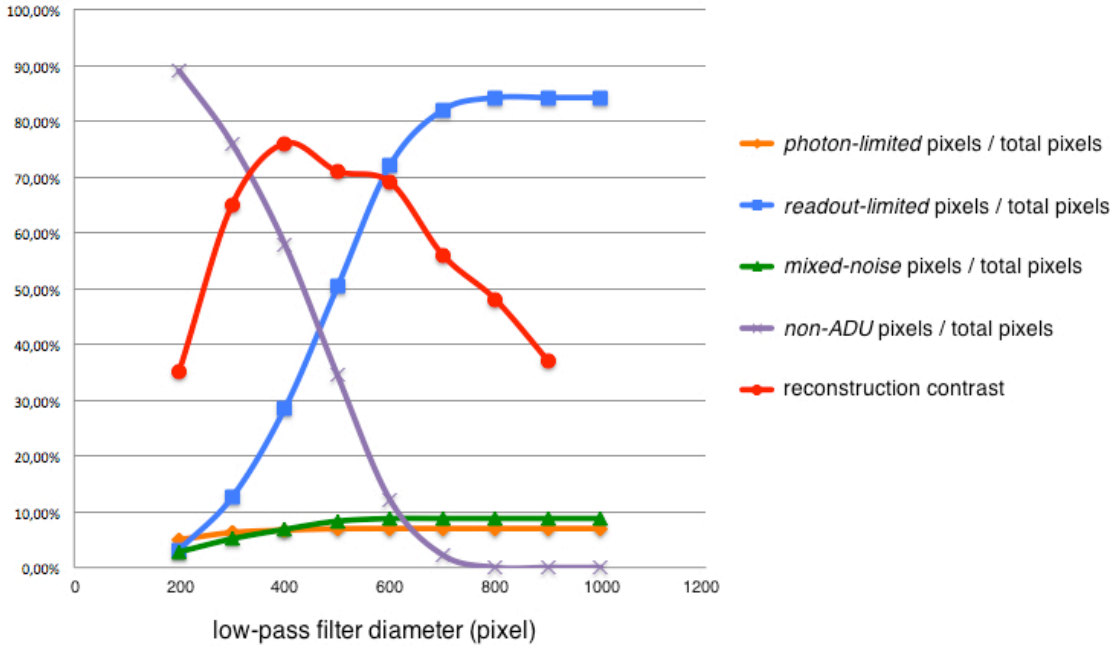

Fig. 3.22. Evolution of the four kinds of pixels with different filter diameters. The curves are the ratios between each kind of pixel number to the total pixel number. The reconstruction contrast curve is also plotted here for comparison.

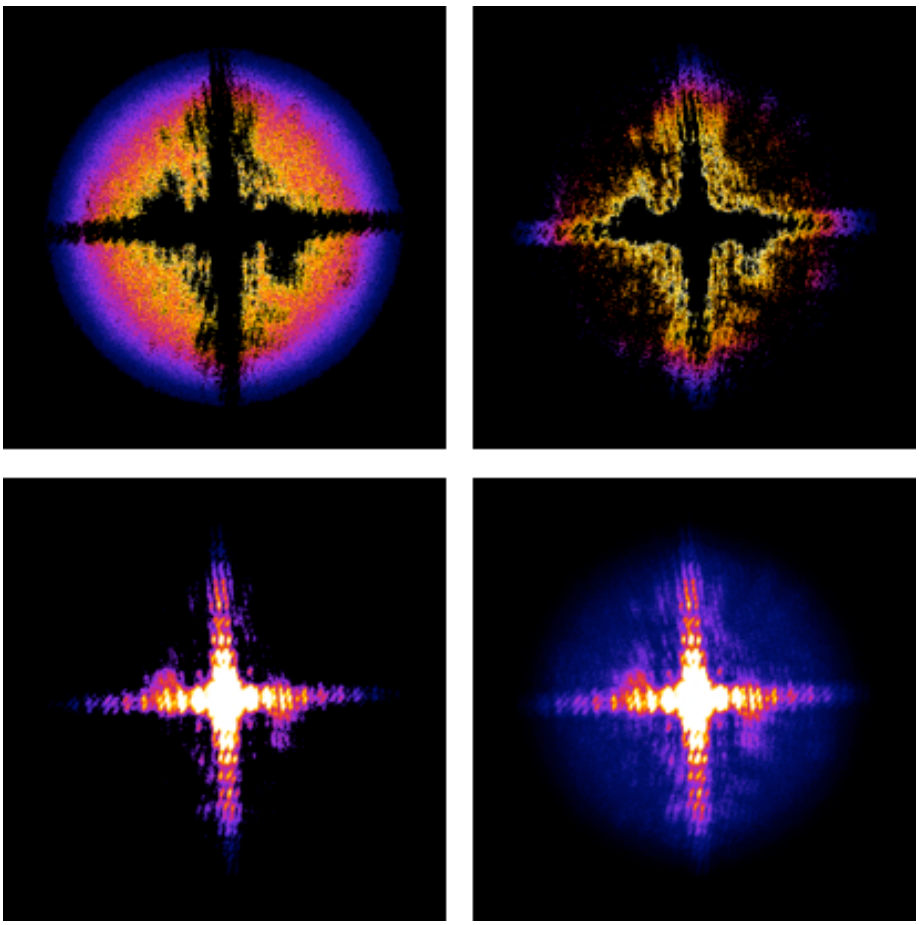

Fig. 3.23. (Top row) Distribution of *readout-limited* pixels (left) and *mixed-noise* pixels (right). (Bottom row) Distribution of photon-limited pixels (left) and total pixels (right). Images are filtered by a super Gaussian filter of 400 pixels diameter.

I present now another example (test object B), which is a geometric grid (1µm x 1µm) with two slits reference (slightly longer than 1µm) separated from the grid far enough to fulfill the holographic separation conditions (Fig. 3.24). The presented single-shot diffraction pattern (Fig. 3.24) is obtained with a readout frequency of 1MHz and within a window size of 600 x 600 pixels at a 2 x 2 binning ratio. The measured diffraction signal is ~ 1.2 x 10^7 photons. The readout noise has a standard deviation of 9.8 ADU and an average of 38 ADU.

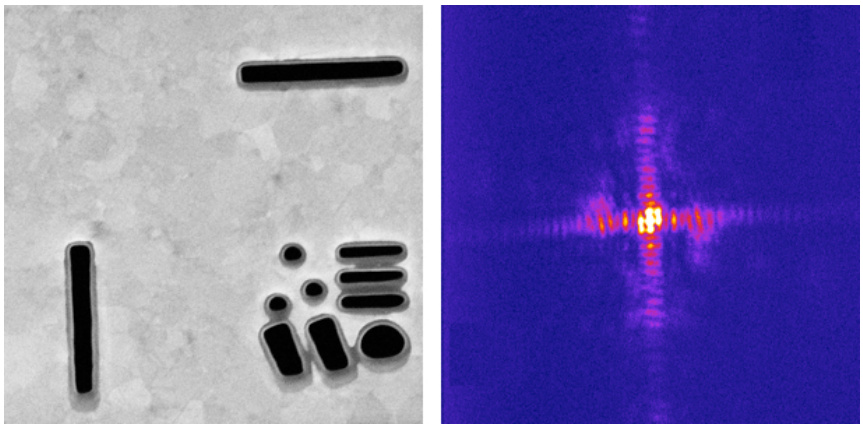

Fig. 3.24. SEM image of the test object B (left) and the measured diffraction pattern (right).

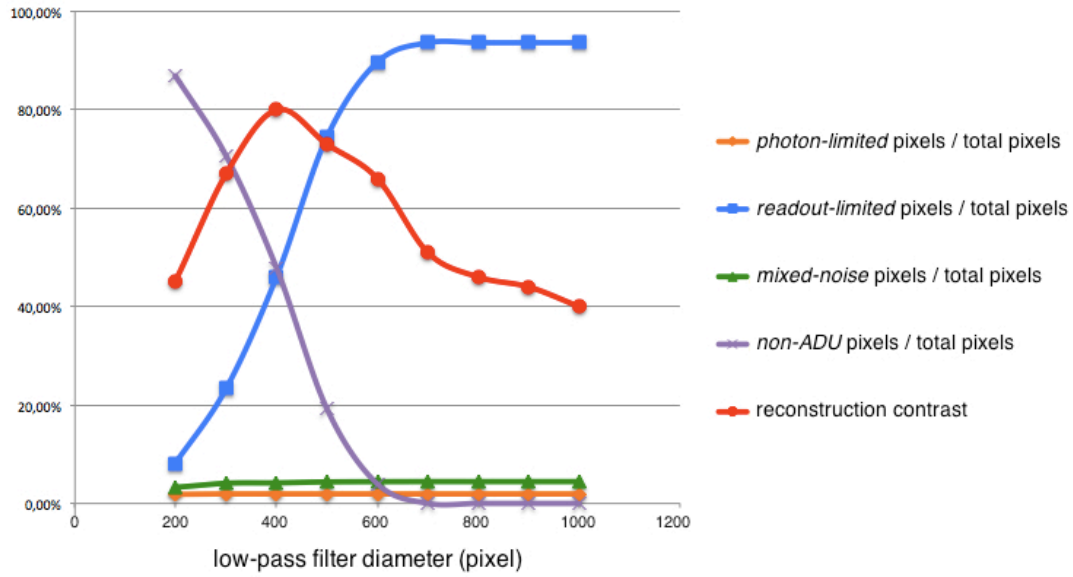

Fig. 3.25. Evolution of the four kinds of pixels with different filter diameters. The curves are the ratios between each kind of pixel number to the total pixel number. The reconstruction contrast curve is also plotted here for comparison.

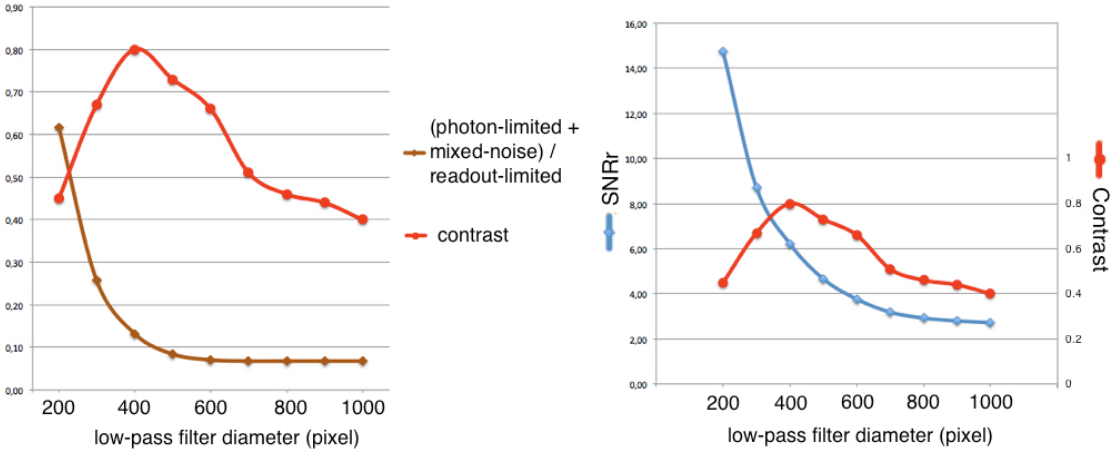

Fig. 3.26. (left) The blue curve presents the evolution of the ratio between (*photon-limited* + *mixed-noise*) pixels and the *readout-limited* pixels. (right) SNR_r evolution (blue curve) and the reconstruction contrast (red curve).

Using the same analysis method, similar results are obtained for the four kinds of pixels evolution (Fig. 2.25). The reconstruction contrast is again maximized (0.8) at a diameter = 400 pixels. Fig. 2.26 presents the variation of the ratio between (*photon-limited* + *mixed-noise* pixels) and *readout-limited* noise. The reconstruction contrast is enhanced to a relatively good range (> 0.6) when this ratio begins to increase. And the latter has a good agreement with the SNR_r in their evolution behavior. It confirms that the noise energy in the reconstruction image has a large contribution from the readout noise, which limits the reconstruction quality. Fig. 3.27 is a reconstruction of object B with filter diameter = 400 pixels. Note that, reconstructions without low-pass filter are also resolved (Fig. 3.27 left) for this object due to the one-dimensional reference. The multiplicative filter is order 1 for one-dimensional reference and two for two-dimensional references. Therefore, the amplification of the readout noise is less important with slit reference than square reference, which is the advantage of one-dimensional reference. However, the resolution of the two-dimensional reference is theoretically non-limited, compared to the resolution limitation in the perpendicular direction of the slit reference.

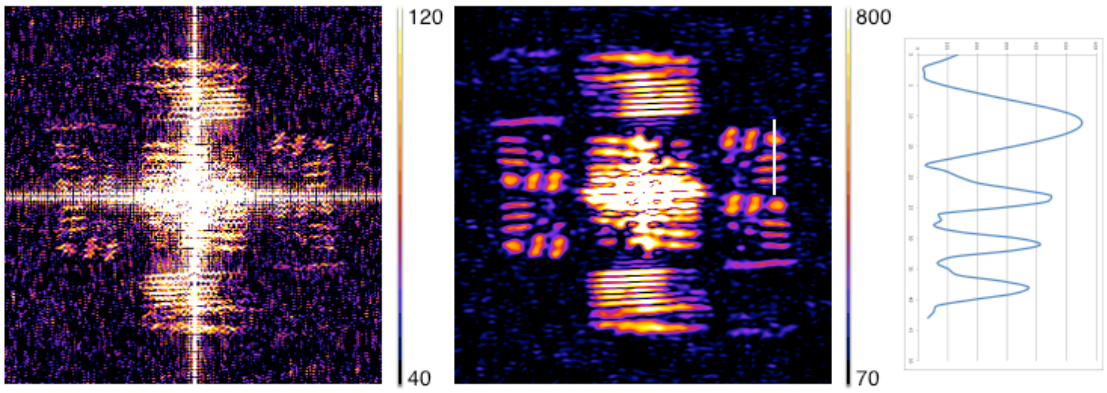

Fig. 3.27. Reconstruction of test object B without (left) and with (center) a low-pass filter diameter of 400 pixels. (right) Profile of the reconstructed object at the white line position.

III.9a HERALDO reconstruction and noise: Detection stage optimization with multiple shot acquisition

As demonstrated in the previous examples, the reconstruction of our diffraction patterns is mainly limited by the amplified readout noise. Therefore, the optimization of the detection stage will then focused on the readout noise. First, we can increase the incident harmonic beam flux by shots accumulation to have a higher signals/pixel ratio. Thus more pixels are then *photon-limited* or *mixed-noise*. Fig. 3.28 presents a comparison between single-shot and multiple-shot acquisition of the test object C, which is the same geometric grid (1µm x 1µm) with two square references (slightly larger than the object) just beside it, which offer four independent reconstructions in one acquisition. Please refer to the caption of Fig. 3.28 for the detailed explanation of the reconstruction geometry. The measured 5-shot diffraction pattern has 2.9 x 10^8 photons and the single-shot acquisition has 5.9 x 10^7 photons. The ratio between the measured photons is ~ 4.9. The standard deviation of the readout noise is 8.8 ADU and 9.6 ADU respectively for the single-shot and the 5-shots detections, with a same average of 33 ADU. Both images are recorded within a window size of 1200 x 1200 non-binning pixels and the readout frequency is 1MHz. Comparing the analysis result (Table 3.2) of the 1-shot and 5-shot best reconstructions (Fig. 3.28 second row), which correspond to the highest reconstruction contrast, the *photon-limited* and *mixed-noise* pixels are increased by 3.4 and the SNR_r is increased by 1.5. Applying the Equation 3-6, we can get following equations:

$$SNR_{r\_single-shot} = \frac{S_1}{P_1 + L_1} = 2.95$$

$$SNR_{r\_five-shot} = \frac{S_5}{P_5 + L_5} = 4.51$$

where S is the signal energy, P and L are noise energy contributed respectively by the photon noise and the readout noise. And we have $S_5 = 5S_1$ and $P_5 = 5P_1$. Since the readout frequency and hardware binning ratio is the same, we have $L_5 = L_1$. Thus

$$\frac{P_1}{L_1} = 1.31$$

$$\frac{P_5}{L_5} = 6.55$$

The single-shot acquisition has equivalent photon noise and readout noise contributions in its reconstruction, while the 5-shot reconstruction is mainly influenced by the photon noise. The disadvantage of the accumulation is the eventual blur of the diffraction pattern due to the instable beam position, and radiation damage for certain samples.

	Filter diameter	$\frac{photon + mix}{readout}$	$\frac{photon + mix}{total}$	SNR_r	Theoretical resolution	Reconstruction contrast
1-shot	600 pixels	0.12	2.73%	2.95	75 nm	0.61
5-shot	800 pixels	0.26	9.38%	4.51	56 nm	0.75

Table 3.2. Analysis results of 1-shot and 5-shot best reconstructions.

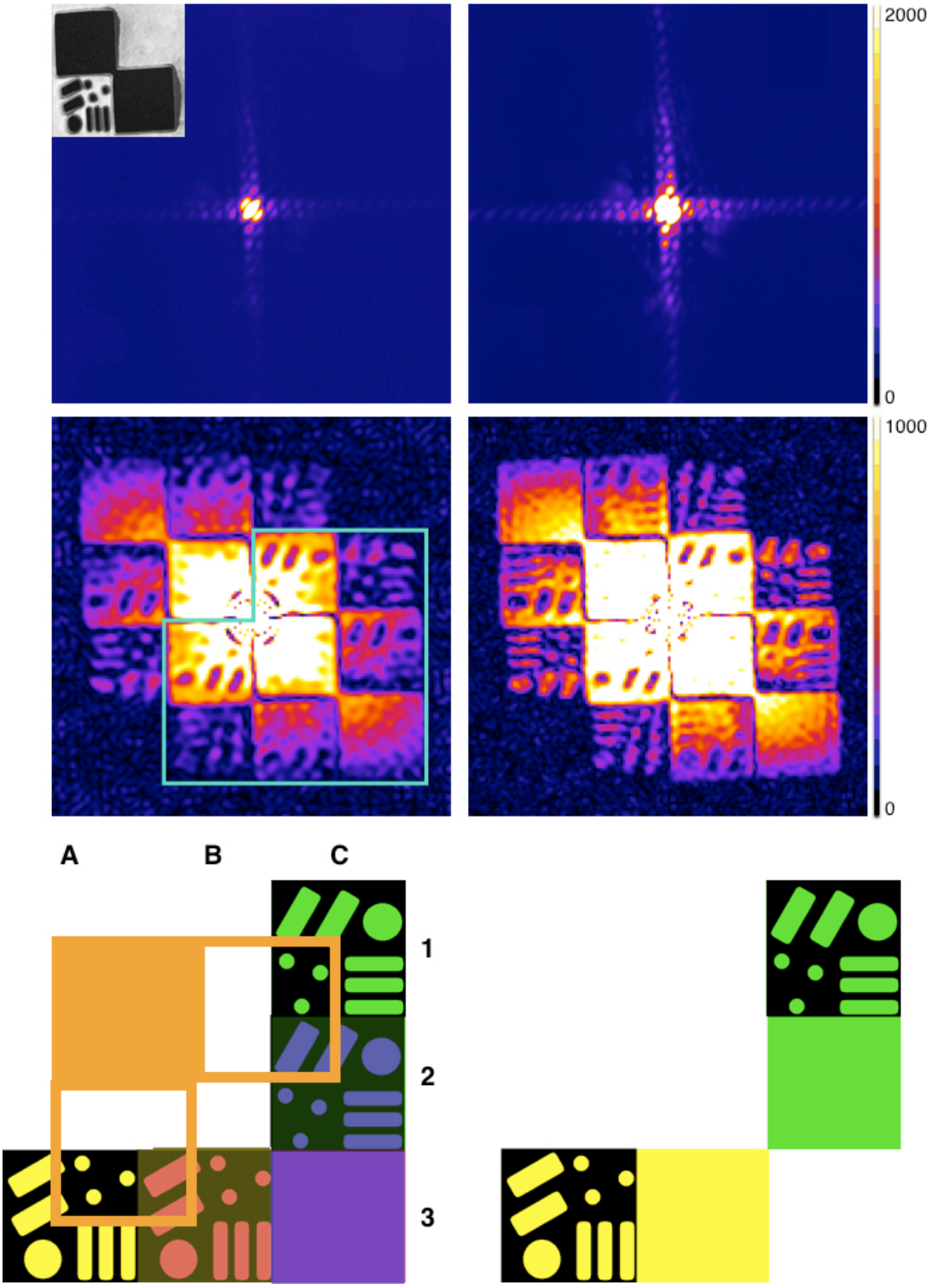

Fig. 3.28. Diffraction patterns (first row) and best reconstructions (second row) for single-shot (left) and 5-shot (right) detections of object C. The SEM image of object C is presented at the left-top. (third row) Reconstruction geometry: the yellow, red, blue and green rectangles (object with one square reference) are 4 independent reconstructions related to the 4 corners of the two orange hollow-squares (object centered on the corner). The orange full-square presents the object position. Yellow and red reconstructions are in the same direction, and the green and blue ones in the other. There is signal superposition of yellow reference and red object at B3, of green reference and blue object at C2, and of red reference and blue reference

at C3. Moreover, the C1 and C2 corners are Dirac functions of opposite sign (+ and -) after derivation (refer to slit reference). Therefore, we observe the positive and negative reconstructions at C1 and C2 in the experimental results.

III.9b HERALDO reconstruction and noise: Detection stage optimization with hardware binning

The detection can also be optimized with the *hardware* binning option. The test object D (Fig. 3.29. top left) has the same geometric grid with one square reference close to the object. The total test object size is ~ 2µm x 2µm, and the reference can provide three independent reconstructions. Considering the sampling ratio limit, I choose the hardware binning ratio of 1x1, 2x2 and 3x3. The detected diffraction patterns are presented in Fig. 3.29, with a zoom-in of a region (white square) where signals are confused with noises in 1x1 binning and are then emphasized in 2x2 and 3x3 binning. Note that the measured diffraction signal is 2.7 x 10^7, 1.5 x 10^7 and 1.2 x 10^7 photons respectively for 1x1, 2x2 and 3x3 binning. With less diffracted signals, hardware binning is still able to extract the signal out of the noise, which can then be used for the image reconstruction. The readout noise for different hardware binning ratio is similar, with measured values of 8.8, 10 and 9.6 respectively for 1x1, 2x2 and 3x3 binning ratio.

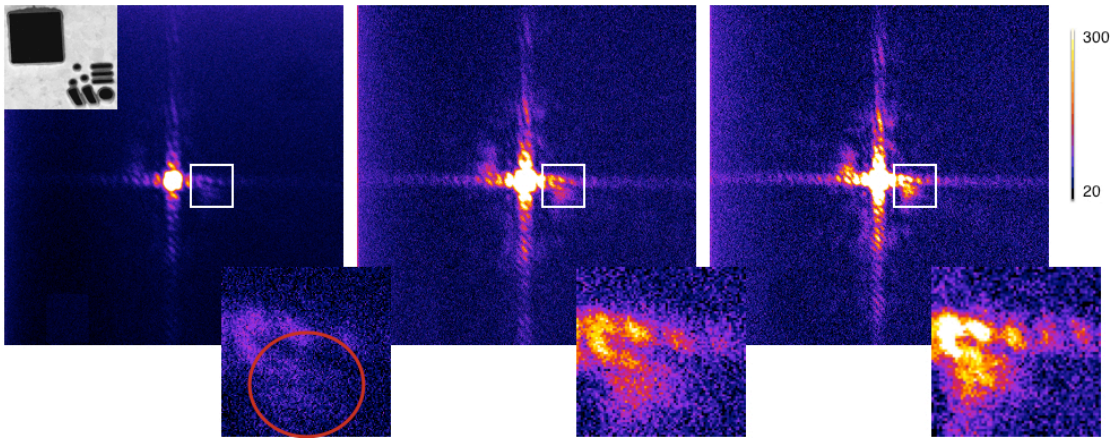

Fig. 3.29. Diffraction patterns for 1x1, 2x2 and 3x3 binning ratio (from left to right) of the test object D (top left). The zoom-in pictures correspond to the white square in each image and the red circle indicates the region where signals are extracted using higher binning ratio. The window size for each hologram (from left to right) is respectively 1200 x 1200 pixels, 600 x 600 pixels and 467 x 467 pixels. All the images are presented with the same color scale.

The reconstructions are realized with the same low-pass filter diameter of 400 pixels for 1x1 binning, 200 pixels for 2x2 binning and 130 pixels for 3x3 binning. The results (Fig. 3.30) present clear improvement of the SNR_r when applying a higher binning ratio. Since the SNR_r does not take account of the resolution, I plot the profile at the white line position for each reconstruction to compare the achieved resolution (Table 3.3). The contrast is improved by hardware binning but the effect is not dramatic. Comparing the (photon-limited + mixed-noise)/total pixels percentage, 3x3 binning ratio does not extract more signal from noise and in this case, the 2x2 binning is enough. Note that the three horizontal slits of the object are not

resolved in any of the three reconstructions.

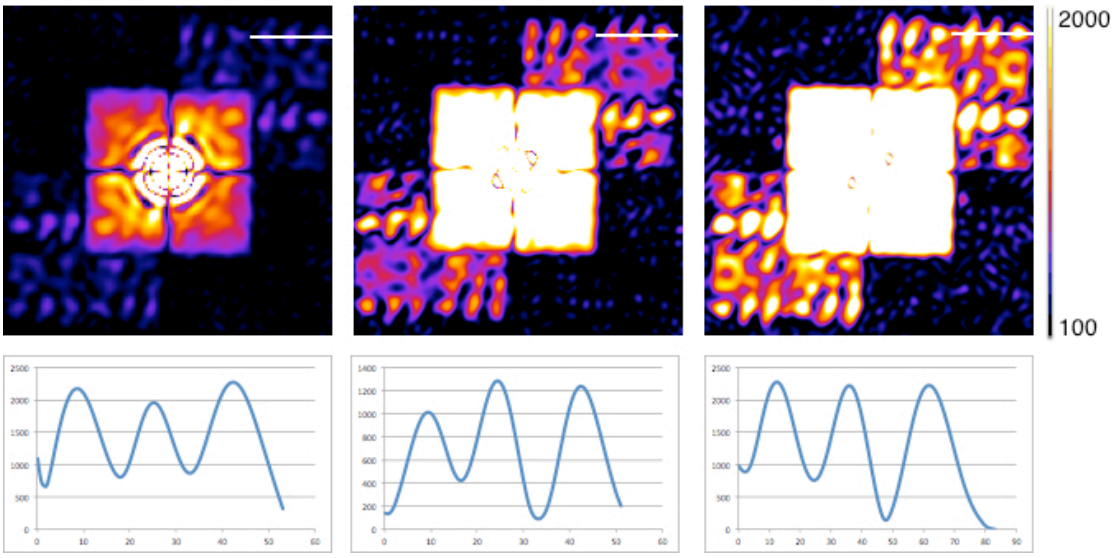

Fig. 3.30. Reconstructions of the diffraction patterns in Fig. 3.29 with 1x1, 2x2 and 3x3 binning ratio (from left to right). The plotted profile corresponds to the white line position. All images are presented with the same color scale.

Analysis / Binning	Filter diameter	$\frac{photon + mix}{readout}$	$\frac{photon + mix}{total}$	SNR_r	Theoretical resolution	Contrast
1x1	400 pixels	0.11	1.14%	2.55	113 nm	0.64
2x2	200 pixels	0.33	2.76%	4.8	113 nm	0.68
3x3	130 pixels	0.35	2.80%	7.55	113 nm	0.69

Table 3.3. Analysis results of 1x1, 2x2 and 3x3 binning ratio reconstructions, with the same low-pass filter diameter (400 non-binning pixels).

After tuning the different parameters, the best reconstruction is achieved with a filter diameter of 200 pixels on 3x3 binning diffraction pattern (Fig. 3.31 white square). The measured reconstruction contrast is 0.67 and 0.71 for horizontal and vertical directions, with $SNR_r = \sim 3$. All the components of the object is resolved, especially the three slits and the three small holes.

This example shows clearly the signal improvement by using a proper hardware binning. Higher binning ratio does not always lead to more signals extracted from noise. And, one should always remember to respect the sampling ratio of the diffraction pattern. The other

advantage of hardware binning is to reduce the long readout time when using 100kHz readout frequency.

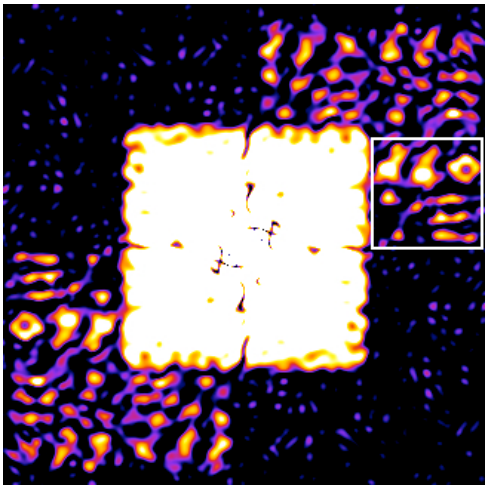

Fig. 3.31. Best reconstruction (white square) realized with a low-pass filter of 200 pixels diameter on the 3x3 binning diffraction pattern.

III.9c HERALDO reconstruction and noise: Detection stage optimization with the readout frequency

We consider now the test object A (Fig. 3.18). The diffraction patterns recorded with 1 MHz and 100 kHz readout frequencies are shown in Fig. 3.32. The two diffraction patterns have equivalent signals (~ 2 x 10^7 photons). The readout noise's standard deviation is 10 ADU and 4ADU respectively for 1 MHz and 100 kHz, with the same noise average (~ 30 ADU). Images are taken with 2x2 binning ratio and a window size of 600 x 600 pixels. Reconstructions (Fig. 3.33) are made with a low-pass filter of respectively 300, 400 and 500 pixels diameter. According to the analysis results (Table 3.4, correspond to the reconstructions in the yellow square), SNR_r is increased by a factor of ~ 1.4 for 100 kHz reconstructions, with about 2 times more *photon-limited* and *mixed-noise* pixels. The resolution (contrast) is also better with 100 kHz readout frequency. Moreover, the reconstructions associated to another reference (in green square), which is difficult to be resolved (due to bad illumination of the reference), are better reconstructed at a 100 kHz readout frequency.

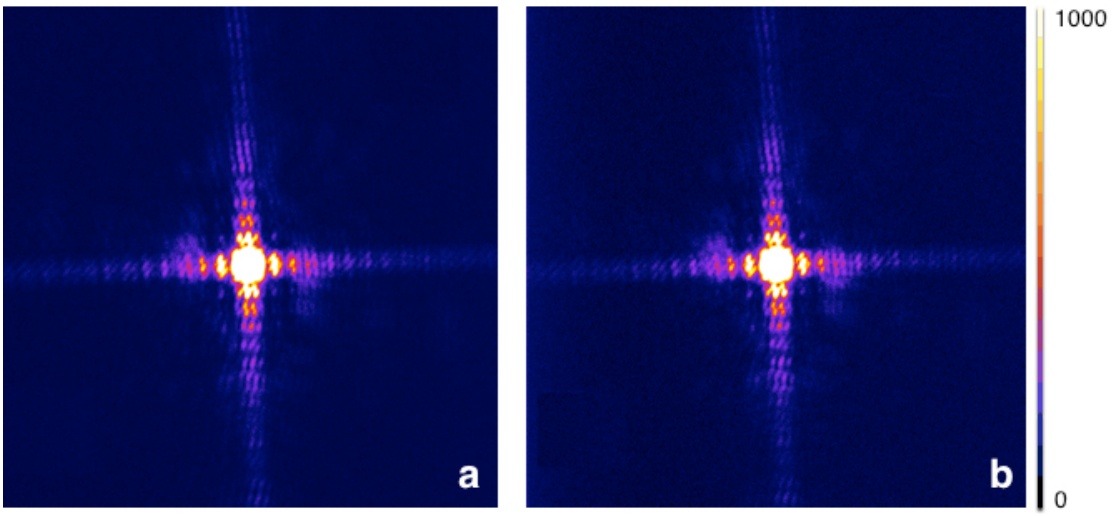

Fig. 3.32. Diffraction patterns taken with 100 kHz (a) and 1 MHz (b) on test object A.

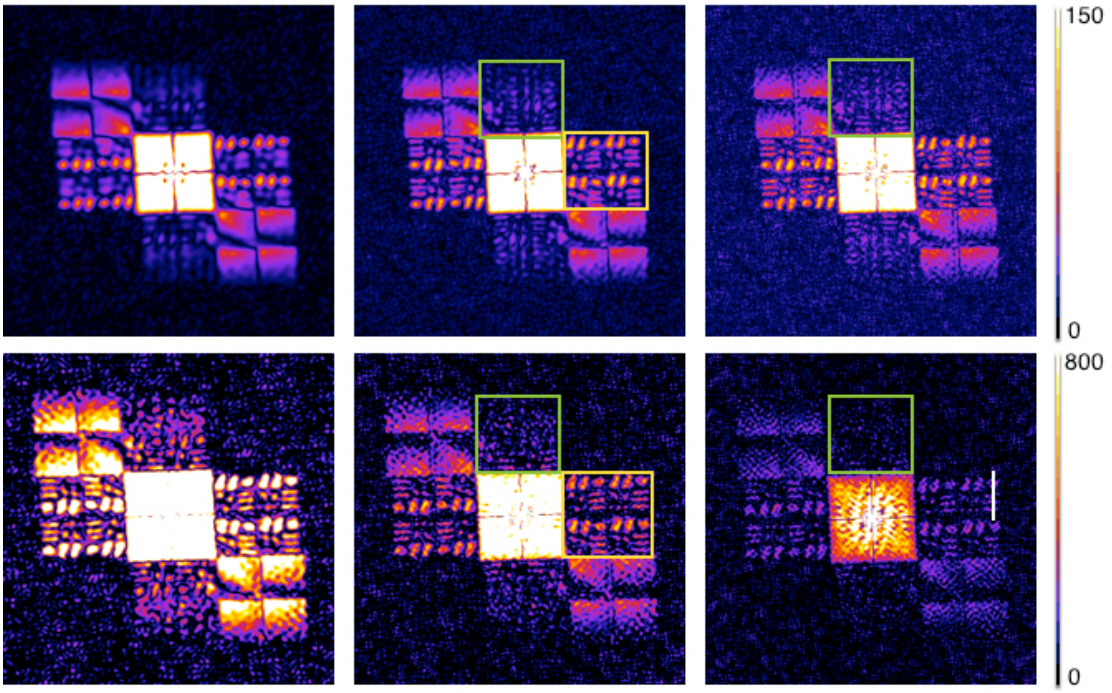

Fig. 3.33. Reconstructions of the diffraction patterns obtained at 100 kHz (first row) and 1 MHz (second row). They are made with filter diameters of 300, 400 and 500 pixels (from left to right). Green and yellow squares are associated to different square reference. The reconstruction contrast in Table 3.4 is measured at the white line position.

Analysis / Frequency	Filter diameter	$\frac{photon + mix}{readout}$	$\frac{photon + mix}{total}$	SNR_r	Theoretical resolution	Contrast
1 MHz	300 pixels	0.36	6.73%	3.83	75 nm	0.66
100 kHz	300 pixels	0.91	11.42%	5.1	75 nm	0.65
1 MHz	400 pixels	0.19	7.24%	2.24	56 nm	0.71
100 kHz	400 pixels	0.47	13.54%	3.33	56 nm	0.76
1 MHz	500 pixels	0.12	7.76%	1.7	45 nm	0.59
100 kHz	500 pixels	0.30	15.25%	2.45	45 nm	0.71

Table 3.4. Analysis results of the reconstructions.

III.9d HERALDO reconstruction and noise: other reference configurations

We have tested other HERALDO reference configurations. The test object E (Fig. 3.34E) is a geometric grid (1 μm x 1 μm) located in a large square (2 μm x 2 μm), which offers three independent reconstructions. The test object F (Fig. 3.34F) has the same geometric grid with two right-angled and isosceles triangles (1 μm x 1 μm), which also offers three independent reconstructions associated to their corners. Note that the reconstruction associated to the right angle is the same as the one associated to a square reference. Diffraction patterns of the test object E is taken within a window size of 1200 x 1200 pixels without binning (Fig. 3.34a) and 600 x 600 pixels with a 2x2 binning ratio (Fig. 3.34b). The measured diffractions have a 1.5 x 10^7 photons and 2.1 x 10^7 photons with and without binning, respectively. Reconstructions are made with the same low-pass filter diameter: 400 pixels for non-binning and 200 pixels for 2x2 binning. Similar to previous results, the 2x2 binning provides a better reconstruction quality. In fact, two reconstructions of the non-binning diffraction pattern are not clearly resolved and the measured contrast of the other one is only 0.48, compared to 0.5 ~ 0.63 for the three reconstructions of 2x2 binning.

The test object F is imaged with a lower flux harmonic beam than that of the object E (Fig. 3.34) The 10-shot acquisition of the object F contains about 8 x 10^7 photons. It is due to the low optimization of the harmonic generation, probably caused by the position deviation of the IR laser beam before the focusing lens. In fact, IR beam properties are influenced by its propagation in the air before the focusing lens. The beam position at the lens plane is

influenced by the room temperature, which is supposed to remain stable and cool during the experimental time. However, sometimes the strong temperature variation outside the building influences the room temperature that is tuned by air-conditioners (especially during the summer). This problem is later corrected by the laser modal filter with a servo system. The diffraction pattern is recorded within a window size of 1300 x 1300 pixels without binning. The readout noise is 9.5 ADU (standard deviation). Reconstructions from different references (blue and green square) are presented in Fig. 3.34f-g. The reconstruction quality is not comparable to the 5-shot acquisition of test object C (Fig. 3.28), probably due to a combination effect of low flux and low coherence harmonic beam generated in non-optimized conditions.

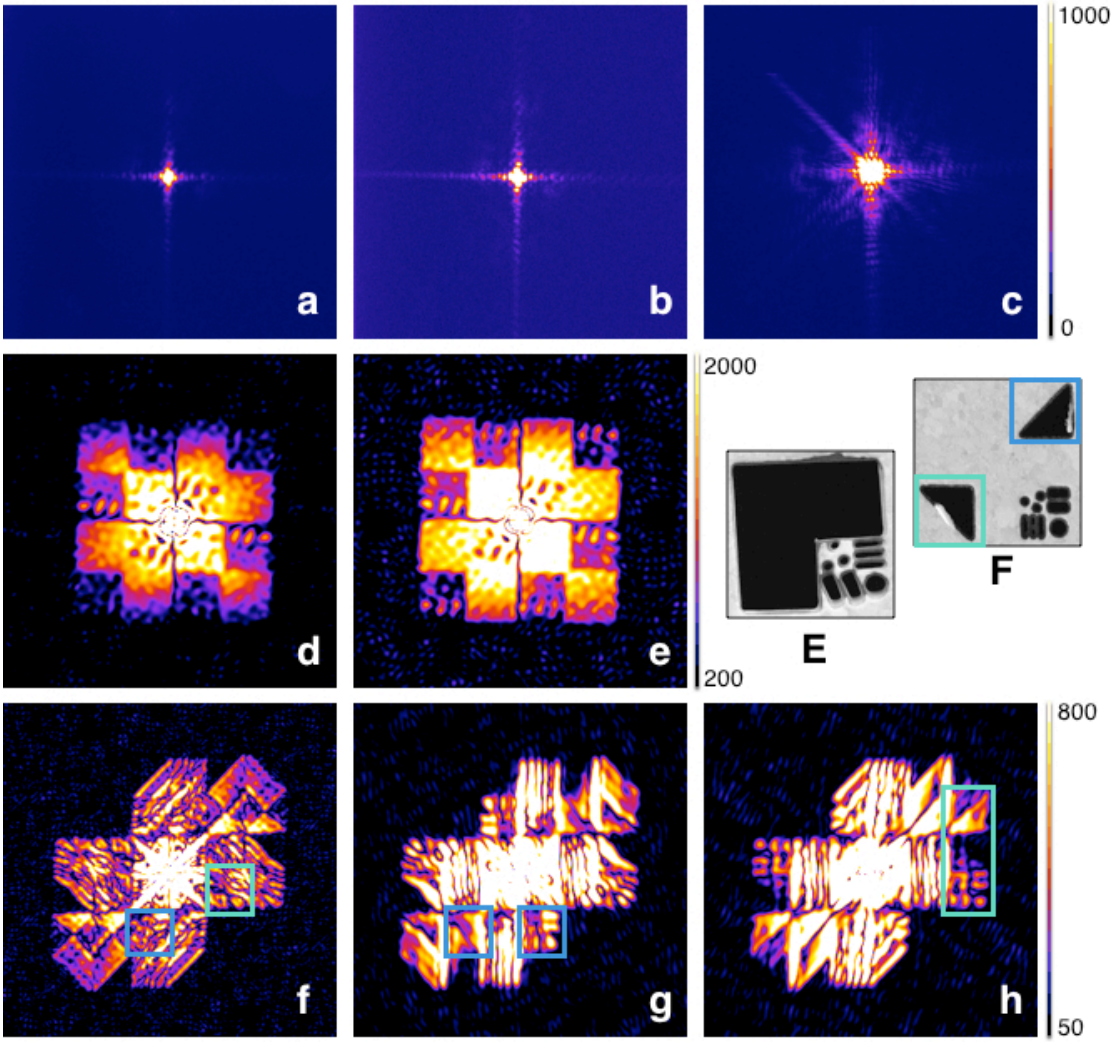

Fig. 3.34. The test object E is reconstructed from a single-shot acquisition (b). The reconstructions (e) of 2x2 binning ratio present better quality than non-binning ones (d). The test object F is reconstructed with 10-shot acquisition (c). The reconstructions in green (f,h) and blue squares (f,g) are respectively associated to the references in green and blue square in the SEM image.

III.9e HERALDO reconstruction and noise: conclusion

We have first tested HERALDO with one-dimensional reference (slit) and two-dimensional reference (square). The step-to-step reconstruction process shows that the main obstacle for our experiment is the amplified readout noise located at high spatial frequency region. The amplification is introduced by the multiplicative filter applied on the diffraction pattern in the Fourier space, which corresponds to a differential operator for the autocorrelation in object space. The amplified noise then degrades significantly the reconstructions after the invers Fourier transform. Thus, a low-pass filter in the Fourier space is required to eliminate the amplified noise. The analysis of different type pixels (*photon-limited*, *mixed-noise* and *readout-limited* pixels) presents the effectiveness of the low-pass filter with different diameter in Fourier space. In object space, the SNR_r and the contrast of the reconstruction characterize the reconstruction quality and the resolution. However, the latter is limited by the low-pass filter. Secondly, we have investigated the detection parameters (hardware binning, readout frequency, accumulation) to reduce the readout noise in the diffraction patterns. Different object-reference positions for two-dimensional references have been tested. In summary, the square reference does not provide higher reconstruction ability, compared to the slit reference. Due to the higher amplification of the readout noise by the former, the slit reference is a better choice for HERALDO technique on our harmonic beamline. However, the square or two-dimensional references are probably better for FEL facilities. Indeed, since the radiation flux and the photon energy are much higher, the diffraction pattern will be close to photon-limited. Compared to the FTH, which can also be considered as a special case of HERALDO, the latter presents higher reconstruction quality due to the signal amplification by the extended reference.

III.10 CDI reconstructions of HERALDO objects

To compare the reconstruction ability of CDI and HERALDO, we have made test objects of the geometric grid without any references. The diffraction pattern of such object (Fig. 3.35a) has much lower signal (2 ~ 4 x 10^6 photons) than HERALDO objects, which has additional signal contribution from the extended references. The diffraction surface of the CDI geometric grid (1 µm x 1 µm) is 8 times smaller than the lambda object (3 µm x 2.8 µm). It has similar surface as the Young's double slits (2 x 1.5 µm x 0.3 µm) but with more complex structures. In this case, the phase retrieval code is not able to converge.

Meanwhile, the phase retrieval code succeeds in reconstructing the HERALDO geometric grid with its references. The test object is similar to object A (the geometric grid is 1 µm x 1 µm large), but with fabrication default for the square references (the material inside the square is not completely removed) (Fig. 3.35d). It limits the HERALDO reconstruction from the corner close to it but in principle should not degrade the reconstruction by the phase retrieval code.

Fig. 3.35 presents two reconstructions (e,f) corresponding respectively to single-shot diffraction patterns containing 2.3 x 10^7 photons (b) and 1.1 x 10^7 photons (c). Diffraction patterns are taken within a window size of 2048 x 2048 pixels without binning and at a

readout frequency of 1 MHz. The difference of the reconstruction quality is due to the different signal strength. In the better reconstruction (Fig. 3.35e), the geometric grid is well resolved with a contrast equivalent to HERALDO results, and the defaults of the two references has also been reconstructed. Note that the curved edge at the left side of the square above the geometric grid is the reconstruction of the fabrication default. The little space between the non-removed material and the square edge in the SEM image is not resolved in the reconstruction. The noise in the red square of Fig. 3.35f is due to the ambiguity of the phase retrieval code. During the iterative process, the reconstructions of each iteration switched between three configurations so that the geometric grid is sometimes at right bottom, sometimes at left top and sometimes at both positions. With more diffraction signals, the code is able to go beyond this problem, as presented in the better reconstruction. Note that both CDI reconstructions use high software binning (5x5 for f and 4x4 for e) to get higher SNR (associated to the photon noise), which means that the extraction of the diffraction signal is more difficult in CDI process.

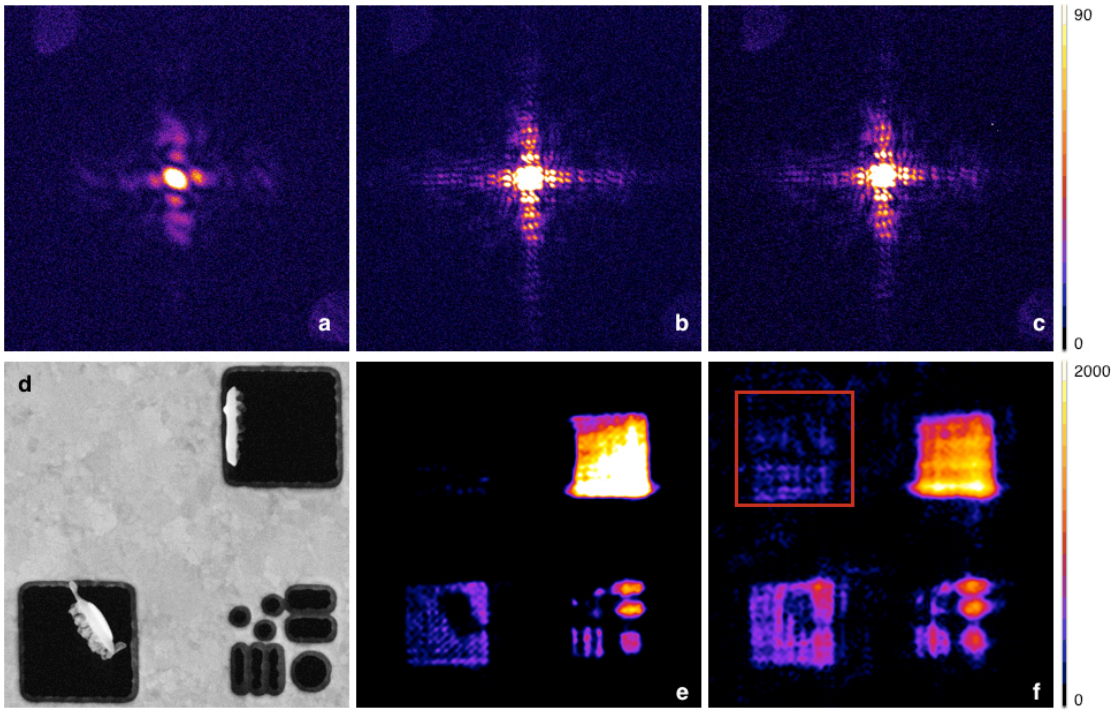

Fig. 3.35. (a) Single-shot diffraction pattern of CDI geometric grid. (b,c) Single-shot diffraction patterns of the HERALDO geometric grid. (d) SEM image of the sample. (e,f) reconstructions by phase retrieval code. The reconstruction (e) and (f) are respectively coherent averages of 37 and 50 reconstructions after 1000 iterations.

The following example is another demonstration of the CDI reconstruction of a HERALDO object. The test object (Fig. 3.36a) is "lambda" (1.3 µm x 1.8 µm) with two slits slightly larger than the lambda. The slit width is 150 nm. The single-shot diffraction pattern has ~ 1.2 x 10^7 photons, recorded within a window size of 2048 x 2048 pixels without binning. The CDI reconstruction (Fig. 3.36b) shows equivalent quality as the HERALDO reconstructions (Fig. 3.36c,d). The former is made with 4x4 software binning and the latter is made with low-pass filter of 400 pixels diameter. Note that in the CDI reconstruction, the lambda looks like a superposition of a vertical slit and itself. This is also due to the ambiguity of the phase retrieval code. Indeed, the position of the vertical slit is difficult to identify during the

iteration process, since the center part of the lambda has a similar geometry as the vertical slit. It has no problem to identify the horizontal slit because no similar structure presents in the "lambda" object. The resolution of the CDI reconstruction is estimated to be ~ 115 nm by the PRTF, which is equivalent to the HERALDO ones (10%-90% criterion). From these examples, we can conclude that extended references amplify the signals diffracted from the object that can help the convergence of the phase retrieval code. Moreover, the latter need higher SNR of the diffraction pattern to reconstruct the object than the HERALDO process. However, CDI does not require a reference, which is an advantage for certain applications.

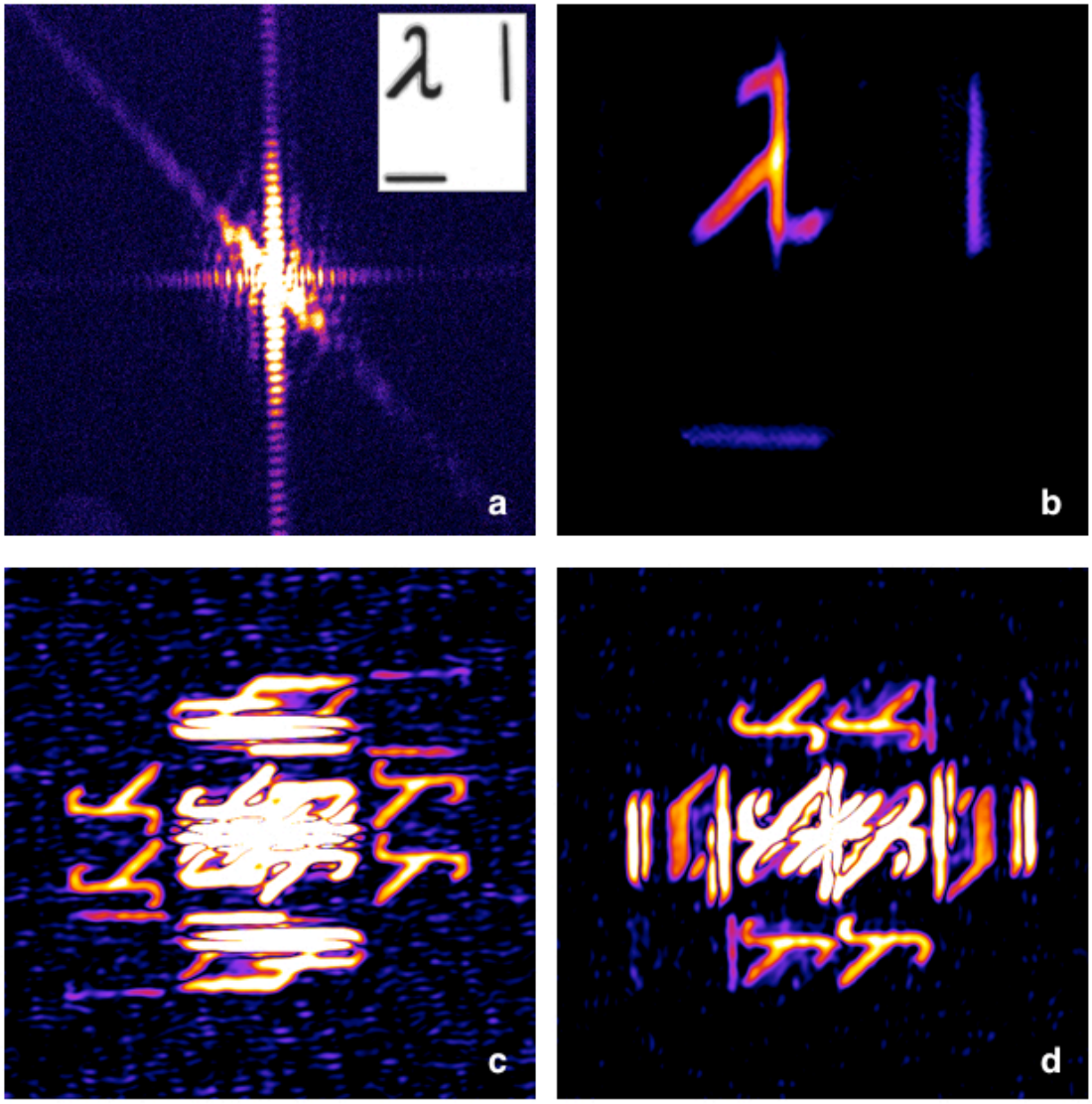

Fig. 3.36. (a) Single-shot diffraction pattern of the HERALDO object (inset). (b) CDI reconstruction result, which is the average of 50 reconstructions after 1000 iterations. (c,d) HERALDO reconstructions.

III.11 Conclusion

In this chapter, I have presented the experimental results of CDI, HERALDO and FTH techniques. In the CDI section, coherence requirement has been discussed and analyzed quantitatively using Young's double slits diagnostics. I showed that the reconstructions are not converging for a contrast of interference fringes lower than 0.5. In the second part, the HERALDO process has been investigated step-by-step. Our finding is that the readout noise is the main obstacle in our experiments. A low-pass filter is the solution for this problem, which compensate the amplification of the readout noise by the multiplicative filter. Various demonstrations show that the reconstruction quality can be improved by the optimization of the detection stage and a carefully chosen low-pass filter diameter. The comparison between FTH, one-dimensional and two-dimensional HERALDO shows that the slit reference is the best holographic configuration for our harmonic beam, according to its photon energy and photon flux properties. Finally, application of phase retrieval code on the HERALDO samples demonstrate that the extended reference amplifies the signals diffracted from the object. It also shows the higher requirement of SNR for CDI reconstruction compared to HERALDO. In conclusion, both CDI and HERALDO have their own advantage and default depending on the experimental conditions. This careful analysis presented here will guide us in choosing the best imaging technique for the imaging application of magnetic nano-domains (Chapter IV).

Paper III

Paper III reports the experimental results and the analysis of the HERALDO test object "φ". It is the first demonstration of the HERALDO using a table-top harmonic source. The spatial resolution, around 110nm, is obtained from a single ultrafast shot. The equivalent reconstruction capability compared to the CDI gives us an alternative choice for imaging applications. The biggest advantage is the non-ambiguous, fast and direct reconstruction from the measured diffraction pattern. If we use a two dimensional extended reference the resolution is, in theory, no longer limited by the reference size. Our experiment shows that the fabrication of the references can limit the quality of holographic reconstruction. Now, we have two reliable imaging configurations (CDI and HERALDO) for applications in various scientific areas.

*Published, PRL **105** 093901 (2010)*

Single-shot Femtosecond X-Ray Holography Using Extended References

D. Gauthier,[1] M. Guizar-Sicairos,[2] X. Ge,[1] W. Boutu,[1] B. Carré,[1] J. R. Fienup,[2] and H. Merdji[1,3,*]

[1]*CEA-Saclay, IRAMIS, Service des Photons, Atomes et Molécules, 91191 Gif-sur-Yvette, France*
[2]*The Institute of Optics, University of Rochester, Rochester, New York, 14627, USA*
[3]*PULSE Institut for Ultrafast Energy Science, Stanford Linear Accelerator Center, Stanford University, 2575 Sand Hill Road, Menlo Park, California 94025, USA*

(Received 4 February 2010; revised manuscript received 15 July 2010; published 24 August 2010)

In the context of x-ray lensless imaging, we present a recent approach for Fourier transform holography based on the use of extended references. Major advances shown here rely on a high signal efficiency and on the direct image reconstruction of the object performed by a simple linear derivative. Moreover, the extended holographic reference is easy to manufacture and can be applied to a variety of imaging experiments. Here we demonstrate single-shot imaging with a table-top, laser-based coherent soft x-ray source. A spatial resolution of 110 nm was obtained with an integration time of 20 fs.

DOI: 10.1103/PhysRevLett.105.093901 PACS numbers: 42.40.−i, 42.30.Wb, 87.59.−e

Lensless imaging using coherent x rays has demonstrated great potential in recent years especially with new ultrafast coherent x-ray sources, the free electron laser (FEL) [1–4], and high harmonics generation (HHG) [5–7]. This technique has attracted much attention due to its application in ultrafast nanoscale imaging. Indeed, these bright flashes of x-ray light can capture snapshots of dynamical processes even in dense matter and at a mesoscopic scale [4]. In this context, various lensless coherent imaging schemes have been explored using x rays, including, for example, coherent diffractive imaging [8], keyhole diffractive imaging [9], and Fourier transform holography [10–12].

Imaging without image forming optics is based on the measurement of the intensity diffracted from an object illuminated by a coherent x-ray beam. In this technique the two-dimensional complex-valued object transmissivity can be retrieved from the measured far-field scattered amplitude using either iterative phase retrieval or direct holographic techniques. For Fourier transform holography (FTH) a point source in the vicinity of the object generates a reference wave that interferes with the object's scattered wave at the detector plane [10–13]. Thus, the phase and amplitude information of the object are encoded in the intensity of the holographic diffraction pattern, the hologram.

One advantage of FTH is that the complex-valued image is retrieved in a noniterative and unambiguous fashion with a simple reconstruction algorithm, namely, an inverse Fourier transform of the hologram. This is a valuable alternative to computationally intensive iterative algorithms which attempt to solve the phase retrieval problem of reconstructing an image from coherent diffractive imaging (CDI) data [8,14]. The possibility of reliably retrieving a closed-form, unique solution makes holography an attractive lensless configuration and holds potential in the recent context of ultrafast single-shot imaging using an x-ray free electron laser or a table-top high harmonic source.

In the x-ray regime, various schemes have been proposed to go beyond the limitations imposed in standard holography, as, for example, the use of complicated references [15], large references [16], or multiples references [17]. More recently a holographic scheme based on a uniformly redundant array of references was successfully demonstrated at the Hamburg FLASH soft x-ray free electron laser [18]. Although this scheme increases the signal to noise ratio (SNR) of the reconstruction, the direct inversion of the hologram relies on quantitative knowledge of this reference structure. The latter is significantly affected by the difficult manufacturing process. Such an approach is also difficult to scale down to fine resolution accessible at hard x-ray wavelengths where a reference and a reconstruction procedure robust to manufacturing errors should be used.

In standard FTH there is a compromise in the determination of the size of the reference point source between the two requirements: (i) the resolution given by the reference size, and, (ii) the flux through the reference for observing interference fringes with a good contrast [15,16]. The hologram fringe visibility depends on the relative amplitudes of the fields diffracted by the object and the reference, respectively, and is clearly maximum when these amplitudes are equal. The use of extended references allows increasing the fringe visibility, especially at larger scattering angles (which correspond to higher resolution) where the scattering signal may be weak. The hologram is subsequently more efficiently recorded than in standard FTH. This improves the image reconstruction with substantially enhanced quality and resolution as compared with a point source reference.

In this Letter we demonstrate single-shot femtosecond x-ray holography using a recently developed approach; holography with extended reference by autocorrelation

linear differential operation (HERALDO) [19–21]. This lensless imaging scheme preserves the deterministic reconstruction properties of FTH. The analytical uniqueness of the solution directly retrieved as a complex-valued image from the hologram. HERALDO is a more general approach to FTH, using boundary waves of more general extended objects as holographic references. The reconstruction procedure is robust and simple to implement. It is based on the application of linear differential operators to the field autocorrelation, i.e., the inverse Fourier transform of the hologram. In our setup, the extended references used around the nanoscale test object "φ" are linear slits [see Fig. 1]. The directional derivative (in the direction of the slit) is applied during the reconstruction process, which then provides two independent reconstructions of the object "φ", each associated with the slit extremities [Figs. 1 and 2]. As in FTH, each reconstruction has an associated twin image that does not provide additional information. The HERALDO image processing is indicated by the $\frac{d}{d\rightarrow}F^{-1}\{\text{hologram}\}$ symbol in Fig. 1.

The test object and the linear reference slits were patterned using a focused ion beam at a resolution of about 20 nanometers on a freestanding Si_3N_4 membrane of 225 nm thickness. A 50 nm layer of gold was deposited on the membrane so that the sample has a pure amplitude transmittance. The test object "φ" has a 2 μm $\times$ 1.7 μm overall size, with 200 nm to sub-100 nm details [Fig. 2(a)]. The horizontal and vertical reference slits have a width of, respectively, 130 and 145 nm. The two slits are slightly longer than the object dimensions, and they are etched at sufficient distance from the object to satisfy the separation conditions for a holographic reconstruction [19]. Each reference slit has a scattering area of about $\sim$0.3 μm^2 which is about 1/3 that of the object.

For the experiment, the sample was illuminated with the 25th harmonic ($\lambda = 32$ nm) of the table-top infrared femtosecond laser LUCA (Laser Ultra Court Accordable) at the CEA-Saclay research center, France. The source delivers up to 4×10^{10} photons (0.25 μJ) per pulse, within a spectral bandwidth $\lambda/\Delta\lambda = 150$ and $\sim$20 fs pulse duration [5]. The soft x-ray beam transport and focalization has been optimized using an x-ray wave front sensor [22]. Typically, 2×10^9 photons hit the sample within a focal spot of 5 μm in diameter, corresponding to an intensity of $\sim 10^{11}$ W/cm^2. The transverse and longitudinal coherence lengths at the sample are $\sim$10 μm and $\sim$5 μm, respectively. These are well within the requirements for holography.

We measured the far-field diffraction pattern of the sample exit wave, the hologram, using an x-ray CCD camera [Fig. 1] placed at a distance $z = 20$ mm from the sample. The full CCD chip contains 2048 $\times$ 2048 square pixels with a size $p = 13.5$ μm. The number of incident

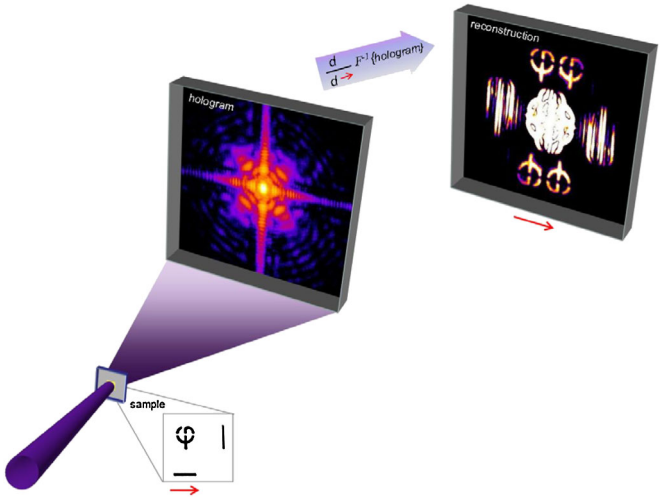

FIG. 1 (color online). Schematic view of the HERALDO experimental setup. Hologram acquisition from sample ("φ" object + reference slits) scattering using a soft x-ray coherent high harmonic beam at 32 nm wavelength. The reconstruction is straightforwardly obtained by computing the directional derivative along the reference slit direction (red arrow) of the inverse Fourier transform of the hologram (i.e., the autocorrelation of the sample transmission). The reconstruction process is symbolized by the operator $\frac{d}{d\rightarrow}F^{-1}\{\text{hologram}\}$.

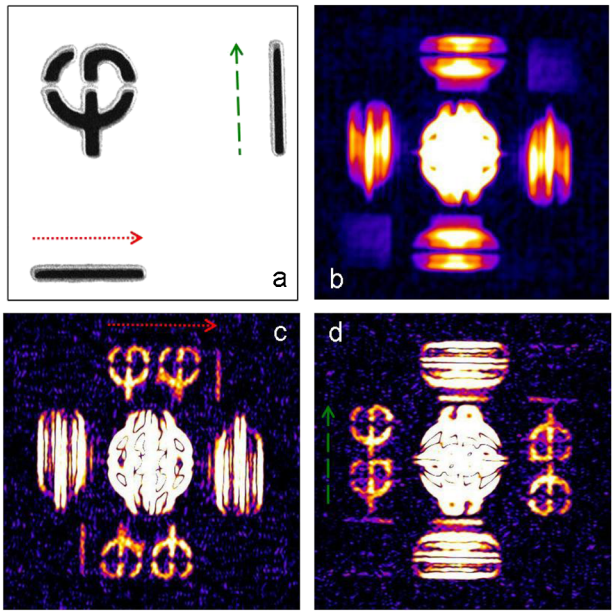

FIG. 2 (color online). Image reconstruction. (a) Scanning electron micrograph (SEM) of the sample showing the "φ" test object and the two references slits (2.1 μm slit length). (b) Field autocorrelation given by the inverse Fourier transform of the hologram. The four cross-correlations of the "φ" object with the references surrounds the central part, as well as the cross-correlation of the two references slits. (c),(d) Numerical derivatives of the field autocorrelation along the two slit directions (indicated by red dotted and green dashed arrows) which lead to the reconstruction of the "φ" object. We obtain two independent images from each extremity of the slit references.

photons diffracted by the sample and detected by the CCD (quantum efficiency of 40% at 32 nm) is about $\sim 2 \times 10^7$ in single shot.

A typical measured hologram is shown in Fig. 3(d). We clearly see the scattering from the two reference slits in the vertical and horizontal axes of the hologram which shows coherent interference with the field scattered from the object. The field autocorrelation [see Fig. 2(b)] is computed from the single-shot hologram through an inverse Fourier transform. The image reconstructions shown in Figs. 2(c) and 2(d) are obtained by computing the derivatives of the field autocorrelation. The design with 2 slits, respectively, horizontal and vertical, provides 4 independent reconstructions, one for each slit extremity, and 4 twin images. Notice that, next to the reconstructed object, each slit end reconstructs also the other reference slit.

From Figs. 2(c) and 2(d) and the field autocorrelation, we get insight into the x-ray intensity distribution on the sample. In particular, the 4 independent reconstructions of the object and the reference exhibit different contrasts, higher for derivation along the horizontal than the vertical slit. Moreover, the references are better illuminated on their inner part (e.g., right side of horizontal slit).

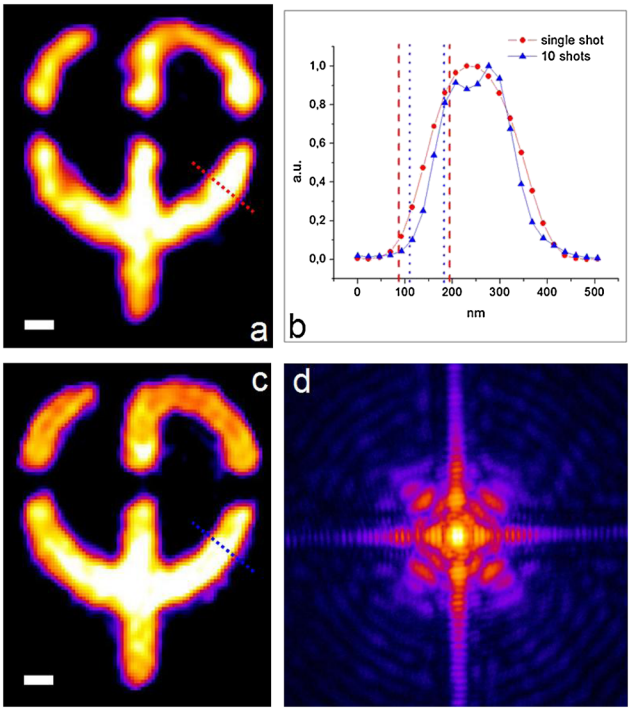

FIG. 3 (color online). Modulus of the final reconstructed image obtained by averaging the 4 independent reconstructions of (a) single shot and (c) 10 shots acquisition. The scale bar is 200 nm and pixel size is 23 nm. (b) Plot profile of the single shot (red line) and 10 shots (blue line) results showing, respectively, a resolution of 105 and 74 nm. (d) Measured hologram of the 10 shots acquisition displayed in logarithmic scale on a 720×720 pixels square which corresponds to 7.63 μm^{-1} maximum spatial frequency.

This inhomogeneous contrast is attributed to the slightly different patterns (slightly different widths) of the two slits, and a decreasing x-ray intensity from the center to the sample periphery. The object however is uniformly illuminated.

In the reconstruction process the hologram was first filtered to select the spatial frequencies with sufficient SNR. A polynomial product was then applied in the Fourier domain [19,20]. This operation, equivalent to a directional derivative in the object space, facilitates differentiation at arbitrary angles. The image quality was improved by subpixel registration [23] and by averaging of the 4 individual complex-valued reconstructions to increase the SNR [17]. Care was also taken to match a global phase between the reconstructions to maximize the signal constructive interference. The final high quality reconstructed image is shown in Fig. 3(a). Using a 10% to 90% edge transition criterion on different edges of the object [see Fig. 3(b) for a typical plot profile], we determined a spatial resolution of 110 nm ($\sim 3.4\lambda$) for the single-shot image. This is in good agreement with the SNR limitation of our measurement at the high scattering angles. The equivalent half period resolution of 110 nm corresponds to a maximum spatial frequency of 4.55 μm^{-1} in the hologram (i.e. a half scattering angle of 144 mrad) above which the scattered signal cannot be extracted due to the noise.

We have performed multishot reconstruction [Fig. 3(c)] by accumulation of 10 shots of 20 fs duration each (the x-ray CCD camera exposure was set to half a second) [see recorded data on Fig. 3(d)]. This was possible because the single-shot exposure is below the damage threshold of the sample. We have estimated, with the multishot reconstruction, the resolution limit given by the manufacturing of the feature size of the reference structures. Using the same resolution criteria as the single-shot we obtained a resolution of 80 nm for the multishot reconstruction [Fig. 3(c)]. Note that the holographic fringes are well resolved and that the scattered signal is observed at a spatial frequency up to 7.63 μm^{-1}. This is above the spatial frequency of 6.25 μm^{-1} (equivalent to 80 nm resolution in the object plane). Practically, the manufacture resolution limit can be estimated by calculating the point spread function (PSF) of the reconstruction using the derivative of the scanning electron micrograph (SEM) image of the slit. This gives us an equivalent resolution limit of 80 nm that is the limit imposed by our HERALDO reference design. We conclude that the resolution for 10 shots acquisition is limited by the slit width designed for the single-shot experiment. But this setup is versatile so that, beyond this experimental demonstration, the width of the reference slit can be easily adjusted to various experimental requirements.

This work enables an efficient future use of holography to capture snapshots of ultrafast phenomena at a nanometer scale using harder x rays. This technique goes beyond the

limitation imposed by conventional Fourier transform holography, in particular, because of the high signal contribution of the reference and effective noise filtering (especially for Poisson limited data) from the reconstruction procedure. The potential for this technique for higher resolution lies in its ability to be scaled down to shorter wavelength. Higher resolution can be obtained by using crystal edges, carbon nanotubes, or metallic nanowires as references to image viruses, cells or nanostructures. For these configurations having a method that is robust against reference defects and nonuniform illumination will be crucial. Our results show that HERALDO has the required robustness and gives good quality reconstructions under significantly inhomogeneous reference illumination and defects. Moreover, the combination of HERALDO with the design of a very large scattering reference [19] could be appropriately used to image weak scatterers such as biomolecules [24,25]. The single-shot demonstration of HERALDO using a soft x-ray femtosecond source also opens other possibilities. First, our femtosecond x-ray flash can take a snapshot of the object before radiation damage occurs. Second, dynamical imaging of nonreproducible ultrafast phenomena at the nanoscale can be performed. The noniterative and unambiguous image reconstruction process makes HERALDO robust to capture space and time amplitude and phase variations associated to complex physical or biological processes. Investigation of ultrafast phase transitions in mesoscopic systems, ultrafast spin reversals of magnetic nanodomains, or large molecule rearrangements in biological environments are some examples of accessible dynamics. Shorter HHG wavelength down to the water window and magnetic L edges can be used for such applications [26–28].

We acknowledge financial support from the EU-LASERLAB (RII3-CT-2003-506350) programs, from French ministry of research though the 2009 ANR grants ''I-NanoX'' and ''Femto-X-Mag'', from the ''Triangle de la Physique'' through the COX grant and the C'NANO research program though the X-NANO grant and also support from the U.S. Department of Energy through the Stanford PULSE Center. We acknowledge Marc Billon, Cédric Baumier, Mike Bogan, Phil Bucksbaum, Franck Fortuna, Julien Gautier, D. Garzella, O. Gobert, J.-F. Hergott, Xiaochi Liu, Jan Lüning, Stefano Marchesini, Alessandra Ravasio, and Philippe Zeitoun for grateful discussion and support.

*hamed.merdji@cea.fr

[1] H. Chapman *et al.*, Nature Phys. **2**, 839 (2006).
[2] H. Chapman *et al.*, Nature (London) **448**, 676 (2007).
[3] A. P. Mancuso *et al.*, New J. Phys. **12**, 035003 (2010).
[4] A. Barty *et al.*, Nat. Photon. **2**, 415 (2008).
[5] A. Ravasio *et al.*, Phys. Rev. Lett. **103**, 028104 (2009).
[6] R. L. Sandberg *et al.*, Opt. Lett. **34**, 1618 (2009).
[7] J. Schwenke *et al.*, J. Mod. Opt. **55**, 2723 (2008).
[8] J. Miao, P. Charalambous, J. Kirz, and D. Sayre, Nature (London) **400**, 342 (1999).
[9] B. Abbey *et al.*, Nature Phys. **4**, 394 (2008).
[10] I. McNulty *et al.*, Science **256**, 1009 (1992).
[11] S. Eisebitt *et al.*, Nature (London) **432**, 885 (2004).
[12] A. S. Morlens *et al.*, Opt. Lett. **31**, 3095 (2006).
[13] G. W. Stroke, *Introduction to Coherent Optics and Holography* (Academic Press, New York, 1969).
[14] J. R. Fienup, Appl. Opt. **21**, 2758 (1982).
[15] A. Szoke, J. Imaging Sci. Technol. **41**, 332 (1997).
[16] H. He *et al.*, Appl. Phys. Lett. **85**, 2454 (2004).
[17] W. F. Schlotter *et al.*, Appl. Phys. Lett. **89**, 163112 (2006).
[18] S. Marchesini *et al.*, Nat. Photon. **2**, 560 (2008).
[19] M. Guizar Sicairos and J. R. Fienup, Opt. Express **15**, 17592 (2007).
[20] M. Guizar Sicairos and J. R. Fienup, Opt. Lett. **33**, 2668 (2008).
[21] S. G. Podorov, K. M. Pavlov, and D. M. Paganin, Opt. Express **15**, 9954 (2007).
[22] J. Gautier *et al.*, Eur. Phys. J. D **48**, 459 (2008).
[23] M. Guizar-Sicairos *et al.*, Opt. Lett. **33**, 156 (2008).
[24] S. Boutet *et al.*, J. Electron Spectrosc. Relat. Phenom. **166–167**, 65 (2008).
[25] T. Shintake, Phys. Rev. E **78**, 041906 (2008).
[26] J. Seres *et al.*, Nature (London) **433**, 596 (2005).
[27] J. Seres *et al.*, Nature Phys. **6**, 455 (2010).
[28] P. Arpin *et al.*, Phys. Rev. Lett. **103**, 143901 (2009).

Paper IV

Abstract

We have recently demonstrated single-shot femtosecond x-ray holography of 110 nm spatial resolution [1], using a recently developed approach: Holography with extended reference by autocorrelation linear differential operation (HERALDO) [2,3]. This lens-less imaging technique is a more general approach to the Fourier transform holography (FTH), which provides fast, direct and non-ambiguous reconstructions. One of the major advantages is that the reconstruction resolution is no longer limited by reference size as in FTH. Moreover, HERALDO leads to higher signal efficiency than the classical coherent diffractive imaging (CDI) and the FTH due to the signal amplification using extended references. For all the lens-less imaging techniques, the signal-to-noise ratio (SNR) is one of the main issue for reconstruction quality. Due to the noise-amplification by the linear differential operator of HERALDO, the SNR has significant influences on the reconstructions of diffraction patterns that are readout noise limited, such as single-shot acquisitions on harmonic beamline. Here, we demonstrate the step-by-step analysis of the HERALDO reconstruction process, regarding the SNR, the different noises and different configurations of the extended references. With the comparison between the various configurations of FTH and HERALDO, we conclude that the one-dimensional slit reference is the optimized configuration for readout noise limited experiments.

[1] D. Gauthier *et al.*, *Phys. Rev.Lett.* **105** 093901 (2010)
[2] M. Guizar Sicairos and J. R. Fienup, *Opt. Express* **15** 17592 (2007)
[3] M. Guizar Sicairos and J. R. Fienup, *Opt. Lett.* **33** 2668 (2008)

Note

This article is in preparation. The experimental results, analysis and discussions, which will be presented in this article, are included in the holographic techniques section of Chapter III.

Chapter IV
Application: Magnetic dynamics

IV.1 Introduction

The demonstrations of coherent diffraction imaging techniques (CDI and HERALDO) on simple test objects in the previous chapter have shown robust image reconstruction quality and the potential of resolving concrete problems in various scientific areas from physics to biology. The optimization and standardization of the high flux harmonic beamline (Chapter II) provide a reliable high soft X-ray flux with a stable beam quality (intensity, pulse duration, spatial profile, beam position, etc.) from shot to shot, all combined with a natural synchronization with the IR pump laser. The HHG beamline competes well with FEL facilities, which suffer from synchronization jitter and instabilities of the beam quality. We present here the first imaging application of our harmonic beamline: the study of demagnetization dynamics of ferromagnetic materials with magnetic nanodomains structure.

The first demonstration of imaging magnetic nanodomain structure using coherent X-rays has been achieved by S. Eisebitt and coworkers at the synchrotron facility in DESY, Germany [1]. In their work (see Fig. 4.1a), the random (or labyrinthine) magnetic structure was reconstructed by FTH technique (see Chapter III, section…) using a soft X-ray beam at 778 eV photon energy (wavelength = 1.59 nm), which corresponds to the L_3 absorption edge of Co (Cobalt). Due to the magnetic resonance at this edge, the optical index is a natural contrast between spin up and down regions. The small angle scattering of the magnetic structure [2,3,4] forms a hologram (diffraction pattern) of a broad ring composed of individual speckles. The reconstruction (Fig. 4.1b) was obtained from accumulated diffraction patterns of a total exposure time of 500 seconds, having a good agreement with the scanning transmission X-ray microscopy (STXM) image. The spatial resolution is estimated to be 50 nm, which is limited by the size of the pinhole reference. The authors expected a single-shot imaging of such nano-magnetic structure with upcoming XFEL facilities, which "will open the door for taking ultrafast movies of processes on the nanometer length scale".

This fascinating foreseen future of dynamic studies of nano-magnetism can lead to knowledge explosion on fundamental physical phenomena (such as spin dynamics and transport in such materials) and great technology progress for creating new social benefits (Fig. 4.2).

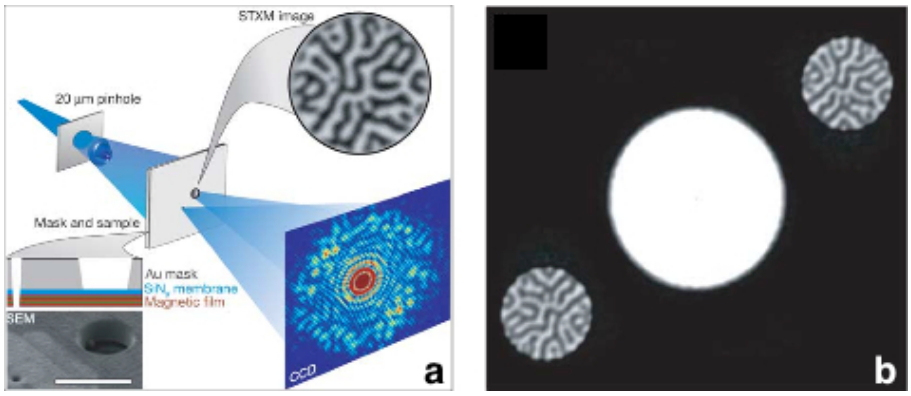

Fig. 4.1. (a) Scheme of the S. Eisebitt *et al.* experiment setup. The circularly polarized X-ray beam was firstly filtered by a pinhole to have sufficient spatial coherence. The light then illuminates the Co/Pt multilayer film and a pinhole reference. The diffraction pattern (hologram) was detected by the CCD camera located in far field. The STXM image of the magnetic sample is shown here. (b) The holographic reconstruction of the hologram. Pictures are extracted from Ref. 1.

Fig. 4.2. Grand challenges in nano-magnetism related to various issues from new materials to computer technology, which can lead to economy boost and military technology enhancement. Picture extracted from Ref. 5.

The nano-magnetism is a new emerging area, specific to magnetic structures having dimensions in the submicron range. This new era of research in magnetism, which is one of the oldest scientific domains, deals with the behavior of the spin-orbit (SO) interaction and exchange (EX) coupling occurring on femtosecond time scale (Fig. 4.3). This is much faster than the magnetic field. The study and controlling of such phenomena is thus not possible by traditional method (magnetic field). Since the first demonstration of demagnetization of a ferromagnetic Nickel film on a sub-picosecond time scale by a 60 fs laser pulse [6], manipulation and controlling of magnetization by ultrafast laser pulses has become a hot research topic. In 2007, C. Stanciu *et al.* have demonstrated the all-optical magnetization

reversal on a GdFeCo magnetic alloy sample by a single 40 fs laser pulse [7]. This opens up new routes in data storage or ultrafast information processing. While the progress made in time scale, the spatial resolution is still limited by the wavelength of the probing radiation with such visible-wavelength ultrafast laser. X-ray beams provided by synchrotron facilities are able to resolve nanometric spatial resolution, but suffered from relative poor time resolution (except slicing method which has the drawback of a very low photon number). Moreover a high number of X-ray probe photons is required to perform single-shot studies. The combination of the time and spatial resolution and high coherent photon flux can be achieved on powerful FEL facilities. Recently, nondestructive magnetic resonant scattering using single FEL pulse has been reported by C. Gutt *et al.* in 2010 [9]. The probing pulse intensity threshold has been investigated on Co/Pt multilayer samples on magnetic nanodomain structure.

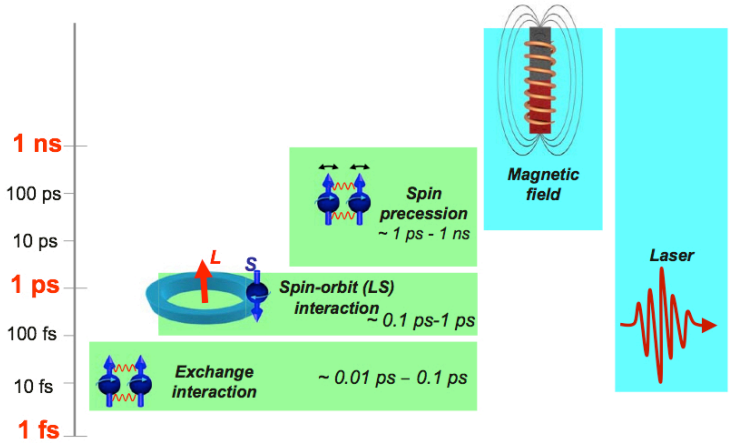

Fig. 4.3. Time scale of the magnetic phenomena, compared to magnetic field and ultrafast laser pulses. Picture extracted from Ref. 10.

In 2009, C. La-O-Vorakiat *et al.* have demonstrated the first demagnetization study of a magnetic Permalloy grating using a table top HHG source [8]. However the signal had to be accumulated over thousands of shots preventing the observation of non-reversible processes. Single-shot probe is required to answer intriguing non-reversible phenomena in magnetism. Using our high flux harmonic beamline, we expect visualizing in a single flash the magnetic dynamic of the nanodomain structure with a high spatial resolution on a femtosecond time scale. In this context, three laboratories came together to take the fascinating challenge: the research group of J. Luning at Laboratoire de Chimie Physique-Matière et Rayonnement (LCPMR, Paris, France) is in charge of the magnetic sample fabrication and provide theoretical support of magnetism; the group of P. Zeitoun at Laboratoire d'Optique Appliquée (LOA, Palaiseau, France) is focusing on reversible phenomena studies using their high repetition but low flux harmonic source; and our research group aims on the single-shot magnetic resonant scattering for studying irreversible phenomena taking the benefits of our high flux harmonic beamline. This FEMTO-X-MAG project has been financially supported by the Agence Nationale de la Recherche (ANR, France).

IV.2 Magnetic samples

The first step in this project is to fabricate the magnetic samples. Since we aim at single-shot imaging of nanodomain structure, high flux harmonic beam is required. The L_3 absorption edge of cobalt (778 eV) where magnetic contrast (about 50%) between spin up and spin down magnetic domains is not accessible with our harmonic beamline. Here we chose to probe the sample at the cobalt $M_{2,3}$ absorption edge at 60eV. This photon energy can be easily reached with a significant flux using HHG in Argon or Neon gas (see following section).

The magnetic samples are [Co/Pd] multilayers fabricated by magnetron sputtering technique [11] on a thin silicon nitride membrane. The ratio between Co and Pd and the total layer number are variable in order to study different combinations on our harmonic beamline (section IV.4c). The magnetic nanodomains structure presented on these samples can be prepared in two different configurations: labyrinthine or well-aligned stripes (Fig. 4.4), depending on the fabrication procedure. The black and white parts of the MFM images present nanodomains of opposite magnetic directions (spin up and down), which are normal to the film surface. The typical nanodomain width can vary from several tens of nanometers to about 100 nm depending on the material composition. We can adapt the sample size for different experiment geometry. For example, sample from 250 x 250 μm^2 down to 50 x 50 μm^2 size have been tested during our experiments. Since the sample fabrication is reproducible, we can prepare numerous samples of same kind for irreversible studies. Note that samples can be easily demagnetized when approaching magnetic fields, such as magnet and hard disk. In addition, the oxidation of the materials can lead to sample's deterioration. Therefore, the transportation and conservation of such samples should be carefully treated and keep in vacuum condition as far as possible.

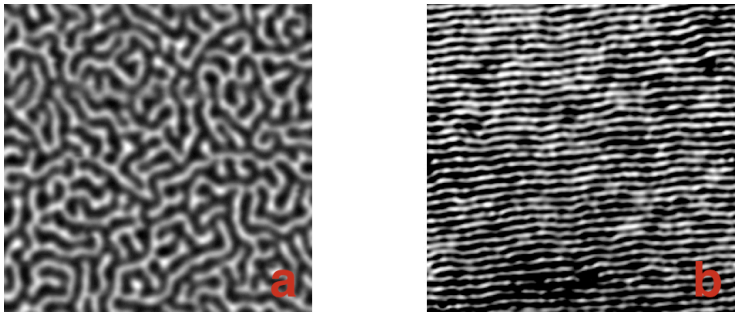

Fig. 4.4. Magnetic Force Microscopy (MFM, [12]) images of Co/Pd samples. The magnetic nanodomain structure can be prepared as labyrinthine (a) or well-aligned stripes (b) using an in-plane demagnetization procedure [23, 24].

The origin of the resonant magnetic scattering is based on the interactions (SO and EX) occurring between the core levels and the valence bands [14]. As a consequence, the optical index ($n_{\pm}$) of the two nanodomains (with up and down magnetization directions) around the absorption edges of such materials are different, which can be described as:

$$n_{\pm} = 1 - (\beta \pm \Delta\beta) + i(\delta \pm \Delta\delta) \qquad \text{(Eq. 4-1)}$$

where $\Delta\beta$ and $\Delta\delta$ represent respectively the real (dispersion term) and imaginary (absorption term) parts of the optical index difference between spin up and down nanodomains. Note that this technique is element-specific due its mechanism. The referential values of $\Delta\beta$ and $\Delta\delta$ for $M_{2,3}$ edge of Cobalt are extracted from the Ref. 13 and drawn below (Fig. 4.5). It gives us a first insight of the target material and helps us for the experimental design.

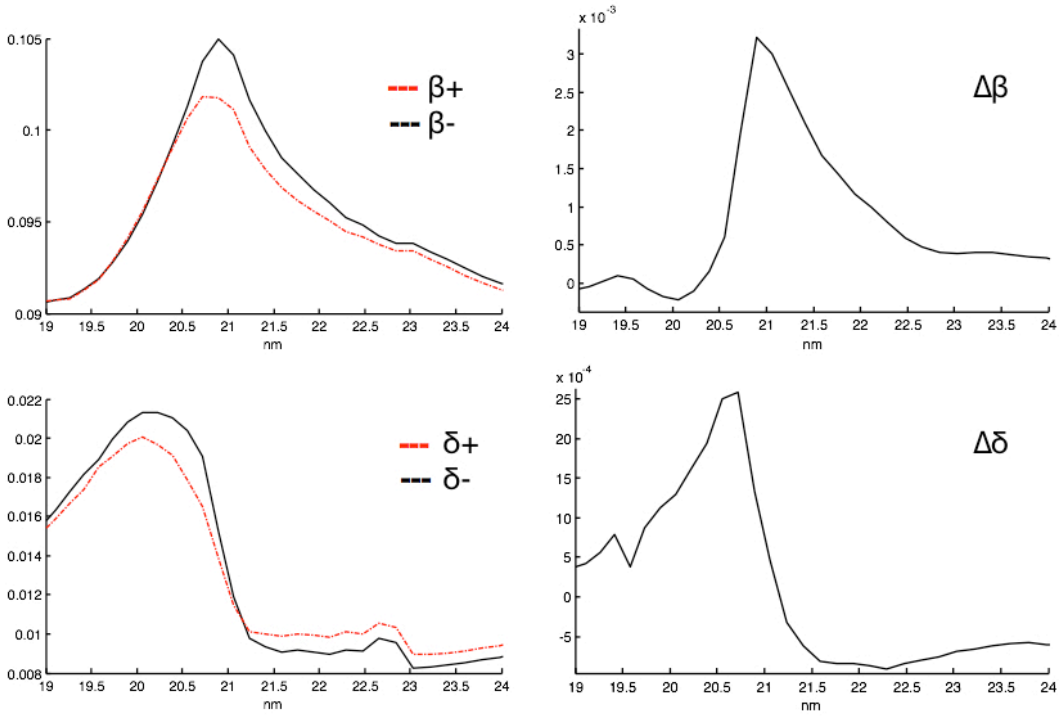

Fig. 4.5. The left column curves present the β and δ evolutions around $M_{2,3}$ edge of Cobalt for the two kinds of nanodomains. The right column curves are the subtraction results $\Delta\beta$ and $\Delta\delta$ (i.e. the optical index difference).

In the diffraction configuration of the High flux harmonic beamline, only one harmonic order can be reflected by the multiplayer coating of the parabola, and changing the harmonic order involves making a new parabola coating. Therefore, we have to select the best harmonic order for the single-shot imaging, which means having the strongest scattering signal. For this purpose, we have first accomplished spectrum studies of HHG in different configurations, and secondly magnetic scattering studies within a large spectral bandwidth (about 20 eV). In fig. 4.6, I have plotted the evolution of the term $(\Delta\beta^2 + \Delta\delta^2)$ that reflects the scattering efficiency of our sample. We observe that the 37th (57.35 eV) and 39th (60.45 eV) harmonics are close to the resonant peak of the cobalt's M edge. The 35th (54.24 eV) and 41^{rst} (63.55 eV) harmonics are already sitting on the sides of the peak and will have a low scattering efficiency.

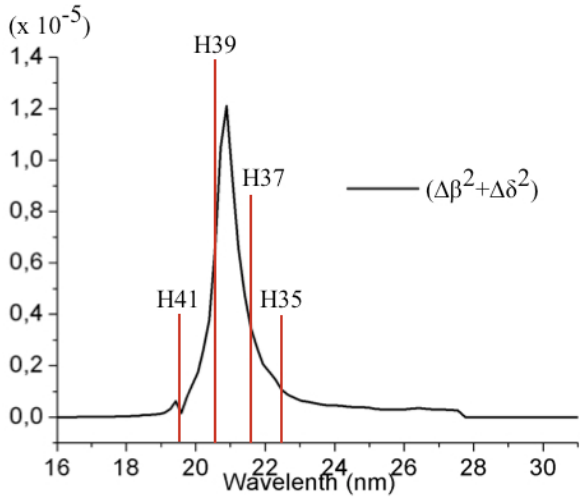

Fig. 4.6. Possible harmonic candidates for single-shot imaging of our Co/Pd samples. The black curve is the evolution of the term $(\Delta\beta^2 + \Delta\delta^2)$, which presents a peak around 60 eV at the $M_{2,3}$ edge of Cobalt. The closest harmonic orders to this peak are H37 and H39.

IV.3 HHG spectrum studies

The experimental setup for HHG spectrum studies is presented in Fig. 4.7. The optics chamber is switched to the "spectrum configuration" with a set of toroidal mirror (focal length of 0.75 m) and a plane grating. A movable photomultiplier tube (PMT) located at 1.5 m from the Toroidal mirror detects the harmonic signals going through a thin slit. With the motorized rotation of the plane grating, we are able to record HHG spectra. When the photomultiplier tube is moved out, the XUV CCD camera located at 3.5 m from the toroidal mirror can detect the spatial profile of the harmonic pulses in far field. Al filters (150 nm thickness) are located at different positions in the beam path to cut the residual infrared light and reduce the harmonic beam intensity if necessary.

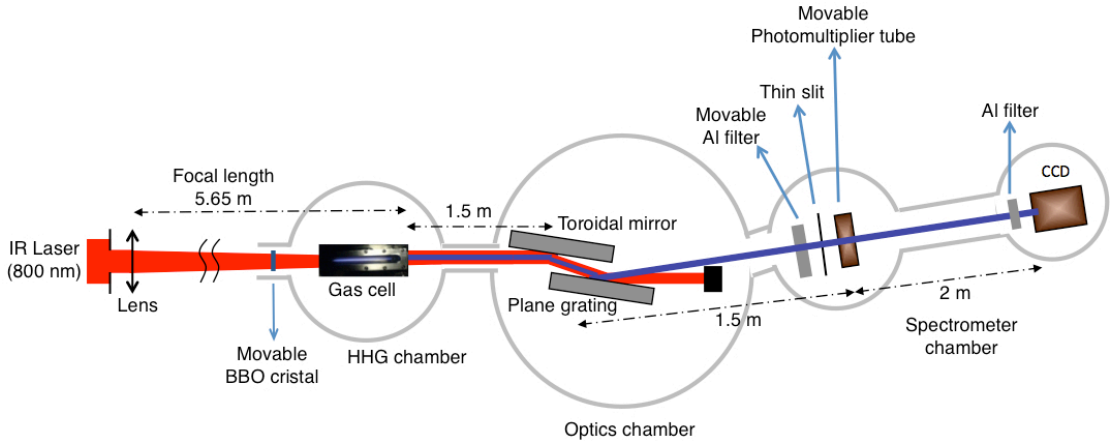

Fig. 4.7. Experimental setup for HHG spectrum studies. HHG Spectrum and harmonic beam spatial profile can be measured respectively by the photomultiplier tube and the XUV CCD camera.

We first investigate the HHG in Argon gas for H37 and H39. We started with the optimum generation condition for H25 (Chapter II, section II.3) with the laser modal filtering. The PMT recorded the harmonics spectra by rotating the plane mirror to have a scan over a large spectral range from H49 (76 eV) to H13 (20.15 eV). Note that the Al filter transmission has a brief cut-off at around 17 nm (corresponding to H47) and a "plateau" from 17 nm to 40 nm (see Fig. 4.8). For an Al filter of 150 nm thick, the variation of its transmission from H45 to H35 is smaller than 5%. Considering the oxidation of the Al filter, the transmission of Al_2O_3 layer also has small variations (less than 10%) for the same spectral range. Thus we can neglect the influence of the Al filter during spectrum studies. The following spectra presented in this section are either taken with one Al filter or none, which will be specified in the figures' captions.

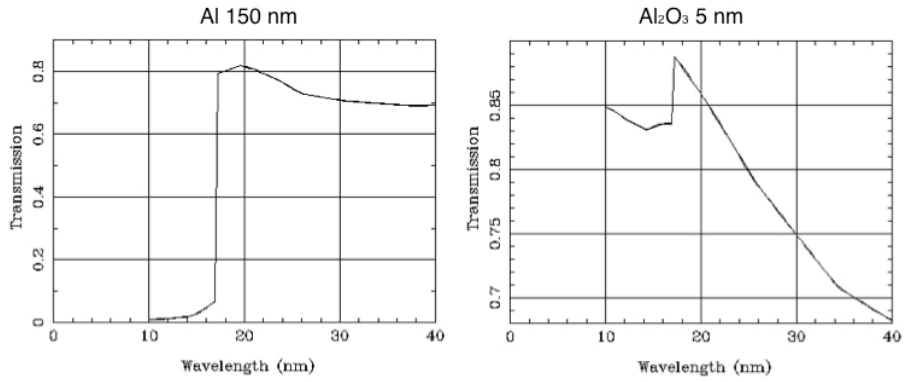

Fig. 4.8. The transmission curves of an Al filter of 150 nm thick (left side) and an Al_2O_3 layer of 5 nm thick (right side), based on the database of the Center for X-ray Optics.

In the Argon HHG spectrum, H37 and H39 are located in the *cut-off* region. The measured amplitude for H37 is greatly reduced by a factor more than 10 compared to H25, while H39 is in the noise (Fig. 4.9). Optimization of the generation parameters did not improve the signals of H37 and H39. Meanwhile, we have investigated the HHG in Neon gas whose harmonic conversion efficiency is in general an order of magnitude lower than in Argon, but has a farther extension of its *plateau* region. Fig. 4.10 shows a typical spectrum of HHG in Neon from H29 to H49, with generating parameters: gas cell length = 6.5 cm, gas pressure = 50 mbar, beam aperture = 24 mm, laser energy = 23 mJ. Note that in this spectrum, the harmonic generation is not yet optimized for H37 and H39. As the gain coefficient of the PMT is different to the one for Argon spectrum, these two spectra are normalized to each other by a careful calibration of the PMT. As clearly shown in the comparison between Argon and Neon HHG generation (Fig. 4.10), signals of H37 and H39 generated in Neon are at least two times stronger than in Argon. Therefore, we decided to use Neon gas as generation medium for magnetic experiments.

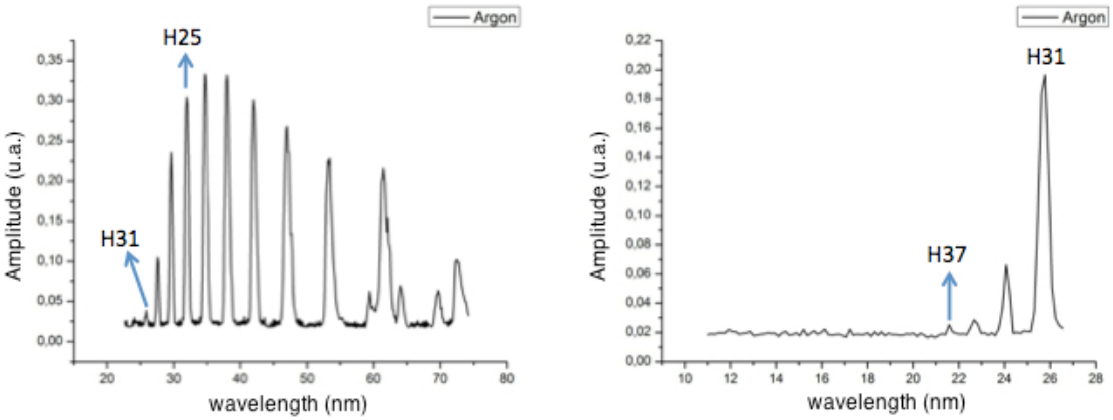

Fig. 4.9. HHG spectrum in Argon (left side) present a *cut-off* regime. The zoom out of the *cut-off* region (right side) shows a low H37 peak and that the H39 is within the noise. Both spectra are taken without Al filter.

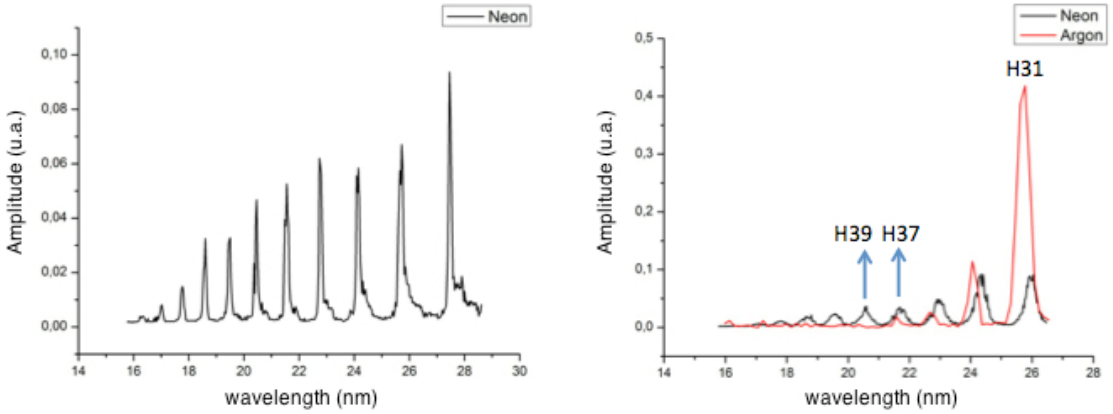

Fig. 4.10. HHG spectrum in Neon (left side) presents a farther *cut-off* compared to Argon. The comparison between normalized Neon and Argon spectra (right side) shows stronger signals of H37 and H39 in Neon.

In fact, neither H37 nor H39 correspond to the top of the resonant peak of the Cobalt $M_{2,3}$ edge (Fig. 4.6). The scattering efficiency will double, if H37 or H39 could be shifted to the center of the resonant peak. According to previous works, it is possible to blueshift the harmonics in the spectrum due to the self-phase modulation of the laser pulse caused by ionization in gas medium [15,16,17], and due to the nonadiabatic effect driven by the rapid increase in the femtosecond laser electric field [18,19]. Large blueshifts can even cover the interval between odd harmonics [18,19]. Several generation parameters can result in a blueshift, such as laser intensity, laser pulse duration and gas density. By varying the beam aperture, laser energy, gas pressure and the laser pulse duration in our experiment, we have taken spectra in different generating conditions to study the possibility of shifting H37 or H39 to better match the resonant peak. Compared to the initial generating condition, there is no spectral shift when changing beam aperture, laser energy or gas pressure (Fig. 4.11a). We observed a tiny spectral shift (~ 0.26 eV) to blue or red direction with a harmonic signal decreasing when varying the pulse duration (Fig. 4.11b). The initial pulse duration is 50 fs

and is stretched up to about 90 fs. Unfortunately, we did not get any significant spectral shift to center one harmonic order to the resonant peak. Note that these spectra are taken with one Al filter that the peak corresponding to H47 is reduced due to the filter cut-off.

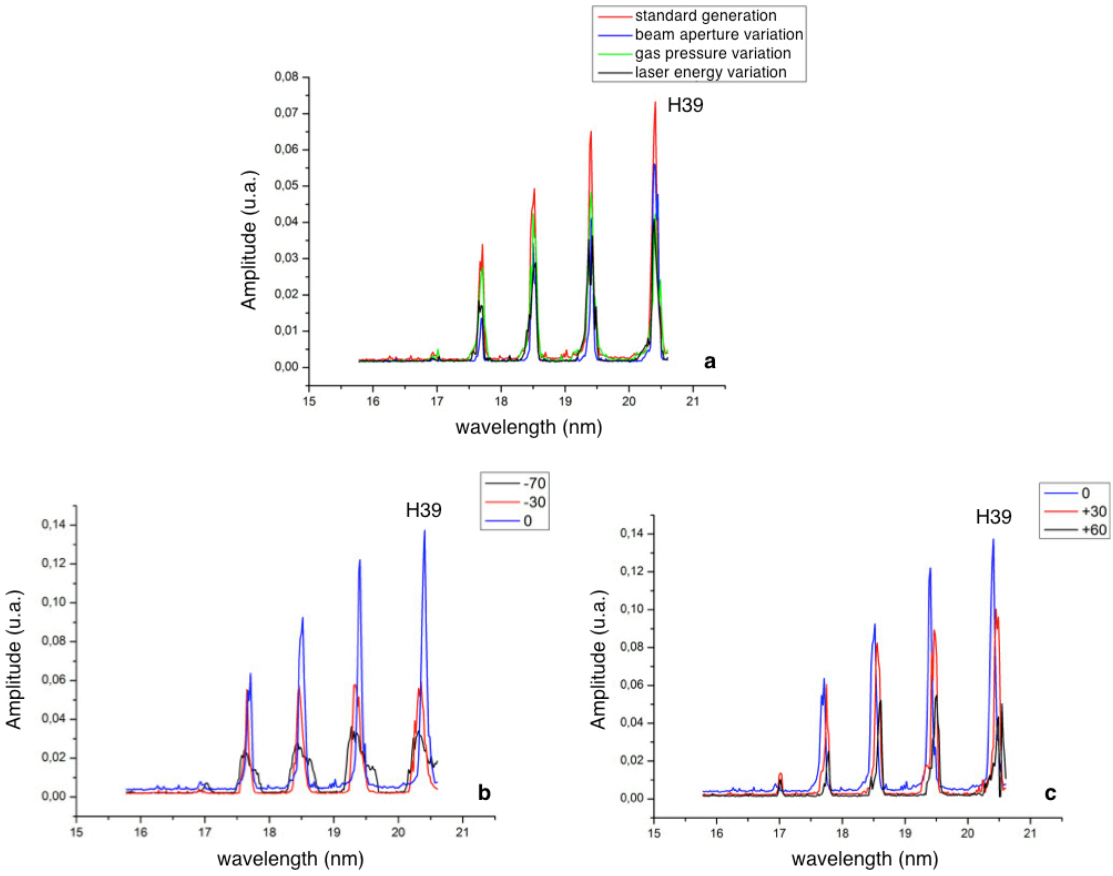

Fig. 4.11. Results of the spectral shift studies by changing beam aperture, gas pressure, laser energy (a) and laser pulse duration (b,c). Spectra are taken with one Al filter, normalized and compared to the initial generating condition (red curve in a, blue curves in b and c).

Another possible method to reach a photon energy closer to the high scattering efficiency (Co M-edge) is to use the even order harmonic H38 (58.89 eV). The latter can be generated in a "ω + 2ω" configuration (two-color HHG) that one adds the second harmonic (SH) of the driving laser pulse to break the inversion symmetry of Fourier transform in the HHG process [20, 21, 22]. In our experiment, we have inserted a 0.2 mm thick Beta Barium Borate (BBO) type I non-linear crystal at 1 m before the gas cell to generate the SH. Thus both odd and even harmonic are generated by the mixed laser pulse "ω + 2ω". Note that two-color HHG not only provides a possible candidate (H38) for single-shot imaging, but also a finer spectral sampling for magnetic scattering experiments. We can reduce the spectral sampling from 3.1 eV (one-color) to 1.55 eV (two-color HHG). Fig. 4.12b presents the HHG spectrum obtained in the "ω + 2ω" generation configuration. The amplitude ratio between odd and even harmonics is close to one. In general, the measured harmonic signals in "ω + 2ω" configuration is about 4 times lower than in one-color configuration. Nevertheless, H38 benefits from a larger scattering efficiency compared to H37 and H39. Thus, in the following magnetic scattering experiments, we are focused on the behavior of H37 and H39 in the one-color configuration

and H38 in the two-color one.

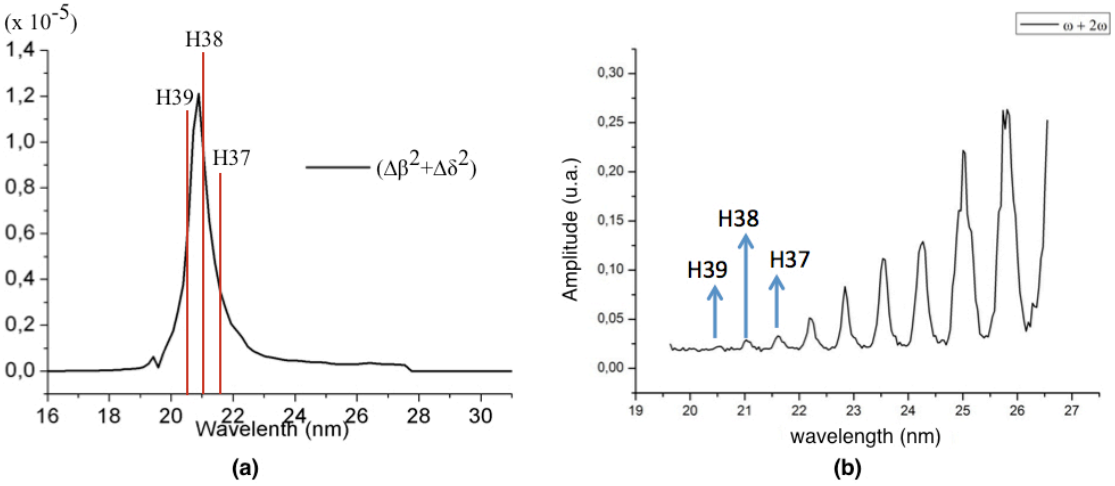

Fig. 4.12. (a) Location of H37, H38 and H39 on the magnetic resonant peak of the Cobalt $M_{2,3}$ edge. (b) Spectrum of two-color HHG, taken without Al filter.

IV.4 Scattering experiments of magnetic samples

The experimental setup has been changed for the magnetic scattering experiments, as presented in Fig. 4.13. The PMT and the thin slit are removed. We have located an IR shield with a pinhole to select the desired harmonic order and filter possible IR reflections from the optics chamber. Magnetic samples are located on a motorized sample holder at the focus of the toroidal mirror where the harmonic beam size is estimated to be around 150 µm. The XUV CCD camera is mounted on a translation stage behind the sample holder, thus we can change the distance between the CCD camera and the sample from 2 to 5 cm. The CCD camera is protected by an Al filter mounted at its entrance window. The transmission of this Al filter (150 nm thick) has been measured to be ~ 10%.

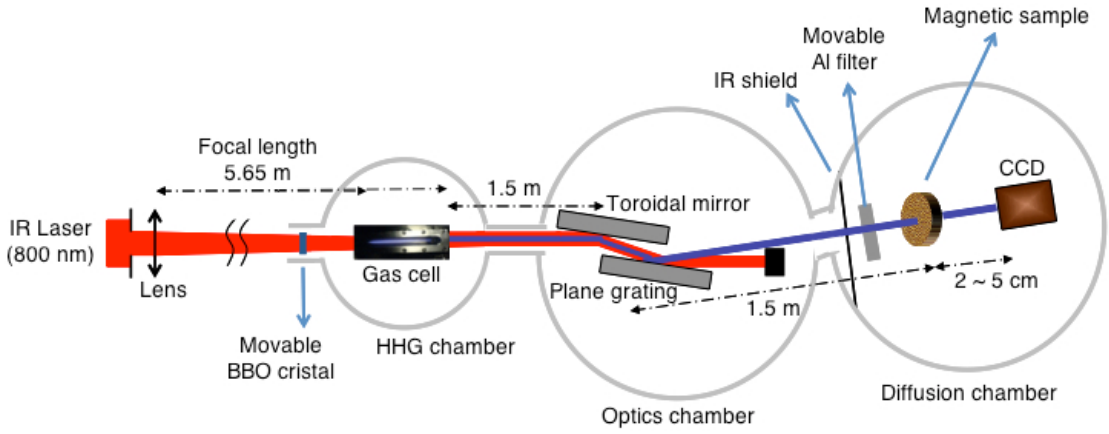

Fig. 4.13. Experimental setup for magnetic scattering experiments.

Before doing magnetic scattering experiments, we have optimized the one-color and two-color HHG for H37 to H39 using the same process presented in Chapter II. The optimum parameters values for one-color HHG is: beam aperture = 25~27 mm, gas pressure = 46~50 mbar, gas cell length = 5~6 cm, effective laser energy = 24~28 mJ and the focus position is 0 ~ 2 cm behind the gas cell output. The optimum values for two-color HHG are slightly different. Fig. 4.14 shows typical images detected by the CCD camera for H37 and H39 in one-color generation and H38 in two-color generation. The measured harmonic beams have a few 10^6 photons/pulse for H37 and H39, and ~ 5 x 10^5 photons/pulse for H38. Since the CCD camera is protected by an Al filter, the harmonics photon number is estimated to be one order of magnitude higher at the focus of the Toroidal mirror. Note that the harmonics are stretched in the spectral direction (horizontal direction in Fig. 4.14) of the grating. It should be due to the grating's aberration, since it is not observed in the diffraction configuration with the parabola. The elliptical spatial profile does not have negative influence for magnetic scattering experiments in this section, because first the samples are in general much larger than the harmonics spots and second we are not in imaging configuration.

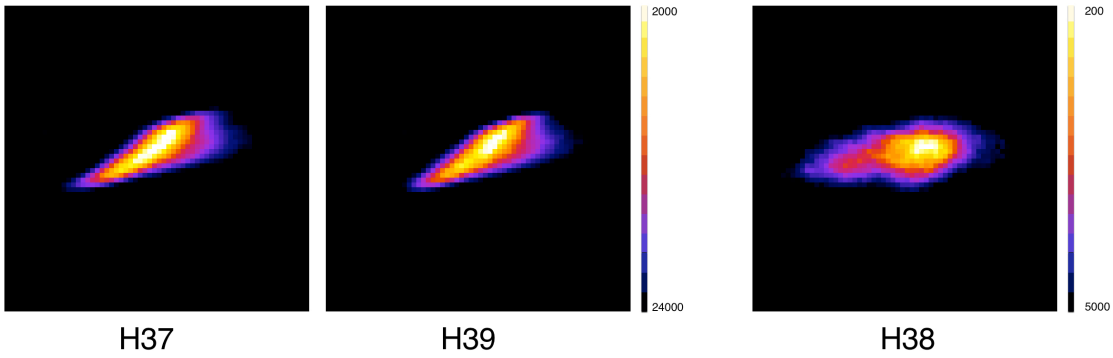

Fig. 4.14. Typical harmonic spatial profiles of H37 and H39 in one-color generation and H38 in two-color generation.

IV.4a Scattering experiments of magnetic samples: first try

The first magnetic sample investigated is 250µm x 250µm large, containing 30 layers of [Co(4Å)/Pd(6Å)] with labyrinthine nanodomains structure (observed in MFM images after fabrication). We have observed a scattering ring due to the labyrinthine structure when illuminating the magnetic sample by harmonics from H33 to H42 with 10-shot accumulation. In the one-color generation, scattering signals are maximized at H37 and H39, and quickly reduced for the other harmonic orders. In two-color generation, scattering signals are maximized at H38 and slightly reduced for H37 and H39, then quickly decreased for the other ones. Single-shot scatterings are detected only for one-color generation. Fig. 4.15 presents the measured scattering rings of the concerned harmonic orders in 1 and 10 shots, with a 10 x10 binning ratio of the CCD camera detection (signals of 100 pixels are integrated into one large pixel). We are surprised by the experiment results that scattering ring can be clearly observed for such a large spectral bandwidth. In fact, the resonant peak is quite narrow that scattering ring should be hardly observed for harmonics other than H37 ~ H39. It is possible that the scattering signal is not purely "magnetic". But meanwhile, the average radius of the scattering

rings varies linearly with the harmonic orders (shorter wavelength got smaller radius). This should be related to the magnetic effect, because the sample is "homogenous" for the harmonic beam if we neglect the magnetic contribution. This sample has been tested at LOA with H37 before we investigate it at CEA. According to their experimental results, the scattering efficiency for H37 is ~10^{-5}, which agrees with the values published in Ref. 13. Note that the experimental scattering efficiency D is calculated as the ratio between the scattered photon number and the incident photon number. In our experiment, the calculated scattering efficiency is ~ 10^{-3} for H37 to H39, and ~ 10^{-4} for the adjacent harmonic orders. After carefully checking our beamline and numerical calculations, we didn't find possible reasons to explain this abnormal high scattering efficiency. Moreover, the result has been reproducible during the whole experiment run time (about 10 days) both in one-color and two-color generations. To clarify the problem, we have sent the sample to LCPMR (team of Prof. Jan Lüning) to do again the MFM image scans. Unfortunately, no magnetic nanodomain structures were observed. It could be due to demagnetization during transport. After that, we have investigated more than 15 magnetic samples with various parameters (sample size, multilayer number, ratio between Co and Pd, nanodomains structure organization, etc.), among which there is the sample of the same type as the first one. Using exactly the same scattering process, we have obtained a lower scattering efficiency that agrees with the reference values and the experimental results obtained at LOA. We conclude that the abnormal high scattering efficiency of the first sample should be related to the magnetic sample itself, but not our beamline or experimental process. The reason for this remains unknown, since we have no similar observation on the other magnetic samples.

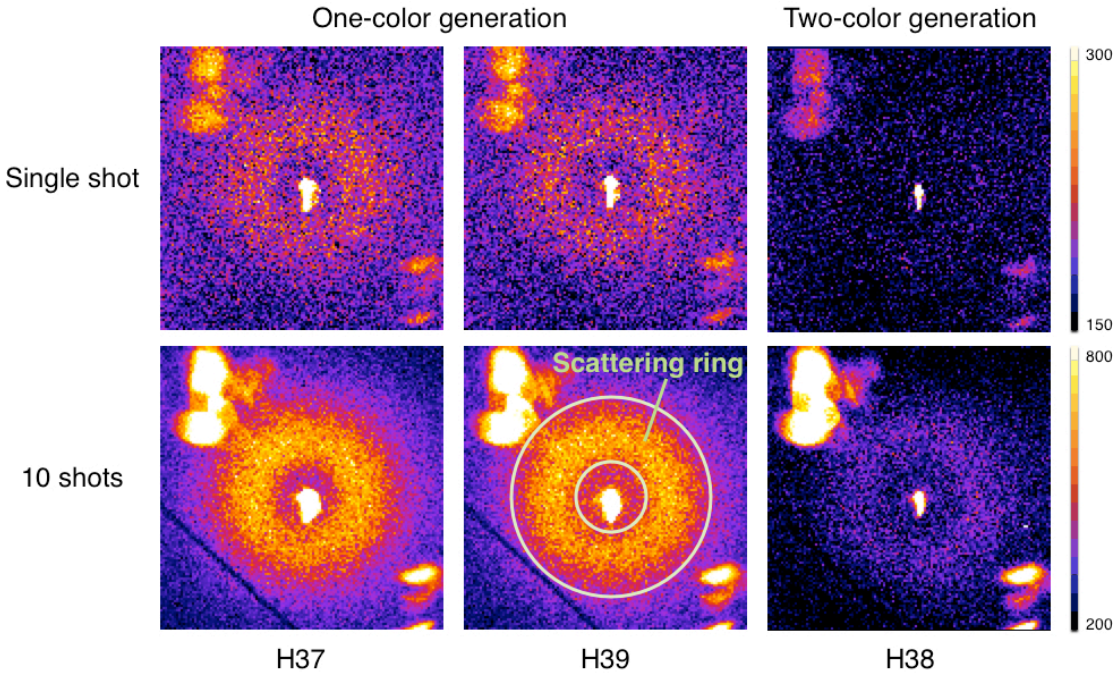

Fig. 4.15. Measured scattering ring (between the two circles) from H37 to H39 in single-shot and 10-shot accumulation. Signals at the left-top and right-bottom corners are background noise. The black line at the left-bottom is a line beam blocker in front of the CCD camera, which is not served in this experiment. The saturated signal in the center is the transmitted harmonic beam. Note that images are obtained using a 10 x 10 binning ratio with the CCD camera.

IV.4b Scattering experiments of magnetic samples: Paper V and Paper VI

Paper V and Paper VI present the experimental results and analysis of the magnetic scattering experiments. The experiments are focused on:

1) Single-shot detection of magnetic scattering to demonstrate the possibility of single-shot imaging of magnetic nanodomains structures using our table-top harmonics beamline. Nanometric spatial resolution on a femtosecond flash is obtained. This shows the high potential of capturing nanoscale movies of the ultrafast magnetic dynamics for either reversible or irreversible ultrafast phenomena. This was previously believed to be possible only on large-scale FEL (XFEL) facilities
2) Spectral studies over a large bandwidth (20 eV) with a sampling step of 1.55 eV (two-color generation) in both single-shot and multiple-shot regime on various magnetic samples. We have been able to identify and discriminate scattering signals of cobalt and palladium at different absorption edges. The single-shot spectral study opens the route toward the study of a broad range of complex mesoscopic systems, as for example nanoscale phase transitions.

Paper V presents the study of a magnetic sample, which contains 15 layers of [Co(4Å)/Pd(8Å)] with aligned nanodomains structure (acting like a transmission grating). Two well-defined Bragg peaks are observed in single-shot and multiple-shot regime, from which we estimate the nanodomains width to be 62.5 nm with a distribution of ± 7 nm in multiple-shot detections and ± 10 nm in single-shot detections. This agrees with the MFM measurements of the sample (70 nm ± 5 nm). The comparison between single and multiple shot detections demonstrates that single-shot detections are reliable for studies both in scattering efficiency measurements and spatial properties of the sample. In addition, scattering signals are observed at the palladium N edge, around 51 eV (H33 signal).

Paper VI presents the study of two samples composed of respectively 20 layers (sample "A") and 30 layers (sample "B") of [Co(4Å)/Pd(6Å)] with aligned (A) or labyrinthine (B) nanodomains structures. Spectral studies are done with two-color generations to refine the sampling ratio compared to Paper V. Single-shot detections are realized both for aligned and labyrinthine organizations. The nanodomains width in sample B is estimated to be 108 nm ± 70 nm with measured scattering efficiency in the 10^{-6} range, which agrees with theoretical values. The nanodomains width is reduced to 91 nm ± 6 nm in sample A, due to a better alignment organization during the magnetization process. The resonant peak of palladium N edge is clearly observed and resolved in all samples.

IV.4c Scattering experiments of magnetic samples: fundamental and exhaustive studies

This campaign was motivated by finding the magnetic nanodomains behavior for various sample compositions. It has practical interest to design future imaging and time resolved experiments and is of great interests for understanding the fundamental physics of

nanomagnetism. The large spectral bandwidth and the fine sampling setup of our harmonic beamline are ideal for such experiments. Rich information can be extracted from single and multiple shot detections.

Exhaustive magnetic scattering studies over a large spectral bandwidth are done with following sample types, grouped in 5 main series:

1) SiN(30nm)/Al(10nm)/ [Co(4Å)/Pd(6Å)](N layers)/Al(3nm), where N= 15, 20, 30 and 40.
2) SiN(30nm)/Al(10nm)/Pd(1nm)/[Co(4Å)/Pd(2Å)](N layers)/Al(3nm), where N=20, 30 and 40.
3) SiN(30nm)/Al(10nm)/ [Co(4Å)/Pd(8Å)](N layers)/Al(3nm), where N=15 and 20.
4) SiN(30nm)/Al(10nm)/Pd(1nm)/ [Co(2Å)/Pd(2Å)](N layers)/Al(3nm), where N=20, 30, 40, 50, 60 and 80.
5) Cobalt and Nickel samples:
    a. SiN(30nm)/Al(10nm)/ [Co(4Å)/Ni(8Å)](10 layers)/ [Co(4Å)/Pd(2Å)](20 layers)/Al(3nm)
    b. SiN(30nm)/Al(10nm)/Pd(1nm)/ [Co(2Å)/Pd(2Å)](20 layers)/ [Co(4Å)/Ni(8Å)](20 layers)/ [Co(2Å)/Pd(2Å)](20 layers)/Pd(2nm)

In general, magnetic layers (texts in blue) are protected by a thin layer of Al, and held by a substrate of SiN and Al. Each membrane contains more than 10 samples of the same type with different sample aperture varying from 50 µm to 250 µm. Note that in the fifth group, palladium is partially replaced by nickel because of its higher photon transmission in the concerned spectral region. The demand of various sample compositions also pushes the sample fabrication technique, for example, the magnetic nanodomains in fourth group were initially thought to be unstable to remain without external magnetic field.

In the first step, we have performed the statistical studies. The data analysis and the theoretical modeling are on going. The research results will be published in the near future. Here we would like to present few experimental results. For each sample series, simple demonstrations like scattering efficiency curve or scattering image are shown in Fig. 4.16. Note that we have observed the resonant peak of palladium in some cases but not in others. As a first interpretation we explain this by the magnetic interaction effect between cobalt and palladium, which strongly depends on the composition sample ratio. A theoretical model is under progress. In general, we have observed the same magnetic behavior on the same type samples that is important for some kind of irreversible studies, in which a new sample is required for each shot.

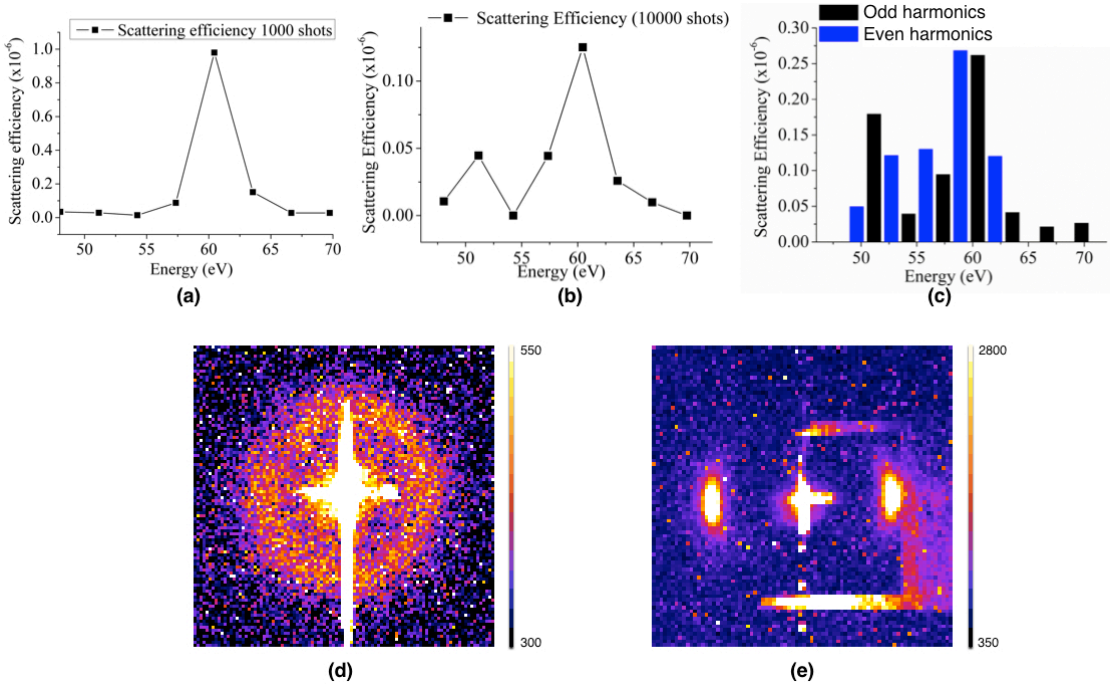

Fig. 4.16. (a), (b) and (c) are measured scattering efficiencies respectively for sample series (3) with 15 layers, (2) with 40 layers and (1) with 20 layers. (a) and (b) are performed with one-color generation, and (c) with two-color generation. (d) and (e) are snapshots of scattered photons measured by the CCD camera respectively for sample series (4) with 20 layers and (5a). Both images are taken with H39 and an exposure time of 300 seconds (6000 shots). The center is well saturated. (d) is obtained using a 5 x 5 binning of CCD camera and (e) is 10 x 10 binning. The signals at the top and the bottom of (e) are background noise.

IV.5 Next step: coherent diffractive imaging and time-resolved pump-probe experiments

During my thesis, I have been working on the design of a pump-probe experiment. The experiment is undergoing. I detail here the preparatory study.

Exploring the ultrafast dynamic phenomena of the magnetic samples can be carried out using the same experimental setup as in the previous section to benefit from the large spectral bandwidth, or we can use the diffraction configuration of our beamline to benefit from higher harmonic intensity. In the diffraction configuration, the total beamline transmission (optics + filters) is about 10 times higher than in the spectrum configuration. Moreover, the focal spot would be 50 times smaller. We can expect a harmonic beam with 3 to 4 orders of magnitude more intense. We would also benefit from a better spatial profile and a lower background noise. The actual parabola (for 32 nm) will be replaced by a new one coated with a multilayer optimized for H39 (20.5 nm). This choice has been guided by the statistic studies presented before, exhibiting a better scattering signal at H39 than at other harmonics. The new parabola has already been tested for coherent imaging on test samples (like the “lambda” in Chapter III). In the pump-probe experiment, the pump beam will be extracted from the laser beam

before the focusing lens and then controlled by a time-delay stage. The entire beam path of the pump beam will be enclosed in long tubes to have better stability during propagation and for security reasons.

The coherent imaging of the magnetic nanodomains will be carried out in the diffraction configuration, first in single-shot regime of static sample and then in time-resolved experiments. Note that in the spectrum configuration, the oversampling ratio has not been respected, thus it is impossible to inverse the scattering pattern to get an image. The X-ray magnetic scattering is a complex combination of interactions between the X-ray beam and the magnetic sample's electric charge distribution and magnetization density, which is also sensitive to the polarization state of the X-ray beam [25,26]. In the transmission geometry of our experiment with magnetic multilayers presenting an out-of-plane anisotropy, the light will scatter preferentially with circularly polarization states (right or left handed) [4]. Our harmonic beam is linearly polarized. This can be considered as a composition of two beams with opposite circular polarizations of equal amplitude. In our magnetic scattering studies presented in the previous sections, the magnetic properties are deduced by the integral of the scattered photons and the spatial distribution of the Bragg peaks or scattering ring. Thus there is no problem to use our linearly polarized harmonic beam for such studies. However, neither phase retrieval algorithms nor holographic techniques can be simply implemented on scattering patterns using linearly polarized light, because of the addition of incoherent magnetic and charge scattering photons to the detected signal.

To overcome the incoherent addition problem, the "simplest" way is to use circularly polarized beam for imaging experiments, as the demonstration [1] mentioned at the beginning of this Chapter. A recent communication has reported image reconstruction of magnetic nanodomains using holography with extended reference technique and circularly polarized synchrotron source [30]. Our collaborators from LOA have developed a HHG polarization-controlling device [27] to modify the linearly polarized harmonic beam to 100% circular polarization. Then, imaging reconstruction of magnetic structures can be accomplished by CDI or holographic techniques as demonstrated with test objects in Chapter III. However, the circular polarization is obtained at the cost of photon flux. Indeed, the total efficiency of the polarization-controlling device is estimated to be ~ 3.6%. With the low scattering efficiency of the samples, we will probably need multiple-shot accumulation to have enough photons for image reconstruction.

Recently, some approaches using linearly polarized light have been proposed [28,29] for magnetic structure imaging. However, two or more detections are required in such approaches. Moreover, the principle of these approaches is to separate charge and magnetic scattering components by subtraction of two images, and one of that is obtained by saturating the magnetic sample with the presence of an external magnetic field. Thus, the magnetic nanodomains may be altered within this process [31]. Very recently, a single-shot approach based on CDI and magnetic resonant scattering has been proposed for future pump-probe experiments of magnetic nanodomains imaging at FEL facilities [32]. In this approach, the authors assume that the nondichroic absorption of the magnetic sample is uniform. The charge scattering can be modeled as the simple diffraction of the sample aperture (a mask covering the magnetic sample to provide *isolated object* condition for CDI) that varies slowly away from its edges. Therefore, the charge scattering can be removed from the scattering pattern by "subtracting a smooth surface from the autocorrelation of the object". This

approach can also be applied using our harmonic beamline for single-shot imaging. This is the more promising method for single-shot imaging compared to the polarization-controlling device. In fact, we can also use holographic techniques with linearly polarized beam, if the reference wave is "magnetic". The latter may be obtained by covering the magnetic samples a mask composing of a sample aperture and a reference aperture and assuring that the reference aperture selects nanodomains of the same magnetization direction, which is technically difficult. Moreover, extended reference is not possible for this configuration, due to the nanodomains' small size (smaller than the size of the reference) and its spatial organization. This approach is more suitable at FEL facilities than our harmonic beamline, considering the much higher photon flux provided by those large-scale sources. At last, a recent demonstration of lens-less X-ray imaging in reflection geometry [33] could be an alternative configuration to the widely used transmission geometry. However the inversion problem of the oversampled diffraction pattern still need to be generalized.

IV.6 Conclusion

In this chapter, I have presented an ongoing imaging application in nanomagnetism in the framework of collaboration between three interdisciplinary laboratories. The main research goal is to realize the real space imaging of ultrafast phenomena occurring on magnetic nanodomain structures with a high spatial and time resolution. The concerned imaging methods are the coherent diffractive imaging techniques (CDI, FTH and HERALDO) presented in Chapter III. The experiment was or will be realized in four steps: 1) spectral studies of the Cobalt absorption edge ($M_{2,3}$); 2) Magnetic resonant scattering in samples' static states for magnetic properties study (such as scattering efficiency, nanodomains width and distribution…) over a large spectral bandwidth, completed by statistic studies of various magnetic sample types; 3) Single-shot imaging of magnetic nanodomain structure; 4) pump-probe experiment for ultrafast magnetic phenomena (reversible and irreversible). The experimental results of the first two steps are promising. We aim at capturing the "movie" of the magnetic nanodomains modification on femtosecond time scale, which will open new gate for understanding the spin-orbital and exchange interactions. From this experiment, we can see that the High flux harmonic beamline is a polyvalent and easy-for-manipulation setup suitable for a wide range of research applications. Combining with the lens-less imaging techniques, we demonstrate a powerful experimental tool for studying ultrafast phenomena in various scientific areas.

Paper V

Paper V presents the study of a magnetic sample, which contains 15 layers of [Co(4Å)/Pd(8Å)] with aligned nanodomains structure (acting like a transmission grating). Two well-defined Bragg peaks are observed in single-shot and multiple-shot regime, from which we estimate the nanodomains width to be 62.5 nm with a distribution of ± 7 nm in multiple-shot detections and ± 10 nm in single-shot detections. This agrees with the MFM measurements of the sample (70 nm ± 5 nm). The comparison between single and multiple shot detections demonstrates that single-shot detections are reliable for studies both in scattering efficiency measurements and spatial properties of the sample. In addition, scattering signals are observed at the palladium N edge, around 51 eV (H33 signal).

Submitted.

Single shot detection of magnetic resonant elastic scattering using table-top high laser harmonic generation

M. Ducousso,[1] X. Ge,[1] W. Boutu,[1] D. Gauthier,[1] B. Barbrel,[1] F. Wang,[1] A. Borta,[1] A.-I. Gonzalez,[1] M. Billon,[1] B. Vodungbo,[2] J. Gautier,[2] P. Zeitoun,[2] R. Hawaldar,[3] B. Tudu,[3] R. Delaunay,[3] M. Tortarolo,[3] J. Lüning,[3] and H. Merdji[1]*

[1]*CEA-Saclay, IRAMIS, Service des Photons, Atomes et Molécules, 91191 Gif-sur-Yvette, France*

[2]*Laboratoire d'Optique Appliquée, ENSTA ParisTech – CNRS – Ecole Polytechnique, Chemin de la Hunière, 91761 Palaiseau, France*

[3]*Laboratoire de Chimie Physique, Université Pierre et Marie Curie, UMR du CNRS (7614), 11 Rue Pierre et Marie Curie, 75005 Paris, France*

**Corresponding author: hamed.merdji@cea.fr*

Ultra-bright femtosecond X-ray pulses available at free electron lasers enable single shot investigations of irreversible ultrafast phenomena with nanometer spatial resolution. Here, we demonstrate that intense tabletop soft X-ray laser harmonics allow similar studies. We use a single 20 fs laser pulse to measure the spatial arrangement of a magnetic nano-domain structure with sub-100 nanometer spatial resolution by resonant scattering around the cobalt M-edge. Moreover, the technique being element specific we have been able to identify magnetic scattering at the palladium N-edge (around 51 eV), which indicates a significant induced magnetization in the Pd layers of our Co/Pd multilayer structure.

Magnetism is one of the oldest and most intriguing scientific disciplines, which macroscopic manifestations have always attracted attention. Its applications are present in many aspects of our daily life, from medical imaging to data storage in modern microelectronic devices. Driven by the development of nanotechnologies, new applications are emerging, such as nano-bio-magnetic sensors or Magnetic Random Access Memory.[1] Current research activities concern control and manipulation of magnetization at nanometer length scales.[2] For instance, the ultimate speed of magnetization reversal and the underlying mechanism of ultrafast spin (re-)organization have yet to be elucidated. [3,4]

New insight into ultrafast dynamics can be expected from time-resolved imaging of a sample's magnetization on its relevant nanometer length scale. This requires a technique that combines a spatial resolution of a few tens of nanometers with femtosecond time resolution. Moreover, understanding how the local scale processes contribute to the macroscopic demagnetization imposes to carry out these time-resolved imaging experiments over large (micrometer) areas and long time delays from femto- to nano- or even microseconds. Such requirements offer a stimulating challenge for the development of novel light sources and instrumentations. Here, we demonstrate that table-top ultra-short soft X-ray laser harmonics allow realizing such experiments.

X-ray radiation is well suited to characterize magnetic properties since strong magnetic contrast is obtained for photon energies matching magnetically dichroic absorption resonances.[5] Sum rules allow inferring from these dichroism spectra quantitative information about the spin and orbital moment of the ground state of the magnetic sample.[6-8] Due to their short wavelength and rather large penetration depth, X-rays are also ideally suited for coherent diffractive imaging of micrometer sized samples.[9] In such a lensless imaging experiment, a monochromatic and spatially coherent X-ray beam is used to illuminate a sample and the resulting (small angle) scattering pattern is recorded in the far field. About 10 nm spatial resolution has been demonstrated in several experiments,[10] while the ultimate achievable spatial resolution is in principle only limited by the wavelength itself. Lensless microscopy techniques have been applied to image the

magnetic domain structure of ferromagnetic materials using photon energies around magnetic dichroic resonances.[11,12]

Initially magnetism experiments were performed using soft X-rays from third generation synchrotron radiation sources. However, the pulse duration available at those facilities, typically a few tens of picoseconds, prevents their use for the investigation of ultrafast (femtosecond) magnetization dynamics. In addition, due to the low number of photons per pulse, signal accumulation is required over many X-ray pulses. This excludes in particular the investigation of non-reversible phenomena which require single X-ray shot data acquisition.

These limitations can be overcome at XUV/X-ray Free Electron Lasers (XFELs), which provide transversely coherent X-ray pulses of femtosecond pulse duration with up to 10^{13} photons. Indeed, snapshot coherent X-ray diffraction imaging has been demonstrated,[13] and recently applied to image a magnetic nano-domain structure.[14] However, a current limitation of XFEL sources is the large shot to shot variation of many beam parameters (in particular, intensity, energy and arrival time), which limits the achievable sensitivity when following the evolution of a system. These issues may be solved in the next future using for example self seeding schemes. However, a more accessible source would offer an interesting alternative for realizing such studies.

Table-top high harmonic generation (HHG) sources, based on an intense commercially available femtosecond infrared laser have already demonstrated nanoscale imaging.[15,16] Coherent ultra-short (from femtosecond down to attosecond) soft X-ray pulses are generated up to hundreds electron volt, covering resonance edges of most magnetic elements.[17-19] They are naturally synchronized with the laser source, thus providing a jitter free ultrafast IR pump – X-ray probe set-up. Finally, pulses are intense enough to record single shot data.[16,20] These properties make HHG sources well suited for studying irreversible magnetic processes occurring down to nanometer scales.

First studies of magnetization phenomena using a HHG source have recently been reported. La-O-Vorakiat *et al.* performed XUV transverse magneto-optic Kerr effect (T-MOKE) experiments to follow the demagnetization dynamics of Permalloy with element

sensitivity.[21] Using resonant magnetic scattering, the capability of HHG source for probing magnetization properties with nanometer spatial resolution was demonstrated by Vodungbo *et al.* on Co/Pd sample.[22] However, all these studies averaged over multiple shot exposures, thus revealing only the reproducible part of the investigated magnetization phenomenon.

In this letter, we report the first femtosecond single shot characterization of a magnetic nano-domain structure from a table-top soft X-ray laser-harmonic source. We have measured from the far field scattering pattern the spatial properties of the magnetic domain structure at a sub-100 nm scale. The maximum magnetic scattering efficiency is measured close to the cobalt M-edge (60 eV). Multiple laser shot measurements from 45 to 70 eV have been also conducted. They confirm the single shot observations and evidence magnetic scattering signal in the palladium layer at 51 eV (Pd N-edge). The results are discussed in details in the following sections.

The resonant scattering experiment was performed with the table-top infrared femtosecond laser LUCA (Laser Ultra Court Accordable at CEA-Saclay research center (France)) delivering 50 fs, 50 mJ pulses at 800 nm at a 20 Hz repetition rate. For Co/Pd magnetic studies, HHG emission in the 40-70 eV photon energy range has been optimized by a systematic study of the generation parameters. A hollow-core fiber is used to improve the infrared laser beam profile and wavefront through modal spatial filtering. HHG phase matching is thus enhanced, increasing the generation efficiency by about a factor 4. The setup of the HHG experiment is depicted in Fig. 1. In brief, soft X-rays are generated by focusing the laser beam in a cell of variable-length, which is filled with a low-pressure noble gas. With the best parameters (see Fig. 1) we generate high laser harmonics up to order 51 with a few times 10^9 photons/pulse in harmonic 39 (H39), which energy is close to the cobalt $M_{2,3}$ edge (60 eV). The pulse duration is estimated to be 20 fs.[16] The generated XUV pulses are focused onto the sample by a toroidal mirror in a 4f configuration to a focal spot diameter of ~250 µm. Harmonic selection is achieved with a blazed plane grating and a pinhole (see Fig. 1). The measured flux on the sample is ~10^7 photons per pulse for H39 with a pulse duration of ~60 fs due to temporal stretching

by the grating monochromator. The scattering patterns are detected in the far field using a soft X-ray in-vacuum charge-coupled device (CCD) camera.

The investigated sample is a ferromagnetic [Co (4 Å)/Pd (8 Å)]$_{15}$ multilayer film exhibiting out-of-plane anisotropy,[22] which has been grown by magnetron sputtering on a 30 nm thin silicon nitride membrane. Using an in-plane demagnetization procedure, a magnetic domain structure of aligned stripe domains can be prepared as shown by the MFM image in Fig. 1. From this image we find a characteristic domain width of 70 nm, with a ±5 nm wide domain size distribution.

The aligned magnetic domains with alternatively up and down magnetization directions exhibit a dichroic optical index around the energy of the $M_{2,3}$ resonance. Thus, the sample itself acts on the incident X-ray beam like a transmission grating. To quantify this interaction we define the scattering efficiency D as the ratio between the number of scattered photons and the number of incident photons on the sample. Under the first-order Born approximation, D is expressed as

$$D(E) \sim T(E)\,(Ed)^2\,[\Delta\beta(E)^2+\Delta\delta(E)^2] \qquad (1)$$

where T, d and E stand for the sample's optical transmission, the thickness of the resonant material and the photon energy. $\Delta\beta$ and $\Delta\delta$ are the real and imaginary part of the difference between the optical indexes of the two opposite magnetization directions, respectively. Relation (1) implies that the scattering intensity is proportional to the square of the magnetization of the sample, $\langle M^2 \rangle$.[23] One further notes that the efficiency increases quadratically with the thickness of the resonant material, but is proportional to the sample's transmission, which itself decreases exponentially with the sample thickness. Using Eq. (1) and literature values for the optical index of Co around the $M_{2,3}$ edge,[24] we can estimate the efficiency to be ~10^{-5} at 59 eV. In addition, we calculate that the magnetic scattering signal should be detectable in a ~10 eV window around the M-edge.

The resonant magnetic scattering efficiency has been investigated from multiple laser shots in the 45 to 70 eV spectral range in the Fraunhofer regime. Typical scattering patterns, accumulated over 400 laser shots, are shown using the same color scale as insets

in Fig. 2. We note that the photon flux on sample does not lead to sample damage nor modifications of the magnetic domain structure (estimated temperature increase of 10^{-1} K in the sampled area).[4] Studies in the accumulative regime are thus possible and can be compared to single shot results without ambiguities due to a deterioration of the sample characteristics. As the magnetic nano-domains are aligned, the magnetic grating can be considered as monodimensional giving rise to well-defined first diffraction order peaks.[22] By integration of the scattering intensity recorded for H29 to H45, we characterize the scattering efficiency of the magnetic sample for the 45 to 70 eV photon energy range. Measurements are compared with calculated values based on Eq. (1). This comparison is shown in Fig 2: Simulations are presented in panel (a) and experimental results are shown in (b). Measurements performed for several identical samples and various accumulation times lead to similar scattering efficiency values. Finally, we note that our data are in good agreement with the calculations and previous estimations.[22]

One notices that the photon energy of the maximum of the calculated scattering efficiency (Fig. 2(a)) deviates by about 1 eV from the position of the highest experimental value (Fig. 2(b)). This difference is related to the experimental sampling using discrete laser harmonics, as illustrated comparing the plots with symbols in Fig. 2(a) and (b). Hence, while none of the harmonics matches exactly the maximum of the scattering efficiency, the resonance is sufficiently large, ~2.3 eV of full width at half maximum (FWHM), so that H39 still exhibits a strong scattering efficiency. We also observe a small increase in the experimentally detected scattering efficiency around 51 eV, i.e using H33, Fig. 2(b). We interpret this observation as an indication of resonant scattering at the N_3 edge of palladium, which is located at 50.9 eV. This implies that the proximity of the ferromagnetic Co layers induces a significant magnetization transfer to the Pd layers, which then exhibit the same magnetic domain structure as present in the Co layers. However, it could not be simulated on Fig. 2(a) as the complex optical indexes of the palladium magnetic domains at the N-edge are not available in the literature. We obtain from our measurements a scattering efficiency around the Pd resonance of $\sim 1.5 \times 10^{-6}$.

We next discuss the resonant magnetic scattering from a single XUV laser harmonic shot using H39. Multiple and single shot scattering patterns are compared in Fig. 3(a) and 3(b), respectively. We note that the scattering signal is well detected in both cases. The oversampling ratio related to the experimental arrangement does not allow the numerical reconstruction of the image of the sample using phase retrieval algorithms.[10] However the data are rich in information, since such small angle scattering diagrams reveal a statistical description of the spatial properties of the sample. Scattering efficiencies are also derived from the single shot data.

The spatial organization of the magnetic domains can be deduced from the integral of the scattering intensity as a function of the azimuthal angle φ. This is plotted in Fig. 3(c) and 3(d) for multiple and single shot detection, respectively. The two symmetric peaks, separated by 180°, exhibit a FWHM of about 8 ± 0.5° in the multiple shot acquisition and 12 ± 1° in the single shot detection. This value indicates that the nano-domains are well oriented (close to the vertical axis), as was previously revealed by the MFM image in Fig. 1. The larger angle obtained for the single shot detection is due to a loss of statistics related to the reduced number of photons.

The average size of the nano-domains is inferred from the spatial integration of the scattering intensity as a function of the wave vector transfer q. Normalized intensity values are presented by the symbols in Fig. 3(e) and 3(f) for multiple and single shot detection, respectively. The lines give the result of the best pseudo-Voigt fit of multiple (continuous line) and single (dash line) shot data. In both cases the fits reproduce the data well, which illustrates the good agreement between the measurements. The maximum of the scattering intensity is determined to be in both cases at $q = 0.049 \pm 2.10^{-4}$ nm^{-1}, which corresponds to a real space periodicity of 125 nm. This value corresponds to an average nano-domains size of 62.5 nm. The domain size distribution width $\pm \Delta q$ (inferred from the FWHM of the measured scattering intensity) is found to be $\Delta q = 3.10^{-3} \pm 4.10^{-4}$ nm^{-1} for multiple shots detection and $\Delta q = 4.10^{-3} \pm 6.10^{-4}$ nm^{-1} for single shot detection. We finally measure nano-domains of 62.5 nm width with a distribution of ±7 nm from multiple shots detection and ±10 nm from single shot detection. In both cases, we note a good correlation with the MFM measurements.

In summary, we report ultrafast single shot investigations of the magnetic nano-domain structure of a thin ferromagnetic Co/Pd multilayer film exhibiting out-of-plane anisotropy. These studies have been realized using femtosecond soft X-rays from an optimized table-top high harmonic generation source. We have accurately measured the spectral scattering efficiency of the sample from 45 to 70 eV using multiple shot acquisitions. The cobalt M-edge and the palladium N-edge signatures have been detected with scattering efficiencies of 10^{-5} and $2x10^{-6}$, respectively.

Using the 39^{th} harmonic, which is close in energy to the magnetically dichroic Co $M_{2,3}$ absorption edge, we have measured the average size of the magnetic domains to be 62.5 nm, with a size distribution of ±7 nm in multiple shot and ±10 nm in single shot in good agreement with MFM characterization. This validates the single shot capability of our table top facility. The next step, under progress, is to obtain images of the magnetic domains using a similar set-up as previously used.[16,20] We note that circularly polarized light will not be necessary.[12,25] Expected numbers in this configuration will allow focusing more than 10^8 photons in a 5 µm diameter spot allowing single shot imaging. Using a pump-probe setup, reversible and non-reversible magnetization dynamics will be accessed with nanometer length and femtosecond time resolution.

Acknowledgements: We acknowledge the Saclay SLIC laser team and Mathieu Durero. We acknowledge financial support from the European Union through the EU-LASERLAB and the EU–FP7 ATTOFEL and X-Motion programs, from the French ministry of research through the 2009 ANR grants ”I-NanoX” and ”Femto-X-Mag”, from the ”Triangle de la Physique” through the COX grant and the C’NANO research program through the X-NANO, DYNAVO and DYNAVOPosDoc grants.

Figure captions:

FIG. 1. (Color online) Arrangement of the experimental setup. Optimized HHG parameters are obtained for 27 mJ of infrared laser pulse energy (selected by a 27 mm aperture in the beam path), focused by a lens of 5.5 m focal length in the center of a 5 cm long cell, which is filled with 4.8 Torr of neon. The CCD camera has 13.5x13.5 μm^2 pixel size. In order to shield the detector from scattered infrared light to improve the signal-to-noise ratio, a 150 nm thick aluminum filter is placed in front of the CCD camera using a lightproof holder. The camera chip is operated at 233 K and 10x10 hardware binning combined with a high gain is used. A MFM image of the illuminated sample and a detected diffusion pattern (from multiple shot exposure) are present in insets.

FIG. 2. (Color online) Scattering efficiency from 45 to 70 eV (H29 to 45). The expected scattering efficiency from Rel. (1) is plotted on Fig. (a). The circles in figure (b) represent the measured scattering efficiency on the table-top setup (the dotted line is there to guide the eye). Error bars are evaluated from dispersion of several measurements performed independently. The star symbols in (a) are positioned at the discrete harmonic photon energies. The insets show the corresponding recorded scattering patterns. Well-defined Bragg peaks, corresponding to the domain periodicity, are observed.

FIG. 3. (Color online) Multiple shot (400) vs. single shot detection of the resonant magnetic scattering detection at the Co M-edge and measurements of the spatial properties of the nano-domains. The multiple shot detection of the magnetic scattering resonance is shown on Fig. (a) and the single shot detection is shown on Fig. (b). The azimuthal integration as function of the angle φ (arbitrary origin) is shown on Fig. (c) for multiple shot detection and Fig. (d) for single shot detection. The radial integration of the detection (symbols) as a function of q is presented on Fig. 2(e) (multiple shot detection) and 2(f) (single shot detection) with the best pseudo-Voigt fit of the data (continuous and dash lines, respectively). The central part of the scattering patterns with the pixels saturated because of the direct beam has been removed prior to integrations.

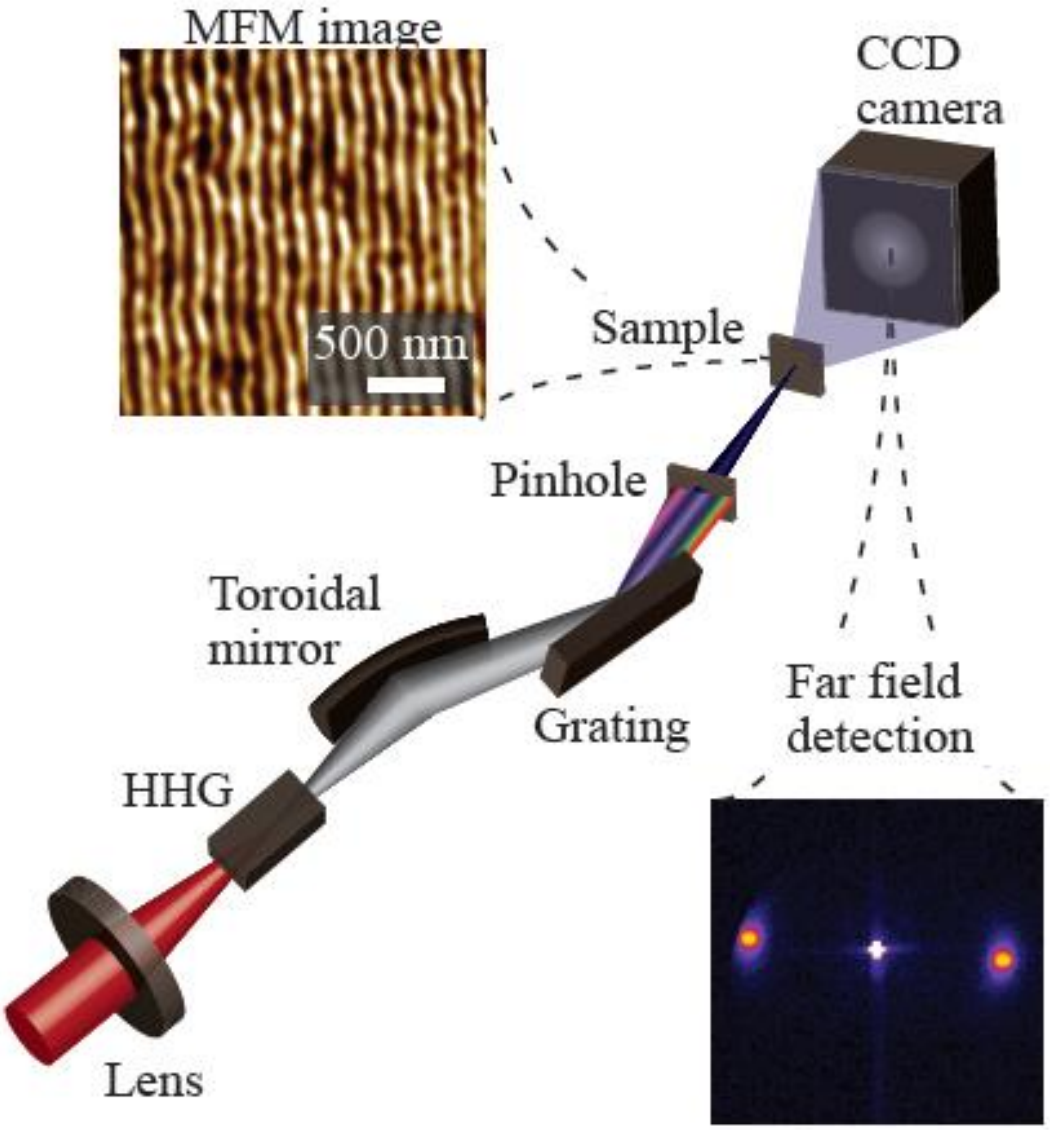
MFM image
500 nm
CCD
camera
Sample
Pinhole
Toroidal
mirror
Grating
Far field
detection
HHG
Lens

Figure 1

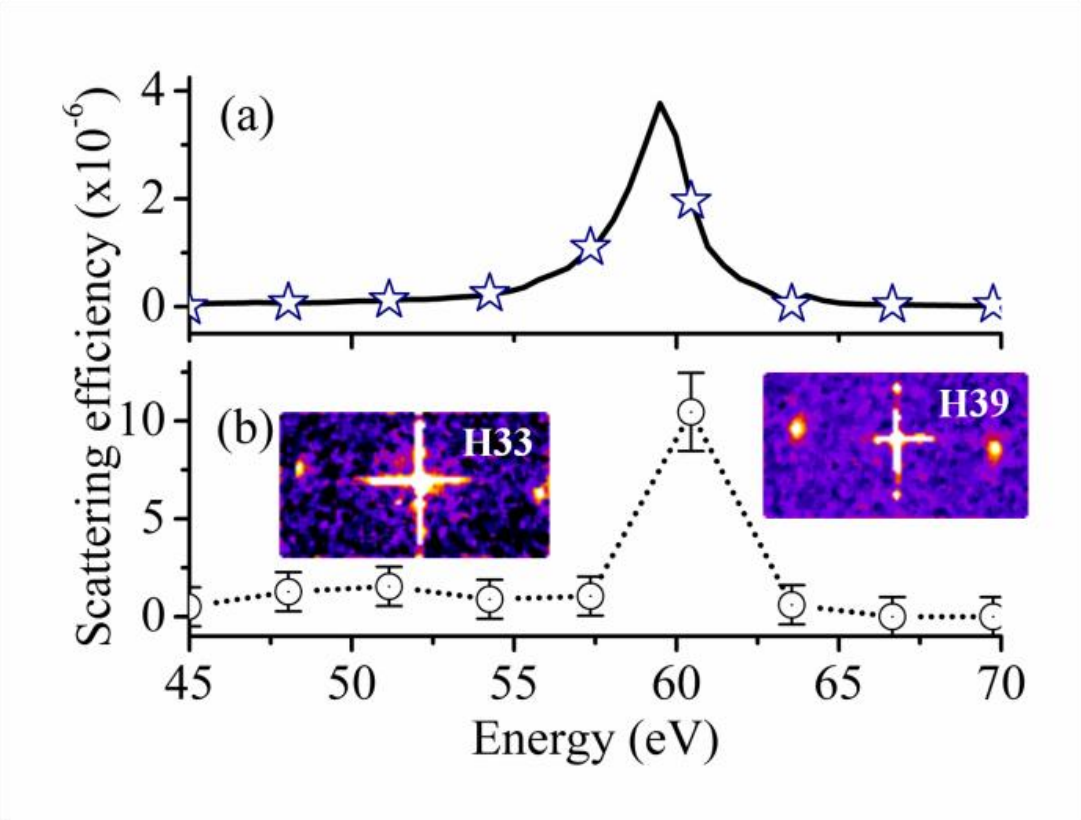
(a)
(b)
H33
H39
Scattering efficiency (x10^{-6})
Energy (eV)
0
2
4
0
5
10
45
50
55
60
65
70

Figure 2

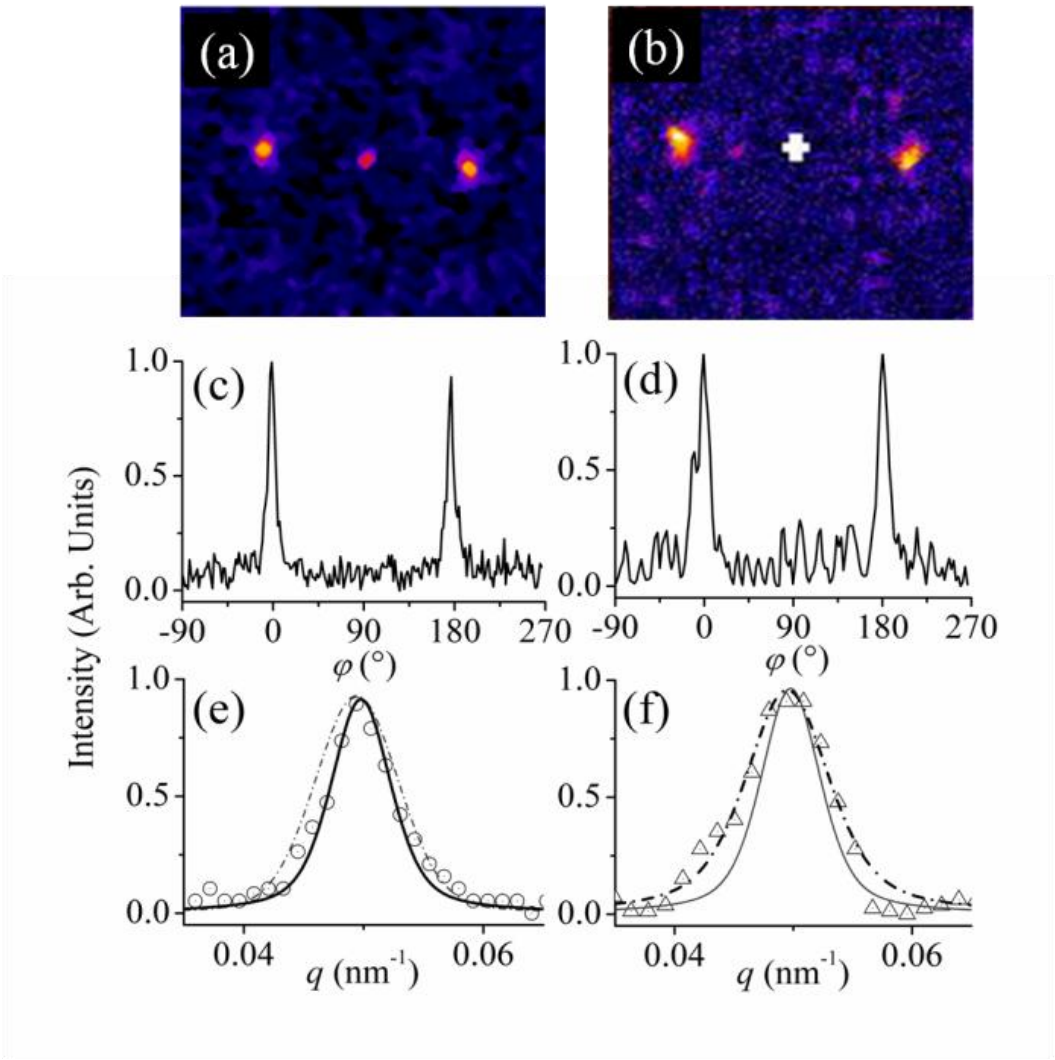
(a)
(b)
(c)
(d)
(e)
(f)
Intensity (Arb. Units)
1.0
0.5
0.0
-90
0
90
180
270
φ (°)
0.04
0.06
q (nm-1)

Figure 3

1 S. D. Bader, Reviews of Modern Physics **78,** 1 (2006).

2 S. S. P. Parkin, M. Hayashi, and L. Thomas, Science **320,** 190-194 (2008).

3 E. Beaurepaire, J. C. Merle, A. Daunois, and J. Y. Bigot, Physical Review Letters **76,** 4250 (1996).

4 C. Gutt, S. Streit-Nierobisch, L. M. Stadler, B. Pfau, C. M. Günther, R. Könnecke, R. Frömter, A. Kobs, D. Stickler, H. P. Oepen, R. R. Fäustlin, R. Treusch, J. Feldhaus, E. Weckert, I. A. Vartanyants, M. Grunze, A. Rosenhahn, T. Wilhein, S. Eisebitt, and G. Grübel, Physical Review B **81,** 100401 (2010).

5 J. Stöhr and H. C. Siegmann, *Magnetism: from fundamentals to nanoscale dynamics*, Vol. 15 (Springer Berlin, Germany, 2006).

6 B. T. Thole, P. Carra, F. Sette, and G. van der Laan, Physical Review Letters **68,** 1943 (1992).

7 P. Carra, B. T. Thole, M. Altarelli, and X. Wang, Physical Review Letters **70,** 694 (1993).

8 J. Stöhr and H. König, Physical Review Letters **75,** 3748 (1995).

9 J. Miao, P. Charalambous, J. Kirz, and D. Sayre, Nature **400,** 342 (1999).

10 J. Miao, R. L. Sandberg, and C. Song, Selected Topics in Quantum Electronics, IEEE Journal of**,** 1-1 (2012).

11 S. Eisebitt, J. Luning, W. F. Schlotter, M. Lorgen, O. Hellwig, W. Eberhardt, and J. Stohr, Nature **432,** 885 (2004).

12 J. J. Turner, X. Huang, O. Krupin, K. A. Seu, D. Parks, S. Kevan, E. Lima, K. Kisslinger, I. McNulty, R. Gambino, S. Mangin, S. Roy, and P. Fischer, Physical Review Letters **107,** 033904 (2011).

13 H. N. Chapman, A. Barty, M. J. Bogan, S. Boutet, M. Frank, S. P. Hau-Riege, S. Marchesini, B. W. Woods, S. Bajt, W. H. Benner, R. A. London, E. Plonjes, M. Kuhlmann, R. Treusch, S. Dusterer, T. Tschentscher, J. R. Schneider, E. Spiller, T. Moller, C. Bostedt, M. Hoener, D. A. Shapiro, K. O. Hodgson, D. van der Spoel, F. Burmeister, M. Bergh, C. Caleman, G. Huldt, M. M. Seibert, F. R. N. C. Maia, R. W. Lee, A. Szoke, N. Timneanu, and J. Hajdu, Nature Physics **2,** 839 (2006).

14 T. Wang, D. Zhu, B. Wu, C. Graves, S. Schaffert, T. Rander, L. Müller, B. Vodungbo, C. Baumier, D. P. Bernstein, B. Bräuer, V. Cros, S. d. Jong, R. Delaunay, A. Fognini, R. Kukreja, S. Lee, V. Lopéz-Flores, J. Mohanty, B. Pfau, H. Popescu, M. Sacchi, A. B. Sardinha, F. Sirotti, P. Zeitoun, M. Messerschmidt, J. J. Turner, W. F. Schlotter, O. Hellwig, R. Mattana, N. Jaouen, F. Fortuna, Y. Acremann, C. Gutt, H. A. Dürr, E. Beaurepaire, C. Boeglin, S. Eisebitt, G. Grübel, J. Lüning, J. Stöhr, and A. O. Scherz, Physical Review Letters (accepted).

15 R. L. Sandberg, A. Paul, D. A. Raymondson, auml, S. drich, D. M. Gaudiosi, J. Holtsnider, R. a. I. Tobey, O. Cohen, M. M. Murnane, H. C. Kapteyn, C. Song, J. Miao, Y. Liu, and F. Salmassi, Physical Review Letters **99,** 098103 (2007).

16 A. Ravasio, D. Gauthier, F. R. N. C. Maia, M. Billon, J. P. Caumes, D. Garzella, M. Géléoc, O. Gobert, J. F. Hergott, A. M. Pena, H. Perez, B. Carré, E. Bourhis, J. Gierak, A. Madouri, D. Mailly, B. Schiedt, M. Fajardo, J. Gautier, P. Zeitoun,

P. H. Bucksbaum, J. Hajdu, and H. Merdji, Physical Review Letters **103,** 028104 (2009).

17 P. Agostini and L. F. DiMauro, Reports on Progress in Physics **67,** 813 (2004).

18 J. Seres, E. Seres, A. J. Verhoef, G. Tempea, C. Streli, P. Wobrauschek, V. Yakovlev, A. Scrinzi, C. Spielmann, and F. Krausz, Nature **433,** 596-596 (2005).

19 M. C. Chen, P. Arpin, T. Popmintchev, M. Gerrity, B. Zhang, M. Seaberg, D. Popmintchev, M. M. Murnane, and H. C. Kapteyn, Physical Review Letters **105,** 173901 (2010).

20 D. Gauthier, M. Guizar-Sicairos, X. Ge, W. Boutu, B. Carre, J. R. Fienup, and H. Merdji, Physical Review Letters **105,** 093901 (2010).

21 C. La-O-Vorakiat, M. Siemens, M. M. Murnane, H. C. Kapteyn, S. Mathias, M. Aeschlimann, P. Grychtol, R. Adam, C. M. Schneider, J. M. Shaw, H. Nembach, and T. J. Silva, Physical Review Letters **103,** 257402 (2009).

22 B. Vodungbo, A. B. Sardinha, J. Gautier, G. Lambert, M. Lozano, S. Sebban, E. Meltchakov, F. Delmotte, V. Lopez-Flores, J. Arabski, C. Boeglin, E. Beaurepaire, R. Delaunay, J. Lüning, and P. Zeitoun, Europhysics Letters **94,** 54003 (2011).

23 H. C. Mertins, P. M. Oppeneer, J. Kunes, A. Gaupp, D. Abramsohn, and F. Schäfers, Physical Review Letters **87,** 047401 (2001).

24 S. Valencia, A. Gaupp, W. Gudat, H.-C. Mertins, P. M. Oppeneer, D. Abramsohn, and C. M. Schneider, New Journal of Physics **8,** 254 (2006).

25 S. Flewett, S. Schaffert, J. Mohanty, E. Guehrs, J. Geilhufe, C. M. Günther, B. Pfau, and S. Eisebitt, Physical Review Letters **108,** 223902 (2012).

Paper VI

Paper VI presents the study of two samples composed of respectively 20 layers (sample "A") and 30 layers (sample "B") of [Co(4Å)/Pd(6Å)] with aligned (A) or labyrinthine (B) nanodomains structures. Spectral studies are done with two-color generations to refine the sampling ratio compared to Paper V. Single-shot detections are realized both for aligned and labyrinthine organizations. The nanodomains width in sample B is estimated to be 108 nm ± 70 nm with measured scattering efficiency in the 10^{-6} range, which agrees with theoretical values. The nanodomains width is reduced to 91 nm ± 6 nm in sample A, due to a better alignment organization during the magnetization process. The resonant peak of palladium N edge is clearly observed and resolved in all samples.

Submitted.

Sub-100 nanometer lensless probing of Co/Pd magnetic nanodomains using a table-top femtosecond soft X-ray harmonic source

X. Ge,[1] M. Ducousso,[1] W. Boutu,[1] B. Barbrel,[1] D. Gauthier,[1] F. Wang,[1] A. Borta,[1] A.-I. Gonzalez,[1] B. Iwan,[1] M. Billon,[1] M. Perdrix,[1] D. Guillaumet,[1] F. Lepetit,[1] B. Vodungbo,[2] J. Gautier,[2] P. Zeitoun,[2] R. Hawaldar,[3] B. Tudu,[3] R. Delaunay,[3] M. Tortarolo,[3] J. Lüning,[3] and H. Merdji[1]*

[1]*CEA-Saclay, IRAMIS, Service des Photons, Atomes et Molécules, 91191 Gif-sur-Yvette, France*

[2]*Laboratoire d'Optique Appliquée, ENSTA ParisTech – CNRS – Ecole Polytechnique, Chemin de la Hunière, 91761 Palaiseau, France*

[3]*Laboratoire de Chimie Physique Matière et Rayonnement, Université Pierre et Marie Curie, UMR du CNRS (7614), 11 Rue Pierre et Marie Curie, 75005 Paris, France*

*Corresponding author: hamed.merdji@cea.fr

Sub-100 nanometer lensless probing of Co/Pd magnetic nanodomains using a table-top femtosecond soft X-ray harmonic source

We present recent developments of our table-top femtosecond high flux harmonic beamline. High harmonic generation (HHG) optimization in a single and two-color infrared laser pulse mode is investigated at high laser energy. Up to 10^9 photons are generated between 40 and 80 eV in a single femtosecond laser shot. The soft X-ray light is applied to characterize at the nanoscale the magnetic network of Co/Pd multilayer samples using small angle scattering. Cobalt and palladium magnetic resonant edges, respectively at 60 and 51 eV, are identified and investigated. A two-color HHG sampling allows to resolve them over a large spectral band. The palladium resonance, which was not expected, is attributed to a significant transmission from the cobalt magnetic layers to the palladium layers. The phenomenon is investigated in various samples, which differs in composition and number of layers. The spatial organization of magnetic nano-domains is also inferred with sub-100 nanometers spatial resolution from a single femtosecond soft X-ray flash. These results open the gate for broad ultrafast dynamics studies in Nanoscience.

Keywords: Femtosecond laser, high harmonic generation, resonant elastic scattering, single shot probing, ultrafast spectroscopy, nanomagnetism

1. Introduction

The invention of new revolutionary materials always leads to new era of technologies, particularly in communication and energy areas. Understanding the properties of these materials requires accurate observation of the physical and/or chemical evolution in structure (spatial) and in dynamic (temporal) of the studied object on ultrashort time scales (from attoseconds down to femtoseconds) and on extremely small space coordinates (from angstroms down to nanometers). In nanoscience, there is a clear and pressing need for new techniques to track ultrafast processes at a nanometer scale. Ultrafast light pulses of very short wavelengths would be ideal to visualize such transient phenomena, such as Free Electron Lasers (FELs) or high order harmonics. Spectral studies are also necessary when tracking material properties around resonances. A light source tunable over a large spectral bandwidth would be advantageous for such studies. Moreover, investigations of irreversible phenomena impose single-shot acquisitions which require using a high brightness probe pulse. The intense X-ray pulses available at FELs seems to be an ideal source for such studies [1]. However, recent demonstrations of single-shot diffractive imaging using table-top high harmonic generation (HHG) promise another possible way for ultrafast nanoscale studies [2-4]. The sub-100 nm spatial resolution obtained in these works is suitable for various applications.

Here, we present recent advances in the characterization of magnetic nano-domains using our table-top high flux harmonic beamline. Such convenient and low cost laboratory sources are a good alternative to synchrotrons or FELs for numerous studies, from spectral to time and spatially resolved measurements. Intense HHG pulses are used here to characterize the spatial arrangement of magnetic nanodomains. Moreover, the broadband spectrum of HHG facilitates the studies around magnetic resonant edges [5-7]. The tunability of the source allows scanning around the different resonance edges. The transfer of magnetism between different material layers is observed. In this communication, we also demonstrate that the table-top high flux harmonic beamline allows performing single shot characterization of the magnetic spatial organization. This opens new routes for the investigations of magnetic phenomena such as the ultrafast all optical control of magnetic materials [8,9] giving light into the complex interplay of interactions spanning a wide range of degrees of freedom. Combining nanometer and femtosecond resolutions in a time resolved imaging investigation would certainly provide additional clues.

The first section presents on the development of our high flux harmonic beamline. We report our recent effort in tuning the source and pushing its yield for spectral studies and single-shot soft X-ray scattering measurements of magnetic nano-domains. The second section is dedicated to the description of magnetic samples and the resonant scattering set-up. The experimental results of the magnetic measurements are reported in the third section.

2. High flux XUV harmonic beamline

2.1 Optical configuration for spectrally resolved magnetic investigations

Recent demonstrations of single-shot coherent imaging on our table-top harmonic source at the CEA Saclay research center (France) have demonstrated a high flux harmonic beamline providing intense XUV single pulse available for nanometric imaging with femtosecond time resolution [3,4,10]. In these communications, the probing light is the 25^{th} harmonic (λ=32 nm, @38.7 eV) of a 800 nm infrared laser, generated in argon gas. Single shot coherent imaging has been demonstrated with a sub-100nm spatial resolution mainly limited by the signal and the wavelength. Using shorter wavelengths would lead to better spatial resolution, and would furthermore allow studies around resonance edges of numerous materials.

We report here our results on the generation of a high flux harmonic source around the cobalt M-edge corresponding to a wavelength of 20 nm (E=60 eV). The experimental setup is presented in Fig.1. The optimization of the HHG yield has been performed to fulfill the requirements for the magnetic scattering investigation presented in the next sections. We have focused on improving the HHG intensity and the spatial profile, and on tuning the spectrum of the harmonics to better match the cobalt M-edge. The harmonic beamline is driven by the table-top Ti:sapphire laser system LUCA (Laser Ultra Court Accordable), which delivers up to 50 mJ energy pulses at 800 nm with a pulse duration of 50 fs and a repetition rate of 20 Hz. The beam is then focused using a long focal length lens (f = 5.56 m) into a variable length gas cell filled with neon. The motorized gas cell has an adjustable length between 0 cm and 15 cm and a gas pressure controller. Phase matching is mainly adjusted by finely tuning the beam diameter with a diaphragm set just before the lens. The HHG spectrum is analyzed using a set of a toroidal mirror (f = 0.75 m) and a blazed grating arranged in a 4f configuration. A pinhole placed after the grating is used to select a single harmonic order. A movable photomultiplier placed at 1.5 m from the toroidal mirror detects the harmonic signals going through the

pinhole. When the photomultiplier is moved out, an X-ray charge-coupled device camera located at 3.5 m from the toroidal mirror is used to investigate the harmonic far field spatial profile. Aluminium filters (150 nm thickness) are located at different positions in the beam path to cut the residual infrared light and reduce the harmonic beam intensity to avoid the detector saturation. Then, for magnetic investigations, the sample is placed at the focus of the toroidal mirror and the scattering patterns are detected using the X-ray CCD camera set in the far field. During these measurements, the camera is cooled down to 233 K to reduce the detection noise.

2.2 Optimization of the high harmonics generation in the 60 eV energy range

The optimization study of HHG in neon has been carried out for the 37th (57.4 eV) and the 39th (60.5 eV) harmonics, which are the closest ones to the Cobalt M-edge. First, we have upgraded the loose focusing scheme reported in ref. [3] which allows coupling a high amount of laser energy (few tens of mJ) in the generating media. Since the HHG phase matching depends on the IR laser focusing quality and its propagation in the generating medium, the wave front and the spatial profile of the IR laser along with its temporal properties have important roles in the HHG process. In order to enhance the HHG yield and the beam properties we have used a modal filtering through an optical fibre with an active pointing stabilization to optimize the infrared laser beam quality at the focus. This results in a quasi-Gaussian beam with up to 40 mJ of laser energy. As a result, the HHG signal has been strongly improved: the beam is very stable from shot to shot in shape, intensity and position. This was also reproducible from one day to the other (which was not the case in our previous work).

Second, we have explored systematically the different parameters: beam aperture, gas pressure, cell length, IR laser energy and lens focus position. Following the methodology of Ge et *al.* [10], we looked for HHG conditions that optimize both the harmonic flux and the far field spatial distribution of the beam. There is an optimum range of the laser focus between 0 and 5cm behind the gas cell output. If the laser is focused before the gas cell output, the intensity and the spatial profile of the harmonic beam become worse while approaching the laser focus towards the gas cell input. When the laser focus goes further behind the gas cell output (maximum 8 cm behind, limited by the translation stage of the lens), the harmonic beam intensity decreases slowly and its spatial profile remains relatively good. This phenomenon is related to the self-guiding of the laser pulse during the propagation in the

generating medium. The self-guiding effect can enhance the laser properties (such as the laser intensity distribution) and the phase-matching condition. It has been shown that these conditions strongly depend on the gas cell position [11] with respected to the focused laser. When the gas jet is located before the laser focus, Kim et *al*. observed that the harmonic beam intensity increases dramatically (two orders of magnitude higher). Our experimental results show similar effect on the generated harmonic beam with about three times higher intensity. More importantly, the spatial profile of harmonic beam is more homogeneous in the optimum range. The best parameters values for the generation of H39 are listed in table 1. The harmonic flux of H37 and H39 rise routinely up to 10^9 photons per pulse after optimization, which is one order of magnitude lower than what can be generated in argon at longer wavelength (H25, λ=32 nm). It agrees well with the ratio of harmonic generation efficiency between argon and neon.

2.3 High harmonics energy tuning to match the resonances edges of the inspected materials

The purpose of the HHG beam optimization at high laser energy is to perform quantitative magnetic scattering studies. However the source has a discrete spectral distribution composed of odd harmonic of the driving infrared laser frequency. This prevents an accurate characterization of the magnetic resonances. A way to increase the spectral sampling and to match the magnetic resonances would be to tune the harmonic beam. Indeed, neither H37 nor H39 correspond to the top of the resonant peak of the Cobalt $M_{2,3}$ edge (see Fig.3). The scattering efficiency would double, if H37 or H39 could be shifted to the center of the resonant peak. Unfortunately, the fundamental energy of the laser cannot be tuned to get harmonics matching the exact value of the cobalt M-edge resonance.

According to previous works, it is possible to blue-shift the harmonics in the spectrum due to the self-phase modulation of the laser pulse caused by ionization in gas medium [12,13,14], and due to the nonadiabatic effect driven by the rapid increase in the femtosecond laser electric field [15,16]. Large blue-shifts can cover the interval between odd harmonics [15,16]. Several parameters can be tuned to induce a blue-shift, such as laser intensity, the laser pulse duration and the gas density. We have taken spectra in different generating conditions to study the possibility of shifting H37 or H39 to better match the resonant peak. We have been varying the beam aperture, the laser energy, the gas pressure but a spectral shift was observed only when varying the laser chirp. The recorded shifts are presented in Fig. 2. For each figure,

the plot in line is the same reference (optimized) value of pulse duration, related to the optimized distance between the gratings of the laser pulse compressor. On Fig. 2(a), one can observe a blue shift with respected to the reference, while on Fig. 2(b) a red shift appears. Such variations are related to the laser chirp, negative in Fig. 2(a) and positive in Fig 2(b). In all cases, chirping the laser reduces the HHG yield. This is mainly due to the stretch of the laser pulse from the initial pulse duration of 50 fs to 90 fs for the higher chirps. Unfortunately, we did not get any significant spectral shift to center one harmonic order to the resonant peak as the shift is rather small, of about 0.26 eV either to the red or to the blue direction.

Another possible method to reach a photon energy closer to the high scattering efficiency of the cobalt M-edge is to use the even order harmonic H38 (58.89 eV). The latter can be generated in a "ω + 2ω" configuration (two-color HHG). By mixing the fundamental and its second harmonic, we break the inversion symmetry in the HHG process and generate both odd and even harmonics [17]. In the context of magnetic studies, this would give to a finer spectral sampling of the scattering properties. Moreover the 38^{th} harmonic order (at an energy of 58.9 eV) lies very close to the cobalt maximum scattering efficiency. Fig. 1 presents the spectra of one-color (red columns) and two-color (gray columns) generation, obtained by inserting a 0.2 mm thick Beta Barium Borate (BBO) type I crystal in the beam path before the cell. Note that the two spectra were acquired for different generation conditions, the optimum set of parameters being different in each case. The sharp cut-off of the one-color spectrum is due to the aluminum filter's cut-off. The harmonic flux in the two-color generation scheme is reduced by a factor of about 4 compared to the one-color geometry. In addition, the cutoff of the HHG is shifted towards lower energies (from 70 eV to 62 eV), as previously reported [17]. However, the odd and even harmonic orders are efficiently generated around the cobalt M-edge.

3. Optical measurements of magnetic networks at the nanoscale

3.1. ***Samples and measurement principles***

Our optimized soft X-ray beamline has been used to characterize the scattering from magnetic nanodomains. The first samples consisting of [Co/Pd] multilayers are fabricated by magnetron sputtering technique on a 30 nm thin silicon nitride membrane [18]. Sample "A" is composed of 20 layers of [Co(4Å)/Pd(6Å)] and forms a square membrane of 200x200 μm^2. Sample "B"

has 30 layers of [Co(4Å)/Pd(6Å)] on a square membrane of 250x250 μm^2. The magnetic nano-domains structures presented on these samples are prepared in two different configurations: well-aligned stripes (sample "A") and labyrinthine (sample "B") (Fig. 3), depending on the fabrication procedure. The width of the nanodomains results from the balance between magnetostatic energy versus domain walls energy and varies with the film thickness [19]. Labyrinth (aligned) stripe domains can be obtained from demagnetization of the film with perpendicular (in-plane) external magnetic field. The alignment of the domains leads to a size reduced by ~30% compared to a labyrinthine spatial organization [19].

The origin of the resonant magnetic scattering is based on the interactions (spin-orbit and exchange interactions) occurring between the core levels and the valence bands [20]. As a consequence, the optical index ($n_{\pm}$) of the two nanodomains (with up and down magnetization directions) around the absorption edges of such materials are different, which can be described as:

$$n_{\pm} = 1 - (\beta \pm \Delta\beta) + i * (\delta \pm \Delta\delta), \qquad \text{(Eq. 1)}$$

where $\Delta\beta$ and $\Delta\delta$ represent respectively the real (dispersion term) and imaginary (absorption term) parts of the optical index difference between spin up and down nanodomains. The magnetic contrast can be observed at the $M_{2,3}$ absorption edge of the cobalt at 60eV. Due to the optical index difference between the nanodomains having up and down spin states, the samples act as a transmission grating for the incoming light. Small-angle scattering (SAXS) detection is used to investigate the magnetic properties and the spatial organization of the nanodomains. A diffraction pattern will evolve from two well-defined Bragg peaks in the case of well-aligned stripes (Fig. 1) to a scattering ring if the structure is completely disordered (Fig. 4). Provided that the pattern oversampling conditions are fulfilled, an image of the nano-domains can be reconstructed using coherent diffractive imaging techniques and phase retrieval algorithms [21]. This was not the goal of this experiment. We are concerned here by extracting spatial information from the far field scattering pattern. Its efficiency *D* is defined as the ratio between the number of scattered photons with respect to the number of incident photons. *D* can be estimated by the following relation:

$$D(E) \sim T(E)\,(Ed)^2\,[\Delta\beta(E)^2+\Delta\delta(E)^2], \qquad \text{(Eq. 2)}$$

where T, *d* and E are the sample's optical transmission, the thickness of the resonant material and the photon energy. Using the data of cobalt optical index from the literature [22], the

scattering efficiency of the sample is estimated in the 10^{-8} range for photon energies far away from the Co M-edge, and around 10^{-6} for photon energies close to the resonant edge.

3.2 Spectral measurement of the magnetic scattering efficiency using the "ω+2 ω" high harmonic configuration

Using both one-color and two-color generation schemes, we have measured the magnetic scattering efficiency over a large spectral bandwidth from 45 eV to 70 eV. Magnetic samples are located on a nano-motorized holder at the focus of the toroidal mirror where the harmonic beam size is estimated to be around 200 μm of diameter. The CCD camera is mounted on a translation stage behind the sample holder so that the distance between the detector and the sample can be adjusted from 2 to 5 cm. Figure 3 presents the measured scattering efficiency diagram of sample "A". The experimental values (open and full symbols for odd and even harmonics, respectively) are mean values over thousands of shots. We observe two scattering maxima located at 51 and 60 eV. The results are compared to the simulations (black line) extracted from Eq. (2) (note that the simulations include only the cobalt optical indexes). One can note the good agreement around the cobalt M-edge resonance. The simulation is adjusted to the experiment using a proportionality factor of α=0.8. This value can be related to the accuracy of the simulated complex optical indexes [22]. Additional errors come from the determination of to the direction of the easy magnetization axis *Ms* of the sample with respect to the incident optical wave vector. Indeed, the easy magnetization axis of the sample results from the competition between the magneto-crystalline anisotropy and the shape anisotropy [23]. They induce out-of-plane and in-plane easy magnetizations, respectively. *Ms* can thus be tilted with respect to the direction normal to the sample surface. However the measurement gives access only to the direction of the incident wave vector k_i, as illustrated in inset of Fig. 3. M_s should then be located in a 30° cone according to the measurement.

The fine spectral sampling provided by the two-color HHG source allows us to visualize the resonance peaks. The main peak around 60 eV corresponds to the photons scattered by the cobalt magnetic layers. At lower photon energies, we also measured a weaker resonance peak, not reproduced by the numerical simulation. This peak corresponds to the palladium N-edge, at 51 eV. This resonance was not expected, as the magnetization of the palladium was not thought to be detectable, *i.e.* the magneto-optic values of the sample at the Pd N-edge were thought negligible. This implies that a significant magnetization has been transmitted in the sample from the cobalt to the palladium. Further measurements and analysis are necessary to

understand the physics behind this behavior.

3.3 Single-shot measurements of the magnetic nanodomains network

The low scattering efficiency from the magnetic nanodomains requires intense X-ray pulses to reach the single laser shot regime, mandatory for time resolved studies of optically induced demagnetization. This would give access to irreversible phenomena occurring for example at high energy density excitation. The scattering efficiency of H38 is slightly better than H39. However, H39 benefits of 4 times higher incident flux. Because of the tradeoff between flux and scattering efficiency, a higher signal to noise ratio has been achieved for H39 than H38, which is critical for scattering patterns analysis. H39 is consequently the more suitable order for our single-shot experiments. We present in this section the experimental results obtained on sample "B".

The uniform radial distribution of the scattered photons into a ring centered on the direct beam is the signature of the labyrinthine organization of the magnetic network. This is a less favorable situation as it leads to a lower signal to noise ratio. According to the transmission and the optical index of the sample, the scattering efficiency is estimated to be 1.08×10^{-6} for H37 (57.4 eV) and 1.13×10^{-6} for H39 (60.5 eV) (see table 2). To compensate for the low scattering efficiency, we have pushed the HHG source to its extreme yield (10^9 photons per shot) by coupling the maximum IR laser energy available but at the cost of the shot to shot stability. Figure 4 presents two single-shot scattering patterns measured using H37 and H39. The scattering rings are clearly visible. We found a good agreement of the scattering efficiency in the 10^{-6} range at both energies. Single-shot scattering signals have only been detected for H37 and H39, close to the edge. The center spots corresponding to the direct beam saturate the CCD camera and are taken into account during the analysis. The average size of the nano-domains is calculated from the spatial integration of the detected scattering ring as a function of the wave vector transfer, q. Normalized measurements (symbols) and the best pseudo-Voigt fit of the data are presented in Fig. 4. The maximum of the scattering intensity is detected at $q = 0.029 \pm 3 \times 10^{-4}$ nm^{-1}. At this position, we calculated the average size of the nano-domains, equal to 108 nm. The nano-domains width distribution ($\pm\Delta q$) is given by the full width half maximum of the integrated scattering intensity. We measured $\Delta q = 0.022 \pm 5 \times 10^{-4}$ nm^{-1} for H37 (57.4 eV) and $\Delta q = 0.018 \pm 3 \times 10^{-4}$ nm^{-1} for H39 (60.5 eV). These two values correspond to a domain width distribution of ± 90 nm and ± 70 nm, respectively. We have performed the same analysis for sample "A", presenting aligned nano-

domains. From the measured scattering pattern, we deduced an average nano-domains size of 91 nm and a width distribution of ± 6 nm, which is significantly lower than sample "B". This difference is related to the thickness of the magnetic sample, and to the difference into the spatial organization of the magnetic network, i.e. aligned versus labyrinthine [21,24].

3.4 Investigations of various [Co/Pd] magnetic samples around Co M-edge and Pd N-edge

After the single shot demonstrations, we have performed exhaustive studies of different magnetic samples. The goal was to optimize the magnetic scattering efficiency by varying the sample composition. It has practical interest for the design of future single shot imaging and time resolved experiments and, beyond this, it gives insight into the underlying physics of magnetism at a nanometer scale.

Experiments are realized over a large spectral bandwidth using the two colors spectral sampling setup. This allows resolving the samples scattering both the palladium N-edge and the cobalt M-edge. We have studied various samples that differ in the magnetic layers repetition number and in the thickness of one magnetic element with respect to the other. The samples are described in table 3. The total thicknesses of the cobalt and of the palladium in the inspected samples range from 40 to 160 nm and from 40 to 240 nm, respectively, while the layers repetition number varies from 15 to 80. The measurements of the scattering efficiency of the samples around the Cobalt M-edge are presented on Fig. 5(a,c) while measurements around the palladium N-edge are reported on Fig. 5(b,d). We have also plotted the results as a function of the repetition number of the layers (fig. 5(a,b)) and as a function of the thickness of the resonant material at the inspected energy (fig. 5(c,d)). As a general behavior of the magnetic scattering efficiency, we observed for all the samples that the magnetic scattering efficiency decreases when the sample gets thicker. This can be explained from Eq. 2: the scattering efficiency increases quadratically with the thickness of the resonant material, but is proportional to the sample's transmission, which itself decreases exponentially with the sample thickness. In Fig. 5(a,c), a maximum scattering efficiency of $2.4\ 10^{-5}$ at the Co M-edge has been measured for a cobalt thickness of 40 nm. This is one order of magnitude higher than the value measured for sample B used for the single shot measurements, which has a cobalt thickness of 120 nm. Note that, it is impossible to further increase the scattering signal by reducing the cobalt thickness below 40 nm. Indeed, a minimum thickness is necessary to create an out of plane magnetic anisotropy. This sets a limit to the maximum

scattering efficiency of the magnetic samples.

In Fig. 5(b,d), we note that the scattering of palladium has not been observed for all the samples. Actually, we explain this by the fact that a minimal thickness of cobalt between layers of palladium is required to induce a significant transfer of magnetism. Our results show that a thickness of 2 Å of cobalt between layers of Palladium is not enough to induce a magnetic activity in the palladium layers, as illustrated on fig. 5(b). 4 Å of cobalt between layers of Palladium is measured to be the minimum thickness to induce a magnetization of the palladium layers. Similarly to cobalt, the magnetic scattering efficiency of palladium increases when decreasing the material thickness. At the Pd N-edge, a maximum of 1.5 10^{-5} efficiency is measured for a palladium thickness of 40 nm. The high transfer of magnetization is ensured for this sample by a cobalt thickness of 80 nm. However for this value, we observe a low scattering efficiency at the Co M-edge (Fig 5a,c).

4. Conclusion

In summary, we have first reported on the optimization of one-color and two-color HHG beamline in neon, providing from 10^8 to 10^9 photons per pulse. We have presented then single and multiple-shot investigations of the X-ray scattering from [Co/Pd] magnetic nano-domains of various [Co/Pd] compositions using a table-top high flux harmonic beamline. Using the two-color HHG configuration, we have realized spectral studies over a 20 eV bandwidth with a sampling step of 1.55 eV that allows resolving both cobalt and palladium magnetic resonances, respectively at 60 eV and 51 eV photon energies. Moreover, we have demonstrated that spatial information of the magnetic nano-domains organization can be extracted from single-shot measurements with nanometric spatial resolution in femtosecond flash of light. Note that the single shot studies were performed with a modest scattering efficiency of $1x10^{-6}$. A study of the magnetic scattering efficiency of various samples, which differ in the repetition number of layers and in their composition, has been conducted. We have observed a maximum scattering efficiency of $2.4x10^{-5}$ at the Co M-edge for a Co thickness of 40 nm and $1.5x10^{-5}$ at the Pd N-edge for a Pd thickness of 40 nm. In the next future, this result will allow improving the scattering signal by one order of magnitude in the single shot studies. This is also promising for single shot real-space imaging of the magnetic domains using phase retrieval approaches.

These experiments have demonstrated the potential of intense HHG beamlines for physical investigation in solid states physics. For instance, the multiple-shot acquisition allows a fine spectral study of a physical behavior. The single-shot scattering experiments pave the way for future ultrafast dynamic studies, particularly for the observation of irreversible phenomena, such as laser-induced demagnetization. More generally, it gives access to studies of a broad range of complex mesoscopic systems, as for example nanoscale phase transitions and photo-chemistry.

Acknowledgements: We acknowledge the Saclay SLIC laser team. We acknowledge financial support from the European Union through the EU-LASERLAB and the EU–FP7 ATTOFEL and X-Motion programs, from the French ministry of research through the 2009 ANR grants ”I-NanoX” and ”Femto-X-Mag”, from the ”Triangle de la Physique” through the COX grant and the C’NANO research program through the X-NANO, DYNAVO and DYNAVO PosDoc grants. The authors RH and BT and would like to thank the European Commission for Postdoctoral and Doctoral fellowships through Erasmus Mundus program.

Figure 1. Schema of the experimental setup. Two HHG spectrums are presents in inset. The high intensity spectrum is recorded in a classical HHG scheme and the lower intensity spectrum is obtained using a two-color scheme, generating odd and even harmonic orders. A typical detected scattering pattern is also presented. (The color version of this figure is included in the online version of the journal.)

Table 1. Optimum value empirically identified to generate around 10^9 photons per pulse at 60 eV. More photons can be generated using different parameters but at the expense of the spatial profile and the reproducibility of H39 laser pulse characteristics from shot to shot.

Figure 2. Blue (a) and red (b) shifts of high harmonics with respects to the reference: the optimized HHG (line). In both figures, when the pulse duration is increased (by changing the distance between the gratings of the optical compressor), the blue/red shift increases. The observed shifts are smaller than 0.26 eV. (The color version of this figure is included in the online version of the journal.)

Figure 3. Measured scattering efficiency on the HHG table-top setup (symbols) confronted with the theoretical model (continuous line). The experimental data are obtained by calculating the ratio between the number of the scattering photons detected on the CCD camera with respect to the number of incident photons. The theoretical model is adjusted using a scaling factor. This factor can be related to an angle between the incident optical wave vector and the magnetization of the sample, as presented in inset. The figure illustrates the principle of the inspected sample: it is a multilayer of 20 repetitions of [Co(4 Å)/Pd(6 Å)], that forms magnetic nanodomains, as revealed with the MFM image. (The color version of this figure is included in the online version of the journal.)

Table 2. Transmissivity of sample “B” and sum of the square of the real and imaginary parts of the optical index difference between spin up and down nanodomains for H37 and H39.

Figure 4. Single-shot magnetic scattering patterns of a multilayer of 30 repetitions of [Co(4 Å)/Pd(6 Å)] for two incident photon energies: H37 and H39. The domains in the structure have random orientation, leading to the detection of a scattering ring. A radial integration of the scattering ring (symbols) as a function of q is presented, with the best

pseudo-Voigt fit of the data (lines). The central part of the scattering patterns with saturated pixels caused by the direct beam has been removed before doing integrations. (The color version of this figure is included in the online version of the journal.)

Figure 5. Measured magnetic scattering efficiencies at the Cobalt M-edge (a,c) and at the Palladium N-edge (b,d) for various [Co/Pd] samples. Configurations of the samples are [Co(2Å)/Pd(2Å)] (squares), [Co(4Å)/Pd(2Å)] (stars), [Co(4Å)/Pd(6Å)] (triangles) and [Co(4Å)/Pd(8Å)] (circles). Plots are presented as function of the repetition number of the multilayers (a,b), and the cumulate thickness of the resonant material (c,d). (The color version of this figure is included in the online version of the journal.)

[1] Gutt, C.; Streit-Nierobisch, S.; Stadler, L. M.; Pfau, B.; Günther, C. M.; Könnecke, R.; Frömter, R.; Kobs, A., Stickler, D.; Oepen, H. P.; Fäustlin, R. R.; Treusch, R.; Feldhaus, J.; Weckert, E.; Vartanyants, I. A.; Grunze, M.; Rosenhahn, A.; Wilhein, T.; Eisebitt, S.; Grübel, G. Phys. Rev. B 2010, 81, 100401.

[2] Sandberg, R. L.; Paul, A.; Raymondson, D. A.; Hädrich, S.; Gaudiosi, D. M.; Holtsnider, J.; Tobey, R. I.; Cohen, O.; Murnane, M. M.; Kapteyn, H. C.; Song, C.; Miao, J.; Liu, Y.; Salmassi, F. Phys. Rev. Lett. 2007, 99, 098103.

[3] Ravasio, A.; Gauthier, D.; Maia, F. R. N. C.; Billon, M.; Caumes, J. P.; Garzella, D.; Géléoc, M.; Gobert, O.; Hergott, J. F.; Pena, A. M., Perez, H.; Carré, B.; Bourhis, E.; Gierak, J.; Madouri, A.; Mailly, D.; Schiedt, B.; Fajardo, M.; Gautier, J.; Zeitoun, P.; Bucksbaum, P. H.; Hajdu, J.; Merdji, H. Phys. Rev. Lett. 2009, 103, 028104.

[4] Gauthier, D.; Guizar-Sicairos, M.; Ge, X.; Boutu, W.; Carre, B.; Fienup, J. R.; Merdji, H. Phys. Rev. Lett. 2010, 105, 093901.

[5] La-O-Vorakiat, C.; Siemens, M.; Murnane, M. M.; Kapteyn, H. C.; Mathias, S.; Aeschlimann, M.; Grychtol, P.; Adam, R.; Schneider, C. M.; Shaw, J. M.; Nembach, H.; Silva, T. J. Phys. Rev. Lett. 2009, 103, 257402.

[6] La-O-Vorakiat, C.; Turgut, E.; Teale, C. A.; Kapteyn, H. C.; Murnane, M. M.; Mathias, S.; Aeschlimann, M.; Schneider, C. M.; Shaw, J. M.; Nembach, H. T.; Silva, T. J. Phys. Rev. X 2012, 2, 011005.

[7] Ducousso, M.; Ge, X.; Boutu, W.; Gauthier, D.; Barbrel, B.; Wang, F.; Borta, A.; Gonzalez, A.-I.; Billon, M.; Vodungbo, B.; Gautier, J.; Zeitoun, P.; Hawaldar, R.; Tudu, B.; Delaunay, R.; Tortarolo, M.; Lüning, J.; Merdji, H. Phys. Rev. B Rap. Comm., submitted for publication.

[8] Beaurepaire, E.; Merle, J. C.; Daunois, A.; Bigot, J. Y. Phys. Rev. Lett. 1996, 76, 4250.

[9] Kirilyuk, A.; Kimel, A. V.; Rasing, T. Rev. Mod. Phys. 2010, 82, 2731.

[10] Ge, X.; Boutu, W.; Ducousso, M.; Wang, F.; Borta, A.; Ducousso, M.; Gonzalez, A.I.; Carré, B.; Guillaumet, D.; Perdrix, M.; Gobert, O.; Gautier, J.; Lambert, G.; Maia, F.R.N.C.; Hajdu, J.; Merdji, H. Opt. Express, in press.

[11] Kim, H. T.; Kim , I. J.; Lee, D. G.; Hong, K.-H.; Lee, Y. S.; Tosa, V.; Nam, C. H. Phys. Rev. A 2004, 69, 031805(R)

[12] Kan, C.; Capjack, C. E.; Rankin, R.; Burnett N. H. Phys. Rev. A 1995, 52, 4336

[13] Wahlström, C.-G.; Larsson, J.; Persson, A.; Starczewski, T.; Svanberg, S.; Salières, P., Balcou, Ph. ; L'Huillier, A. Phys. Rev. A 1993, 48, 4709

[14] Miyazaki, K.; Takada, H. Phys. Rev. A, 1995, 52, 3007

[15] Shin, H. J.; Lee, D. G.; Cha, Y. H.; Hong, K. H.; Nam, C. H. Phys. Rev. Lett. 1999, 83 2544

[16] Shin, H. J.; Lee, D. G.; Cha, Y. H.; Kim, J.-H.; Hong, K. H.; Nam, C. H. Phys. Rev. A 2001, 63, 053407

[17] Lambert, G.; Gautier, J.; Hauri, C. P.; Zeitoun, P.; Valentin, C.; Marchenko, T.; Tissandier, F.; Goddet, J. P.; Ribiere, M.; Rey, G.; Fajardo, M.; Sebban, S. New J. Phys. 2009, 11, 083033.

[18] Kelly, P.J.; Arnell, R.D. Vacuum 2000, 56, 159-172.

[19] Hellwig, O.; Berger, A.; Kortright, J. B.; Fullerton, E. E. J. Magn. Magn. Mater 2007, 319, 13.

[20] Lovesey, S.W. ; Collins, S.P. X-ray Scattering and Absorption by Magnetic Materials; Oxford University Press: USA, 1996.

[21] Turner, J. J.; Huang, X.; Krupin, O.; Seu, K. A.; Parks, D.; Kevan, S.; Lima, E.; Kisslinger, K.; McNulty, I.; Gambino, R.; Mangin, S.; Roy, S.; Fischer, P. Phys. Rev. Lett., 2011, 107, 033904.

[22] Valencia, S.; Gaupp, A.; Gudat, W.; Mertins, H.-C.; Oppeneer, P. M.; Abramsohn, D.; Schneider, C. M. New J. Phys. 2006, 8, 254.

[23] Stöhr, J.; Siegmann, H. C. Magnetism: from fundamentals to nanoscale dynamics; Springer: Berlin, Germany, 2006.

[24] Hellwig, O.; Berger, A.; Fullerton, E. E. Phys. Rev. Lett. 2003, 91, 197203.

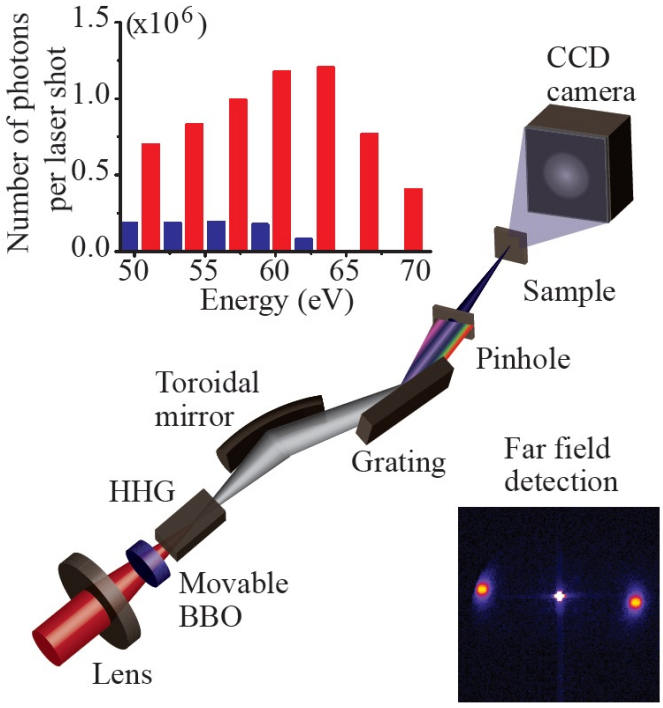
Number of photons per laser shot
1.5
(x10^6)
1.0
0.5
0.0
50
55
60
65
70
Energy (eV)
CCD camera
Sample
Pinhole
Toroidal mirror
Grating
Far field detection
HHG
Movable BBO
Lens

Figure 1

Parameters	Value
beam aperture	25~27 mm
gas pressure	46~50 mbar
gas cell length	5~6 cm
laser energy	24~28 mJ
focus position (behind the gas cell output)	0 ~ 2 cm

Table 1

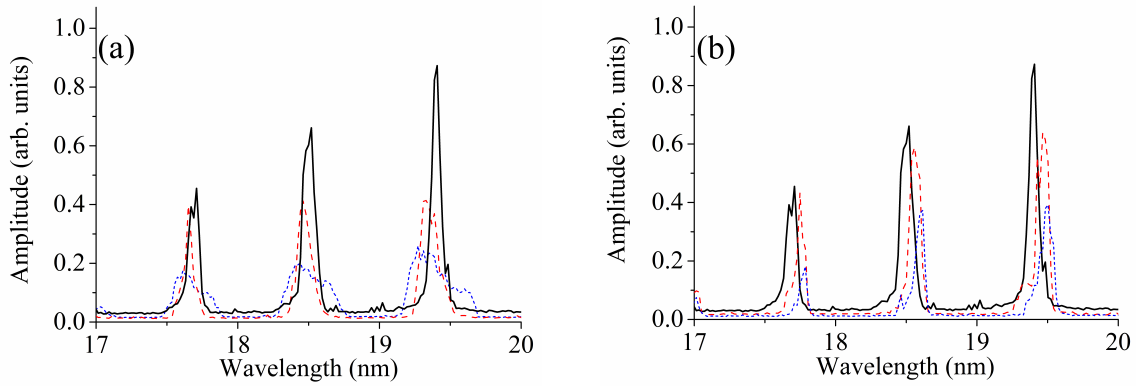
(a)
(b)
Amplitude (arb. units)
Wavelength (nm)
1.0
0.8
0.6
0.4
0.2
0.0
17
18
19
20

Figure 2

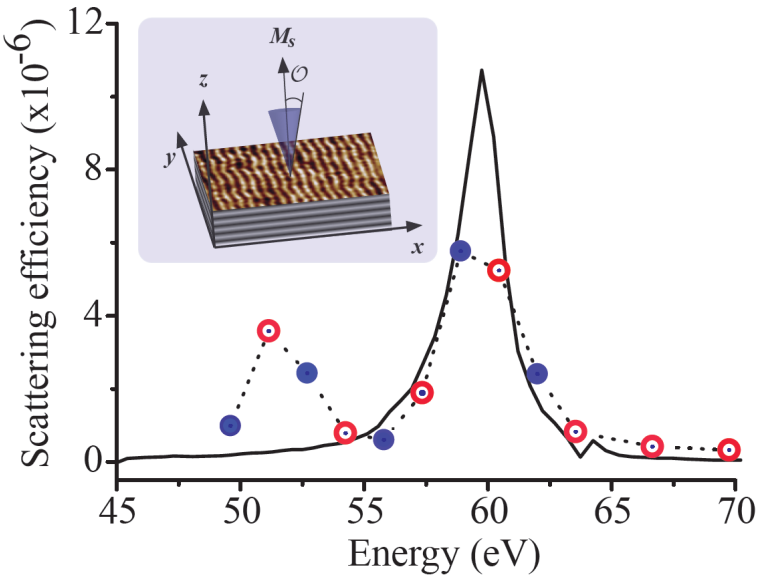
Scattering efficiency (x10^{-6})
12
8
4
0
45
50
55
60
65
70
Energy (eV)
M_s
z
y
x

Figure 3

Energy (eV)	57.4	60.5
T(E)	0.0518	0.0304
$[\Delta\beta(E)^2+\Delta\delta(E)^2]$ $(x10^{-6})$	1.08	1.13

Table 2

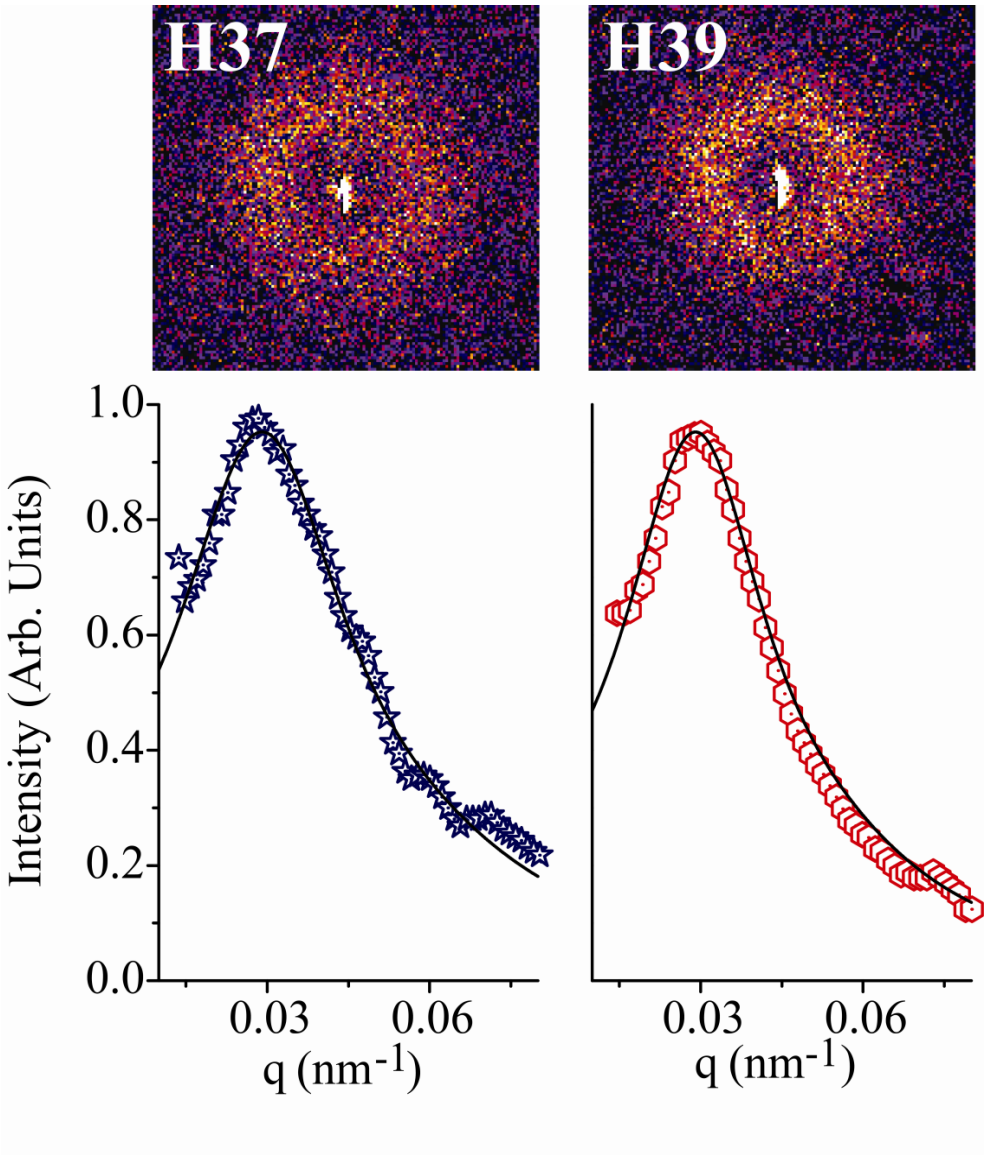
H37
H39
Intensity (Arb. Units)
1.0
0.8
0.6
0.4
0.2
0.0
0.03
0.06
q (nm-1)
0.03
0.06
q (nm-1)

Figure 4

Sample	Repetitions
[Co(2Å)/Pd(2Å)]	20, 40, 50, 60, 80
[Co(4Å)/Pd(2Å)]	20, 30, 40
[Co(4Å)/Pd(6Å)]	15, 20, 30, 40
[Co(4Å)/Pd(8Å)]	15, 20

Table 3

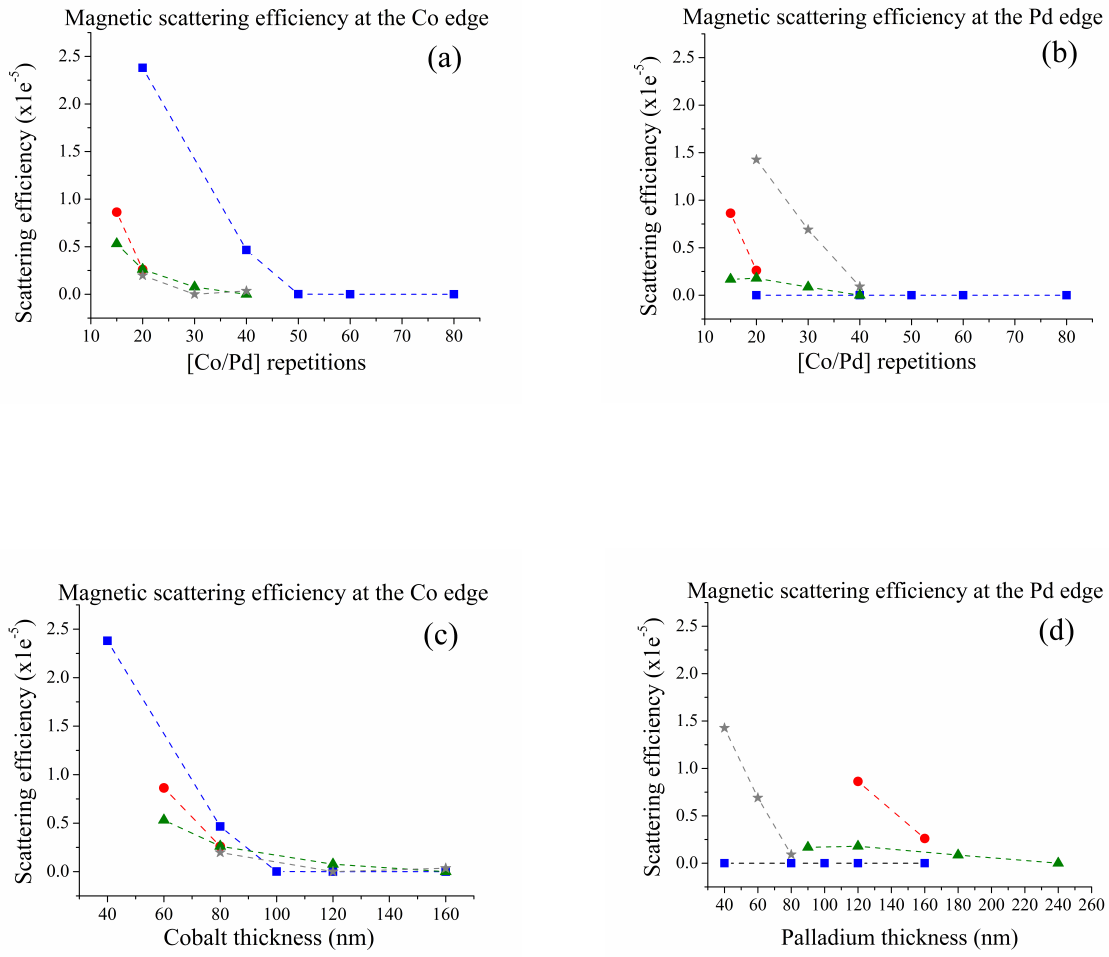
Magnetic scattering efficiency at the Co edge
(a)
Scattering efficiency (x1e-5)
[Co/Pd] repetitions
Magnetic scattering efficiency at the Pd edge
(b)
Scattering efficiency (x1e-5)
[Co/Pd] repetitions
Magnetic scattering efficiency at the Co edge
(c)
Scattering efficiency (x1e-5)
Cobalt thickness (nm)
Magnetic scattering efficiency at the Pd edge
(d)
Scattering efficiency (x1e-5)
Palladium thickness (nm)

Figure 5

Chapter V
Perspectives and General Conclusion

V.1 Perspectives: Source and diagnostics upgrades

I summarized here few perspectives studies started during my Ph.D. thesis work.

Harmonic source down to 4nm wavelength

The experimental results of coherent diffractive imaging presented in Chapter III and the application to magnetic scattering from Chapter IV show that the photon flux of our harmonic beam is still the main limiting factor, especially for single-shot experiments. Thus, the future beamline upgrade will be focused on increasing the photon flux. This may be realized for instance by generating harmonics from ions in a pre-formed plasma [1]. Recent researches [1-3] have demonstrated enhanced HHG in noble gases in a capillary discharge, presenting an extended *plateau* and an increased harmonic flux. For example, the Ar *cut-off* has been extended to 275 eV [2] and the flux around 90 eV from Xe with a discharge is two orders of magnitude higher than the one without pre-ionization discharge [1]. This effect relies on the *plateau* extension rule,

$$h\upsilon_{max} = I_p + 3.17U_p \qquad \text{(Eq. 5-1)}$$

in which the ionization potential I_P depends on the generation gas. As an example, using our beamline, switching from argon ($I_P = 15.7\ eV$) to neon ($I_P = 21.6\ eV$) moves the *cut-off* position from order 33 to order 61. However, the efficiency of the generation drops by more than one order of magnitude. This can be circumvented by using singly ionized argon ($I_P = 27.7\ eV$), which should push the *cut-off* well below 10 nm. M. Zepf and colleagues [4] have demonstrated phase matched high harmonic generation in argon ions with a significant number of photons (up to 10^9) down to 4 nm. In this work, the argon atoms were ionized using the same laser pulse that generates the harmonics. However, several research groups have tried to reproduce their results without success. To generate high order harmonics from an ionized medium, one can dissociate the ionization step from the harmonic generation step. Instead of using a laser, we propose to use a high voltage discharge as in Ref. 1 and 2. The timing between the discharge and the femtosecond laser will be controlled to optimize the ion population. A capillary will act as a beam guide to compensate for the phase mismatch induced by the free electrons. A discharge cell will be developed in collaboration with the group of Dr. C. Russo (Grupo de Lasers e Plasmas, Instituto Superior Técnico, Lisboa, Portugal) and will be tested at the very end of my thesis work. The main challenge will be to deal with the phase mismatch and the loss of the laser intensity due to the laser defocusing. The future HHG scheme on our harmonic beamline will probably be the combination of the HHG from ions and quasi phase matching [5] to provide higher harmonic beam flux. Single-

shot studies should then be facilitated. Finally, soft X-ray harmonic pulse of short wavelength (4-10 nm) will highly improve the spatial resolution in the coherent imaging.

Complete single-shot coherence characterization

The beam's spatial coherence is a key factor for all the coherent imaging techniques, as demonstrated in Paper I and in the examples of FTH reconstructions (Chapter III, section III.6). However, the Young's double slits experiment can only measure the spatial coherence at one given position of the harmonic beam in one acquisition. Therefore, to characterize the entire beam spot, one should combine the measurements of multiple acquisitions from a complete set of inter slit distances. This prevents any single-shot characterization of the full beam. Single-shot 2D characterization with a single interferogram can be achieved using a nonredundant array of apertures (NRA). The NRA proposed and demonstrated with visible lasers in Ref. 6 is made of nine pinholes (Fig. 5.1a) in well-chosen positions that create a non-redundant superposition of the beam spots (Fig. 5.1b) for interference measurement (Fig. 5.1c). The spatial coherence of the beam (Fig. 5.1d) can then be calculated at the position of each spot. Therefore, a more complete characterization of the spatial coherence across the beam is achieved. Note that in both Young's double slits and NRA measurements, the knowledge of the beam's intensity distribution is necessary for calculating the spatial coherence, and is usually assumed to be uniform for simplification. Thus, single-shot measurement of the spatial coherence will always rely on the statistics of the intensity distribution, which introduces a systematic deviation in the measurements. However, it is possible to retrieve the spatial coherence from one single acquisition without complementary intensity measurement. We have designed and fabricated two "coherence patterns" similar to NRA (Fig. 5.2) for our harmonic beamline. Applying the Fourier transform on the diffraction pattern of these "coherence patterns", we can measure the amplitude of each peak ($A_{n,m}$), which is associated with a pair of pinholes (n,m) and given by the following equation:

$$A_{n,m} = \sqrt{I_n I_m}\mu_{n,m} \qquad \text{(Eq. 5-2)}$$

where I_n and I_m are the intensities of the pinholes (n,m), and $\mu_{n,m}$ is the spatial coherence associated to the pair of pinholes. In this equation, we have three unknown variables (I_n, I_m and $\mu_{n,m}$) and one measured term ($A_{n,m}$). In the NRA experiment, the spatial coherence ($\mu_{n,m}$) is deduced with I_n and I_m given by the intensity measurement of the beam. Here, we assume that the three pinholes in the small area of the beam center (red circles in Fig. 5.2) are identical in intensity and each pair of pinholes has the same spatial coherence. For each group of four pinholes that has the three pinholes inside the red circle and one outside (Fig. 5.2a), we will have a set of six equations of Eq. 5-2 with six variables: $I_1 = I_2 = I_3 = I_{center}$, I_4, $\mu_{1,4}$, $\mu_{2,4}$, $\mu_{3,4}$ and $\mu_{1,2} = \mu_{1,3} = \mu_{2,3} = \mu_{center}$. Therefore, we can deduce the intensity and the spatial coherence for all the pinholes, and the spatial coherence map of the single harmonic pulse. Note that this approximation is true in the case of our harmonic beamline and can be generalized to other experimental setups. These "coherence patterns" will be tested in the next experiment campaign during the HHG upgrade.

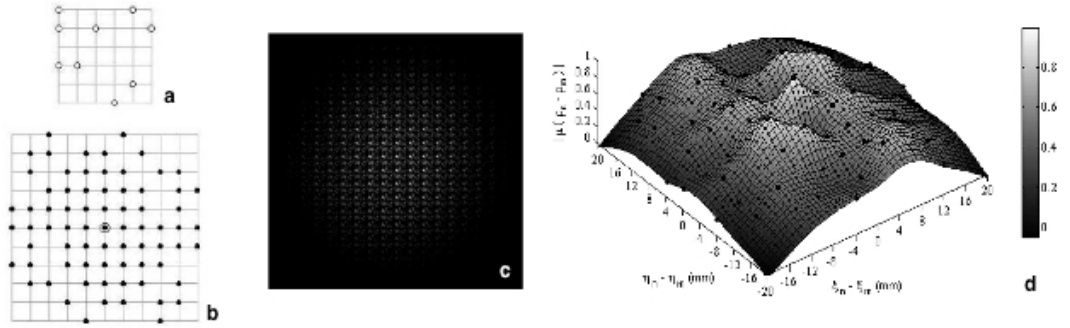

Fig. 5.1. Principle and experimental demonstration of the NRA spatial coherent measurement. Pictures are extracted from Ref. 6. (a) The NRA is composed of nine pinholes whose autocorrelation (b) has equal amplitudes for all autocorrelation peaks (filled circles) except the center one (open circle). (c) is the measured interferogram of a diode laser (635 nm) and (d) is the deduced spatial coherence of the beam from (b).

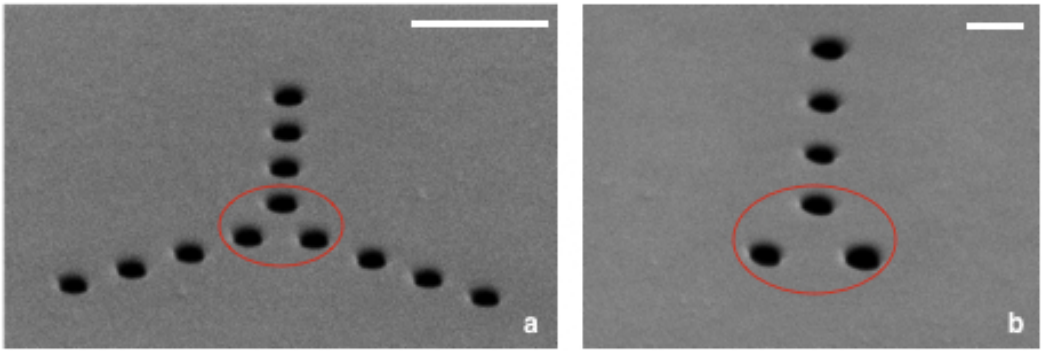

Fig. 5.2. SEM images of the "coherence patterns" that will be used for characterizing our harmonic beam. The white bar in each image is 1 μm. Note that the images are taken with a view angle of about 60 degrees.

V.2 Perspectives: 3D imaging

The imaging techniques presented in this thesis work are two-dimensional reconstruction of test objects. For many scientific applications, especially in biology and medical imaging, 3D information of the sample is necessary. The typical way to make 3D reconstructions is the tomography method [7]. It requires multiple acquisitions of different observation angles to records multiple 2D projections, which are assembled in a full 3D image. This could be a problem if radiation damages occur during the long acquisition. Another example is given by 3D dynamic studies. In a pump probe experiment, the object can be irreversibly transformed or destroyed after interaction with the pump pulse, preventing any multiple acquisitions scheme. It is sometimes possible to prepare multiple identical samples but this is rather difficult or even impossible for many systems that cannot be easily duplicated. To overcome this problem and to simplify the sample preparation, retrieving 3D information in a single-shot scheme is necessary.

Single-shot stereo imaging

One possible solution is based on the human vision: stereo imaging. Our right and left eyes take two 2D images at different observation angles of the object and the brain combines these images to give the perception of 3D depth. This is not real 3D imaging but already provides more information about an object than a 2D image. Fig. 5.3 presents stereo imaging examples of nanoplankton samples realized with a scanning electron microscope [8]. After the first image (photos in gray scale), the biological samples were tilted by about 5 degrees to take the second image. These two images are then turned into red and green, and combined by the red-green anaglyph method [9]. With red-green glasses, one can see 3D planktons from the combined image.

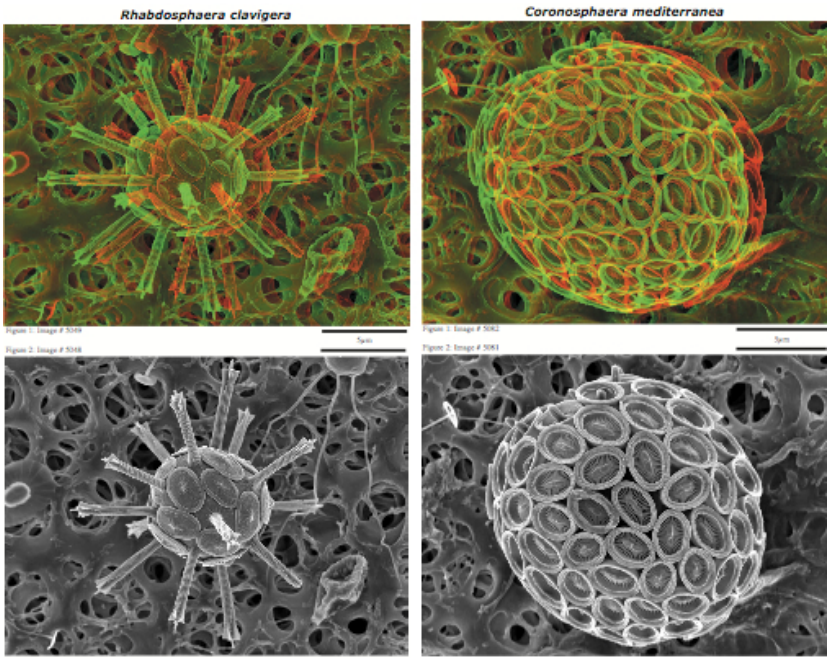

Fig. 5.3. Stereo images (red-green photos) of plankton samples made by digital combination of SEM images (gray scale) taken at different observation angles. Picture extracted from Ref. 8.

I have been working in the implementation of the first single-shot stereo imaging using high harmonic generation. The idea is to realize two parallel beams that will be focused at the same point by the off-axis parabola. The separation of the main beam is realized with two grazing incidence silicon mirrors (Fig. 5.4) before the parabolic mirror. Half of the harmonic beam is reflected by the "mirror 1" in Fig. 5.4 and the other half goes straight to the parabola. The reflected half-beam is then reflected by the "mirror 2" toward the parabola. The two half-beams are focused by the parabola onto the sample. The distance between the two parallel beams is about 20 mm, which is acceptable by the numerical aperture of the parabola. As the two beams are parallel they are focus at the same point with an angle of ~ 6°. Note that in this geometry the two beams are not synchronized. A new setup with a femtosecond synchronization of the two beams is currently under design.

After interaction with a sample, the two beams generate two diffraction patterns that are collected by our CCD camera in a single acquisition (Fig. 5.5a,b). The first test object is 3D

HERALDO samples with slit references. We use an up-warped etching process to have 3D depth, with different motifs, such as the grid presented in Fig. 5.5a. Since the half-beams have lower flux due to the beam separation and additional mirror reflection, we use the slit references to increase the reconstruction ability. Fig. 5.5c,d present a preliminary result of HERALDO reconstructions associated to the diffraction pattern (Fig. 5.5b). The slit references and the borders of the up-warped pattern are well resolved, but the grid motif is not clear. Further work on the reconstruction is under progress. Further work on biological samples will also be realized (nanoplankton sample have already been prepared).

Time-resolved three-dimensional imaging studies that are currently limited by the need for multiple views of the same sample will be then possible. It is expected to get single-shot images with 3D perception down to sub-100 nm spatial resolution.

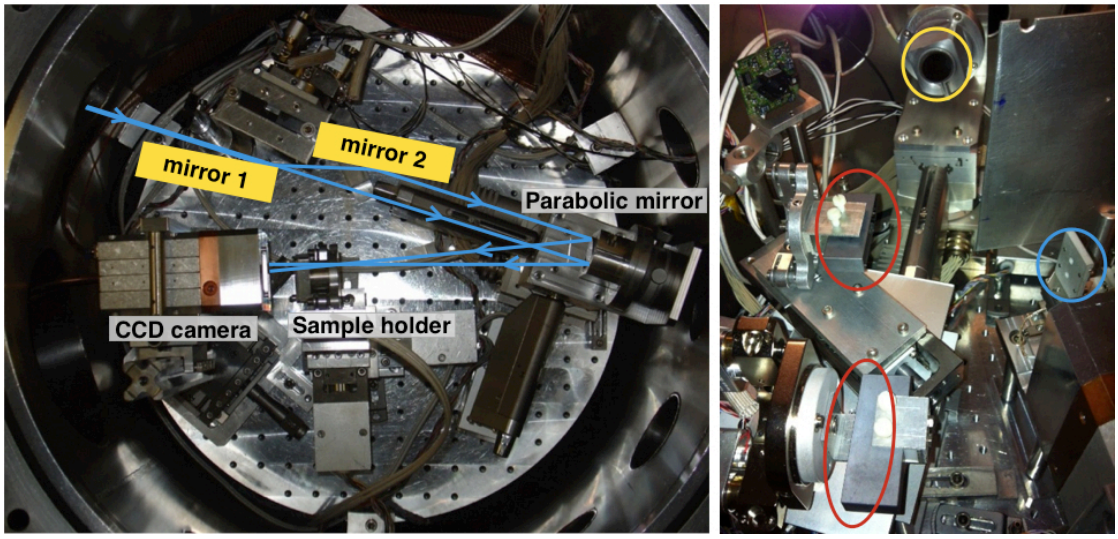

Fig. 5.4. Picture of the experimental setup for stereo imaging. In the left one, blue lines indicate the beam propagation and yellow squares are the silicon mirrors installed for beam separation. The two-mirror system is also shown in the picture at right (red circles) as well as the parabola (yellow circle) and the sample (blue circle).

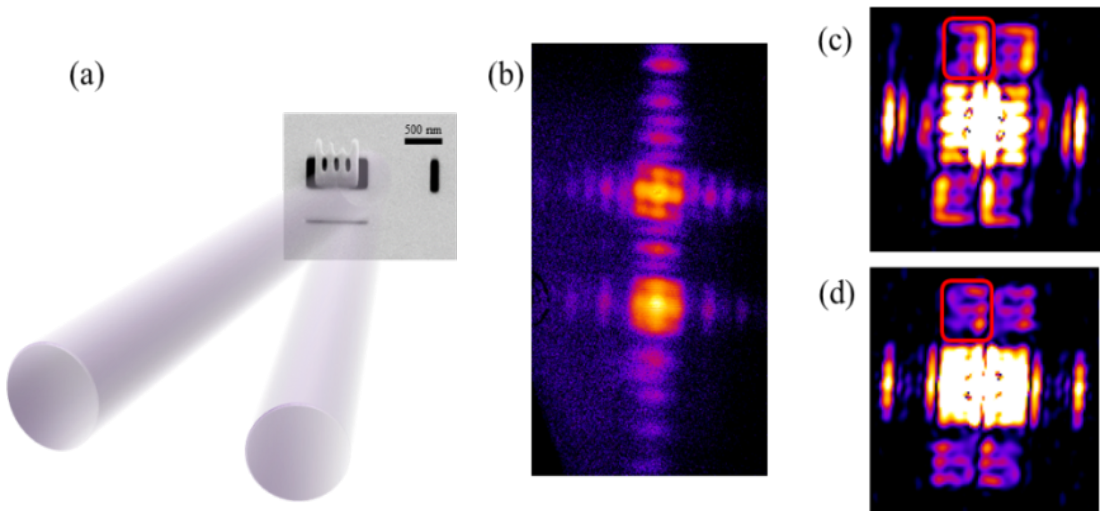

Fig. 5.5: Stereo-imaging. (a) SEM image of a test sample with two schematized incident XUV beams. The two black lines are HERALDO references. (b) First experimental diffraction

pattern (September 2012). (c) and (d) Inversion of the holograms. The red squares delimit one reconstruction.

Ankylography

Another solution is a novel imaging concept recently proposed by the research group of J. Miao, called ankylography, which "under certain circumstances enables complete 3D structure determination from a single exposure using a monochromatic incident beam" [10]. Ankylography is a coherent imaging technique based on phase retrieval that uses the same experimental setup as CDI. Compared to CDI, Ankylography requires one more oversampling condition due to the third dimension (the beam propagation direction) and the phase retrieval algorithm processes in three dimensions for the reconstruction. In principle, a finite object illuminated by a coherent beam scatters waves on the Ewald sphere. The measured 2D diffraction pattern collected by the CCD camera is a projection of that sphere, in which the 3D structure information of the object is encoded. The 3D reconstruction is then possible by turning the measured diffraction pattern into a 3D spherical pattern. Fig. 5.6 shows a demonstration of the ankylography on experimental data using a table-top kHz high harmonic source [10]. The fabrication defaults observed in the SEM image of the object (Fig. 5.6e) are reconstructed by the ankylography technique (Fig. 5.6b,c) using the spherical diffraction pattern (Fig. 5.5a) calculated from a multiple-shot acquisition.

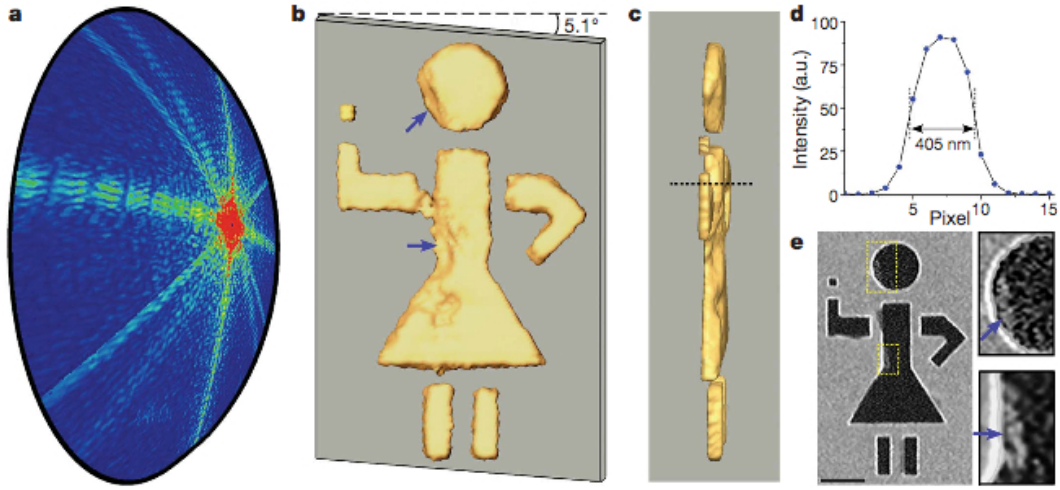

Fig. 5.6. Demonstration of ankylography. Picture extracted from Ref. 10.

Single-shot studies of this technique have been launched at our harmonic beamline. While the experimental setup and the samples configurations are under continuous improvement, I present here only the very first experiment I was part of (Fig. 5.7). The samples are placed on a rotation stage, allowing us to study the different 3D imaging techniques (the XUV beam splitter was not available at that time). The 3D sample is composed of two opaque membranes (the same type as used for CDI and HERALDO in chapter III) separated by about 3 µm, with a grid etched using a FIB. By rotating the sample, we could acquire the two views necessary for stereo imaging. Single views could also be used for ankylography. Fig. 5.7a is the 2D reconstruction of the well-aligned grids (0°), while Fig. 5.7b presents a different view at another orientation where the slits of the first membrane are partially covered by the second

one. The preliminary results do not have sufficient quality for stereo combination. The analysis is under progress to refine the reconstructions. Fig. 5.7.c is the single-shot ankylography reconstruction of the diffraction pattern taken at 0° (same as Fig. 5.7a). The reconstruction has been performed by researchers of J. Miao's group. The green part of the 3D image indicates the volume where photons went through. The shape of the slits of the two membranes is clearly reconstructed. New data have since been obtained, using other samples and improved experimental conditions. The analysis is under way. Note that the phase retrieval process requires a powerful computer cluster and several hours of computing time to perform a single reconstruction. This is one disadvantage of ankylography compared to stereo CDI. The latter requires only a personal computer. However, the ability to obtain complete 3D information from single views promises a bright future in various scientific areas.

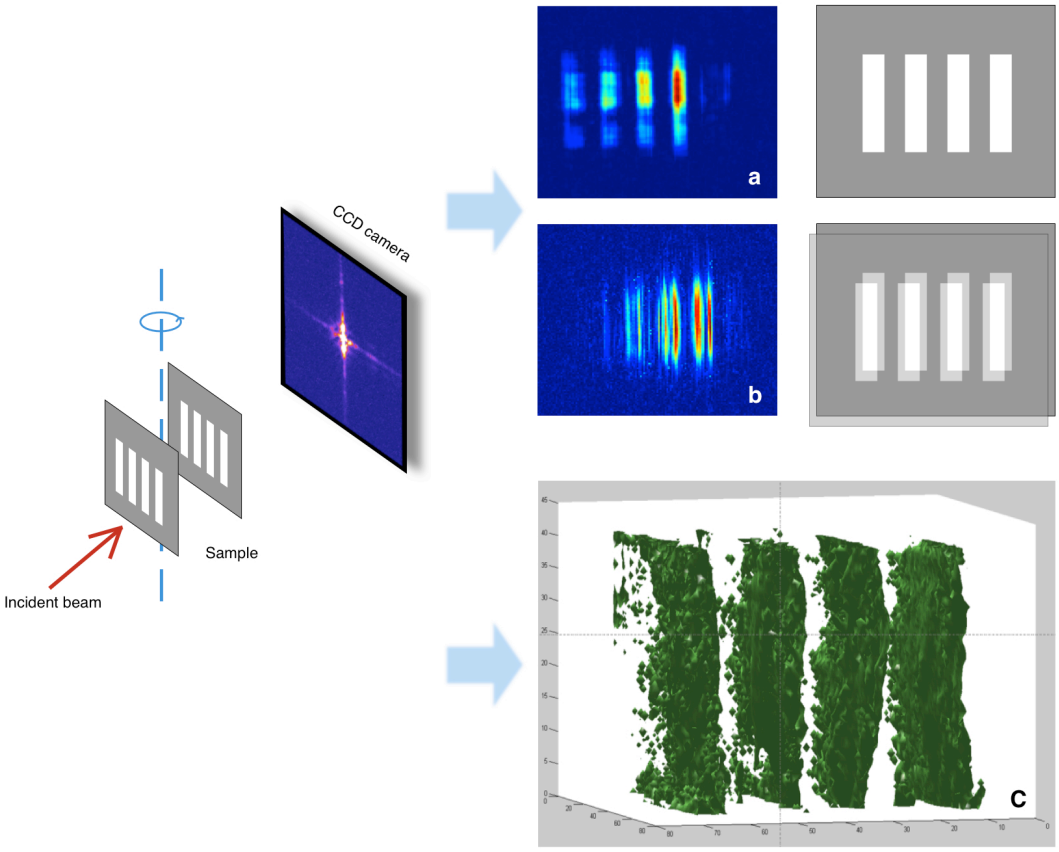

Fig. 5.7. One of the experimental schemes for stereo and ankylography imaging, and the preliminary reconstruction results.

V.3 General conclusion

The objective of this thesis was to develop and analyze different coherent diffractive imaging techniques using an XUV high-order harmonic beam and to implement their first physical application.

The theoretical background of the coherent imaging (or lens-less imaging) was presented in ***Chapter I*** from the image formation in the Fraunhofer diffraction regime to the different reconstruction processes of CDI, FTH and HERALDO. The two main branches of lens-less imaging, CDI and holographic techniques, have their own advantages. The latter provides quick, direct and non-ambiguous reconstruction of the object, while the iterative algorithms usually converge to reliable solutions after thousands of iterations. However, the need of a proper reference in holographic techniques limits the field of applications. The reference may be technically difficult or even impossible to manufacture or to set at the proper distance from the object. However, the spatial coherence of the light source is the key factor for both reconstruction processes. A reduced coherence can prevent the phase retrieval algorithms convergence. The high-order harmonic source, which I used during this thesis work is intrinsically qualified for the coherent requirement and is able to deliver high flux beam thanks to the recent development of the High flux harmonic beamline.

Chapter II introduced the development and progress of the beamline. Using the 25^{th} harmonic of the laser (λ = 32 nm) a 120 nm spatial resolution was obtained in the CDI reconstruction of a test object from single-shot acquisitions in 2009. This encouraging first lens-less imaging demonstrated the relevance of CDI at HHG beamlines. It has been the starting point of this thesis work. An extensive study of the harmonic generation beam quality has been carried out under various generation conditions. We have used various diagnostics such as wave front sensor or Young's double slits to provide crucial information for coherent imaging such as wave front quality, beam flux, spatial coherence and harmonic focal spot profile. The HHG parameters have been optimized for a balanced compensation between the 3 key factors: the coherence, the flux and the wave front quality. CDI reconstruction analysis of the interferogram of the Young's double slits confirmed the coupled influence of these beam characteristics. We also implemented a laser modal filtering system to optimize the IR pump laser. The IR laser presents a quasi-Gaussian beam profile after propagation in a hollow core fiber, which consequently improved the HHG efficiency by a factor of 2.5 in Argon and 6 in Neon. In addition, the filtered laser beam position is thus stabilized, ensuring a continuous high HHG quality during day-long experiments. The optimization at each stage of the beamline and the standardization of the harmonic generation have been crucial for the success of the coherent imaging experiments and the applications performed during my thesis. Moreover, this demonstrated that compact and inexpensive HH sources are a very interesting alternative to large-scale free electron laser facilities.

Chapter III presents the demonstrations of single-shot CDI and holographic imaging techniques, followed by quantitative analysis. In the CDI section, we have reached sub-80 nm spatial resolution from single-shot acquisition (20 fs), which is ~ 2.5λ (λ=32 nm). The coherence requirements for CDI have been discussed using a Young's double slits diagnostic. Our finding is that the phase retrieval algorithms do not converge for a contrast of interference fringes lower than 0.5. The importance of the coherence has also been demonstrated in the FTH reconstructions using a geometric grid test sample. A high flux low coherence beam does not allow the reconstruction of the detail of the sample, while a lower beam flux with higher spatial coherence leads to a well-resolved image reconstruction. We

conclude that the beam coherence and the beam flux are the key parameters for lens-less imaging. In this context, the HERALDO configuration can amplify the diffraction signal thanks to the extended references. A "mathematical tricks" is then used to overcome the resolution limitation imposed by the reference size. Experimental demonstrations of HERALDO with 1D and 2D references have proven the robust reconstruction process. A spatial resolution of 110 nm has been achieved with single-shot acquisition for a test object of ~ 2 x 2 μm². Step-by-step analysis of the reconstruction process shows the significant influence of the readout noise, which is amplified by the HERALDO operator in Fourier space. A low-pass filter is the solution to overcome this main obstacle. Meanwhile, detection stage optimizations, valid for all the coherent imaging techniques, have been discussed. The comparison between FTH and HERALDO showed that HERALDO with a slit reference is the best holographic configuration for our harmonic beam, since we are mainly limited by the beam flux in the single-shot regime. The comparison between CDI and HERALDO confirmed the effectiveness of the signal amplification by extended references. It is however not possible to say whether one is better than the other since this depends on the given experimental conditions. CDI and HERALDO are not only alternative but also complementary to each other. The choice of the best imaging technique for a concrete application should be based on a careful analysis of experimental conditions.

Chapter IV presents an application to ultrafast nanomagnetism. This was the first physical application realized using the High flux harmonic beamline and coherent imaging techniques. The scattering of (Co/Pd) nanodomain magnetic structures has been measured in single-shot. HHG spectral optimization has been conducted in argon and neon gases to match the requirements for magnetic studies, which required here a work wavelength around the cobalt absorption M-edge (around 39^{th} harmonic). A comparison between HHG quality using filtered and non-filtered IR laser pump has been carried out in the meantime. The HHG optimization procedure and conclusions presented in Chapter II have been applied (except for the wave front measurement) to perform the magnetic studies. Measurements of magnetic scattering from nanodomain structures have been realized over a large spectral bandwidth in both single-shot and multiple-shot acquisitions, from which magnetic properties of the nanodomain samples have been deduced. Spectral analysis showed an unexpected resonant peak, which corresponds to the palladium component of the sample. Real space image reconstructions of the scattering patterns were not possible since the oversampling condition was not respected due to experimental constraints. However full statistical information about the samples has been inferred. The cobalt M-edge and the palladium N-edge signatures have been detected with scattering efficiencies of 10^{-5} and $2x10^{-6}$, respectively. At the 39^{th} harmonic, which is close in energy to the magnetically dichroic Co $M_{2,3}$ absorption edge, we have measured an average magnetic domain size of 62.5 nm, with a size distribution of ±7 nm in multiple shot and ±10 nm in single-shot, in good agreement with MFM characterization. This validates the single-shot capability of the High flux harmonic beamline. The next step, under progress, is to obtain images of the magnetic domains using a similar set-up. It also paved the way for their dynamical study with the under-construction pump probe experiment setup. The combination of dynamic and real space imaging in the near future will open the gate for understanding the spin-orbital and exchange interactions.

This magnetic application also illustrated the recent development of a versatile harmonic beamline, which is now a standardized, stable and powerful beamline providing intense soft X-ray coherent photons with tunable wavelength from 40 to 15 nm in this work and down to 4

nm in the next few years. Combining with the CDI, HERALDO and the under-developing 3D imaging techniques, our High flux harmonic beamline is suitable and ideal for a wide range of flash imaging applications from physics to biology. We foresee a bright future for ultrafast dynamic studies with real space reconstructions of nanometric spatial resolution.

Bibliography

Introduction

1. "Visual acuity of the human eye" http://www.ndt-ed.org/EducationResources/CommunityCollege/PenetrantTest/Introduction/visualacuity.htm
2. "Nature Milestones in Light Microscopy", (October 2009) http://www.nature.com/milestones/milelight/timeline.html
3. E. Abbe, "Beiträge zur Theorie des Mikroskops und der mikroskopischen Wahrnehmung". *Archiv für Mikroskopische Anatomie* **9**, 413–418 (1873)
4. R. Erni *et al.*, "Atomic-Resolution Imaging with a Sub-50-pm Electron Probe", *Phys. Rev. Lett.* **102**, 096101 (2009)
5. J. Kirz, "The history and future of X-ray microscopy", *Journal of Physics: Conference Series* **186** 012001 (2009)
6. "The complete Eadweard Muybridge" http://www.stephenherbert.co.uk/muybCOMPLEAT.htm
7. "The Nobel Prize in Chemistry 1967" http://www.nobelprize.org/nobel_prizes/chemistry/laureates/1967/
8. P.M. Paul, *et al.*, "Observation of a train of attosecond pulses from high harmonic generation", *Science* **292** 1689–1692 (2001)
9. M. Hentschel *et al.*, "Attosecond metrology", *Nature* **414** 509–513 (2001)
10. M. Drescher et *al.*, "Time-resolved atomic inner-shell spectroscopy", *Nature* **419** 803-807 (2002)
11. R. Kienberger *et al.*, "Atomic transient recorder", *Nature* **427** 817-821 (2004)
12. Hiromichi Niikura *et al.*, "Probing molecular dynamics with attosecond resolution using correlated wave packet pairs", *Nature* **421** 826-829 (2003)
13. S. Koke et *al.*, "Direct frequency comb synthesis with arbitrary offset and shot-noise-limited phase noise", *Nature Photonics* **4** 462-465 (2010)
14. A. Hasegawa, "Free electron laser", *Bell system technical journal* **57** 8 (1978)
15. D. Sayre, "The squaring method: a new method for phase determination", Acta Cryst. 5 60-65 (1952)
16. J.R. Fienup, "Reconstruction of an object from the modulus of its Fourier transform", Optics Letters 3 27-29 (1978)
17. R.W. Gerchberg and W.O. Saxton, "A practical algorithm for the determination of phase from image and diffraction plane pictures", Optik 35 237-246 (1972)
18. H. Chapman and K. Nugent, "Coherent lensless X-ray imaging", Nature Photonics 4 833-839 (2012)
19. J. W. Miao et al., "Extending the methodology of X-ray crystallography to allow imaging of micrometre-sized non-crystalline specimens", Nature 400 342-344 (1999)
20. H. Chapman *et al.*, "Femtosecond diffractive imaging with a soft-X-ray free-electron laser" *Nature Physics* **2** 839-843 (2006)
21. H. Chapman *et al.*, "High-resolution ab initio three-dimensional x- ray diffraction microscopy", *J. Opt. Soc. Am. A* **23** 1179-1200 (2006)

22. A. Barty *et al.*, "Ultrafast single-shot diffraction imaging of nanoscale dynamics", *Nature Photonics* **2** 415-419 (2008)
23. H. Jiang *et al.*, "Quantitative 3D imaging of whole, unstained cells by using X-ray diffraction microscopy", *Proc. Natl. Acad. Sci. U.S.A.* **107** 11234-11239 (2010)
24. A.P. Mancuso *et al.*, "Coherent imaging of biological samples with femtosecond pulses at the free-electron laser FLASH", *New J. Phys.* **12** 035003 (2010)
25. R.L. Sandberg et al., "Lensless Diffractive Imaging Using Tabletop Coherent High-Harmonic Soft-X-Ray Beams", Phys. Rev. Lett. 99 098103 (2007)
26. A. Ravasio *et al.*, "Single-Shot Diffractive Imaging with a Table- Top Femtosecond Soft X-Ray Laser-Harmonics Source", *Phys. Rev. Lett.* **103** 028104 (2009)

Chapter I

1. K. Burkhard, *et al.*, "Transmission and emission x-ray microscopy: operation modes, contrast mechanisms and applications", *Journal of Physics: Condensed Matter* **23** 083002 (2011)
2. M.R. Howells, *et al.*, "An assessment of the resolution limitation due to radiation-damage in X-ray diffraction microscopy", *Journal Of Electron Spectroscopy And Related Phenomena* **170** 4-12 (2009)
3. Q. Shen, *et al.*, "Diffractive imaging of nonperiodic materials with future coherent X-ray sources", *Journal Of Synchrotron Radiation* **11** 432-438 (2004)
4. J.C.H. Spence, *et al.*, "Phase recovery and lensless imaging by iterative methods in optical, X-ray and electron diffraction", *Phil. Trans. R. Soc. Lond. A* **360** 875 (2002)
5. I. McNulty, *et al.*, "High-Resolution Imaging by Fourier Transform X-ray Holography", *Science* **256** 1009-1012 (1992)
6. J.R. Fienup, "Phase retrieval algorithms: a comparison", *Appl. Opt.* **21** 2758 (1982)
7. J.R. Fienup, "Reconstruction of an object from the modulus of its Fourier transform", *Opt. Lett.* **3** (1) 27 (1978)
8. J.R. Fienup, "Reconstruction of a complex-valued object from the modulus of its Fourier transform using a support constraint", *J. Opt. Soc. Am. A* **4** (1) 118 (1987)
9. Y.M. Bruck and L.G. Sodin, "On the ambiguity of the image reconstruction problem", *Opt. Commun.* **30** 304–8 (1979)
10. R.H.T. Bates, "Fourier Phase Problems Are Uniquely Solvable In More Than One Dimension", *Underlying Theory. Optik* **61** (3) 247-262 (1982)
11. D. Gabor, "A New Microscopic Principle", *Nature* **161** (4098) 777-778 (1948)
12. J.W. Goodman, "Introduction to Fourier optics", *Roberts & Co.* (2005)
13. M. Guizar-Sicairos and J.R. Fienup, "Holography with extended reference by autocorrelation linear differential operation", *Opt. Express* **15** (26) 17592 (2007)
14. S.G. Podorov, et al., "A non-iterative reconstruction method for direct and unambiguous coherent diffractive imaging", *Opt. Express* **15** (16) 9954 (2007)
15. L.M. Stadler, *et al.*, "Hard X Ray Holographic Diffraction Imaging", *Physical Review Letters* **100** (24) 245503 (2008)
16. S. Eisebitt, *et al.*, "Lensless imaging of magnetic nanostructures by X-ray spectro-holography", *Nature* **432** (7019) 885 (2004)
17. H. He, *et al.*, "Use of extended and prepared reference objects in experimental Fourier transform x-ray holography", *Applied Physics Letters* **85** (13) 2454 (2004)

18. W.F. Schlotter, “Multiple reference Fourier transform holography with soft x rays”, *Appl. Phys. Lett.* **89** (16) 163112 (2006)
19. S. Marchesini, *et al.*, “Massively parallel X-ray holography”, *Nat. Photon.* **2** (9) 560 (2008)
20. O. Hellwig, *et al.*, “Magnetic imaging with soft x-ray spectroholography”, *J. Appl. Phys.* **99** 08H307 (2006)
21. A. McPherson, *et al.*, “Studies of multiphoton production of vacuum-ultraviolet radiation in the rare gases”, *J. Opt. Soc. Am. B* **4** (4) 595 (1987)
22. M. Ferray, “Multiple-harmonic conversion of 1064nm radiation in rare gases”, *J. Phys. B* **21** L31 (1988)
23. T. Brabec and F. Krausz, “Intense few-cycle laser fields: Frontiers of nonlinear optics”, *Rev. Mod. Phys.* **72** 545 (2000)
24. J.L. Krause, *et al.*, “High-order harmonic generation from atoms and ions in the high intensity regime”, *Physical Review Letters* **68** (24) 3535 (1992)
25. P.B. Corkum, “Plasma perspective on strong field multiphoton ionization”, *Phys. Rev. Lett.* **71** 1994 (1993)
26. K.J. Schafer, *et al.*, “Above threshold ionization beyond the high harmonic cutoff”, *Phys. Rev. Lett.* **70** 1599-1602 (1993)
27. M. Lewenstein, *et al.*, “Theory of high-harmonic generation by low-frequency laser fields”, *Physical Review A* **49** (3) 2117 (1994)
28. P.M. Paul, *et al.*, “Observation of a train of attosecond pulses from high harmonic generation”, *Science* **292** 1689–1692 (2001)
29. G. Lambert, *et al.*, “Injection of harmonics generated in gas in a free-electron laser providing intense and coherent extreme-ultraviolet light”, *Nature Physics* **4** 296-300 (2008)
30. M. Born and E. Wolf, “Principles of Optics: Electromagnetic Theory of Propagation, Interference and Diffraction of Light”, *Cambridge University Press* 7th edition (1999)
31. P. Thibault, “Algorithmic Methods In Diffraction Microscopy”, thesis work at *Faculty of the Graduate School, Cornell University* (2007)
32. M. Guizar-Sicairos, “Methods for Coherent Lensless Imaging and X-Ray Wavefront Measurement”, thesis work at *The Institute of Optics Arts, Sciences and Engineering, Edmund A. Hajim School of Engineering and Applied Sciences, University of Rochester, Rochester, New York* (2010)
33. D. Gauthier, “Imagerie nanométrique ultra-rapide par diffraction cohérente de rayonnement extrême-UV produit par génération d’harmoniques d’ordre élevé”, thesis work at *Université Paris Sud XI, Orsay, France*, (2012)
34. F.R.N.C. Maia, *et al.*, “Hawk: the image reconstruction package for coherent X-ray diffractive imaging”, *Journal of Applied Crystallography* **43** (6) 1535-1539 (2010)
35. D. Attwood, “Soft X-Rays and Extreme Ultraviolet Radiation: Principles and Applications”, *Cambridge University Press* (2007)
36. P. P. Ewald, “Zur Theorie der Interferenzen der R ̈ontgenstrahlen in Kristallen”, *Physikalische Zeitschrift* **14** 465–472 (1913)
37. H.N. Chapman, *et al.*, “High-resolution ab initio three-dimensional x-ray diffraction microscopy”, *J. Opt. Soc. Am. A* **23** (5) 1179 (2006)
38. D. Sayre, “Some implications of a theorem due to Shannon”, *Acta Crystallographica* **5** 843 (1952)
39. J. Miao and D. Sayre, “On possible extensions of x-ray crystallography through

diffraction-pattern oversampling", *Acta Cryst. A* **56** 596–506 (2000)
40. H. Nyquist, "Certain topics in telegraph transmission theory", *Proceedings of the IEEE* **90** (2) 280 (2002)
41. C.E. Shannon, "Communication in the Presence of Noise", *Proceedings of the IRE* **37** (1) 10 (1949)
42. E. Wolf, "Is a Complete Determination of the Energy Spectrum of Light Possible from Measurements of the Degree of Coherence?", *Proceedings of the Physical Society* **80** (6) 1269–1272 (1962)
43. A. Walther, "The Question of Phase Retrieval in Optics", *Acta Optica* **10** (1) 41–49 (1963)
44. R.W. Gerchberg and W.O. Saxton, "Practical Algorithm For Determination Of Phase From Image And Diffraction Plane Pictures", *Optik* **35** (2) 237 (1972)
45. V. Elser, "Phase retrieval by iterated projections", *J. Opt. Soc. Am. A* **20** (1) 40 (2003)
46. R. Luke, "Relaxed averaged alternating reflections for diffraction imaging", *Inverse Problems* **21** (1) 37–50 (2005)
47. S. Marchesini, "Benchmarking iterative projection algorithms for phase retrieval", *arXiv:physics*/0404091 (2004)
48. G.J. Williams, "Effectiveness of iterative algorithms in recovering phase in the presence of noise", *Acta Cryst. A* **63** 36-42 (2007)

Chapter II

1. A. Rundquist, *et al.*, "Phase-Matched Generation of Coherent Soft X-rays", *Science* **280** (5368) 1412-1415 (1998)
2. E. Constant, *et al.*, "Optimizing High Harmonic Generation in Absorbing Gases: Model and Experiment", *Phys. Rev. Lett.* **82** 1668-1671 (1999)
3. R. Bartels, *et al.*, "Shaped-pulse optimization of coherent emission of high-harominc soft X-rays", *Nature* **406** 164-166 (2000)
4. M. Schüner, *et al.*, "Absorption-Limited Generation of Coherent Ultrashort Soft-X-Ray Pulses", *Phys. Rev. Lett.* **83** 722-725 (1999)
5. Y. Tamaki, *et al.*, "Highly Efficient, Phase-Matched High-Harmonic Generation by a Self-Guided Laser Beam", *Phys. Rev. Lett.* **82** 1422-1425 (1999)
6. J.F. Hergott, *et al.*, "Extreme-ultraviolet high-order harmonic pulses in the microjoule range", *Physical Review A* **66** (2) 021801 (2002)
7. S. Kazamias, *et al.*, "Global Optimization of High Harmonic Generation", *Physical Review Letters* **90** (19) 193901 (2003)
8. C.G. Wahlstrom, *et al.*, "High-order harmonic generation in rare gases with an intense short-pulse laser", *Phys. Rev. A* **48** (6) 4709–4720 (1993)
9. W. Boutu, "Dynamique de la génération d'harmoniques dans les atomes et les molecules", thesis work at *Université Paris Sud XI, Orsay, France*, (2007)
10. W. Boutu, *et al.*, "Scaling of the generation of high-order harmonics in large gas media with focal length", *Physical Review A* **84** (5) 053819 (2011)
11. A. Ravasio *et al.*, "Single-Shot Diffractive Imaging with a Table-Top Femtosecond Soft X-Ray Laser-Harmonics Source", *Physical Review Letters* **103** 028104 (2009)
12. J.C. Solem and G.C. Baldwin, "Microholography of living organisms", *Science* **218** 229-235 (1982)

13. R. Neutze, *et al.*, "Potential fro biomolecular imaging with femtosecond X-ray pulses", *Nature* **406** 752-757 (2000)
14. P. Mercère, *et al.*, "Hartmann wave-front measurement at 13.4 nm with $\lambda_{EUV}/120$ accuracy", *Opt. Lett.* **28** 1534-1536 (2003)
15. J. Gautier, *et al.*, "Optimization of the wave front of high order harmonics", *Eur. Phys. J. D* **48** 459-463 (2008)
16. J.W. Goodman, "Introduction to Fourier optics", *Roberts & Company Publishers,* 3rd edition (2005), page 491
17. H.T. Kim, *et al.*, "Optimization of high-order harmonic brightness in the space and time domains", *Physical Review A* **69** (3) 031805 (2004)
18. P.M. Celliers, *et al.*, "Spatial Filter Pinhole for High-Energy Pulsed Lasers", *Appl. Opt.* **37** 2371-2378 (1998)
19. J. Lohbreier, *et al.*, "Maximizing the brilliance of high-order harmonics in a gas jet", *New Journal of Physics* **11** 023016 (2009)
20. C. Valentin, *et al.*, "High-order harmonic wave fronts generated with controlled astigmatic infrared laser", *J. Opt. Soc. Am. B* **25** (7) B161 (2008)
21. S. Kazamias, *et al.*, "High order harmonic generation optimization with an apertured laser beam", *The European Physical Journal* **21** (3) 353 (2002)
22. W. Boutu, *et al.*, "High-order-harmonic generation in gas with a flat-top laser beam", *Physical Review A* **84** (6) 063406 (2011)
23. M. Nisoli, *et al.*, "High-Brightness High-Order Harmonic Generation by Truncated Bessel Beams in the sub-10-fs Regime", *Phys. Rev. Lett.* **88** 033902 (2002)
24. P. Villoresi, *et al.*, "Optimization of high-order harmonic generation by adaptive control of a sub-10-fs pulse wave front", *Opt. Lett.* **29** 207 (2004)
25. M. Nisoli, *et al.*, "Generation of high energy 10 fs pulses by a new pulse compression technique", *Appl. Phys. Lett.* **68** 2793 (1996)
26. E. Marcatili and R. Schmeltzer, "Hollow metallic and dielectric waveguides for long distance optical transmission and lasers", *Bell Syst. Tech. J.* **43** 1783–1809 (1964)
27. E. Snitzer, "Cylindrical Dielectric Waveguide Modes", *J. Opt. Soc. Am.* **51** 491-498 (1961)
28. C. Iaconis and I.A. Walmsley, "Spectral Phase Interferometry for Direct Electric-Field Reconstruction of Ultrashort Optical Pulses", *Opt. Lett.* **23** 792–794 (1998)
29. M.W. Sasnett, "Propagation of multimode laser beams - the M2 factor", *Physics and Technology of Laser Resonators,* D.R. Hall and P.E. Jackson, Hilger (1989).
30. A.E. Siegman, "How to (Maybe) Measure Laser Beam Quality", *DPSS (Diode Pumped Solid State) Lasers: Applications and Issues*, M. Dowley, ed., Vol. 17 of *OSA Trends in Optics and Photonics* (Optical Society of America, 1998), paper MQ1. K.Strehl,"Aplanatische und fehlerhafte Abbildung im Fernrohr", *Zeitschrift für Instrumentenkunde* **15** 362-370 (1895)

Chapter III

1. "Introduction: Focused ion beam systems" http://www.fibics.com/fib/tutorials/introduction-focused-ion-beam-systems/4/
2. M. Born and E. Wolf, "Principles of Optics: Electromagnetic Theory of Propagation, Interference and Diffraction of Light", *Cambridge University Press* 7th edition

(1999)
3. D. Shapiro, *et al.*, "Biological imaging by soft x-ray diffraction microscopy", *Proc. Natl. Acad. Sci. U.S.A.* **102** (43) 15343-15346 (2005)
4. A. Ravasio, *et al.*, "Single-Shot Diffractive Imaging with a Table- Top Femtosecond Soft X-Ray Laser-Harmonics Source", *Phys. Rev. Lett.* **103** 028104 (2009)
5. S. Marchesini, *et al.*, "Coherent X-ray diffractive imaging: applications and limitations", *Opt. Express* **11** (19) 2344 (2003)
6. M.R. Howells, *et al.*, "An assessment of the resolution limitation due to radiation-damage in X-ray diffraction microscopy", *Journal Of Electron Spectroscopy And Related Phenomena* **170** (1-3) 4-12 (2009)
7. "Signal-to-noise ratio" Http://www.princetoninstruments.com/cms/index.php/ccd-primer/172-signal-to-noise-ratio
8. M. Guizar-Sicairos, "Methods for Coherent Lensless Imaging and X-Ray Wavefront Measurement", thesis work at *The Institute of Optics Arts, Sciences and Engineering, Edmund A. Hajim School of Engineering and Applied Sciences, University of Rochester, Rochester, New York* (2010)

Chapter IV

1. S. Eisebitt, *et al.*, "Lensless imaging of magnetic nanostructures by X-ray spectro-holography", *Nature* **432** (7019) 885 (2004)
2. J.P. Hannon, *et al.*, "X-ray resonance exchange scattering", *Phys. Rev. Lett.* **61** 1245–1248 (1988)
3. J.B. Kortright, *et al.*, "Soft-x-ray small-angle scattering as a sensitive probe of magnetic and charge heterogeneity", *Phys. Rev. B* **64** 92401 (2001)
4. S. Eisebitt, *et al.*, "Polarization effects in coherent scattering from magnetic specimen: Implications for x-ray holography, lensless imaging, and correlation spectroscopy", *Phys. Rev. B* **68** 104419 (2003)
5. S.D. Bader, "Opportunities in nanomagnetism", *Rev. Mod. Phys.* **78** 1 (2006)
6. E. Beaurepaire, *et al.*, "Ultrafast Spin Dynamics in Ferromagnetic Nickel", *Physical Review Letters* **76** (22) 4250 (1996)
7. C.D. Stanciu, *et al.*, "All-optical Magnetic Recording with Circularly Polarized Light", *Phys. Rev. Lett.* **99** 047601 (2007)
8. C. La-O-Vorakiat, *et al.*, "Ultrafast Demagnetization Dynamics at the M Edges of Magnetic Elements Observed Using a Tabletop High-Harmonic Soft X-Ray Source", *Physical Review Letters* **103** (25) 257402 (2009)
9. C. Gutt, *et al.*, "Single-pulse resonant magnetic scattering using a soft x-ray free-electron laser", *Physical Review B* **81** 100401(R) (2010)
10. A. Kirilyuk, *et al.*, "Ultrafast optical manipulation of magnetic order", *Rev. Mod. Phys.* **82** (3) 2731 (2010)
11. P.J. Kelly and R.D. Arnell, "Magnetron sputtering: a review of recent developments and applications", *Vacuum* **56** 159-172 (2000)
12. Y. Martin and H.K. Wickramasinghe, "Magnetic imaging by 'force microscopy' with 1000 Å resolution", *Appl. Phys. Let.* **50** 1455 (1987)
13. S. Valencia, *et al.*, "Faraday rotation spectra at shallow core levels: 3p edges of Fe,

Co, and Ni", *New Journal of Physics* **8** 254 (2006)
14. S.W. Lovesey and S.P. Collins, "X-ray Scattering and Absorption by Magnetic Materials", *Oxford University Press, USA* (1996)
15. C. Kan, *et al.*, "Spectral and temporal structure in high harmonic emission from ionizing atomic gases", *Phys. Rev. A* **52** 4336-4339 (1995)
16. C.G. Wahlström, *et al.*, "High-order harmonic generation in rare gases with an intense short-pulse laser", *Phys. Rev. A* **48** 4709-4720 (1993)
17. K. Miyazaki and H. Takada, "High-order harmonic generation in the tunneling regime", *Phys. Rev. A* **52** 3007-3021 (1995)
18. H.J. Shin, *et al.*, "Generation of Nonadiabatic Blueshift of High Harmonics in an Intense Femtosecond Laser Field", *Phys. Rev. Lett.* **83** 2544-2547 (1999)
19. H.J. Shin, *et al.*, "Nonadiabatic blueshift of high-order harmonics from Ar and Ne atoms in an intense femtosecond laser field", *Phys. Rev. A* **63** 053407 (2001)
20. G. Lambert, *et al.*, "An optimized kHz two-colour high harmonic source for seeding free-electron lasers and plasma-based soft x-ray lasers", *New J. Phys.* **11** 083033 (2009)
21. J. Mauritsson, *et al.*, "Attosecond Pulse Trains Generated Using Two Color Laser Fields", *Phys. Rev. Lett.* **97** 013001 (2006)
22. C. Winterfeldt, *et al.*, "Colloquium: Optimal control of high-harmonic generation", Rev. Mod. Phys. **80** 117-140 (2008)
23. O. Hellwig, *et al.*, "Domain structure and magnetization reversal of antiferromagnetically coupled perpendicular anisotropy films", *Journal of Magnetism and Magnetic Materials* **319** 13 (2007)
24. O. Hellwig, *et al.*, "Domain Walls in Antiferromagnetically Coupled Multilayer Films", *Phys. Rev. Lett.* **91** 197203 (2003)
25. M. Blume, "Magnetic scattering of x rays (invited)", *J. Appl. Phys.* **57** (1) 15 (1985)
26. D. Gibbs, *et al.*, "Polarization analysis of magnetic x ray scattering (invited)", *Rev. Sci. Instrum.* **60** (7) 1655 (1989)
27. B. Vodungbo, *et al.*, "Polarization control of high order harmonics in the EUV photon energy range", *Opt. Express* **19** (5) 4346 (2011)
28. A. Tripathi, *et al.*, "Dichroic coherent diffractive imaging", *Proc. Natl. Acad. Sci. U.S.A.* **108** 13393 (2011)
29. J.J. Turner, *et al.*, "X-Ray Diffraction Microscopy of Magnetic Structures", *Physical Review Letters* **107** (3) 033904 (2011)
30. A. Thomas, *et al.*, "Magnetic imaging by x-ray holography using extended references", *Optics Express* **19** (17) 16223-16228 (2011)
31. O. Hellwig *et al.*, "Ferromagnetic stripe domain formation in antiferromagnetically-coupled Co/Pt-Co/Ni-Co/Pt multilayers studied via soft x-ray techniques", *Appl. Phys. Lett.* **98** 172503 (2011)
32. S. Flewett, *et al.*, "Method for Single-Shot Coherent Diffractive Imaging of Magnetic Domains", *Phys. Rev. Lett.* **108** 223902 (2012)
33. S. Roy, *et al.*, "Lensless X-ray imaging in reflection geometry", *Nature Photonics* **5** 243 (2011)

Chapter V

1. D.M. Gaudiosi, *et al.*, "High-Order Harmonic Generation from Ions in a Capillary Discharge", *Phys. Rev. Lett.* **96** 203001 (2006)
2. B.A. Reagan, *et al.*, "Enhanced high-order harmonic generation from Xe, Kr, and Ar in a capillary discharge", *Phys. Rev. A* **76** 013816 (2007)
3. E.A. Gibson, *et al.*, "High-Order Harmonic Generation up to 250 eV from Highly Ionized Argon", *Phys. Rev. Lett.* **92** (3) 033001 (2004)
4. M. Zept, *et al.*, "Bright Quasi-Phase-Matched Soft-X-Ray harmonic Radiation from Argon Ions", *Phys. Rev. Lett.* **99** 143901 (2007)
5. E. A. Gibson, *et al.*, "Coherent Soft X-ray Generation in the Water Window with Quasi-Phase Matching", *Science* **302** 95 (2003)
6. A.I. González and Y. Mejía, "Nonredundant array of apertures to measure the spatial coherence in two dimensions with only one interferogram", *J. Opt. Soc. Am. A* **28** (6) 1107 (2011)
7. A.C. Kak, and M. Slaney, "Principles of Computerized Tomographic Imaging", *Society of Industrial and Applied Mathematics*, (2001)
8. H. Andruleit, *et al.*, "Stereo-microscopy of coccolithophores - modern applications for imaging and morphological analysis", *J. Nannoplankton Res.* **28** (1) 1-16 (2006)
9. M. Geisen, *et al.*, "Three- dimensional imaging of coccoliths and coccospheres." Abstract for poster presented at the 8th Conference of the International Nannoplankton Association, 11th-15th September, 2000, Bremen, Germany, Journal of Nannoplankton Research, 22: 100. (2000)
10. K.S. Raines, *et al.*, "Three-dimensional structure determination from a single view", *Nature* **463** 214-217 (2010)